

All-optical time-domain demultiplexing and signal regeneration using 1300 nm semiconductor optical amplifiers

Citation for published version (APA):

Smets, R. C. J. (1999). *All-optical time-domain demultiplexing and signal regeneration using 1300 nm semiconductor optical amplifiers*. [Phd Thesis 1 (Research TU/e / Graduation TU/e), Electrical Engineering]. Technische Universiteit Eindhoven. <https://doi.org/10.6100/IR525484>

DOI:

[10.6100/IR525484](https://doi.org/10.6100/IR525484)

Document status and date:

Published: 01/01/1999

Document Version:

Publisher's PDF, also known as Version of Record (includes final page, issue and volume numbers)

Please check the document version of this publication:

- A submitted manuscript is the version of the article upon submission and before peer-review. There can be important differences between the submitted version and the official published version of record. People interested in the research are advised to contact the author for the final version of the publication, or visit the DOI to the publisher's website.
- The final author version and the galley proof are versions of the publication after peer review.
- The final published version features the final layout of the paper including the volume, issue and page numbers.

[Link to publication](#)

General rights

Copyright and moral rights for the publications made accessible in the public portal are retained by the authors and/or other copyright owners and it is a condition of accessing publications that users recognise and abide by the legal requirements associated with these rights.

- Users may download and print one copy of any publication from the public portal for the purpose of private study or research.
- You may not further distribute the material or use it for any profit-making activity or commercial gain
- You may freely distribute the URL identifying the publication in the public portal.

If the publication is distributed under the terms of Article 25fa of the Dutch Copyright Act, indicated by the "Taverne" license above, please follow below link for the End User Agreement:

www.tue.nl/taverne

Take down policy

If you believe that this document breaches copyright please contact us at:

openaccess@tue.nl

providing details and we will investigate your claim.

All-Optical Time-Domain Demultiplexing and
Signal Regeneration using 1300 nm Semiconductor
Optical Amplifiers

CIP-DATA LIBRARY TECHNISCHE UNIVERSITEIT EINDHOVEN

Smets, Robertus C.J.

All-optical time-domain demultiplexing and signal regeneration using 1300 nm semiconductor optical amplifiers / by Robertus C.J. Smets. - Eindhoven : Technische Universiteit Eindhoven, 1999.

Proefschrift. - ISBN 90-386-1660-0

NUGI 832

Trefw.: optische datatransmissiesystemen / optische signaalverwerking / optische versterkers.

Subject headings: optical communication / optical informationprocessing / optical switches.

Copyright ©1999 by R.C.J. Smets

All rights reserved. No part of this publication may be reproduced, stored in a retrieval system, or transmitted in any form or by any means without the prior written consent of the author.

Typeset by \LaTeX ; printed by University Press Facilities, Eindhoven

All-Optical Time-Domain Demultiplexing and
Signal Regeneration using 1300 nm Semiconductor
Optical Amplifiers

Proefschrift

ter verkrijging van de graad van doctor aan de
Technische Universiteit Eindhoven, op gezag van de
Rector Magnificus, prof.dr. M. Rem, voor een
commissie aangewezen door het College voor
Promoties in het openbaar te verdedigen op maandag
20 september 1999 om 16.00 uur

door

Robertus Christianus Johannes Smets

geboren op 25 september 1971 te Eindhoven

Dit proefschrift is goedgekeurd door de promotoren:

prof.ir. G.D. Khoe
en
prof.dr. A.G. Tijhuis

Copromotor:

dr.ir. H. de Waardt

Acknowledgement

The research described in this thesis started as a joint project between Philips Research Laboratories and The Eindhoven University of Technology end 1994. In a later stadium the project was implemented within the European ACTS project "Upgrade". Internal reorganisations finally led to the take-over of Philips Optoelectronics B.V., at that time already separated from the Philips organisation, by Uniphase Corporation to become Uniphase Netherlands B.V.

I express my gratitude to Dr. John Reid of Uniphase Netherlands B.V. for keeping the project alive during above mentioned reorganisations, streamlining the "Upgrade" project, and last but not least for many discussions on theoretical and practical issues. Without support of John Reid this work could not have been performed the way it has. The author wishes to thank Adie Verboven and Kees Vroomen of Philips Research Laboratories for quick, accurate and high quality work on many optical components. Many thanks go out to Dr. Gerlas van der Hoven and Dr. Leo Spiekman of the Research Division of Uniphase Netherlands B.V. for supplying and discussing semiconductor optical amplifiers. Dr. Bart Verbeek is rendered thanks to for allowing the research to take place in the highly motivating and well skilled research facility of Philips Optoelectronics B.V. and later Uniphase Netherlands B.V.

I have enjoyed the co-operation with Lucent Technologies in Nuremberg, Germany. Thanks go out to B. Teichman, Dr. C. Dorschky and Dr. R. Seitz for providing excellent and very useful high speed receivers with demultiplexers for both the Upgrade and Ph.D. project. Dr. S. Chernikov and Dr. M. Guy of Imperial College are acknowledged for their visit to the Eindhoven University of Technology for experiments that allowed me to gain experience with Raman Amplification.

The author is much obliged to Dr. Huug de Waardt for coaching and periodic technical discussions. I thank Prof. Djan Khoe for gathering funding for this project and removing impediments beyond my reach. Jean Jennen is acknowledged for many technical discussions on modelling of optical components. Hans van den Heuvel, Jean Jennen, Evert Mos, and Ronald Schimmel for supporting educational tasks that were a pleasant intermission of the Ph.D. project.

My parents, sister, partner and close friends have always shown an honest interest into my work. I appreciate the education and mental support they have given me.

Summary

During the last years all-optical signal processing has been demonstrated to be an attractive solution for upgrading the capacity of existing optical networks. In the $1.3\ \mu\text{m}$ window, chromatic dispersion in standard single-mode fibre (SSMF) is minimal, which allows long-haul high-speed transmission to be performed with relative ease. The introduction of polarisation insensitive multiple quantum well semiconductor optical amplifiers (MQW SOA) has led to the construction of long-haul transmission links, that replace conventional in-line electrical regenerators with optical repeater units (ORUs) containing MQW SOAs. When the bit rates of time multiplexed signals become too high to be generated or to be processed after detection, generation and processing can be performed in the optical domain. This processing requires a nonlinear optical component. SOAs qualify for all-optical signal-processing applications because their optical gain saturates nonlinearly. The asymmetrical placement of a saturable optical amplifier in a Sagnac interferometer results in an optical switch. The switch can be closed for a short period of time by feeding a narrow optical pulse into the Sagnac loop which saturates the optical amplifier. In the literature this optical switch is known as the “Terahertz Optical Asymmetrical Demultiplexer”, or TOAD.

In the case of 10 Gb/s to 2.5 Gb/s all-optical demultiplexing, a switch signal is required that consists of narrow optical pulses with a repetition rate of 2.5 GHz. A ring laser has been designed incorporating a SOA of which the round trip gain is modulated externally by a sinusoidal optical signal. A 2.5 GHz train of low jitter optical pulses with a full-width half-maximum time of 12 – 20 ps was generated. In combination with the optical switch, operation resulted in error free demultiplexing to 2.5 Gb/s. A power penalty of 2.3 dB was observed. Power fluctuations at the input of 13 dB did not effect error-free performance.

For all-optical time-domain demultiplexing from 40 Gb/s to 10 Gb/s a similar configuration of the optical switch was used. The purpose of constructing a 40 Gb/s to 10 Gb/s demultiplexer was to investigate 40 Gb/s, ≥ 200 km transmission using SSMF and in-line ORUs. To this end an all-optical clock recovery circuit was constructed that recovers a 10 GHz switch signal from a 10 Gb/s data signal. The circuit is based on a ring laser with a saturable amplifier and a saturable absorber. The absorber consists of a Sagnac interferometer with an asymmetrically placed SOA. An adjustable optical attenuator is also inserted in the Sagnac interferometer and allows asymmetrical excitation and saturation of the SOA. The output pulses of this structure are narrowed replicas of the input pulses. In the remainder of the cavity pulses are broadened. This resulted both theoretically and experimentally in a stable mode-locked pulse train. The pulse duration of the recovered 10 GHz switch pulses amounted to ≤ 5 ps. The recovered switch signal was suitable for error free demultiplexing of a 10 Gb/s signal from a 40 Gb/s signal in a feed-back configuration with the TOAD switch. A power penalty of 2 dB was

observed and at the input a dynamic range of 7.0 dB was achieved. A special procedure was followed to start the system and periodic corrections had to be made while the whole setup was free-running.

This setup was used to bridge 216 km of SSMF incorporating in-line ORUs. To avoid excess gain, the length of the sections were matched to the gain of the ORUs. It has been demonstrated that excess gain results in saturation, pattern effects and increased noise levels which compromises error free transmission. After 216 km this 40 Gb/s signal was demultiplexed to 10 Gb/s and detected error free. A power penalty of 4.0 dB resulted from the 216 km transmission. In addition, all four channels behaved almost identically.

The experimental setup also functioned as a 10 Gb/s all-optical regenerator. Excess gain during transmission was demonstrated to cause distortions resulting in “noise floors” that could be removed by employing the same configuration used in the 40 to 10 Gb/s demultiplexing experiment.

Theoretical analysis of the optical switch reveals a strong dependence on the choice of the optical coupler of the Sagnac interferometer. For quantitative theoretical analysis of the performance of the optical switch, a new definition of channel extinction ratio was introduced. The channel extinction ratio is defined as the quotient of the energy of the forward transmitted window (desired signal) and the energy that leaks through outside this window (undesired signal). Different simulations have been carried out for 40 Gb/s to 10 Gb/s demultiplexing with different parameters for the coupler, amplifier and switch signal. Three amplifier models of increasing complexity were numerically implemented in simulation tools for simulating the TOAD configuration.

In this thesis it is demonstrated that, future 40 Gb/s transmission systems can be realised in the 1.3 μm window using 1.3 μm MQW SOAs. Polarisation-insensitive MQW SOAs can be used both for in-line amplification and as nonlinear element in signal-processing applications like all-optical time-domain demultiplexing, all-optical clock recovery and all-optical regeneration. In future all-optical high-speed networks, several all-optical signal processing applications may be integrated to form nodes that autonomously configure and route data streams.

Contents

1	Introduction	1
1.1	Historical overview of optical transmission	1
1.2	The optical time-domain multiplexing concept	5
1.2.1	Electrical and optical time-domain multiplexing	5
1.2.2	Different classes of OTDM systems	7
1.2.3	Types of optical switches for all-OTDM	9
1.3	Nonlinear transmission and optical solitons	12
1.4	Objective and strategy	16
2	Optical amplification and switching	21
2.1	Introduction	21
2.2	Fibre amplifiers	21
2.2.1	Erbium-doped fibre amplifier	21
2.2.2	Praseodymium-doped fluoride fibre amplifier	22
2.2.3	Raman amplifier	23
2.3	Semiconductor optical amplifier	23
2.3.1	Spatially-concentrated uni-directional noise-less saturable optical amplifier	24
2.3.2	A spatially-concentrated uni-directional noisy saturable optical amplifier	27
2.3.3	A non-zero length bi-directional noisy saturable optical amplifier	29
2.3.4	Parameters of the multiple quantum-well SOA	31
2.4	Sagnac interferometer	34
2.5	The terahertz optical asymmetrical demultiplexer	38
2.5.1	Dirac delta pulse switching of the TOAD with zero length SOA	40
2.5.2	Non-zero pulse width switching of a TOAD with zero length SOA	51
2.5.3	Non-zero pulsewidth switching of the TOAD with non-zero length SOA	59
2.6	Summary	71
3	Key components and system blocks	73
3.1	Optical sources and modulators	73
3.1.1	DFB laser diode	73
3.1.2	External-cavity tuneable mode-locked laser	76

3.1.3	10 Gb/s optical modulator	77
3.2	Optical fibre	78
3.3	Polarisation insensitive MQW amplifier modules	79
3.4	Optical detectors and receivers	82
3.4.1	PIN photodiode based detector	82
3.4.2	2.5 Gb/s receiver	82
3.4.3	10 Gb/s receiver	86
3.4.4	Optically preamplified receiver	89
3.4.5	Theoretical model of an optical receiver	89
3.5	Miscellaneous components	91
3.5.1	Tuneable optical filters	91
3.5.2	Adjustable optical delay lines	92
4	10 Gb/s transmission experiments	95
4.1	RZ (soliton) versus NRZ formatted transmission	95
4.2	Repeatered and unrepeatered RZ transmission	95
4.3	Distributed Raman amplification	104
4.4	Wavelength and input power dependent transmission	106
4.4.1	Introduction	106
4.4.2	Experimental setup	107
4.4.3	Experimental results and interpretation	109
4.4.4	Conclusions and recommendations	114
5	All-optical signal processing systems	117
5.1	All-optical cross gain-switched ring laser	117
5.1.1	Introduction	117
5.1.2	Theory	119
5.1.3	Experimental setup	120
5.1.4	Experimental results and discussion	121
5.1.5	Conclusions and recommendations	123
5.2	10 Gb/s all-optical clock recovery	124
5.2.1	Introduction	124
5.2.2	Theory	126
5.2.3	Experimental setup	133
5.2.4	Results and discussion	134
5.2.5	Conclusion and recommendation	141
5.3	10 Gb/s to 2.5 Gb/s all-OTDM	141
5.3.1	Introduction	141
5.3.2	Experimental setup	141
5.3.3	BER performance versus input powers	145
5.3.4	BER performance versus time delays	150
5.3.5	Miscellaneous experiments	150
5.3.6	Discussion and Conclusions	155
5.4	40 Gb/s to 10 Gb/s all-OTDM	156
5.4.1	Introduction	156
5.4.2	Experimental setup	156

5.4.3	BER performance versus input powers	159
5.4.4	BER performance versus time delays	162
5.4.5	Miscellaneous experiments	162
5.4.6	Discussion and conclusions	165
5.5	216 km, 40 Gb/s transmission using SOAs	165
5.5.1	Introduction	165
5.5.2	Experimental setup of the 216 km transmission system	168
5.5.3	Results and discussion	169
5.5.4	Conclusions and recommendations	177
5.6	All-optical regeneration at 10 Gb/s	178
5.6.1	Introduction	178
5.6.2	Experimental setup	179
5.6.3	Results and discussion	179
5.6.4	Conclusions and recommendations	183
6	Discussion	185
6.1	Long-haul high-speed transmission	185
6.1.1	Dispersion management	185
6.1.2	In-line amplification	186
6.1.3	RZ versus NRZ versus hybrid	187
6.2	all-OTDM, regeneration and all-OCR	188
6.2.1	All optical multiplexing	188
6.2.2	TOAD and other switches for demultiplexing	188
6.2.3	Optical clock recovery configurations	190
6.2.4	Optical regeneration	190
6.3	Implementation in commercial system designs	191
6.3.1	Requirements	191
6.3.2	Stability	191
6.3.3	Integration	191
6.4	Recent and future developments	192
6.4.1	ETDM or OTDM	192
6.4.2	WDM	192
6.4.3	Hybrid multiplexing	193
6.4.4	The future role of (all)-optical signal processing	194
7	Conclusions and recommendations	197
7.1	Conclusions	197
7.2	Recommendations	199
A	List of abbreviations	201
B	Samenvatting	203
C	Curriculum vitae	205

Chapter 1

Introduction

Today, telecommunications are natural elements just the way electricity, water and heating already are. The telephone, Internet and mass media enabled mankind to broaden their horizon. The community has adopted to rely on telecommunication systems to satisfy its needs for information and communication. Comprehensive encyclopaedias with sounds and motion pictures, tele-working and tele-shopping are a few applications that have led to an increasing demand for a larger, faster and more sophisticated communications network. At the trunk level, this network exists of fibre-optic cables. Access to the home is largely based on unshielded twisted pair copper wiring. The demand for more network capacity has challenged researchers to develop and incorporate new technologies, like wavelength-division multiplexing (WDM) and optical time-domain multiplexing (OTDM). In this process researchers encounter physical problems that impose severe limitations. In specific situations one can actually profit from a physical phenomenon that is originally seen as a problem. Chromatic dispersion of optical fibre and optical fibre and amplifier nonlinearities are effects that usually restrict the transmission capacity. However, when properly controlled, some of these effects may sometimes compensate each other, thus improving the performance of optical communication systems.

In this introductory chapter, first a historical overview of the developments in the field of optical communications is given. Subsequently, the concept of optical time-domain multiplexing is explained. A short treatment on nonlinear communications in optical fibre is presented in Sec. 1.3. The last section provides an overview on how the treatment of optical time-domain multiplexing technology is implemented in this thesis.

1.1 Historical overview of optical transmission

Optical fibre

The 1950s can be regarded as the decade where optical fibre characteristics improved to a level where optical transmission became possible [1]. A cladding layer of low refractive index glass surrounding a high refractive index glass core proved to confine light efficiently. During the 1970s fibre losses decreased from 20 dB/km to a value that is close to the limit (Rayleigh scattering and infrared absorption in silica-based fibres) of 0.2 dB/km at 1.55 μm [2], [3]. The

availability of low-loss fibres led to the theoretical and experimental investigation of nonlinear phenomena such as four-wave mixing, self-phase modulation and stimulated Raman and Brillouin scattering. In 1980 optical solitons were observed [4] in optical fibres according to predictions made in 1973 [5]. In the beginning of the 1980s multimode fibre (MMF) was superseded by single-mode fibre (SMF) which led to a vast improvement of direct detection systems. Mode dispersion was no longer a limiting factor. In the 1.3 μm window zero chromatic dispersion allowed bit rates to increase. Although fibre loss was low (0.35 dB/km at 1.3 μm) it still limited the maximum transmission distance. By doping the fibre core in a specific way the dispersion profile could be shifted to higher wavelengths. In the 1.5 μm window zero chromatic dispersion was obtained. By carefully designing the index profiles of the fibre the minimum loss at 1.5 μm became 0.22 dB/km. Not only dispersion-shifted fibre (DSF) but also dispersion-flattened fibre (DFF) has been realised which provides low dispersion across both windows. So far, more than 200 million kilometres of standard single-mode fibre (SSMF) have been installed world wide. Most of this fibre was initially intended for 1.3 μm but is now also being used for 1.5 μm . Today SSMF as well as DSF are being installed that are capable of sustaining communications at 1.5 μm as well as 1.3 μm .

Optical sources

Equally important is the progress in the field of laser physics. In 1953 carrier injection in a P-N junction was proposed to provide stimulated emission, i.e., optical gain [6]. About ten years later, in 1962, the semiconductor laser was demonstrated by several research groups [7], [8]. In the 1970s, difficulties in the fabrication process of laser diodes were solved. Laser diodes, that could be implemented in optical communication systems, were made available. These first lasers were of the Fabry P erot type and were made from GaAs, a binary compound. Large threshold currents and low efficiencies were characteristic for these devices. This progress triggered researchers in the field of optical fibre and vice versa. Over the years new technologies evolved such as the buried heterostructure laser diode which resulted in lower threshold currents and improved efficiencies. Distributed feedback (DFB) laser diodes [9] reduced the large dispersion penalties caused by the broad line-spectrum of the Fabry P erot laser diode. New materials like InGaAsP allowed for smaller band gaps resulting in laser diodes for the telecommunication windows at 1.3 μm and 1.5 μm . In 1985 the first laser diode with a bandwidth beyond 10 GHz was demonstrated [10], rapidly followed by a 16 GHz [11] and a 22 GHz [12] laser diode for the 1.3 μm window and suitable for pulse amplitude modulation.

In addition to the development of semiconductor laser diodes that offer a flat frequency response starting at DC so that they can be employed in direct amplitude modulation schemes, sinusoidally modulated ring lasers that produce short optical pulses of high (peak) intensity have also been developed to investigate fibre nonlinearities. Over the years, several mechanisms to obtain these short pulses have been investigated. First active mode-locking was demonstrated by Ho [13] where 23 ps wide optical pulses were obtained. The introduction of a saturable absorber led to the generation of pulses with widths of less than 10 ps [14]. In addition to mode-locking, gain switching and Q-switching also provided optical pulses. In [15] it was first demonstrated that the relaxation oscillations of a laser diode could be exploited by modulating a laser from below threshold. Twenty picosecond wide optical pulses were observed. Characteristic for gain switching is that the pulse width lies generally above 10 ps.

The introduction of the saturable absorber merged gain switching and Q-switching. Now the saturable absorption controlled the total gain of the laser. Larger inversion can be obtained before a high intensity pulse is emitted. After emission of the pulse, the inversion of the gain medium is reduced to a level slightly above threshold.

Today, actively and passively mode-locked lasers are composed of amplifying, absorbing, phase matching and tuning sections in a Fabry P erot cavity or in a ring cavity. They provide optical pulses with pulse widths below 1 ps and repetition rates from a few GHz to 100 GHz which can be implemented in systems with bit rates exceeding 200 Gb/s [16]. The introduction of the Erbium-doped fibre amplifier introduced additive pulse mode-locking techniques where the fibre nonlinearity causes intensity dependent polarisation rotations resulting in fast saturable absorption when these pulses are discriminated by a polariser [17], [18], [19].

Optical amplification

Optical amplifiers can be divided into two groups, the semiconductor optical amplifiers (SOAs) and the fibre optical amplifiers (FOAs). Semiconductor optical amplifiers are basically semiconductor laser diodes that have no resonators. Since the successful demonstration of the semiconductor laser diode, the device received considerable attention as a potential optical amplifier. In order to increase the gain of the amplifier the reflectivity of the mirrors needs to be eliminated. In 1966 anti-reflective coatings were deposited at the end faces to reduce reflectivities. As in the case of laser diodes, similar advanced structures were used to improve the characteristics of semiconductor optical amplifiers. In the 1990s quantum well laser amplifiers were developed. The main motives were to increase the saturation output power and to improve noise performance. Furthermore, better (anti-reflective) coatings were developed and by placing the endfaces in an oblique position the reflection coefficient could be further reduced. Polarisation insensitive amplifiers with gains beyond 30 dB and saturation output powers up to 16 dB can now be achieved both for the 1.3 μm and 1.5 μm window [20], [21], [22]. Although in 1963 the first fibre lasers were demonstrated it was not before 1987 that a fibre amplifier was realised that could contribute to the ongoing research in optical telecommunications [23]. The advantages of fibre amplifiers are high gain, low noise, polarisation insensitivity and high saturation output power. Today most applications are focused on 1.5 μm fibre amplified systems. Due to a limited number of suitable material compositions the development of a 1.3 μm fibre amplifier is more difficult. It has been demonstrated that 1.3 μm praseodymium-doped fibre amplifiers (PDFAs) providing 25 dB of optical gain can be mounted on a printed circuit board fitting a single slot of a standard telecommunications rack [24].

Wavelength- and time-division multiplexing

Over the years the fibre network had to be updated constantly. Space-division multiplexing is the easiest way of increasing the capacity of the network. This method works well until all the installed fibres are in use and new fibres must be installed which is financially not attractive. Therefore this is not considered a realistic option. Instead, expansion of the network capacity can be achieved by electrically multiplexing several data signals to a signal of higher bit rate, called electrical time-domain multiplexing (ETDM). This multiplexed signal will drive a high-bandwidth laser diode. At the receiver side the bandwidth of the receiver must be en-

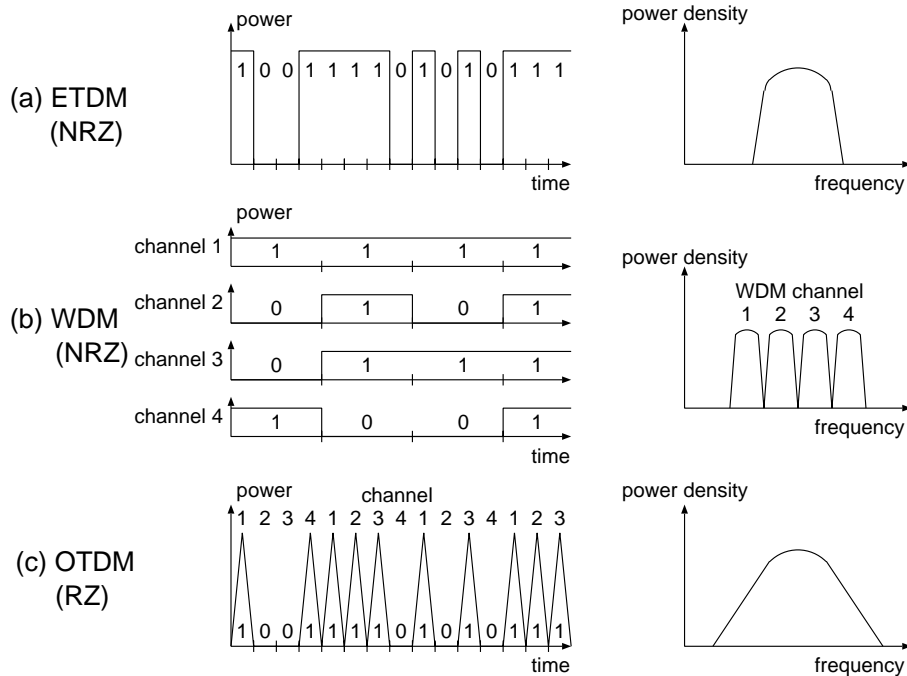


Figure 1.1: (a) Time domain and spectral representation of an electrically time-domain multiplexed signal (ETDM), (b) a wavelength-division multiplexed (WDM) and (c) an optically time-domain multiplexed (OTDM) system. In the case of ETDM and WDM system non-return to zero (NRZ) data formats are used and in the case of the OTDM system a return to zero (RZ) data format is used.

larged and high-speed electronics are needed to demultiplex the received signals to lower bit rates. In the optical frequency domain a scenario suited for telecommunications was proposed by Tomlinson and Aumiller in 1977 [25] which resembles a wavelength-division multiplexed (WDM) system; each separate signal is allocated a specific wavelength. Over the years many different WDM systems have been presented with increasing number of channels per unit bandwidth and transmitting distances beyond 10,000 kilometres [26], [27], [28]. Recently, a commercial system has become available that transmits 40 channels of 2.5 Gb/s using a single optical fibre. The first communication system using optical time-division multiplexing (OTDM) was presented in 1968 by Bell Telephone Laboratories [29], [30]. See Sec. 1.2 for a detailed explanation of OTDM concept. They used a LiTaO_3 sinusoidal polarisation switch [31] to isolate a selected channel. In 1972 a 24 channel OTDM system was evaluated experimentally, [32], and OTDM as a means to upgrade the fibre network became reality. Figure 1.1 depicts for (a) an ETDM, (b) a WDM and (c) an OTDM signal the time domain and spectral representations. ETDM and WDM signals usually contain non-return to zero (NRZ) pulses which are pulses that do not return to zero within one bit time. Consequently, between two successive logical "1"s the optical power remains unchanged. OTDM signals use return to

zero (RZ) pulses which start with zero power and end with zero power within one bit time. Between two successive logical “1”s the optical power reduces to zero. If RZ pulses are narrow enough they can be interleaved without overlap. In the years to follow different optical switches and gates were developed. The performance of the pulsating lasers improved and the free space optics were replaced by fibre optics. The optical switch remained controlled by electrical signals. In 1988 self switching in a nonlinear optical loop mirror (NOLM) was demonstrated and a few years later the same loop was operated with two optical signals; the high intensity signal controlled the throughput of the low intensity signal. At this point all-optical time-domain demultiplexing became a realistic possibility for upgrading the fibre network. Today, WDM and OTDM are well established technologies. A hybrid WDM and OTDM experiment [33] demonstrates that it is possible to multiplex in the wavelength domain four 40 Gb/s signals. Each 40 Gb/s is optically multiplexed in the time domain from four 10 Gb/s signals.

All-optical signal processing and clock recovery

In addition to optical time-domain demultiplexing other optical signal processing functionalities have been realised over the years. From the early 1990s researchers have been focusing on applications like optical wavelength conversion, optical header recognition, optical sampling [34], optical bit rate conversion and optical packet buffering [35], [36], [37], [38]. Some of these all-optical signal processing applications require an optical clock that is extracted from the signal to be processed. All-optical clock recovery was first demonstrated in 1991 [39] at a bit rate of 5 Gb/s using a self pulsating laser diode. In 1993, 40 Gb/s all-optical clock extraction was demonstrated [40]. A passively mode-locked ring laser generated 40 GHz nearly transform limited picosecond pulses. Today, clock recovery circuits based on self pulsating laser diodes [41] as well as all fibre devices [42] have been demonstrated for both the 1.3 μm and 1.55 μm telecommunications window.

1.2 The optical time-domain multiplexing concept

1.2.1 Electrical and optical time-domain multiplexing

In Section 1.1 a short overview of the development of the optical time-domain multiplexing (OTDM) technology was given. The main difference between an electrical and an optical time-domain multiplexed systems is that in ETDM systems the high speed signal is unravelled electronically, i.e. after detection by a photodiode, while in the case of OTDM systems this is done in the optical domain before detection by the photodiode. Figure 1.2 displays schematically an ETDM (a) and an OTDM (b) optical transmission system. In the case of the ETDM system one usually employs a non-return to zero data format because of its bandwidth efficiency. In the case of an OTDM system a return to zero format is mandatory otherwise the optical pulses of the different channels will overlap in time. Most OTDM transmitters are built according to the scheme displayed in Fig. 1.2 where all channels are modulated separately at a low bit rate and interleaved to form the high bit rate line signal. This interleaving can only be performed correctly if the duty cycle, d , of the RZ pulses of the

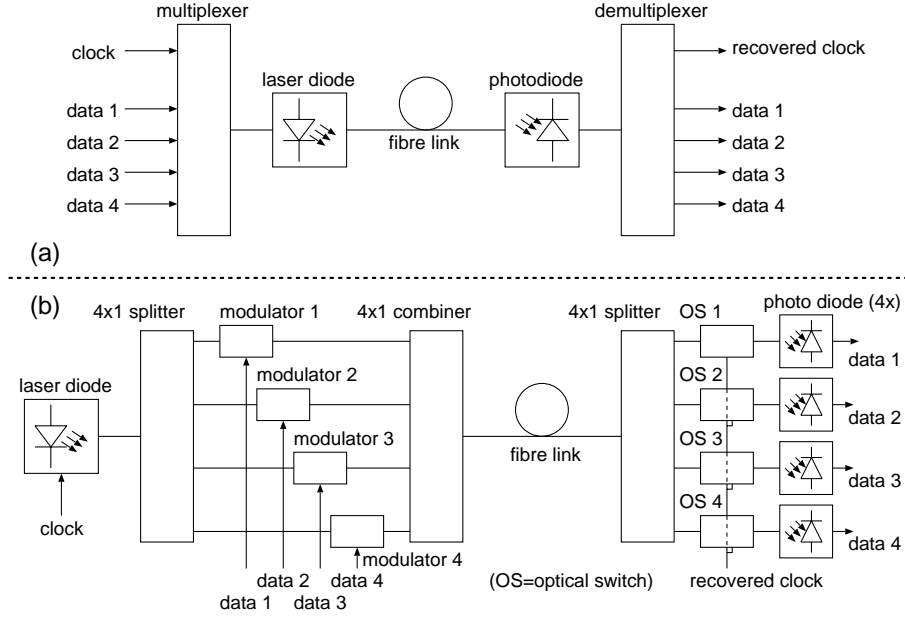


Figure 1.2: (a) An electrically time-domain multiplexed (ETDM) system, (b) An optically time-domain multiplexed (OTDM) system

individual channels satisfies

$$d \leq \frac{1}{N_{channel}}, \quad (1.1)$$

and each channel experiences a different delay equal to a multiple of

$$\tau_{delay} = \frac{T_{b,channel}}{N_{channel}}, \quad (1.2)$$

relative to all other channels. $N_{channel}$ is the number of channels and $T_{b,channel}$ is the bit time of each channel. Figure 1.3 displays an example of four channel multiplexing where for different duty cycles the multiplexed signal is constructed. NRZ signals can be thought of as RZ signals with a duty cycle of 100%. In this example the maximum duty cycle is 25%. In this case the multiplexed signal changes into a NRZ format. If the channels are modulated with a NRZ signal the corresponding multiplexed signal is distorted to an extent where no reconstruction of the original data patterns is possible. In practice, duty cycles below $\frac{1}{N_{channel}}$ are used to avoid beating effects due to interference of the leading and trailing edges of the RZ pulses when they are combined to form the multiplexed signal. Therefore, the optical modulators can only be driven by narrow pulses. This would require large bandwidth optical modulators. Generally NRZ signals have a smaller bandwidth than RZ signals. Instead of a laser source that emits continuous light a source that generates an optical pulse train can be used. If these optical pulses do not stretch out beyond the time interval dictated by the

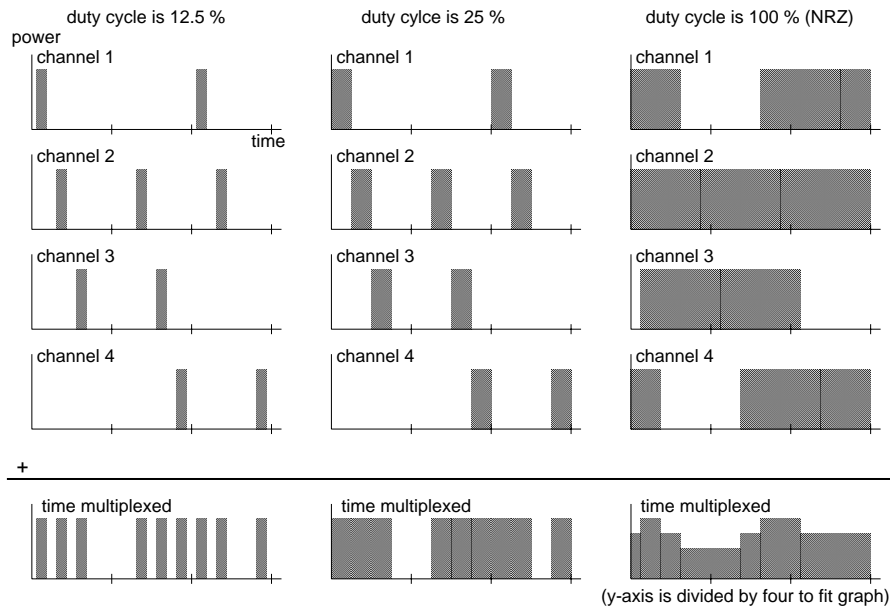


Figure 1.3: Example: For different duty cycles, four data channels and the corresponding time multiplexed signal are constructed. The modulation patterns for channel 1,2,3 and 4 are “101”, “111”, “110” and “011”, respectively.

maximum allowable duty cycle than the electro-optic modulators can be driven by a NRZ data pattern. Electro-optic modulators with a lower electrical bandwidth can now be used.

1.2.2 Different classes of OTDM systems

OTDM systems can be divided into a number of categories depending to what extent optical technologies are utilised. Figure 1.4 displays block diagrams of the three different categories of optical demultiplexing.

1. Electrically controlled optical switching using electrical clock recovery. In this case the optical switches (see Fig. 1.4 (a)) are controlled by an electrical clock signal. In general, a sinusoidal signal is used. Sometimes a third harmonic is added to increase the rising and falling edges of the electrical switch signal in order to improve the contrast of the induced time window. The electrical signal is retrieved from the received signal using conventional clock recovery techniques. LiNbO_3 [43] and electro-absorption modulators [44] are often used and can be cascaded to obtain more switching contrast.
2. Optically controlled optical switching using electrical clock recovery. Here optical switches are controlled by means of an optical signal. In this category, see Fig. 1.4 (b), usually a clock signal is extracted from the detected signal and is fed into a laser diode that provides the optical switch signal [45], [46].

3. Optically controlled optical switching using all-optical clock recovery (Fig. 1.4 (c)). This class is referred to as all-optical time-domain multiplexing. In addition to an all-optical switch, an all-optical clock recovery circuit is required that extracts an optical pulse train from the optical data. To obtain optimal performance the width of the recovered clock pulses must be the same as or smaller than the width of the pulses of the received line signal.

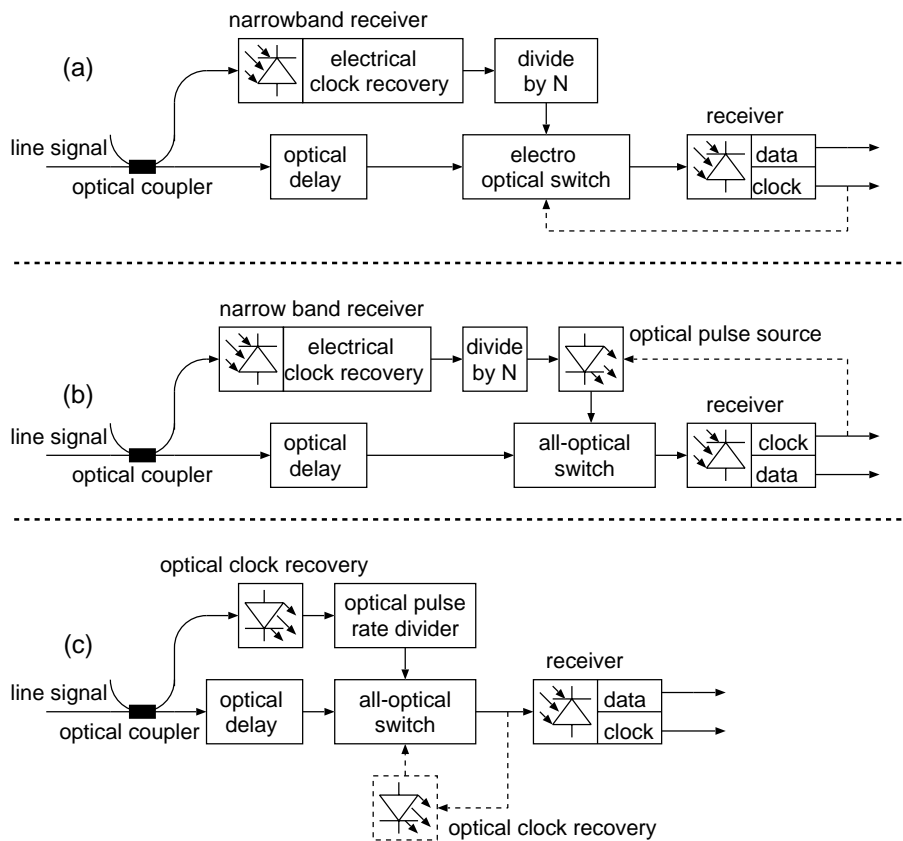


Figure 1.4: (a) Optical demultiplexing with electrical clock recovery, (b) optical clock recovery using an all-optical switch with electrical clock recovery driving a laser pulse source, (c) all-optical demultiplexing with all-optical clock recovery. The dashed lines show alternatives for the generation of the switch signal.

The dashed lines in Fig. 1.4 provide alternative ways to obtain a switch signal. An adjustable optical delay should be inserted into the dashed lines to be able to allow the selection of a desired channel.

1.2.3 Types of optical switches for all-OTDM

Optical switches that can be found in all-optical time-domain systems perform a nonlinear operation on the line signal that consists of time multiplexed channels. Therefore, switching properties are derived from the nonlinear interaction of the switch signal on the line signal via a nonlinear element. Up till now, a limited number of nonlinearities are employed in OTDM switches. The optical fibre nonlinearity and the nonlinear saturation of optical amplifiers are the two most important examples.

Fibre nonlinearity based switches: Nonlinear optical loop mirror

The nonlinear optical loop mirror (NOLM) [47] is the first all-optical switch whose operation relies on fibre nonlinearity, specifically a phase difference induced by self-phase modulation in an optical fibre. Its ability to switch optical solitons has been demonstrated in the work described in [48]. The same year optical demultiplexing was demonstrated [49]. A NOLM based demultiplexer is depicted in Fig. 1.5. Operation of the NOLM is treated only qualitatively because detailed operation can be found in the literature [50].

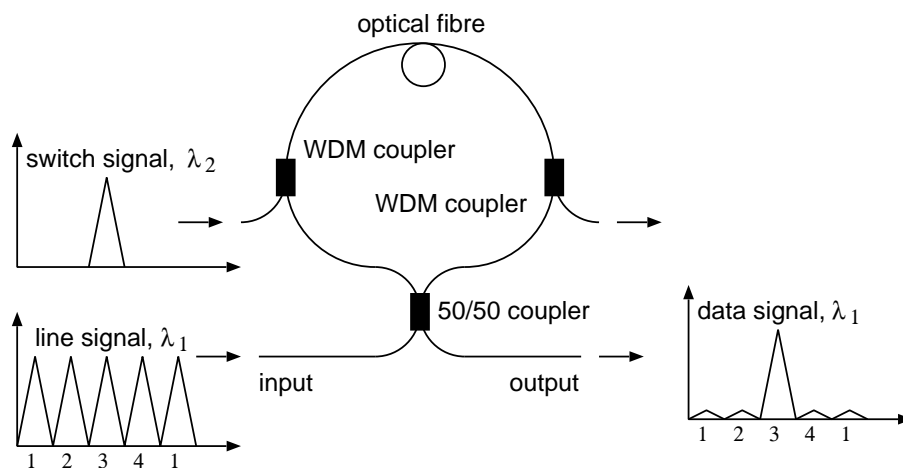


Figure 1.5: A nonlinear optical loop mirror (NOLM) is configured as a four-channel optical demultiplexer. A loose fibre, indicated with no arrow, is considered to be terminated in such a way that no light can enter the fibre and that light leaving the fibre is not reflected.

actively because detailed operation can be found in the literature [50]. A 50/50 coupler splits the low-intensity line signal into a clockwise and counter clockwise travelling signal. The counter clockwise travelling signal has a 90° phase shift with respect to the clockwise travelling signal due to the operation of the coupler. If no switching signal is applied the counter clockwise travelling signal will again experience a 90° phase shift compared to the clockwise travelling signal when coupled to the output port. At the output the two signals that counter propagate in the loop will interfere destructively. According to the law of energy conservation the entire line signal is reflected. If high-intensity switch pulses are present and travel clockwise co-located with the pulses of a pre-determined channel, cross-phase modulation

imposes an additional 180° phase shift on these pulses. In this configuration, cross-phase modulation involves the nonlinear dependence of the refractive index of the fibre and the propagation constant of optical signals in the fibre, on the optical power in the fibre. This way, a high-intensity signal can change the phase of different low-intensity signals. As a result the clockwise and counter clockwise travelling signals will interfere constructively for the selected channel. The remaining pulses, belonging to the not selected channels, interfere destructively, i.e., are reflected. If the fibre loop is made long enough for optical solitons to obtain a time independent phase the switching efficiency can become close to 100%. The fibre nonlinearity is instantaneous and allows for Tb/s switching. If the loop is too long and the difference in wavelength between the switching and line signal is too large, pulse walk-off will occur. A difference in group velocity between the line and switch signals will result in switch pulses that are no longer co-located with the pulses of the pre-determined channel but with neighbouring pulses belonging to not selected channels. As a result constructive interference does not only occur for the desired channel but also for neighbouring channels.

Fibre nonlinearity based switches: Nonlinear amplifying loop mirror

The nonlinear amplifying loop mirror (NALM) contains an optical amplifier inside the loop. It is not the nonlinearity of the amplifier that is responsible for the optical switching but the nonlinear induced cross-phase modulation in the fibre. The principle of operation is similar to

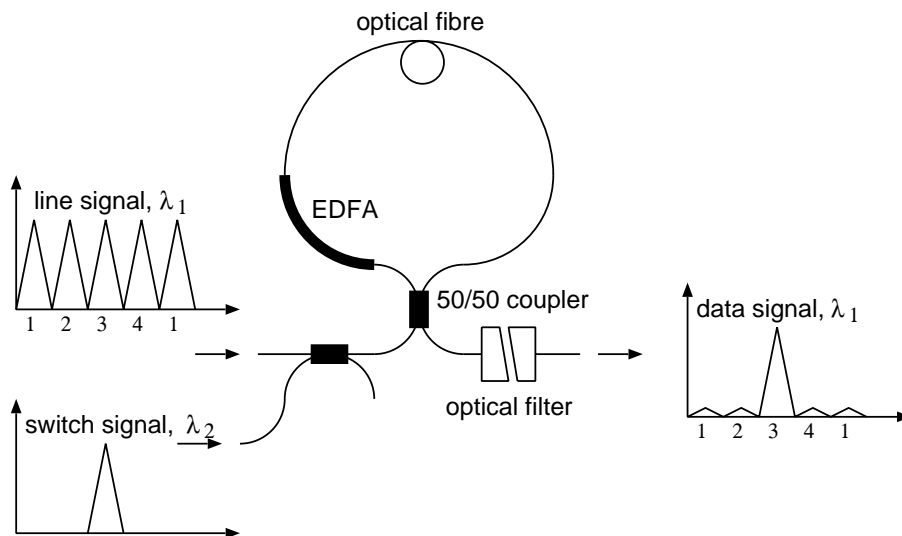


Figure 1.6: A nonlinear amplifying optical loop mirror (NALM) configured as a four-channel optical demultiplexer.

that of the NOLM except that the switch signal propagates clockwise and counter clockwise. Due to the EDFA the clockwise travelling switch pulse becomes stronger than the counter clockwise travelling switch pulse. This allows only the clockwise travelling switch pulse to induce a phase shift (i.e. to add an additional 180 degrees phase shift) on the co-propagating

line signal [51] via cross-phase modulation in the optical fibre. The main advantage of this configuration is that of an improved sensitivity which is equal to the sensitivity of the NOLM divided by the gain of the EDFA, see Fig. 1.6. This configuration only works with a slow amplifier because saturation effects will cause undesirable phase and amplitude distortions on the clockwise and counter clockwise travelling data signals.

SOA nonlinearity based switches: Four-wave mixing

Amplifier nonlinearity based switches rely either on the saturation of the gain or on four-wave mixing (FWM) in an optical amplifier. Four-wave mixing is induced by the nonlinear susceptibility of the amplifier and is largely determined by material properties. FWM is a phenomenon that occurs when two strong signals are present. When phase matching occurs a gain grating is formed by the nonlinear gain which is the result of spectral hole burning [52]. Although there is still an ongoing discussion on the mechanism behind the generation of the gain grating, four-wave mixing is characterised by the generation of two new frequency components equal to

$$\omega_{data,1} = 2\omega_{line} - \omega_{switch}, \quad (1.3)$$

and

$$\omega_{data,2} = 2\omega_{switch} - \omega_{line}. \quad (1.4)$$

Figure 1.7 shows how four-wave mixing in a semiconductor optical amplifier is used to demultiplex a line signal. Strong optical switch pulses are co-propagating with the bits of the

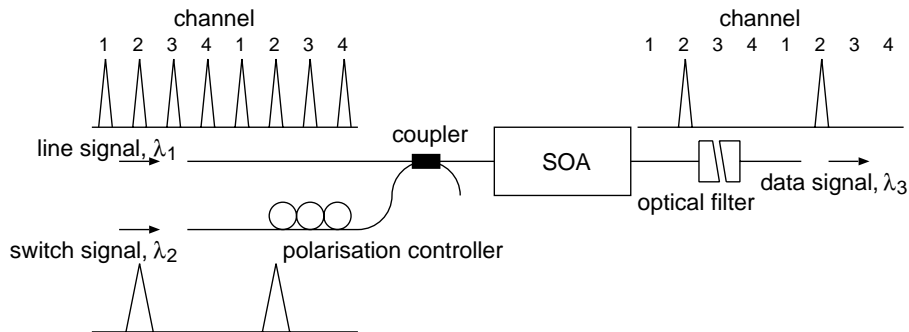


Figure 1.7: Optical demultiplexing using four-wave mixing (FWM). Example shows demultiplexing of channel 2 from four channels.

channel to be demultiplexed and induce FWM. At the output of the amplifier a new frequency component appears that contains only those bits that interacted with the switching pulses. An optical filter is used to discriminate the new signal from the switching and line signals. The FWM efficiency lies in the order of 0.1% to 1% and strongly depends on the frequency separation. The maximum difference in wavelength of the line signal and switch signal for reasonably efficient FWM is only a few nanometres which makes discrimination of the demultiplexed signal difficult.

SOA nonlinearity based switches: Interferometer based switches

Instead of a nonlinear fibre a semiconductor optical amplifier can be implemented in the Sagnac interferometer. Now it is the saturation of the gain that provides phase differences for clockwise and counter clockwise travelling waves. There are two types of optical demultiplexers, the terahertz optical asymmetrical demultiplexer (TOAD) (Fig. 1.8 (a)) and the semiconductor laser amplifier in a loop mirror (SLALOM) (Fig. 1.8 (b)). The TOAD will be treated in detail in Chapter 2. When polarisation insensitive semiconductor optical amplifiers are used, the demultiplexer will be nearly polarisation independent and suitable for implementation in a system. In addition, SOAs are broadband devices and will therefore allow Gb/s wavelength independent demultiplexing. Due to the high gain of the amplifiers they can perform as optical preamplifiers and optical switches in one configuration. If two amplifiers are available then a Mach Zehnder interferometer based optical switch can be constructed (Fig. 1.8 (c)) with the advantage that no optical filter is needed to separate the data signal from the switch signal because the switch signal propagates in the opposite direction.

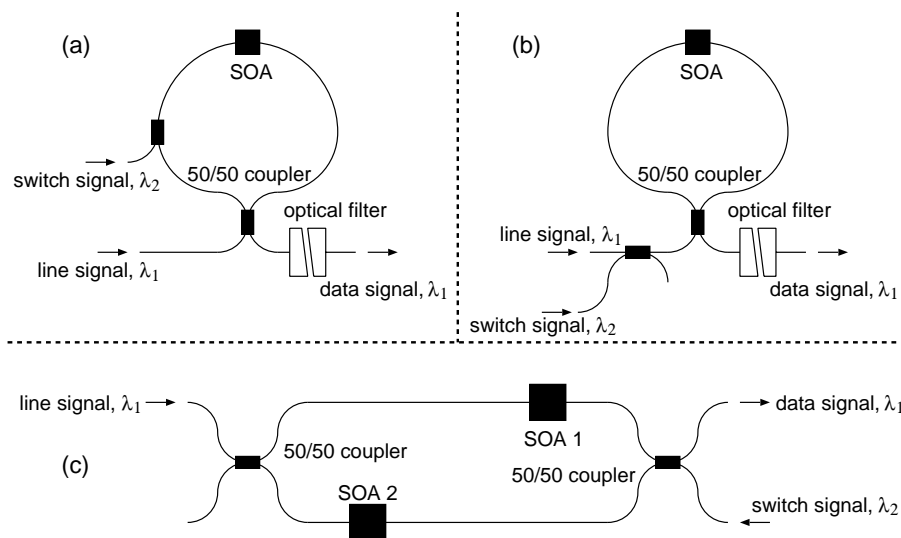


Figure 1.8: Optical demultiplexers using gain saturation of semiconductor optical amplifiers. (a) The terahertz asymmetrical optical demultiplexer (TOAD), (b) the semiconductor laser amplifier in a loop mirror (SLALOM) and (c) a Mach Zehnder interferometer based optical demultiplexer.

1.3 Nonlinear transmission and optical solitons

Nonlinear optical transmission occurs if the propagation properties of an optical pulse depend on the optical power of that pulse. In the case of fibre optics it is the nonlinearity of the optical fibre that can cause distortion of the data signal. In 1973 the idea arose that optical fibres

could support solitons [5] similar to the way they were observed in a shallow boat-channel by John Scott Russell in 1863. Under the right conditions (lossless fibre) chromatic dispersion in optical fibres interacts with self-phase modulation (SPM), induced by an optical pulse strong enough to excite the fibre nonlinearity.

Chromatic dispersion

Chromatic dispersion finds its origin in the wavelength dependence of the refractive index of the optical fibre. Via the propagation parameter $\beta(\omega)$,

$$\beta(\omega) = \frac{n(\omega)\omega}{c} = \beta_0 + \beta_1(\omega - \omega_0) + \frac{1}{2}\beta_2(\omega - \omega_0)^2 + \frac{1}{6}\beta_3(\omega - \omega_0)^3 + \dots, \quad (1.5)$$

with

$$\beta_m = \left[\frac{d^m \beta(\omega)}{d\omega^m} \right]_{\omega=\omega_0}, \quad (1.6)$$

dispersion acts on the phase of the spectral components of the optical field of a pulse in such a way that rising and falling times of leading and trailing edges increase. β_1 is the inverse of the group velocity, the speed with which the envelope of the optical signal travels. The group-velocity dispersion (GVD) parameter, β_2 , is related to the dispersion parameter D according to

$$\beta_2 = -\frac{\lambda^2}{2\pi c}D. \quad (1.7)$$

For standard single-mode fibres (SSMF) dispersion, β_2 and D , becomes zero in the 1.3 μm window (the exact zero-dispersion wavelength depends on the doping profile of the fibre) at wavelength λ_D . For wavelengths $\lambda < \lambda_D$ the dispersion is negative. In this normal dispersion regime higher frequency shifted components of the spectrum travel slower than the lower frequency shifted spectral components. For $\lambda > \lambda_D$ the dispersion is positive. This regime is referred to as the anomalous-dispersion regime where the higher frequency components of an optical pulse travel faster than the lower frequencies in the spectrum. When the wavelength of operation is close to the zero-dispersion point, λ_D , higher order dispersion coefficients like β_3 cannot be ignored [53].

Fibre nonlinearity

In optical fibre the electric field induces nonlinear polarisation, \mathbf{P} , of electric dipoles according to

$$\mathbf{P} = \epsilon_0(\chi^{(1)} \cdot \mathbf{E} + \chi^{(2)} : \mathbf{E}\mathbf{E} + \chi^{(3)} : \mathbf{E}\mathbf{E}\mathbf{E} + \dots), \quad (1.8)$$

with ϵ_0 the permittivity of vacuum and \mathbf{E} the electric field strength. $\chi^{(j)}$ is the j th order susceptibility tensor. For silicon oxide glasses the second-order susceptibility is zero while the third-order susceptibility is responsible for the fibre nonlinear coefficient,

$$\gamma = \frac{n_2\omega_0}{cA_{eff}} = \frac{3\omega_0}{8ncA_{eff}}\text{Re}(\chi_{xxx}^{(3)}), \quad (1.9)$$

with n_2 the nonlinear index coefficient, ω_0 the optical frequency, n the refractive index, c the speed of light and A_{eff} the effective core area. It is this nonlinear coefficient that is responsible for third-harmonic generation, four-wave mixing, nonlinear refraction, and self-phase modulation (SPM). Strong optical pulses of wavelength λ travelling in a fibre over a distance Δz experience a nonlinear phase shift proportional to their power

$$\phi_{NL} = n_2 \frac{2\pi}{A_{eff}\lambda} \Delta z |A(z, \tau)|^2. \quad (1.10)$$

$A(z, \tau)$ is the normalised electric field with respect to the power, $P(z, \tau)$, according to

$$|A(z, \tau)|^2 = P(z, \tau). \quad (1.11)$$

τ is the reduced time. This phase shift causes the trailing edge of an intense optical pulse to turn to the blue side of the optical spectrum while the leading edge turns more red. When $\beta_2 < 0$, the fibre is said to be anomalously dispersive, in this regime blue shifted spectral components will travel faster than red shifted components. As a result the leading edge will travel slower while the trailing edge travels faster. Therefore, the fibre nonlinearity will compress RZ pulses in the anomalous dispersion regime and stretch pulses in the normal dispersion regime where blue shifted components travel slower and red shifted spectral components propagate faster. Figure 1.9 (a) displays a Gaussian pulse with a full-width half-maximum time of one picosecond and a peak power of one milliwatt. It can be clearly seen that the envelope experiences a time dependent frequency shift (chirp). Figure 1.9 (d) shows that the leading edge has become more red and the trailing edge more blue. In combination with anomalous dispersion pulse broadening is reduced [53].

Optical solitons

The equation of motion for the normalised optical field in optical fibre incorporating not only loss and dispersion but also self-phase modulation can be expressed as

$$\frac{\partial A}{\partial z} + \beta_1 \frac{\partial A}{\partial t} + \frac{i}{2} \beta_2 \frac{\partial^2 A}{\partial t^2} + \frac{\alpha}{2} A = i\gamma |A|^2 A \quad (1.12)$$

which is well known as the Schrödinger equation with α the loss of the optical fibre, β_1 the inverse group velocity and β_2 the group-velocity dispersion (GVD) parameter. An analytical solution for a lossless fibre ($\alpha = 0$) was found by employing the inverse scattering theory [54] and more recently by a method using a set of basis functions and an iterative scheme to obtain the coefficients [55]. In a lossless medium ($\alpha = 0$) the solution of Eq. 1.12 is expressed as

$$A(z, \tau) = \sqrt{P_0} \operatorname{sech}\left(\frac{\tau}{\tau_0}\right) \exp\left(\frac{iz|\beta_2|}{2\tau_0^2}\right), \quad (1.13)$$

with P_0 the peak power of the optical soliton,

$$P_0 = N^2 \frac{|\beta_2|}{\gamma \tau_0^2}, \quad (1.14)$$

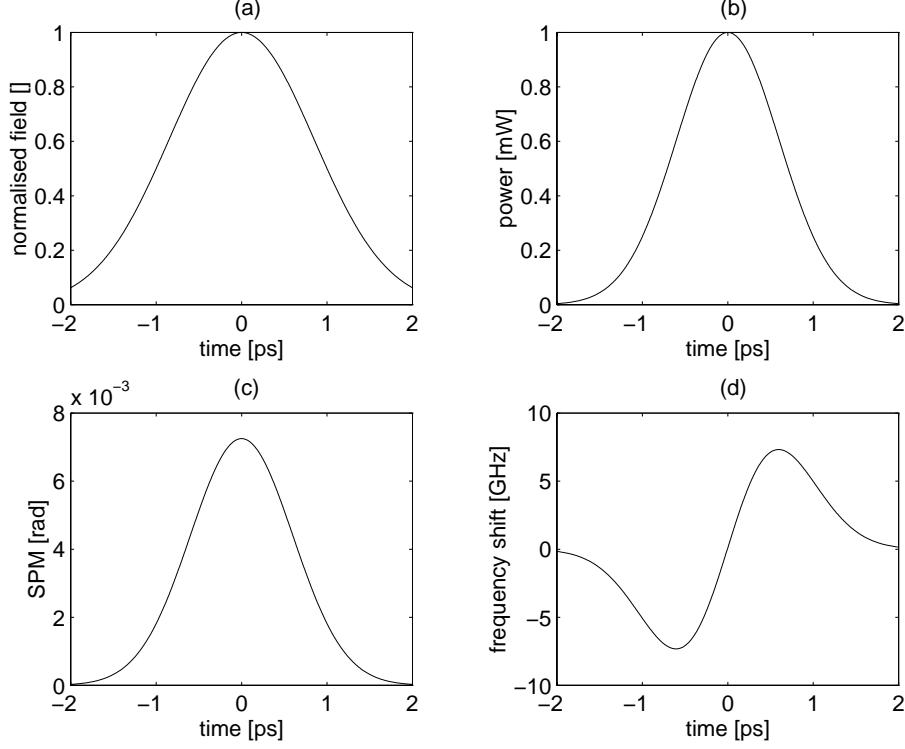


Figure 1.9: (a) Gaussian pulse envelope $A(\tau)$ of the electric field (normalised), (b) power distribution of the pulse, the peak power amounts to one milliwatt, (c) the induced self-phase modulation at $\lambda = 1.3 \mu\text{m}$ over a distance of one kilometre. n_2 is equal to $3 \cdot 10^{-20} \text{ m}^2/\text{W}$, $A_{eff} = 20 \mu\text{m}^2$, (d) chirp imposed on the envelope after $\Delta z = 1 \text{ km}$

where the integer N is the soliton number. The full-width half-maximum time, τ_{FWHM} , of the soliton is proportional to τ_0 ,

$$\tau_{FWHM} = 2 \log(1 + \sqrt{2})\tau_0. \quad (1.15)$$

Apparently solutions exist that do not change shape in an optical fibre. This means that the fibre nonlinearity can be used to fully compensate dispersion. Special attention should be paid to fibre losses as they will cause power levels to drop exponentially along the travelled distance. Self-phase modulation decreases and a significant pulse broadening occurs after a certain distance. By launching solitons with a higher energy into a fibre, additional pulse compression will occur in the first few kilometres of the fibre because more self-phase modulation is experienced while at the last kilometres pulses broaden again due to insufficient self-phase modulation. This kind of transmission is called path average soliton transmission. Extensive literature is available for a more detailed treatment on solitons and nonlinear transmission e.g. [56] and included references.

1.4 Objective and strategy

In Sec. 1.1 the development of 1.3 μm polarisation insensitive quantum well laser amplifiers was touched upon. The research described in this thesis was carried out on the premises of the manufacturer of these amplifiers, Uniphase Netherlands B.V., where these SOAs were available. In this thesis the possibility of employing these amplifiers in OTDM long-haul systems incorporating all-optical clock recovery, see Sec. 1.2, will be investigated.

In Chapter 2 a more detailed view on optical amplification is given. Several models of a polarisation independent semiconductor amplifier are derived. These models are incorporated in a model for the TOAD based optical switch. The performance of this optical switch is demonstrated with respect to amplifier model, amplifier parameters and parameters of the coupler.

Chapter 3 describes key components and functional units like sources, receivers and a variety of other components that play an important role in experiments performed. Models are provided that have been implemented in numerical simulation programs.

Chapter 4 deals with preliminary transmission experiments, numerically and experimentally, to obtain more knowledge and experience on the behaviour of amplifiers configured as in-line optical repeaters. This knowledge proves to be indispensable in future 40 Gb/s experiments. A 10 Gb/s transmission record is achieved both with and without in-line optical repeaters. Chapter 5 describes a novel all-optical cross gain-switched tuneable ring laser that provides jitter free pulses for a 10 Gb/s to 2.5 Gb/s all-OTDM system. Extensive bit error rate (BER) measurements have been performed. A novel 10 Gb/s clock recovery is presented for 40 Gb/s to 10 Gb/s demultiplexing. Subsequently, the all-OTDM setup is used in a record 216 km transmission experiment. Finally the same configuration is demonstrated to improve BER results of experiments conducted in Chapter 4. Chapter 6 discusses the implications of the obtained results with respect to the literature. In Chapter 7 conclusions are drawn and recommendations made with respect to the usability of polarisation insensitive semiconductor optical amplifiers and all-optical demultiplexing and regeneration techniques in 1.3 μm MQW SOA based optical transmission systems.

References

- [1] N.S. Kapany. Fibre optics. VI. image quality and optical insulation. Journal of the Optical Society of America, 49:779, 1959.
 - [2] F.P. Kapron, D.B. Beck, and R.D. Maurer. Radiation losses in glass optical waveguides. Applied Physics Letters, 17:423, 1970.
 - [3] T. Miya, Y. Terunuma, et al. Ultimate low-loss single-mode fibre at 1.55 μm . Electronics Letters, 15:106, 1979.
 - [4] L.F. Mollenauer, R.H. Stolen, and J.P. Gordon. Experimental observation of picosecond pulse narrowing and solitons in optical fibers. Physics Review Letters, 45:1095, 1980.
 - [5] A. Hasegawa and F. Tappert. Transmission of stationary nonlinear optical pulses in dispersive dielectric fibres. Applied Physics Letters, 23:142–144, 1973.
 - [6] J. von Neumann. Notes on the photon-disequilibrium-amplification scheme. IEEE Journal of Quantum Electronics, 23:658, 1987.
-

-
- [7] R.N. Hall, G.E. Fenner, et al. Coherent light emission from GaAs junctions. Physical Review Letters, 9:366, 1962.
- [8] M.I. Nathan, W.P. Dumke, et al. Stimulated emission of radiation from GaAs p-n junctions. Applied Physics Letters, 1:62, 1962.
- [9] K. Sakai, K. Utaka, et al. 1.5 μm range InGaAsP/InP distributed feedback laser. IEEE Journal of Quantum Electronics, 18:1272–1278, 1982.
- [10] K.Y. Lau and A. Yariv. Ultrahigh-speed semiconductor lasers. IEEE Journal of Quantum Electronics, 21:121–138, 1985.
- [11] J.E. Bowers, B.R. Hemmenway, et al. High-speed InGaAsP constricted mesa lasers. IEEE Journal of Quantum Electronics, 22:833–844, 1986.
- [12] R. Olshansky, W. Powazinik, P. Hill, V. Lanzisera, and R.N. Lauer. InGaAsP buried heterostructure laser with 22-GHz bandwidth modulation efficiency. Electronics Letters, 49:839, 1987.
- [13] P.T. Ho, L.A. Glasser, et al. Picosecond pulse generation with CW GaAlAs laser diode. Journal of Applied Physics, 33:241–243, 1978.
- [14] J.P. van der Ziel. Active mode locking of double heterostructure lasers in an external cavity. Journal of Applied Physics, 52:4435–4446, 1981.
- [15] T. Ikegami and Y. Suematsu. Large signal characteristics of directly modulated semiconductor injection lasers. Electron. Comm. Japan, 53B:69–75, 1970.
- [16] R.G.M. Koumans and R. Van Rooijen. Theory for passive mode-locking in semiconductor laser structures including the effects of selfphase modulation, dispersion, and pulse collision. IEEE Journal of Quantum Electronics, 32:478–492, 1996.
- [17] H.A. Haus, E.P. Ippen, and K. Tamura. Additive-pulse modelocking in fiber lasers. IEEE Journal of Quantum Electronics, 30:200–208, 1994.
- [18] H.A. Haus, J.G. Fujimoto, and E.P. Ippen. Structures for additive pulse mode locking. Journal of the Optical Society of America B, 8:2068–2076, 1991.
- [19] H.A. Haus, J.G. Fujimo, et al. Analytic theory of additive pulse and Kerr lens mode locking. IEEE Journal of Quantum Electronics, 28:2086–2096, 1992.
- [20] P.J.A. Thijs, L.F. Tiemeijer, et al. Progress in long-wavelength strained-layer InGaAs(P) quantum-well semiconductor lasers and amplifiers. IEEE Journal of Quantum Electronics, 30:477–499, 1994.
- [21] L.F. Tiemeijer, P.J.A. Thijs, et al. Polarization insensitive multiple quantum well laser amplifiers for the 1300 nm window. Applied Physics Letters, 62:826–828, 1993.
- [22] J.Y. Emery, P. Doussiere, et al. New, process tolerant, high performance 1.55 μm polarization insensitive semiconductor optical amplifier based on low tensile bulk GaInAsP. In Proceedings of the ECOC'97, Oslo, volume 3, pages 165–168, 1996.
- [23] R.J. Mears, L. Reekie, et al. High-gain rare-earth-doped fibre amplifier operating at 1.54 μm . In Technical Digest of the OFC'97, Washington, page 167, 1997.
- [24] Y. Nishida, M. Yamada, and J. Temmyo. Plug-in type 1.3 μm fiber amplifier module for rack-mounted shelves. In Technical digest of the OFC'97, Dallas, pages 108–109, 1997.
-

-
- [25] W. Tomlinson and G. Aumiller. Optical multiplexer for multimode fibre transmission systems. Applied Physics Letters, 31:169, 1977.
- [26] N.S. Bergano, C.R. Davidson, et al. Long-haul WDM transmission using optimum channel modulation: a 160 Gb/s (32*5Gb/s) 9300 km demonstration. In Technical Digest of the OFC'97, Dallas, pages 432–435, 1997.
- [27] M.X. Ma, H.D. Kidorf, et al. 240 km repeater spacing in a 5280 km WDM system experiment using 8*2.5 Gb/s NRZ transmission. IEEE Photonics Technology Letters, 10:893–895, 1998.
- [28] Y. Yano, T. Ono, et al. 2.6 Terabit/s WDM transmission experiment using optical duobinary coding. In Proceeding of the ECOC'96, volume5 post-deadline papers, Oslo, pages 5.3–5.6, 1996.
- [29] R.T. Denton and T.S. Kinsel. Terminals for a high-speed optical pulse code modulation communication system I. 224-Mbit/s single channel. Proceedings of the IEEE, 56:140–145, 1968.
- [30] T.S. Kinsel and R.T. Denton. Terminals for high-speed optical pulse code modulation communication system: II. optical multiplexing and demultiplexing. Proceedings of the IEEE, 56:146–154, 1968.
- [31] R.T. Denton, T.S. Kinsel, and F.S. Chen. 224 Mc/s optical pulse code modulator. Proceedings of the IEEE, 54:1472–1473, 1966.
- [32] T.S. Kinsel and S.F. Chen. Experimental evaluation of an optical time division demultiplexer for twenty-four channels. Applied Optics, 11:1411–1418, 1972.
- [33] W. Pieper, R. Ludwig, et al. 4-Channel*40 Gb/s unrepeated OTDM transmission over 100 km standard fibre. IEEE Photonics Technology Letters, 10:451–453, 1998.
- [34] H. Takara, S. Kawanishi, T. Morioka, K. Mori, and M. Saruwatari. 100 Gbit/s optical waveform measurement with 0.6 ps resolution optical sampling using subpicosecond supercontinuum pulses. Electronics Letters, 30:1152–1153, 1994.
- [35] K.L. Hall and K.A. Rauschenbach. All-optical bit pattern generation and matching. Electronics Letters, 32:1214–1215, 1996.
- [36] K.L. Hall. 40 Gbit/s optical packet buffering. In Technical Digests of the OFC'97, Dallas, pages 251–252, 1997.
- [37] N.S. Patel, K.L. Hall, et al. All-optical rate conversion. In Technical Digest of the OFC'97, Dallas, pages 87–88, 1997.
- [38] J.D. Moores. 80-Gbit/s 9 kbit optical pulse storage loop. In Technical Digests of the OFC'97, Dallas, pages 88–89, 1997.
- [39] P.E. Barnsley, H.J. Wickes, et al. All-optical clock recovery from 5 Gb/s RZ data using a self-pulsating 1.56 μm laser diode. IEEE Photonics Technology Letters, 3:942–945, 1991.
- [40] A.D. Ellis, K. Smith, and D.M. Patrick. All optical clock recovery at bit rates up to 40 Gbit/s. Electronics Letters, 29:1323–1324, 1993.
- [41] B. Sartorius, C. Bornholdt, et al. All-optical clock recovery module based on self-pulsating DFB laser. Electronics Letters, 34:1664–5, 1998.
-

-
- [42] H.K. Lee, C.H. Lee, et al. All-fibre-optic clock recovery from non return to zero format data. In Technical Digest of the OFC'98, San Jose, pages 205–206, 1998.
- [43] A.D. Ellis, T. Widdowson, et al. Transmission of a true single polarisation 40 Gbit/s soliton data signal over 205 km using a stabilised erbium fibre ring laser and 40 GHz electronic timing recovery. Electronics Letters, 29:990–992, 1993.
- [44] W.S. Lee, G. Pettitt, et al. 40 Gbit/s OTDM transmission over a distance of 560 km: system implementation and performance evaluation. Electronics Letters, 32:1685–1686, 1996.
- [45] S. Kawanishi, H. Takara, et al. 100 Gbit/s, 50 km, and nonrepeated optical transmission employing all-optical multi/demultiplexing and PLL timing extraction. Electronics Letters, 29:1075–1077, 1993.
- [46] M. Nakazawa, K. Suzuki, and E. Yamada. NOLM oscillator and its injection locking technique for timing clock extraction and demultiplexing. Electronics Letters, 32:1122–1123, 1996.
- [47] N.J. Doran and D. Wood. Nonlinear-optical loop mirror. Optics Letters, 13:56–58, 1988.
- [48] K.J. Blow, N.J. Doran, and B.K. Nayar. Experimental demonstration of optical soliton switching in an all-fiber nonlinear sagnac intrferometer. Optics Letters, 14:754–756, 1989.
- [49] K.J. Blow, N.J. Doran, and B.P. Nelson. Demonstration of the nonlinear fibre loop mirror as an ultrafast all-optical demultiplexer. Electronics Letters, 26:962–964, 1990.
- [50] B.-E. Olsson. All-optical switching with the nonlinear optical loop mirror. PhD thesis, Electrical and Computer Engineering, Chalmers University of Technology, S-412 96 Göteborg, Sweden, April 1998.
- [51] M.E. Fermann, F. Haberl, et al. Nonlinear amplifying loop mirror. Optics Letters, 15:752–754, 1990.
- [52] K. Kikuchi, M. Kakui, et al. Observation of highly nondegenerate four-wave mixing in 1.5 μm traveling-wave semiconductor optical amplifiers and estimation of nonlinear gain coefficient. IEEE Journal of Quantum Electronics, 28:151–156, 1992.
- [53] G.P. Agrawal. Nonlinear Fiber Optics. Optics and Photonics. Academic Press, New York, second edition, 1995.
- [54] V.E. Zakharov and A.B. Shabat. Exact theory of two-dimensional self-focusing and one-dimensional self-modulation of waves in nonlinear media. Soviet Physics JetP, 34:62–69, 1972.
- [55] H.J.S. Dorren. On the integrability of nonlinear partial differential equations. Journal of Mathematical Physics, 40:1966–1976, 1999.
- [56] A. Hasegawa and Y. Kodama. Solitons in optical communications. Oxford University Press, Oxford, 1995.
-

Chapter 2

Optical amplification and switching

2.1 Introduction

Since the maturation of the laser diode, the development of an optical amplifier evolved as a major research topic to facilitate repeaterless transmission. In Section 2.2 fibre amplifiers are treated because they are the major source of amplification in optical transmission systems. In this section the erbium-doped fibre amplifier is treated followed by the praseodymium-doped fluoride fibre amplifier and the Raman amplifier. In Sec. 2.3 optical amplification by means of semiconductor optical amplifiers is treated in detail as this is of importance to the further understanding of the work presented in this thesis. Three models are presented for the special case of saturation by a Dirac delta pulse, a model that includes wavelength dependent noise and a model that incorporates the physical length of the amplifier. Their nonlinear response to high intensity optical pulses allows SOAs to be implemented in all-optical switches such as the TOAD. Section 2.4 deals with the Sagnac interferometer which is further used in Sec. 2.5 to model the operation of the TOAD. Analytical and numerical simulations have been carried out to demonstrate the dependence of the performance of the switch on a number of parameters.

2.2 Fibre amplifiers

2.2.1 Erbium-doped fibre amplifier

The invention of the erbium-doped fibre amplifier (EDFA) [1] was instrumental to the development of WDM systems which use amplitude shift keying and direct detection techniques. The latter being favourite for the ease of implementation. The main features and principles of operation are touched upon. In a later stadium, a comparison between semiconductor optical amplification and fibre amplification is used to explain the difference in performance between fibre amplifier and SOA based systems. Figure 2.1 shows an EDFA and what kind of components are used. Figure 2.2 (a) displays the energy level diagram of an erbium-doped fibre. The wavelength of the pump laser can range from 514 nm to 1.48 μm . At 1.48 μm the lowest metastable state is pumped. Pumping at 980 nm requires excited electrons to first experience a 1 μs non-radiative decay to the metastable state before they recombine in the

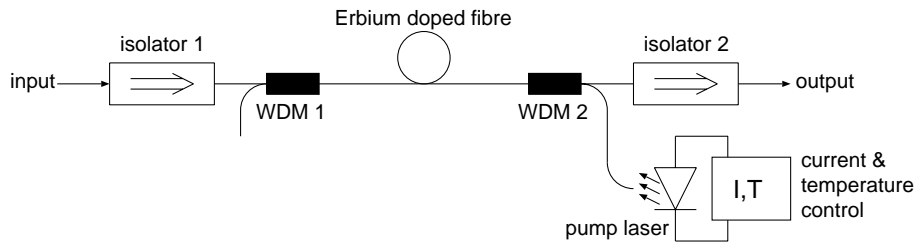


Figure 2.1: Configuration of an erbium-doped fibre amplifier (EDFA). Counter propagated pumping reduces the polarisation sensitivity. Isolators are used to prevent parasitic reflection from re-entering the erbium-doped fibre and amplified spontaneous emission from entering preceding amplifiers. The typical length of the erbium-doped fibre is 10 to 20 m. A pump laser delivers the required pump power (100 mW at 980 nm).

amplifying process. At 980 nm the pump efficiency reaches a maximum gain efficiency. The gain spectrum is centred around $1.53 \mu\text{m}$ and has a bandwidth of about 10 nm. The shape of the gain spectrum depends strongly on the type of co-doping with other rare-earth atoms. Amplifiers with a flat gain region of ≈ 30 nm have been realised. The life time of excited electrons in the metastable state is about 20 ms and decreases to values around 1 ms when the amplifier is driven into saturation. When full inversion occurs, optical gains as high as 50 dB can be achieved. The saturation output power can reach values up to 16 dBm (at 3 dB gain compression). Noise figures between 4 and 5 dB are common and close to the quantum limit of 3 dB for high gain optical amplifiers [2]. When EDFAs are employed in high bit rate communication systems the large carrier life time of EDFAs practically eliminates the pattern effects. This makes the EDFA a well suited candidate for $1.55 \mu\text{m}$ in-line amplification. EDFAs configured as a power booster allow excitation of, for example, fibre nonlinearities and can create the right environment for soliton transmission in both SSMF and DSF. At present much effort is put into broadening and equalising the gain spectrum [3]. Extension towards 1610 nm has already been achieved.

2.2.2 Praseodymium-doped fluoride fibre amplifier

Not only the third telecommunication window ($1.5 \mu\text{m}$ window) is of interest for high speed fibre-amplified communication systems, the $1.3 \mu\text{m}$ window is of particular importance because, for SSMF, the zero dispersion wavelength lies in this window. When fluoride SiO_2 glass is doped with praseodymium and optically excited with a pump laser at 1015 nm, optical gain is observed at $1.31 \mu\text{m}$, according to the energy level diagram of Fig. 2.2 (b) The small signal gain can reach 30 dB with a 3 dB saturation output power of 13 dBm. The carrier lifetime lies in the order of $100 \mu\text{s}$ and can cause pattern effects for high intensity signals even at high bit rates. The quantum efficiency of 40 % is smaller than the efficiency of the EDFA (80 %). Therefore higher pump powers are required. The configuration of PDFAs is similar to the EDFA geometry in Figure 2.1 [3].

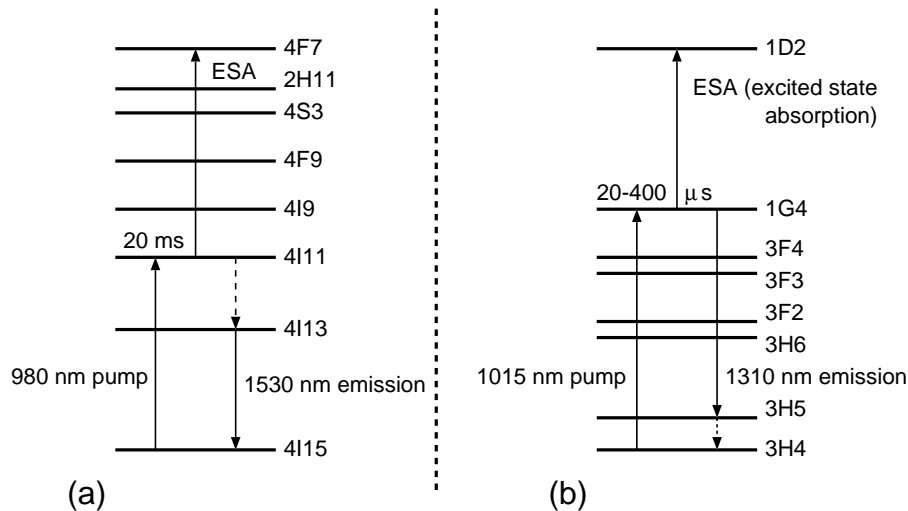


Figure 2.2: Energy levels of an erbium-doped, 980 nm pumped, fibre (a) and a praseodymium-doped fluoride fibre (b). The dashed arrows stand for non-radiative decays

2.2.3 Raman amplifier

Both erbium-doped and praseodymium-doped fibre amplifiers rely on doping of a single-mode fibre to achieve stimulated emission, i.e. gain. This doping is critical as it determines the parameters and behaviour of the amplifier. Raman amplifiers do not require these rare-earth doped fibres. When a standard single-mode fibre is excited by a strong pump signal at $1.24 \mu\text{m}$ Raman scattering induces gain through molecular vibrations in glass at $1.31 \mu\text{m}$. This gain can be used to compensate the 0.4 dB/km fibre loss, thus making the fibre optically transparent. For the third telecommunication window a pump at 1450 nm will give Raman induced gain at $1.55 \mu\text{m}$. The main advantage of Raman amplifiers is that only a pump signal is needed. In addition, Raman induced gain is fast (femto second response time) and determined by the pump. Generally Raman amplifiers do not impose pattern effects on high speed optical signals due to the ultra fast lifetime in SiO_2 . To excite Raman gain high pump levels around one Watt are required. Raleigh scattering and Brillouin coupling between signal and pump is found to limit the maximum pump level and thereby the gain. [4], [5], [6]

2.3 Semiconductor optical amplifier

Ever since the advent of the semiconductor laser diode, semiconductor optical amplifiers have been of interest as a means to provide optical gain. One of the main advantages of semiconductor optical amplifiers is that no long fibre is needed as a gain medium but a short piece of semiconductor material. All fibre amplifiers require optical pumping and in the case of an EDFA or a PDFA a pump laser diode is needed. SOAs however, do not require an optical pump (laser diode) because they are electrically pumped with a low current \leq

500 mA. Employing semiconductor optical amplifiers will therefore reduce the complexity of an optical amplifier module. Today different types of SOAs have been developed. In this thesis polarisation insensitive multiple quantum well laser diode amplifiers have been used. Figure 2.3 displays the structure of the polarisation insensitive laser amplifier. The tensile strained quantum wells provide mainly TM gain and the compressive strained quantum wells provide mainly TE gain. By balancing the ratio of both layers it has been demonstrated that polarisation insensitive gain can be obtained [7]. In this section three models with increasing complexity are described. All models describe a polarisation insensitive amplifier. TE and TM modes are considered to experience the same propagation constant and the gains and saturation output powers are equal for TE and TM amplification. This assumption is not entirely true because in practice small differences of ± 1 dB exist between TE and TM gains. Generally, in cascaded amplifier experiments, with more than four in-line amplifiers, this polarisation sensitivity is averaged out.

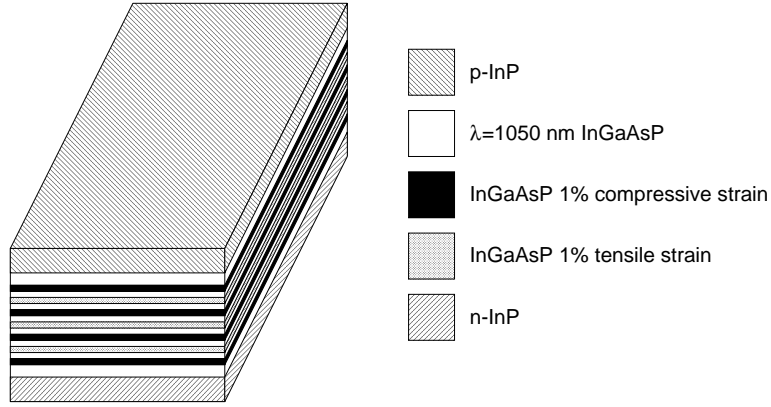


Figure 2.3: Structure of the polarisation insensitive multiple quantum well laser amplifier

2.3.1 Spatially-concentrated uni-directional noise-less saturable optical amplifier

In this section rate equations, applicable to a semiconductor optical amplifier excited by a single-wavelength optical signal which travels in the positive direction, are deduced in accordance with Agrawal and Olsson, [8]. The evolution of a travelling wave in a gain medium is governed by

$$\frac{\partial a(z, t)}{\partial z} + \frac{1}{v_g} \frac{\partial a(z, t)}{\partial t} = \frac{1}{2} [(1 - j\alpha_H)g(N) - \alpha_l] a(z, t), \quad (2.1)$$

where $a(z, t)$ is the slowly varying envelope of

$$A(z, t) = a(z, t) \exp[j(\omega_0 t - k_0 z)]. \quad (2.2)$$

The optical field, $A(z, t)$, is normalised in such a way that the temporal power of the travelling wave is given by

$$P(z, t) = A(z, t) \cdot A^*(z, t) = a(z, t) \cdot a^*(z, t), \quad (2.3)$$

where the asterisk denotes complex conjugation. The internal losses are denoted by α_l , the gain by $g(N)$ which depends on carrier density $N(z, t)$, Henry's linewidth enhancement factor is denoted by α_H and v_g is the group velocity. This model includes neither optical dispersion nor gain dispersion. It must be noted that v_g , α_H , α_l and $g(N)$ are wavelength dependent. The gain is assumed to depend linearly on the carrier density $N(z, t)$, i.e.,

$$g(N) = \Gamma \frac{\partial g(N)}{\partial N} (N(z, t) - N_0), \quad (2.4)$$

where $\frac{\partial g(N)}{\partial N}$ is the gain coefficient, Γ is the confinement factor and accounts for the spread of the optical mode outside the active region of the amplifier and N_0 is the carrier density at transparency. The carrier density is determined by the rate equation:

$$\frac{\partial N(z, t)}{\partial t} = \frac{J(z, t)}{q} - \frac{N(z, t)}{\tau_c} - \frac{g(N)|A(z, t)|^2}{\hbar\omega_0}, \quad (2.5)$$

where τ_c is the carrier lifetime, $J(z, t)$ is the injected current density, q is the elementary charge unit. $\hbar\omega_0$ is the energy of a single photon. The small signal stationary gain $g_0(z, t)$ is defined as, [8],

$$g_0(z, t) = \Gamma \frac{\partial g(N)}{\partial N} \left(\frac{J(z, t)\tau_c}{q} - N_0 \right). \quad (2.6)$$

During amplification of optical signals carriers recombine which leads to a reduction of gain. This process is called saturation. The saturation energy has been determined by Yamamoto *et al.* [9] to be

$$E_{sat} = \frac{\hbar\omega_0\sigma}{\frac{\partial g(N)}{\partial N}}, \quad (2.7)$$

where $\sigma = V/\Gamma L$ is the cross-section area of the optical mode, with V the volume of the active layer. L is the length of the amplifier. This saturation energy should be interpreted as the amount of energy of all amplified photons when the optical gain is reduced to half of the small signal gain. After substitution of Eqs. 2.6 and 2.7 into Eq. 2.5 the gain can be derived from the differential equation

$$\frac{\partial g(z, t)}{\partial t} = \frac{g_0 - g(z, t)}{\tau_c} - \frac{g(z, t)|A(z, t)|^2}{E_{sat}}. \quad (2.8)$$

Substitution of $g(z, t)$ into Eq. 2.1 results in

$$\frac{\partial a(z, t)}{\partial z} + \frac{1}{v_g} \frac{\partial a(z, t)}{\partial t} = \frac{1}{2} [(1 - j\alpha_H)g(z, t) - \alpha_l] a(z, t). \quad (2.9)$$

Equations 2.8 and 2.9 describe the amplification of an optical signal in a bulk SOA [8]. This model includes both saturation and saturation induced phase shifts. The dispersion, which a signal, travelling in the amplifier, experiences is neglected because the single-mode amplifiers used in practice have a length not greater than $800\mu\text{m}$.

Now a window is defined that moves along with the input signal at the same velocity. This window requires a new reduced time variable τ from the transformation i.e. the frame of reference is changed to

$$\tau = t - \frac{z}{v_g}. \quad (2.10)$$

Substitution in Eqs. 2.8 and 2.9 gives a new set of equations

$$\frac{\partial g(z, \tau)}{\partial \tau} = \frac{g_0 - g(z, \tau)}{\tau_c} - \frac{g(z, \tau)|A(z, \tau)|^2}{E_{sat}} \quad (2.11)$$

and

$$\frac{\partial a(z, \tau)}{\partial z} = \frac{1}{2}[(1 - j\alpha_H)g(z, \tau) - \alpha_l]a(z, \tau). \quad (2.12)$$

Eq. 2.12 can now be integrated over the length of the amplifier to transform into an equation between the input and output signal.

$$a_{out}(\tau) = a_{in}(\tau) \exp\left(\frac{1}{2}[1 - j\alpha_H] \cdot h(\tau)\right), \quad (2.13)$$

where $h(\tau)$ is the gain integrated over the amplifier length. α_l is omitted because the amplifier losses are small compared to the optical gain. The differential equation of the gain $g(z, \tau)$ is transformed to

$$\frac{dh(\tau)}{d\tau} = \frac{h_0 - h(\tau)}{\tau_c} - \frac{|a_{in}(\tau)|^2}{E_{sat}}(\exp(h(\tau)) - 1), \quad (2.14)$$

with h_0 being the integrated small signal (unsaturated) gain. In general Eqs. 2.13 and 2.14 can not be solved analytically. Euler's forward integration scheme creates the following iterative equations, suitable for numerical evaluation.

$$h^{n+1} = \Delta\tau \left[\frac{h_0 - h^n}{\tau_c} - \frac{|a_{in}^n|^2}{E_{sat}}(\exp(h^n) - 1) \right] + h^n \quad (2.15)$$

for the gain and for the envelope, Eq. 2.13,

$$a_{out}^{n+1} = a_{in}^{n+1} \exp\left(\frac{1}{2}[1 - j\alpha_H]h^{n+1}\right), \quad (2.16)$$

with $\Delta\tau$ the time discretisation step size. Eqs. 2.15 and 2.16 provide the means to numerically evaluate the amplification of an arbitrary signal in one direction in the absence of noise. Because the z-dependence of this system is eliminated, evaluation of Euler's forward system is fast and stable which makes this model suitable for quick estimations of uncomplicated amplification processes.

2.3.2 A spatially-concentrated uni-directional noisy saturable optical amplifier

In this section the model of Sec. 2.3.1 is expanded to a model that can deal with signals of different wavelength and that is affected by amplified spontaneous emission (ASE). ASE is a broadband noise source that combines with the wavelength dependent optical gain. When SOAs are cascaded this ASE will saturate successive SOAs. This saturation is wavelength dependent because the gain, saturation output power and the input ASE spectrum are wavelength dependent. A model of the ASE should therefore discretise the ASE spectrum in the optical wavelength domain. Changing to a multiple wavelength model means that most parameters become wavelength dependent. Difficulties arise with respect to the distribution of the carrier concentration. The model in Sec. 2.3.1 assumes that every carrier that is pumped into the conduction band contributes to the amplification of the input signal. When multiple quantum well (MQW) SOAs are considered, with tensile strained and compressively strained wells, this is not the case because the carrier distribution in the inverted band(s) results in a multi-level system where multiple transitions occur [7]. In order to determine this gain spectrum, administration of all activities on the different energy bands is required. In the case of a MQW SOA this is a complex issue as precise knowledge of the geometry and doping levels of the quantum wells is neither present nor easily obtained. It is for this reason that a phenomenological model is developed based on the theory presented in Sec. 2.3.1. The introduction of wavelength dependence of the gain results in a propagation equation for an optical signal with wavelength λ .

$$\frac{\partial a(z, t, \lambda)}{\partial z} + \frac{1}{v_g(\lambda)} \frac{\partial a(z, t, \lambda)}{\partial t} = \frac{1}{2}(1 - j\alpha_H(\lambda))g(z, t, \lambda)a(z, t, \lambda) - \frac{1}{2}\alpha_l(\lambda)a(z, t, \lambda). \quad (2.17)$$

The introduction of wavelength dependent gain has consequences for the group velocity, the internal amplifier loss and the linewidth enhancement factor. Generally, they will also change with wavelength. Due to the wavelength dependence of the group velocity, signals at different wavelengths will propagate with different velocities and “walk-off” will occur. In this model the frequency spacing of different input signals will be too small to cause significant walk-off during the propagation in short (length less than 1 mm) SOAs. For the remainder of this thesis the group velocity is considered a constant. In this model the wavelength dependence of the gain is assumed to be larger than the dependence of the amplifier losses on the wavelength. The amplifier loss is assumed to be wavelength independent. For the ease of implementation the line width enhancement factor is treated as a constant. As mentioned before the amplifier produces not only noise but also amplifies input noise. Similar to a normal optical input signal the amplification of spontaneous emission is expressed as

$$\frac{\partial S_{ase}(z, t, \lambda)}{\partial z} + \frac{1}{v_g} \frac{\partial S_{ase}(z, t, \lambda)}{\partial t} = [g(z, t, \lambda) - \alpha_l]S_{ase}(z, t, \lambda) + h \frac{c^2}{\lambda^3} \frac{NF}{2} g(z, t, \lambda), \quad (2.18)$$

where h is Planck’s constant and NF is the noise figure. S_{ase} is the noise power at time t and place z in interval $\lambda + \Delta\lambda$. The first term on the right side accounts for the amplification

and propagation of the ASE. The second term represents ASE added by the amplifier and can be derived from the spectral density of the spontaneous emission,

$$\frac{P_{ase}(z, t, \lambda)}{\partial \lambda} = S_{ase} = h \frac{c^2}{\lambda^3} \frac{NF}{2} g(z, t, \lambda), \quad (2.19)$$

[10]. The noise figure, NF , is divided by two because spontaneous emission acts equally into the positive and negative z -directions. In the case of Eq. 2.18 only powers are considered. The phase of the noise is random and is not incorporated. The wavelength dependent rate equation for the gain becomes

$$\frac{\partial g(z, t, \lambda)}{\partial t} = \frac{g(z, t, \lambda) - g_0(\lambda)}{\tau_c} - \frac{g(z, t, \lambda) |a(z, t, \lambda)|^2 + \int_0^\infty \frac{\lambda'}{\lambda} [S_{ase}(z, t, \lambda')] d\lambda'}{P_{sat}(\lambda) \tau_c}, \quad (2.20)$$

All rate equations depend on the distance, time and wavelength. For fast computation it is desirable to normalise the equation with respect to z . By following the same procedure as in Sec. 2.3.1 the following set of equations is obtained. The amplification of the input signal is governed by

$$a_{out}(\tau, \lambda) = \exp\left(\frac{1}{2}(1 - i\alpha_H)h(\tau, \lambda)\right) a_{in}(\tau, \lambda), \quad (2.21)$$

and the amplification and addition of ASE by

$$S_{ase, out}(\tau, \lambda) = \exp(h(\tau, \lambda)) S_{ase, in}(\tau, \lambda) + h \frac{c^2}{\lambda^3} \frac{NF}{2} \exp(h(\tau, \lambda)), \quad (2.22)$$

The ASE, $S_{ase}(\tau, \lambda)$, is additive to the signal, $a(\tau)$. The amplifier is saturated by both ASE and optical signals. Via saturation induced cross-gain modulation the ASE and the optical signals interact with each other. This interaction can be modelled via the carrier density rate equation but is here incorporated in the rate equation of the integrated gain.

$$\frac{\partial h(\tau, \lambda)}{\partial t} = \frac{h(\tau, \lambda) - h_0(\lambda)}{\tau_c} - \frac{|a(\tau, \lambda)|^2 + \int_0^\infty \frac{\lambda'}{\lambda} [S_{ase}(\tau, \lambda')] d\lambda'}{E_{sat}(\lambda)} (\exp(h(\tau, \lambda)) - 1). \quad (2.23)$$

The second term on the right side of Eq. 2.23 contains the reduction of the gain due to both the signal and ASE. The ASE spectrum $S_{ase}(\tau, \lambda)$ is integrated over the entire wavelength domain. Lower wavelengths (high photon energies) saturate the amplifier more because they consume relatively more carriers when amplified. This has been taken into account by the factor $\frac{\lambda'}{\lambda}$ and the wavelength dependence of E_{sat} . The internal amplifier losses are neglected because the optical gain usually exceeds these losses by an order of magnitude. For numerical evaluation the scheme from Sec. 2.3.1 is employed. The integration in the wavelength domain is evaluated using a first order integration scheme. The following iterative formulas are obtained and implemented in a computer subroutine to compute the amplification of the ASE spectrum numerically:

$$h_i^{n+1} = \Delta\tau \left[\frac{h_i^0 - h_i^n}{\tau_c} - \frac{|a_i^n|^2 + \sum_{j=0}^\infty \frac{\lambda_j}{\lambda_i} P_{ase, j}^n}{E_{sat, i}} (\exp(h_i^n) - 1) \right] + h_i^n, \quad (2.24)$$

$$P_{ase,out,i}^{n+1} = P_{ase,in,i}^{n+1} \exp(h_i^{n+1}) + h \frac{c^2}{\lambda^3} \frac{NF}{2} \exp(h_i^{n+1}) \Delta\lambda \quad (2.25)$$

P_{ase} is the total ASE power in the band $[\lambda_i - \frac{\Delta\lambda}{2}, \lambda_i + \frac{\Delta\lambda}{2}]$.

2.3.3 A non-zero length bi-directional noisy saturable optical amplifier

Up to this point only unidirectional amplifiers have been considered. For many applications bi-directional amplifiers are of importance. Optical time-domain demultiplexers are often based on SOAs where signals enter from both directions. In the following treatment the performance of an optical time-domain demultiplexer is investigated by considering the shape of the switching window. For example, if the bit rate at which a demultiplexer is designed to operate is 40 Gb/s, then the pulse width of the switch signal - the switch signal is the signal used to control the demultiplexer - lies in the order of 1 to 10 ps. This time is of the same order as the propagation delay in an 800 μm SOA. This is the reason that length dependent saturation of the amplifier has to be taken into account. When bit error rate (BER) simulations are performed noise generated by the SOAs needs also to be taken into account. In Sec. 2.3.2 a model has been developed that models the ASE amplification and generation by a SOA. In practice, the input signals to a demultiplexer have been filtered i.e. there is no wide band noise present, only in-band noise. At the output of the demultiplexer a filter is placed to filter the ASE generated by the SOA. As a result only the ASE in the spectrum of the demultiplexed signal is of importance for BER measurements and simulations. The propagation of the bi-directional finite-length noisy amplifier, as given by the following equations:

$$\frac{\partial a_n^+(z, t)}{\partial z} + \frac{1}{v_g(\lambda_n)} \frac{\partial a_n^+(z, t)}{\partial t} = \frac{1}{2}(1 - j\alpha_H(\lambda_n)) \cdot (g(z, t, \lambda_n) a_n^+(z, t) - \frac{1}{2}\alpha_I(\lambda_n) a_n^+(z, t)) \quad (2.26)$$

and

$$\frac{\partial a_n^-(z, t)}{\partial z} - \frac{1}{v_g(\lambda_n)} \frac{\partial a_n^-(z, t)}{\partial t} = \frac{1}{2}(1 - j\alpha_H(\lambda_n)) \cdot (g(z, t, \lambda_n) a_n^-(z, t) - \frac{1}{2}\alpha_I(\lambda_n) a_n^-(z, t)) \quad (2.27)$$

respectively, describe propagation in the positive and negative directions. The propagation of the noise spectrum follows Eqs. 2.26 and 2.27:

$$\frac{\partial S_{ase}^+(z, t, \lambda)}{\partial z} + \frac{1}{v_g(\lambda)} \frac{\partial S_{ase}^+(z, t, \lambda)}{\partial t} = [g(z, t, \lambda) - \alpha_I(\lambda)] S_{ase}^+(z, t, \lambda) + h \frac{c^2}{\lambda^3} \frac{NF}{2} g(z, t, \lambda) \quad (2.28)$$

and

$$\frac{\partial S_{ase}^-(z, t, \lambda)}{\partial z} - \frac{1}{v_g(\lambda)} \frac{\partial S_{ase}^-(z, t, \lambda)}{\partial t} = [g(z, t, \lambda) - \alpha_I(\lambda)] S_{ase}^-(z, t, \lambda) + h \frac{c^2}{\lambda^3} \frac{NF}{2} g(z, t, \lambda). \quad (2.29)$$

respectively, for signals travelling in the positive and negative directions. The gain $g(z, t, \lambda)$ is equivalent to

$$\frac{\partial g(z, t, \lambda)}{\partial t} = \frac{g(z, t, \lambda) - g_0(\lambda)}{\tau_c} - g(z, t, \lambda) \frac{Q(z, t, \lambda)}{\lambda P_{sat}(\lambda) \tau_c}, \quad (2.30)$$

with $Q(z, t, \lambda)$ the total power of the signals and ASE.

$$Q(z, t, \lambda) = (|a^+(z, t, \lambda)|^2 + |a^-(z, t, \lambda)|^2) + \int_0^\infty \frac{\lambda'}{\lambda} [S_{ase}^+(z, t, \lambda') + S_{ase}^-(z, t, \lambda')] d\lambda'. \quad (2.31)$$

Equations 2.26-2.31 do not account for spatial hole burning. Spatial hole burning is caused by beating of two waves which results in increased local saturation. Via the relation between the refractive index and carrier concentration a reflective grating is formed. Carrier diffusion is assumed to reduce the formation of reflective grating patterns that result from interfering positive and negative directed signals. Numerical evaluation of the schemes treated in the previous sections turns out to be very stable because the gain is integrated analytically instead of by a discrete algorithm where errors are accumulated. In the case of the bi-directional finite-length amplifier the amplifier is divided into a number of sections and each section is treated as a bi-directional zero-length amplifier where the signals experience a delay of

$$\Delta t = \frac{\Delta z}{v_g}. \quad (2.32)$$

upon travelling through one section. Figure 2.4 depicts such an amplifier of length L divided into N sections.

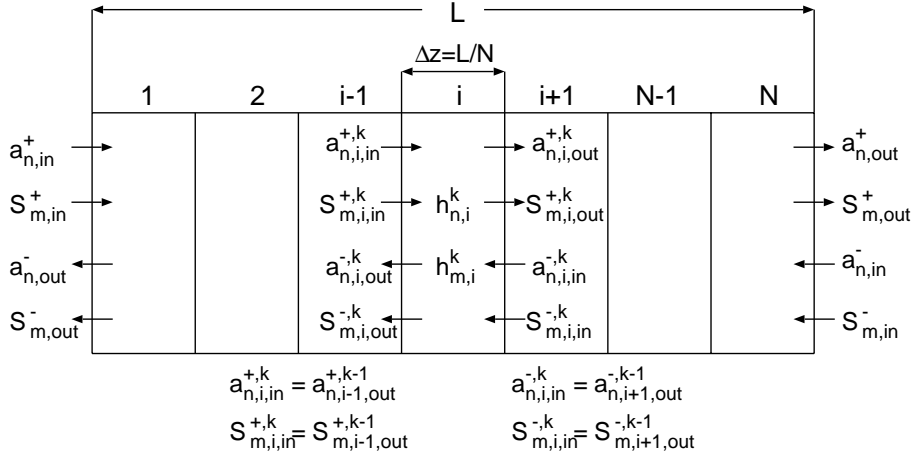


Figure 2.4: Long amplifiers are split up into spatially concentrated sub-amplifiers where gain and saturation are uniform in each section.

In the case of the 40 Gb/s example, signals with pulses as narrow as 2.5 ps require a time discretisation better than $\Delta t = 0.25$ ps. For a $2^7 - 1$ pseudo random bit sequence (PRBS)

this amounts to an array of 12700 data points for each section and each input or output. A 1 mm long amplifier with $v_g = 1 \cdot 10^8$ m/s is divided into 25 sections each having at least two input arrays and two output arrays of 12700 data points. This requires about 32 MB of memory. When the ASE spectrum is modeled with a minimum of 10 intervals a total memory of more than 320 MB is needed which is not very realistic. The ASE spectrum can be modeled with a single wavelength interval under the assumption that the noise figure is wavelength independent. The noise figure of an SOA can be determined by measuring the noise power after a filter with bandwidth B_f located at $\lambda = \lambda_f$. The noise figure can be calculated according to

$$NF_f = \frac{P_{ase,f} \lambda_f^3}{g_f B_f} \frac{2}{c^2 h}, \quad (2.33)$$

where $P_{ase,f}$ is the measured ASE power after the filter, g_f is the total gain of the amplifier. The noise figure can also be determined by measuring the total noise power at the output of the SOA with an imaginary filter located at the peak gain wavelength and a bandwidth equal to the optical bandwidth of the amplifier. Again the noise figure is determined to be

$$NF_p = \frac{P_{ase,p} \lambda_p^3}{g_p B_{SOA}} \frac{2}{c^2 h}, \quad (2.34)$$

with $P_{ase,p}$ the ASE output power of the SOA, λ_p the wavelength where the gain g_p is maximal and B_{SOA} the optical bandwidth of the SOA. Under the assumption that $NF_f = NF_{peak}$, e.g. the noise figure is wavelength independent, the amount of ASE power that is present at λ_{sig} within a band B_{sig} can be estimated to be

$$P_{ase,sig} = P_{ase,p} \frac{\lambda_p^3}{\lambda_{sig}^3} \frac{g_{sig}}{g_p} \frac{B_{sig}}{B_{SOA}}. \quad (2.35)$$

From Eq. 2.35 the ASE in the signal band can be determined if the gain of the signal is known, which is not difficult as the input and output signals are both available. In addition the peak gain should be recorded as well as the total amount of ASE power in both directions. At this point a phenomenological model is available that can be used to estimate bit error rates in systems incorporating bi-directional finite length noisy amplifiers. The model is valid if no broad-band ASE is present at the input of the SOA because it can shift and distort the ASE spectrum to an extent where it is impossible to determine for example λ_p . The expected total amount of computer memory needed will be within 64 MB.

2.3.4 Parameters of the multiple quantum-well SOA

In Sec. 2.3.1, 2.3.2 and 2.3.3 three different phenomenological models for a SOA have been described. In order to use these models the wavelength dependence of the gain and the saturation output power must be determined. Furthermore, noise figure, length, internal loss and the linewidth enhancement factor must be known. In addition there are temperature dependencies and differences for TE and TM polarised light. In this section these parameters are discussed for the 1.3 μm polarisation-insensitive multiple quantum well SOA as depicted in Fig. 2.3.

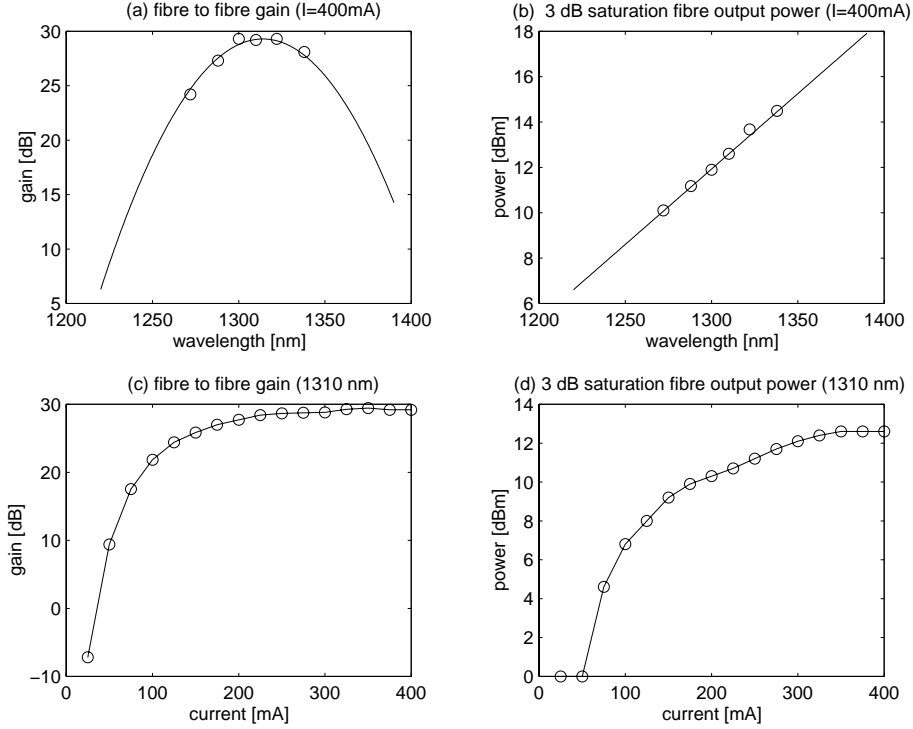


Figure 2.5: (a) The wavelength dependence of the gain is assumed Gaussian shaped and fits the measured data (dots) well. The peak gain amounts to 28 dB at 1314 nm with a 3 dB bandwidth of 68 nm. (b) The saturation output power varies exponentially with the wavelength. At 1314 nm the 3 dB saturated output power is 7.27 dB and the slope is 6.6 dB / 100 nm (c) The gain as a function of the electrical pump current. Currents above the 200 mA do not provide more gain. (d) The saturation output power increases for currents below 400 mA. High saturation output power coincides with a high gain. (Values are measured from fibre to fibre).

Optical gain

The optical gain depends not only on the amount of pumping (amplifier current) but also on the wavelength, input power and temperature. Figure 2.5 displays the dependence on wavelength for measured and fitted data. For MQW SOAs the wavelength dependence fits the Gaussian profile,

$$G_0(\lambda) = G_{peak} \exp\left[-4 \ln 2 \left(\frac{\lambda - \lambda_{peak}}{\Delta\lambda_{3dB}}\right)^2\right], \quad (2.36)$$

where λ_{peak} is the peak wavelength, $\Delta\lambda_{3dB}$ is the 3 dB full-width optical bandwidth and G_{peak} is the peak gain of the device. $G_0(\lambda)$ is the total fibre to fibre small signal gain of the amplifier. In situations of arbitrary wavelength the symbol G will be used instead of $G_0(\lambda)$,

for convenience. For each current and temperature these parameters can be measured and fed into the amplifier model. The effect of saturation of the amplifier can be investigated by using one of the models described in Sec. 2.3.1, 2.3.2 and 2.3.3.[11]

Saturation output power

The 3 dB saturation output power is measured as a function of wavelength and plotted on a logarithmic scale. A linear function describes the wavelength dependence well (Fig. 2.5). If $P_{3dBsat,peak,dB}$ is the 3 dB saturation output power at the peak wavelength, measured in dB and $C_{3dBsat,slope}$ is the slope of the linear function then the 3 dB saturation output power at λ is approximated as

$$P_{3dBsat,dB}(\lambda) = P_{p,3dBsat,dB} + C_{p,3dBsat} \cdot (\lambda - \lambda_p). \quad (2.37)$$

When the amplifier current decreases the saturation output power decreases. Increasing temperature results in a decrease of optical gain and an increase of saturation output power if the reduction of gain is compensated for by applying more bias current. If the loss of gain is not compensated (the SOA current remains unchanged, no additional carriers are pumped into the active layer of the SOA), the saturation output power remains unchanged. It is therefore not possible to decrease the amplifier gain and to increase the saturation output power by controlling either current or temperature of the SOA [11]. If the gain is reduced by decreasing the current, the saturation output power will inevitably be pared down. For each amplifier current and temperature this curve can be found by determination of $P_{p,3dBsat,p,dB}$, $C_{p,3dBsat}$ and λ_p .

Carrier lifetime

The carrier lifetime τ_c is the time an electron remains in the conduction band before it recombines with a hole in the valence band and is determined by the semiconductor material. In the case of the multiple quantum well SOA a τ_c of 200 ps is a good estimation [7].

Internal losses

An estimation of the internal losses can be found by fitting the slope of the amplifier insertion loss versus amplifier length curve. A typical value for the amplifier losses is $\alpha_l = 11.5 \text{ cm}^{-1}$ [12]. In practical situations α_l is neglected with respect to the gain.

Amplifier length

The length of the amplifiers that are used in experiments and in simulations lies between 50 μm and 1200 μm , corresponding respectively to a low and a high gain SOA.

Noise figure

Polarisation resolved noise figure measurements have been carried out on the same type of optical amplifier that was implemented in the optical demultiplexer [13]. For high gain amplifiers the noise figure is at least 3 dB. Additional coupling loss at the input is added. This loss is estimated to lie between 1.5 dB for a very good coupling and 3 dB for average coupling.

The amplifiers used have typical noise factors (fibre to fibre) between 6.0 dB and 8.0 dB. When the input signal rises above -23 dBm the noise figure becomes insensitive to the input power [12]. This is important because the model of Sec. 2.3.3 requires both a wavelength independent noise figure and a saturation independent noise figure.

Linewidth enhancement factor

The linewidth enhancement factor (or Henry's alpha, α_H) has been investigated for the same type of optical amplifier that will be used in the experiments described in this thesis [14]. When an amplifier is saturated beyond the 1 dB gain compression point, α_H does not change significantly once the current increases beyond 200 mA for an 800 μm amplifier. Values between $\alpha_H = 2$ and $\alpha_H = 8$ are considered reasonable given the data presented in references [14] and [15].

2.4 Sagnac interferometer

In Section 1.2.3 several optical switches based on optical interferometry were shown. In this section the Sagnac interferometer is treated because it forms the backbone of the MQW SOA based terahertz optical asymmetrical demultiplexer (TOAD). Figure 2.6 shows a fibre based Sagnac interferometer. The configuration consists of a fibre coupler of which on one side the fibres are connected to form a loop. A polarisation controller is inserted when non-polarisation maintaining fibre is used. Two important issues are touched upon, the polarisation rotation in the optical fibres and cross talk that takes place in the non-ideal coupler.

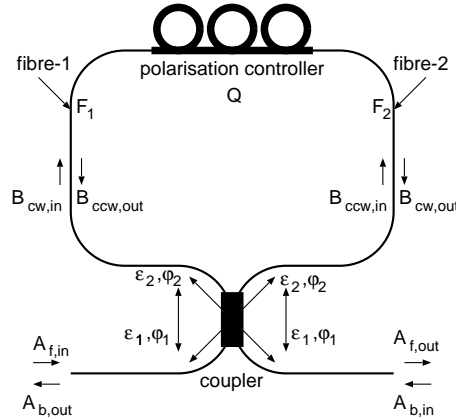


Figure 2.6: Geometry of an all-fibre Sagnac interferometer. F_1 , Q and F_2 are the polarisation transformation matrixes of fibre-1, the polarisation controller and fibre-2, respectively. ϵ_1 and ϵ_2 are the power coupling ratios for “bar” and “cross” coupling. φ_1 and φ_2 describe the phase that a signal experiences for the “bar” and “cross” coupling.

Polarisation rotation in the Sagnac interferometer

Signals that travel the loop in the clockwise or counter clockwise direction will first experience a change in polarisation by a length of fibre connecting the coupler with the polarisation controller, after which a polarisation controller changes the state of polarisation. A third change occurs in the fibre connecting the polarisation controller with the other port of the coupler. The state of polarisation of an optical signal can be represented by a column matrix

$$\mathbf{B}_{in} = \begin{bmatrix} B_{x,in} \\ B_{y,in} \end{bmatrix}. \quad (2.38)$$

Generally, a change in state of polarisation is described by the Jones polarisation transformation matrix, [16],

$$\mathbf{Q} = \begin{bmatrix} \sqrt{\varepsilon} \exp(-j\phi) & j\sqrt{1-\varepsilon} \exp(-j\theta) \\ j\sqrt{1-\varepsilon} \exp(j\theta) & \sqrt{\varepsilon} \exp(j\phi) \end{bmatrix}, \quad (2.39)$$

ε , ϕ and θ provide full control over the polarisation rotating properties of Hermitian matrix \mathbf{Q} . When \mathbf{B}_{in} is incident on a polarisation changing device the output \mathbf{B}_{out} becomes

$$\mathbf{B}_{out} = \mathbf{Q}\mathbf{B}_{in}. \quad (2.40)$$

In the loop of the Sagnac interferometer of Fig. 2.6 the clockwise travelling signal experiences a polarisation transformation equal to

$$\mathbf{B}_{cw,out} = \mathbf{F}_2 \mathbf{Q} \mathbf{F}_1 \mathbf{B}_{cw,in}, \quad (2.41)$$

where \mathbf{F}_1 and \mathbf{F}_2 are the polarisation transformation matrixes of the first and second section of fibre, before and after the polarisation controller, respectively. The counter clockwise travelling signal experiences a polarisation rotation,

$$\mathbf{B}_{ccw,out} = \mathbf{P} \mathbf{F}_1^{*-1} \mathbf{Q}^{*-1} \mathbf{F}_2^{*-1} \mathbf{P} \mathbf{B}_{ccw,in}, \quad (2.42)$$

where the superscripts $(*)$ and (-1) describe complex conjugation and inversion. Matrix \mathbf{P} reverses the y-axis:

$$\mathbf{P} = \begin{bmatrix} 1 & 0 \\ 0 & -1 \end{bmatrix} \quad (2.43)$$

The polarisation transformation matrixes, i.e. \mathbf{F}_1 and \mathbf{F}_2 , can be represented according to Eq. 2.39. Eq. 2.42 is rewritten as

$$\mathbf{B}_{ccw,out} = \mathbf{P} \mathbf{F}_1^T \mathbf{Q}^T \mathbf{F}_2^T \mathbf{P} \mathbf{B}_{ccw,in} = \mathbf{P} (\mathbf{F}_2 \mathbf{Q} \mathbf{F}_1)^T \mathbf{P} \mathbf{B}_{ccw,in}, \quad (2.44)$$

where the superscript (T) indicates a transposition [16]. If the coupler does not change the state of polarisation of the input signals $A_{f,in}$ and $A_{b,in}$ and the coupling parameters ε_1 , ε_2 , φ_1 and φ_2 are the same for TE polarised light and TM polarised light the clockwise change of polarisation must be equal to the change of state of polarisation experienced by the counter clockwise travelling signal i.e.

$$\mathbf{F}_2 \mathbf{Q} \mathbf{F}_1 = \mathbf{P} \mathbf{F}_2^* \mathbf{Q}^* \mathbf{F}_1^* \mathbf{P}. \quad (2.45)$$

This equation is solved for

$$\mathbf{Q} = \mathbf{F}_2^{-1} \mathbf{F}_1^{-1}. \quad (2.46)$$

This solution shows that the function of the polarisation controller is to compensate for the different polarisation rotation in the fibre loop for the clockwise and counter clockwise propagating signals. In the remainder of this thesis the polarisation controller is set to compensate for the change of polarisation in the fibre and coupler. As a result the Sagnac interferometer is assumed to be polarisation independent.

Non-ideal fibre couplers

Equally important is the behaviour of the coupler. The coupler in Fig. 2.6 is characterised by four parameters. ε_1 and ε_2 are the power ratios for “bar” coupling and “cross” coupling, respectively. φ_1 and φ_2 are the respective phases the signal experiences for “bar” and “cross” coupling. These four parameters are used to describe the coupling process regardless of which port(s) is(are) excited. In the case of a lossless coupler ($\varepsilon_1 + \varepsilon_2 = 1$), the phase difference of the signals at the output ports is 90 degrees, i.e. $\varphi_2 - \varphi_1 = 90^\circ$. If $\varepsilon_1 + \varepsilon_2 < 1$ a deviation in phase ($\varphi_2 - \varphi_1$) from the theoretical value of 90° can occur. Due to losses and reflections in non ideal couplers, power is lost or transferred to the other ports without experiencing the theoretical 90° phase shift because in the case of reflections, excitation of symmetric and asymmetric modes (which is responsible for the 90° phase shift) does not apply. In multimode interference couplers (MMIs) non ideal coupling occurs when, for example, there is a mismatch between the position of the output waveguide and the place where an interferometric maximum exists. In theoretical models of fusion-spliced fibre couplers the source of non ideal coupling is portrayed by inhomogeneous and complex dielectric constants that act on the complex coupling coefficients in coupled differential equations that describe the propagation of the optical fields travelling in the coupler [17].

The clockwise and counter clockwise travelling input signals of the fibre loop can be expressed as

$$\begin{aligned} B_{cw,in} &= \sqrt{\varepsilon_1} \exp(j\varphi_1) \cdot A_{f,in} + \sqrt{\varepsilon_2} \exp(j\varphi_2) \cdot A_{b,in}, \\ B_{ccw,in} &= \sqrt{\varepsilon_1} \exp(j\varphi_1) \cdot A_{b,in} + \sqrt{\varepsilon_2} \exp(j\varphi_2) \cdot A_{f,in}, \end{aligned} \quad (2.47)$$

where $A_{f,in}$ is the input signal in the forward direction and $A_{b,in}$ the input signal in the backward direction. Both B_{cw} and B_{ccw} travel through the same fibre and therefore both signals experience the same phase. After a time τ_{loop} the signals leave the loop as

$$\begin{aligned} B_{cw,out} &= \exp(j\omega\tau_{loop}) \cdot B_{cw,in}, \\ B_{ccw,out} &= \exp(j\omega\tau_{loop}) \cdot B_{ccw,in}, \end{aligned} \quad (2.48)$$

for the clockwise and counter clockwise signal. At the ports of the Sagnac interferometer

$$\begin{aligned} A_{f,out} &= \sqrt{\varepsilon_1} \exp(j\varphi_1) \cdot B_{cw,out} + \sqrt{\varepsilon_2} \exp(j\varphi_2) \cdot B_{ccw,out}, \\ A_{b,out} &= \sqrt{\varepsilon_1} \exp(j\varphi_1) \cdot B_{ccw,out} + \sqrt{\varepsilon_2} \exp(j\varphi_2) \cdot B_{cw,out} \end{aligned} \quad (2.49)$$

appear. $A_{f,out}$ and $A_{b,out}$ are the output signal travelling in the forward and backward direction. Substitution of Eqs. 2.47-2.49 results in a relation between the input and output signals.

$$\begin{aligned} A_{f,out} &= [\varepsilon_1 \exp(j2\varphi_1) + \varepsilon_2 \exp(j2\varphi_2)] \cdot A_{f,in} + \\ &\quad 2\sqrt{\varepsilon_1\varepsilon_2} \exp(j(\varphi_1 + \varphi_2)) \cdot A_{b,in}, \\ A_{b,out} &= [\varepsilon_1 \exp(j2\varphi_1) + \varepsilon_2 \exp(j2\varphi_2)] \cdot A_{b,in} + \\ &\quad 2\sqrt{\varepsilon_1\varepsilon_2} \exp(j(\varphi_1 + \varphi_2)) \cdot A_{f,in}, \end{aligned} \quad (2.50)$$

where the factor $\exp(j\omega\tau_{loop})$ has been omitted because it imposes the same phase on both signals and is therefore not of interest.

The Sagnac interferometer acts as a mirror when the condition

$$\varepsilon_1 \exp(j2\varphi_1) + \varepsilon_2 \exp(j2\varphi_2) = 0 \quad (2.51)$$

is fulfilled. This equation implies that only when $\varepsilon_1 = \varepsilon_2$ and $\varphi_2 - \varphi_1 = 90^\circ$ total reflection occurs.

There is however a special case when $\varepsilon_1 = \varepsilon_2$. In the relation between $A_{f,out}$ and $A_{f,in}$ in Eqs. 2.50 the term $\varepsilon_1 \exp(j2\varphi_1)$ is due to the clockwise travelling signal and $\varepsilon_2 \exp(j2\varphi_2)$ is due to the counter clockwise travelling signal. The clockwise travelling signal can experience a change of state of polarisation described by matrix

$$\mathbf{S}_{cw} = \begin{bmatrix} \sqrt{\varepsilon} \exp(-j\phi) & j\sqrt{1-\varepsilon} \exp(-j\theta) \\ j\sqrt{1-\varepsilon} \exp(j\theta) & \sqrt{\varepsilon} \exp(j\phi) \end{bmatrix}, \quad (2.52)$$

Whereas the counter clockwise travelling signal experiences a polarisation transformation described by matrix

$$\mathbf{S}_{ccw} = \mathbf{P} \mathbf{S}_{cw}^T \mathbf{P} = \begin{bmatrix} \sqrt{\varepsilon} \exp(-j\phi) & j\sqrt{1-\varepsilon} \exp(j\theta) \\ j\sqrt{1-\varepsilon} \exp(-j\theta) & \sqrt{\varepsilon} \exp(j\phi) \end{bmatrix}. \quad (2.53)$$

For one specific state of polarisation rotation ($\varepsilon = 0$ and $\phi = 0$) an additional phase difference can be imposed on φ_1 and φ_2 so that full reflection occurs. In this case light polarised along the x-axis is converted to light polarised along the y-axis and experiences a phase shift of $j \exp(-j\theta)$ and $j \exp(j\theta)$ for respective the clockwise and counter clockwise travelling signals. By the same token, light polarised along the y-axis is converted to light polarised along the x-axis and experiences a phase shift of $j \exp(j\theta)$ and $j \exp(-j\theta)$ for the clockwise and counter clockwise travelling signals. This implies that light polarised along the x-axis, (y-axis), experiences an improved reflectivity and light polarised along the y-axis, (x-axis), experiences a reduced reflectivity. Consequently, the Sagnac interferometer has become polarisation sensitive. The above can be observed experimentally. The configuration depicted in Fig. 2.6 has been built and extended with a polarisation controller at the input. The polarisation controllers are composed of a half-wave plate and a quarter-wave plate that can be rotated to change the state of polarisation of the light. Both wheels have a scaled read out ranging from 0° to 360° . The input signal is a 1 mW, 1310 nm continuous wave signal generated by a DFB laser diode. First, the output signal is minimised and the settings of both polarisation controllers are recorded. Secondly, the input polarisation controller is adjusted such that the output is maximised. Any difference between these measured values indicates a polarisation sensitivity of the Sagnac interferometer. Now a setting for the polarisation

Table 2.1: Polarisation controller settings and Sagnac output powers for four couplers. The first two lines contain the minimum and maximum output powers which are obtained by changing the input polarisation. The third and fourth lines show the output powers when the polarisation controller in the loop is adjust such that variations in output power are as small as possible.

FBT 118 LI 1300nm					FBT 122 LI 1300nm				
Pol. Ctrl. 1		Pol. Ctrl. 2		P_{out} [μW]	Pol. Ctrl. 1		Pol. Ctrl. 2		P_{out} [μW]
HWP	QWP	HWP	QWP		HWP	QWP	HWP	QWP	
138°	3°	289°	352°	0.21	350°	70°	55°	200°	0.240
120°	245°	289°	352°	17.9	36°	328°	55°	200°	14.20
244°	342°	320°	240°	8.4	205°	64°	141°	164°	3.980
196°	330°	320°	240°	9.2	320°	90°	141°	164°	4.040
FBT 124 LI 1300nm					commercial device 201249				
Pol. Ctrl. 1		Pol. Ctrl. 2		P_{out} [μW]	Pol. Ctrl. 1		Pol. Ctrl. 2		P_{out} [μW]
HWP	QWP	HWP	QWP		HWP	QWP	HWP	QWP	
219°	182°	211°	325°	0.098	130°	245°	20°	75°	0.110
297°	117°	211°	325°	0.450	84°	330°	20°	75°	2.01
62°	68°	91°	72°	0.206	Sagnac interferometer remains polarisation sensitive				
139°	254°	91°	72°	0.218					

controller in the loop is searched such that, when the state of polarisation of the input signal is changed, minimum variations in output power are observed. Again, the readouts of the polarisation controllers are recorded. Table 2.1 gives an overview of the measured positions of the two polarisation controllers for four different couplers. The three couplers, FBT 118 LI, FBT 122 LI and FBT 124 LI are couplers made by Philips Research Laboratories. The fourth coupler is commercially available from a different company. From Table 2.1 it can be seen that a Sagnac interferometer based on coupler FBT 118 LI and FBT 122 LI has become polarisation independent. Coupler FBT 124 LI is also polarisation independent and behaves more ideally than FBT 118 LI and FBT 122 LI because less power is transmitted. The Sagnac interferometer with a commercially available coupler could not be made polarisation insensitive. In the remainder of this chapter polarisation controllers are inserted to compensate for polarisation rotations in *fibres and couplers* where no polarisation rotations are allowed.

2.5 The terahertz optical asymmetrical demultiplexer

Figure 2.7 displays a Sagnac interferometer with a semiconductor optical amplifier inserted in the loop. This configuration called the terahertz optical asymmetric demultiplexer (TOAD) was first proposed by Sokoloff [18]. In addition to the semiconductor optical amplifier, an optical coupler, an adjustable optical delay and a polarisation controller can be found in this Sagnac interferometer based switch. The functionality of the polarisation controller has been

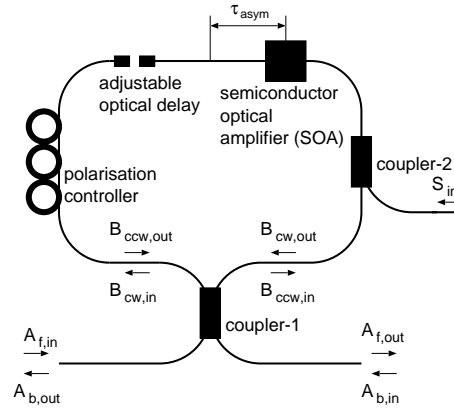


Figure 2.7: Geometry of the TOAD demultiplexer

investigated in detail in Sec. 2.4. Coupler-2 is used to insert signal $S_{in}(\tau)$ which is referred to as the switch signal. The adjustable optical delay is used to change the position of the amplifier in the loop. The input signal, $A_{f,in}$, contains the high bit rate line signal. If the TOAD operates correctly, the output signal, $A_{f,out}$, contains a demultiplexed channel of the line signal. Without the SOA the configuration of Fig. 2.7 acts as a Sagnac interferometer and the input signals are reflected according to the equations in Sec. 2.4. If a SOA is inserted the possibility exists to saturate the amplifier by means of a high intensity switch pulse. When this happens the refractive index of the amplifier changes. As a result the signals that are amplified will experience a different propagation constant before and after the saturation takes place. After saturation the gain recovers slowly compared to the saturation process which is almost instantaneous. In the geometry of Fig. 2.7 the clockwise signal needs $2\tau_{asym}$ seconds more time to reach the amplifier. It is this delay that causes a difference in encountered phase between the clockwise and counter clockwise travelling signals. If this phase difference is 180° then constructive interference occurs in coupler-1 instead of destructive interference and part of the line signal (the channel to be demultiplexed) will appear at the output. The quantitative theoretical operation of the TOAD depends strongly on the amplifier model and the waveform of the switch signal. Important issues are the shape of the switching window and the amount of power of the switch signal. The channel extinction ratio, which can be defined as the ratio of the amount of energy in the switching window and the amount of energy outside the switching window, is an important measure for the performance of the switch. Equally important is the amount of switch power that is needed to achieve switching and the minimum and maximum power of the input line signal. When the input power (of the data signal) is too low, amplifier noise will degrade the performance. On the other hand, when the input power is too high the input signal will saturate the amplifier and switch it self instead of being switched. Consequently, this leads to non error-free operation. In the next subsections the dependence of the channel extinction ratio on different amplifier, coupler and switch signal parameters is investigated theoretically. This is done for a 40 Gb/s to 10 Gb/s demultiplexer which will be realised experimentally in Chapter 5. It will be shown that

finding parameters for optimal performance of the TOAD is complicated and that if they are found, the question remains as to whether they can physically be realised.

2.5.1 Dirac delta pulse switching of the TOAD with zero length SOA

A special case in which the switching window of the TOAD can be analytically determined is the case where Dirac delta pulses control the switching properties of the amplifier. The amplifier is assumed to be spatially concentrated.

Amplifier response to a Dirac delta pulse train

A Dirac delta pulse is a theoretical pulse of zero duration and infinite power. However the energy of the pulse has a finite value E_{switch} . In this section, the gain response of an optical saturable amplifier to a periodic Dirac delta pulse signal is determined. It must be noted that the frequency spectrum of a train of Dirac delta pulses extends from minus infinity to infinity, thus beyond the bandwidth of the amplifier. In addition infinitely small pulses do not exist in any practical situation. However, the exercise below suits the demonstration of operation of the TOAD and expresses the formation of a temporal window by an analytical formula. The periodic signal is mathematically described as

$$P_{in}(\tau) = E_{switch} \sum_{n=-\infty}^{\infty} \delta(\tau - nT_b) \quad (2.54)$$

T_b is the time between two Dirac pulses. E_{switch} is the energy that is contained in one pulse. The average power is therefore $P_{in,avg} = E_{switch}/T_b$. The rate equation that describes the gain of a spatially concentrated optical amplifier is given by (see Section 2.3.1)

$$\frac{\partial h(\tau)}{\partial \tau} = \frac{h_0 - h(\tau)}{\tau_c} - \frac{P_{in}(\tau)}{E_{sat}} \cdot (\exp(h(\tau)) - 1). \quad (2.55)$$

The delta pulse excitation allows Eq. 2.55 to be split up into an equation that describes the fast saturation at times $t = nT_b$,

$$\frac{\partial h(\tau)}{\partial \tau} = -\frac{P_{in}(\tau)}{E_{sat}} \cdot (\exp(h(\tau)) - 1). \quad (2.56)$$

and in an equation that describes the relatively slow recovery between the Dirac pulses,

$$\frac{\partial h(\tau)}{\partial \tau} = \frac{h_0 - h(\tau)}{\tau_c}. \quad (2.57)$$

This separation is allowed under the assumption that saturation takes place immediately and infinitely fast so that during saturation the gain does not recover (first term on the right side of Eq. 2.55). For pulses that have a finite duration this derivation is not valid. However if a small error is acceptable, input pulses with a pulse width smaller than $0.001\tau_c$ can be treated. For a typical value of 200 ps for τ_c , pulses with a full-width half-maximum pulse width τ_{fwhm} of 0.2 ps are acceptable. The gain before the Dirac pulses enter the amplifier is equal to

$h(-\xi + nT_b) = h_2 < h_0$, with ξ infinitely small. The periodic nature of the input signal prevents a complete recovery of the amplifier. Immediately after the input pulse enters the amplifier the gain saturates to a level equal to $h(+\xi + nT_b) = h_1 < h_2$. This can be found by solving Eq. 2.56. The solution can be found by separation of Eq. 2.56 after which the left and right part are integrated over time. This results in

$$\int_{-\xi+nT_b}^{\tau+nT_b} \frac{1}{\exp[h(\tau')] - 1} dh(\tau') = \frac{-1}{E_{sat}} \int_{-\xi+nT_b}^{\tau+nT_b} P_{in}(\tau') d\tau', \quad (2.58)$$

Evaluation of Eq. 2.58 results in an expression for the total amplifier gain around $\tau = nT_b$.

$$h(\tau + nT_b) = -\ln\left[1 - \left\{(1 - \exp(-h(-\xi + nT_b)))\right\} \exp\left(-\frac{E_{in}(\tau + nT_b)}{E_{sat}}\right)\right], \quad (2.59)$$

for $-\xi \leq \tau \leq \xi$, with

$$E_{in}(\tau) = \int_{-\xi+nT_b}^{\tau+nT_b} P_{in}(\tau') d\tau', \quad -\xi \leq \tau \leq \xi. \quad (2.60)$$

Thus linking h_1 to h_2 for ξ going to zero:

$$h_1 = -\ln\left\{1 - \left(1 - \frac{1}{\exp(h_2)}\right) \exp\left(-\frac{E_{switch}}{E_{sat}}\right)\right\}. \quad (2.61)$$

After the amplifier is saturated the excitation will remain zero for a time T_b in which the amplifier recovers according to Eq. 2.57. The solution of this equation is

$$\begin{aligned} h(\tau + nT_b) &= h_0\left(1 - \exp\left(-\frac{\tau + nT_b}{\tau_c}\right)\right) + \\ &h(+\xi) \exp\left(-\frac{\tau + nT_b}{\tau_c}\right), \quad +\xi \leq \tau \leq T_b - \xi. \end{aligned} \quad (2.62)$$

This second equation links h_2 to h_1 when ξ approaches zero.

$$h_2 = h_0\left(1 - \exp\left(-\frac{T_b}{\tau_c}\right)\right) + h_1 \exp\left(-\frac{T_b}{\tau_c}\right). \quad (2.63)$$

From Eqs. 2.59 and 2.62 the total gain is computed

$$\begin{aligned} h(\tau) &= \sum_{n=-\infty}^{\infty} [u(\tau - nT_b) - u(\tau - nT_b - T_b)] \cdot \\ &\left\{ \frac{h_2 - h_1}{1 - \exp\left(-\frac{T_b}{\tau_c}\right)} \left(1 - \exp\left(-\frac{\tau - nT_b}{\tau_c}\right)\right) + h_1 \right\}, \end{aligned} \quad (2.64)$$

where $u(\tau)$ is the unit step function. The response of the amplifier to a periodic pulse train of Dirac delta pulses is now determined. The remainder of this section will be devoted to the terahertz optical asymmetric demultiplexer that is excited by this periodic delta pulse switch signal. The input signal (line signal) that is to be switched is of such low intensity that it does not significantly saturate the amplifier. The amplifier is saturated periodically at times

$\tau = \tau_{phase} + nT_b$. The position of the switching window is controlled inside a T_b wide time interval by τ_{phase} so that a desired channel can be selected. In the remainder of this chapter the input line signal is assumed to be continuous wave so that the visibility of the time window that is created is enhanced and the quantities that determine performance such as the channel extinction ratio, can be determined independently from the shape of the pulses forming the line signal. An optical signal with complex envelope $A_{f,in}(\tau)$ and power $P_{f,in} = |A_{f,in}|^2$ enters the main coupler of the TOAD and is split up into a clockwise and counter clockwise travelling signal

$$B_{cw,in}(\tau) = \sqrt{\varepsilon_1} \exp(j\varphi_1) A_{f,in}(\tau), \quad (2.65)$$

$$B_{ccw,in}(\tau) = \sqrt{\varepsilon_2} \exp(j\varphi_2) A_{f,in}(\tau). \quad (2.66)$$

Both signals experience a complex gain at one point in the Sagnac interferometer. The time at which this occurs depends on the asymmetry of the amplifier and the total length of the loop of the Sagnac interferometer. Without taking the transmission delay of the loop, τ_{loop} , into account, the clockwise and counter clockwise travelling signals return at the main coupler of the TOAD having experienced a complex gain. These signals can be determined to be

$$B_{cw,out}(\tau) = B_{cw,in}(\tau) \cdot \exp\left(\frac{1}{2}(1 - j\alpha_H)h(\tau - \tau_{phase} + 2\tau_{asym})\right), \quad (2.67)$$

$$B_{ccw,out}(\tau) = B_{ccw,in}(\tau) \cdot \exp\left(\frac{1}{2}(1 - j\alpha_H)h(\tau - \tau_{phase})\right). \quad (2.68)$$

In the case $\tau_{asym} = 0$ both clockwise and counter clockwise travelling signals pass the amplifier at the same time and will therefore experience the same propagation constants. Therefore no window in time will open. At the outputs of the Sagnac interferometer the forward directed output, $A_{f,out}$, and backward directed output, $A_{b,out}$, are expressed as

$$\begin{aligned} A_{f,out}(\tau) &= \sqrt{\varepsilon_1} \exp(\varphi_1) \cdot B_{cw,out}(\tau) + \\ &\quad \sqrt{\varepsilon_2} \exp(\varphi_2) \cdot B_{ccw,out}(\tau), \\ A_{b,out}(\tau) &= \sqrt{\varepsilon_1} \exp(\varphi_1) \cdot B_{ccw,out}(\tau) + \\ &\quad \sqrt{\varepsilon_2} \exp(\varphi_2) \cdot B_{cw,out}(\tau), \end{aligned} \quad (2.69)$$

respectively. Substitution of Eqs. 2.66-2.69 gives for the forward directed output, $A_{f,out}$, of the TOAD

$$\begin{aligned} A_{f,out}(\tau) &= A_{f,in}(\tau) \varepsilon_1 \exp(2j\varphi_1) \exp\left(\frac{1}{2}(1 - j\alpha_H)h(\tau - \tau_{phase} + 2\tau_{asym})\right) + \\ &\quad A_{f,in}(\tau) \varepsilon_2 \exp(2j\varphi_2) \exp\left(\frac{1}{2}(1 - j\alpha_H)h(\tau - \tau_{phase})\right), \end{aligned} \quad (2.70)$$

and for the backward directed output, $A_{b,out}$, of the TOAD

$$\begin{aligned} A_{b,out}(\tau) &= A_{f,in}(\tau) \sqrt{\varepsilon_1 \varepsilon_2} \exp(2j(\varphi_1 + \varphi_2)) \cdot \\ &\quad \left[\exp\left(\frac{1}{2}(1 - j\alpha_H)h(\tau - \tau_{phase} + 2\tau_{asym})\right) + \right. \\ &\quad \left. \exp\left(\frac{1}{2}(1 - j\alpha_H)h(\tau - \tau_{phase})\right) \right]. \end{aligned} \quad (2.71)$$

τ_{phase} is the reduced time where the temporal window opens. $2 \cdot \tau_{asym}$ second later the window closes. For $\tau_{phase} = \tau_{asym}$ the window is centred around $\tau = 0$. Substitution of the

analytical expression for $h(\tau)$, Eq. 2.64, leads to the analytical expression for the normalised fields, $A_{f,out}(\tau)$ and $A_{b,out}(\tau)$, and powers,

$$P_{f,out}(\tau) = |A_{f,out}(\tau)|^2 [\varepsilon_1^2 \exp(h(\tau - \tau_{phase} + 2\tau_{asym})) + \varepsilon_2^2 \exp(h(\tau - \tau_{phase})) + 2\varepsilon_1\varepsilon_2 \exp(\frac{1}{2}(h(\tau - \tau_{phase} + 2\tau_{asym}) + h(\tau - \tau_{phase}))) \cdot \cos(2(\varphi_2 - \varphi_1) + \frac{1}{2}\alpha_H(h(\tau - \tau_{phase} + 2\tau_{asym}) - h(\tau - \tau_{phase})))] \quad (2.72)$$

and

$$P_{b,out}(\tau) = |A_{f,out}(\tau)|^2 \varepsilon_1\varepsilon_2 [\exp(h(\tau - \tau_{phase} + 2\tau_{asym})) + \exp(h(\tau - \tau_{phase})) + 2 \exp(\frac{1}{2}(h(\tau - \tau_{phase} + 2\tau_{asym}) + h(\tau - \tau_{phase}))) \cdot \cos(\frac{1}{2}\alpha_H(h(\tau - \tau_{phase} + 2\tau_{asym}) - h(\tau - \tau_{phase})))] \quad (2.73)$$

When an ideal coupler ($\varepsilon_1 = \varepsilon_2 = \frac{1}{2}$ and $\varphi_2 - \varphi_1 = 90^\circ$) is used Eqs. 2.72 and 2.73 reduce to

$$P_{f,out}(\tau) = \frac{1}{4} |A_{f,out}(\tau)|^2 [\exp(h(\tau - \tau_{phase} + 2\tau_{asym})) + \exp(h(\tau - \tau_{phase})) - 2 \exp(\frac{1}{2}(h(\tau - \tau_{phase} + 2\tau_{asym}) + h(\tau - \tau_{phase}))) \cdot \cos(\frac{1}{2}\alpha_H(h(\tau - \tau_{phase} + 2\tau_{asym}) - h(\tau - \tau_{phase})))] \quad (2.74)$$

and

$$P_{b,out}(\tau) = \frac{1}{4} |A_{f,out}(\tau)|^2 [\exp(h(\tau - \tau_{phase} + 2\tau_{asym})) + \exp(h(\tau - \tau_{phase})) + 2 \exp(\frac{1}{2}(h(\tau - \tau_{phase} + 2\tau_{asym}) + h(\tau - \tau_{phase}))) \cdot \cos(\frac{1}{2}\alpha_H(h(\tau - \tau_{phase} + 2\tau_{asym}) - h(\tau - \tau_{phase})))], \quad (2.75)$$

as found in Ref. [19]. A special case occurs if $\tau_{phase} = \tau_{asym}$. The window that will be created when the amplifier is saturated will be centred at $\tau = 0$. Figure 2.8 displays the response of a TOAD without any parameter optimisation. It can be clearly seen that at $\tau = 0$ a 25 ps wide window is located where the forward gain exceeds 80. Outside this window the gain remains below 15. The gain of the SOA causes amplification in both forward and backward direction. The desired, to be switched, interval is amplified more than the undesired, not to be switched, interval. In other words the demultiplexing can be considered as temporal selective amplification. This window can therefore be used to amplify one channel of an optically multiplexed line signal. In this example the demultiplexing ratio is $\frac{2\tau_{asym}}{T_b} = \frac{1}{4} = \frac{1}{N_{channel}}$ allowing a 40 Gb/s signal to be demultiplexed to 10 Gb/s. An important measure of performance is the ratio between the energy in the switching window and the energy outside the window. This ratio will be referred to as the channel extinction

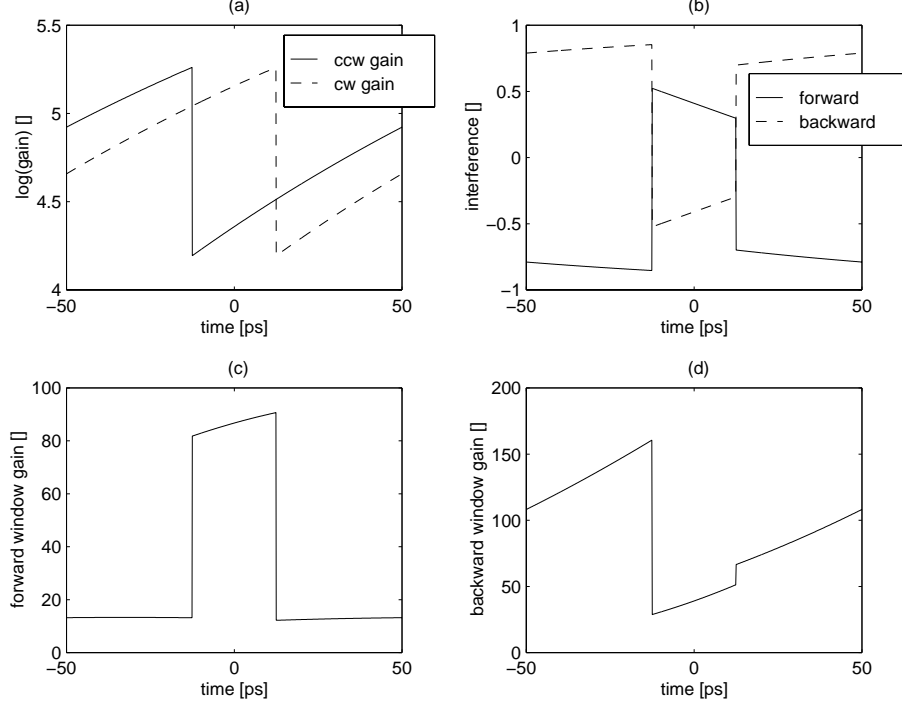


Figure 2.8: (a) Gain that is experienced by the counter clockwise travelling signal (solid curve) and clockwise travelling signal (dashed curve). (b) The cosine term of Eq. 2.72 (solid curve) and the cosine term of Eq. 2.73 (dashed curve), (c) Gain at the forward output (Eq. 2.72), (d) Gain at the backward output (Eq. 2.73). $E_{switch} = 0.1$ pJ, $E_{sat} = 10$ pJ, $T_b = 100$ ps, $T_c = 200$ ps, $T_{asym} = 12.5$ ps, $G = 1000$, $\alpha_H = 5$, $\varepsilon_1 = \varepsilon_2 = 0.5$, $\varphi_1 = 0^\circ$ and $\varphi_2 = 90^\circ$

ration, $R_{channel}$.

$$R_{channel} = \frac{\int_{\tau_{phase} - \frac{T_b}{N_{channel}}}^{\tau_{phase}} P_{out,f}(\tau) d\tau}{\int_{-T_b/2}^{\tau_{phase} - \frac{T_b}{N_{channel}}} P_{out,f}(\tau) d\tau + \int_{\tau_{phase}}^{T_b/2} P_{out,f}(\tau) d\tau} \quad (2.76)$$

If this ratio becomes too small, severe “eye closure” will deteriorate the bit error rate performance of the TOAD based system. The parameters in this model can be divided into three groups. E_{switch} and T_b which are related to the switching signal, τ_c , E_{sat} , G , α_H which are related to the optical amplifier and ε_1 , ε_2 , φ_1 , φ_2 and τ_{asym} which are related to the coupler and geometry of the Sagnac interferometer. All parameters act nonlinearly on the shape of the forward gain window and $R_{channel}$. Figure 2.9 shows how the shape of the window can be influenced by changing the linewidth enhancement factor and the energy of the switch pulses. In the case of $\alpha_H = 0$ the signals in the loop of the TOAD do not experience phase shifts due to the saturation of the amplifier. Only a difference in amplitude is imposed on

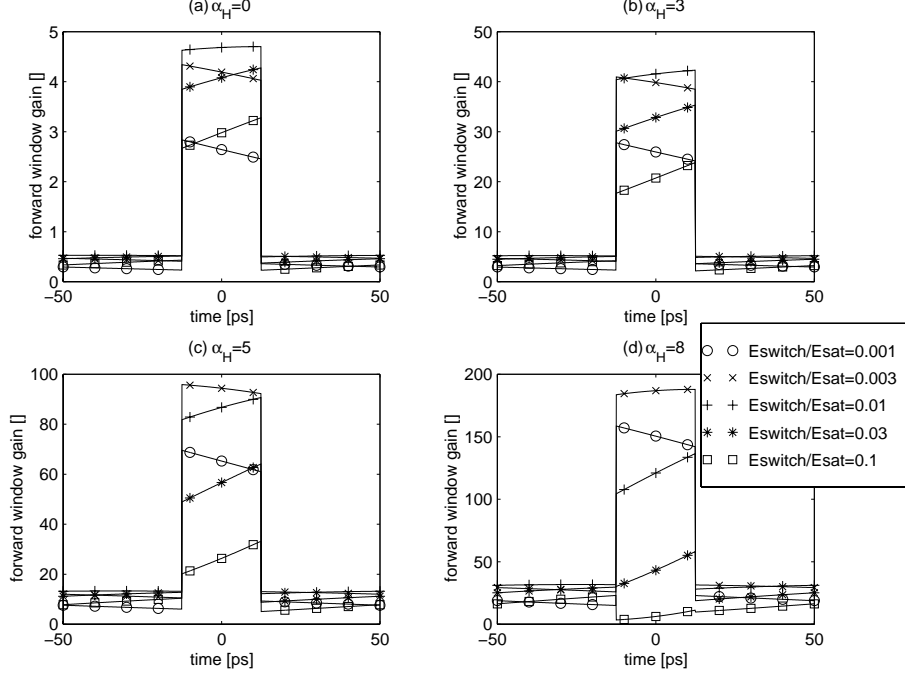


Figure 2.9: Forward gain for different values of α_H and E_{switch}/E_{sat} . $E_{sat} = 10$ pJ, $T_b = 100$ ps, $T_c = 200$ ps, $G = 1000$, $\varepsilon_1 = \varepsilon_2 = 0.5$, $\varphi_1 = 0^\circ$, $\varphi_2 = 90^\circ$ and $T_{asym} = 12.5$ ps.

the signals resulting in very low gain. When α_H increases more power is transferred to the output. However, the channel extinction ratio does not significantly improve. In addition, the optimum switch energy depends on α_H implying that if the current through the amplifier varies, α_H varies and that this can be compensated for by increasing or decreasing the energy of the switch pulses. Significant improvement of the TOAD can be achieved if the phase difference $\varphi_2 - \varphi_1$ deviates from 90° . In Sec. 2.4 it is argued that the transmission of the Sagnac interferometer is expected to increase and the reflectivity to decrease. In Fig. 2.8 (b) the solid curve represents the influence of the phase changes in the loop on the cosine component in Eq. 2.72. Outside the window the curve does not reach -1 which means that the output power of the TOAD can be much lower for this time interval. Inside the window the curve does not reach $+1$ which means that the output power can be much higher. Figure 2.10 shows that when the phase difference $2(\varphi_2 - \varphi_1)$ becomes less than 180° the extinction ratio improves because the signals outside the window will be suppressed. At the same time the signals inside the window will be enhanced. Note that in Fig. 2.10 the scale of the forward and backward window is in dB. In addition, a small change of the coupling coefficients of the coupler, ε_1 and ε_2 , improved the response of the TOAD. Figure 2.10 (b) compared to Fig. 2.8 (c) shows that the channel extinction ratio has improved considerably outside the window and that inside the window more power is passed to the output. The amount of phase shift that is introduced depends on the phase mismatch of the coupler and can not be ad-

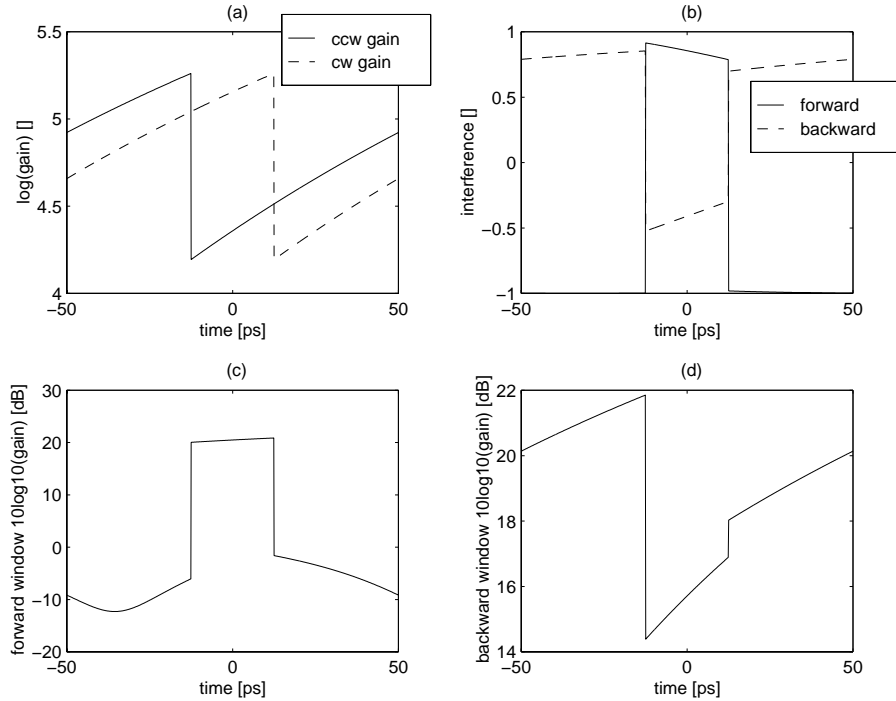


Figure 2.10: (a) Gain that is experienced by the counter clockwise travelling signal (solid curve) and clockwise travelling signal (dashed curve). (b) The cosine term of Eq. 2.72 (solid curve) and the cosine term of Eq. 2.73 (dashed curve), (c) Gain at the forward output (Eq. 2.72), (d) Gain at the backward output (Eq. 2.73). $E_{switch} = 0.1$ pJ, $E_{sat} = 10$ pJ, $T_b = 100$ ps, $T_c = 200$ ps, $T_{asym} = 12.5$ ps, $G = 1000$, $\alpha_H = 5$, $\varepsilon_1 = 0.45$, $\varepsilon_2 = 0.53$, $\varphi_1 = 17.3^\circ$ and $\varphi_2 = 90^\circ$

Table 2.2: Parameters according to the windows of Fig. 2.14 $\tau_{asym} = 12.5$ ps, $T_b = 100$ ps, $T_c = 200$ ps, $E_{switch} = 0.1$ pJ

	(a)	(b)	(c)	(d)
ε_1	0.464	0.385	0.227	0.393
ε_2	0.532	0.462	0.285	0.475
φ_1	17.00°	12.61°	1.86°	8.09°
φ_2	90°	90°	90°	90°
gain G	1000	900	450	350
E_{sat} [pJ]	10	25	14.29	2.0
α_H	4.55	5.1	4.6	2.1

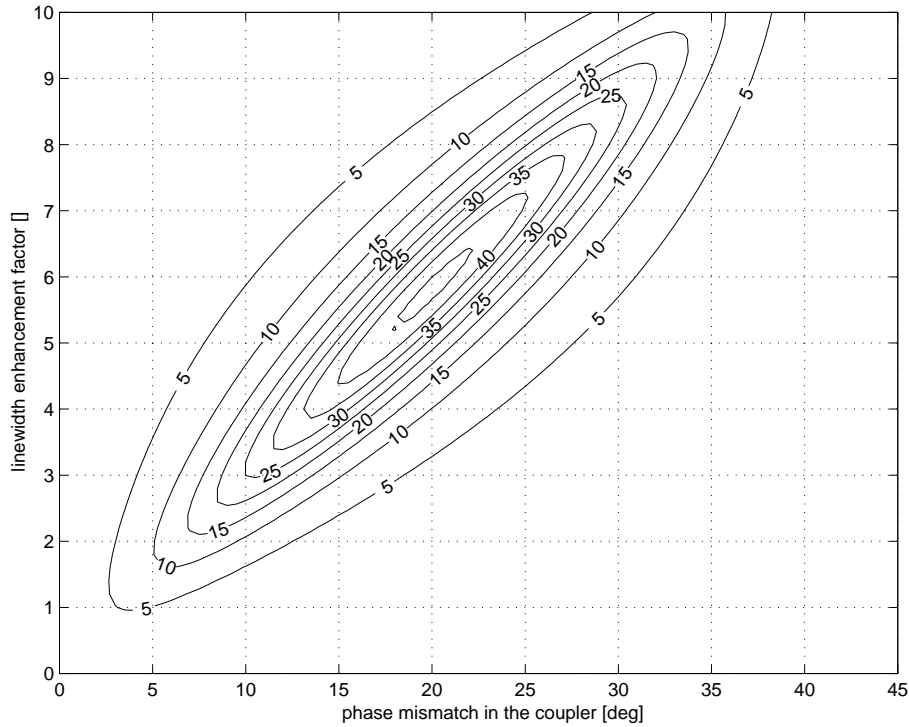


Figure 2.11: $R_{channel}$ versus α_H and $\Delta\varphi_1$. $E_{switch} = 0.1$ pJ, $E_{sat} = 10$ pJ, $T_b = 100$ ps, $T_c = 200$ ps, $T_{asym} = 12.5$ ps, $G = 1000$, $\varepsilon_1 = \varepsilon_2 = 0.4$ and $\varphi_2 = 90^\circ$

justed, unless active couplers are used. What can be adjusted is α_H because this parameter depends on the current and temperature of the amplifier. Figure 2.11 displays the channel extinction ratio as a function of the phase mismatch in φ_1 , $\Delta\varphi_1$, and α_H . It can be clearly seen that in the case of a phase mismatch of zero degrees the extinction ratio will not exceed a factor five. Therefore it is important to use a coupler that exhibits some amount of polarisation independent crosstalk. In combination with an optical amplifier with the correct α_H , this phase mismatch causes a high contrast switch window with low channel crosstalk. The optimum can be found in the inner $R_{channel} = 45$ contour circle and occurs for $\alpha_H \approx 5.85$ and $\Delta\varphi_1 \approx 20^\circ$.

Figure 2.10 was recomputed by changing ε_1 and ε_2 to obtain a higher channel extinction ratio. From Eq. 2.72 it is expected that alteration of the coupling coefficients will lead to performance improvement or degradation depending on the extent the amplitudes of the terms in Eq. 2.72 can be fine tuned. Figure 2.12 shows how the channel extinction ratio depends on the coupling coefficients in the case of a coupler phase mismatch, $\Delta\phi_1 = 20^\circ$ and $\alpha_H = 5.85$. According to this graph it is preferred not to use an ideal 3dB coupler but a coupler that is asymmetric by about 10%.

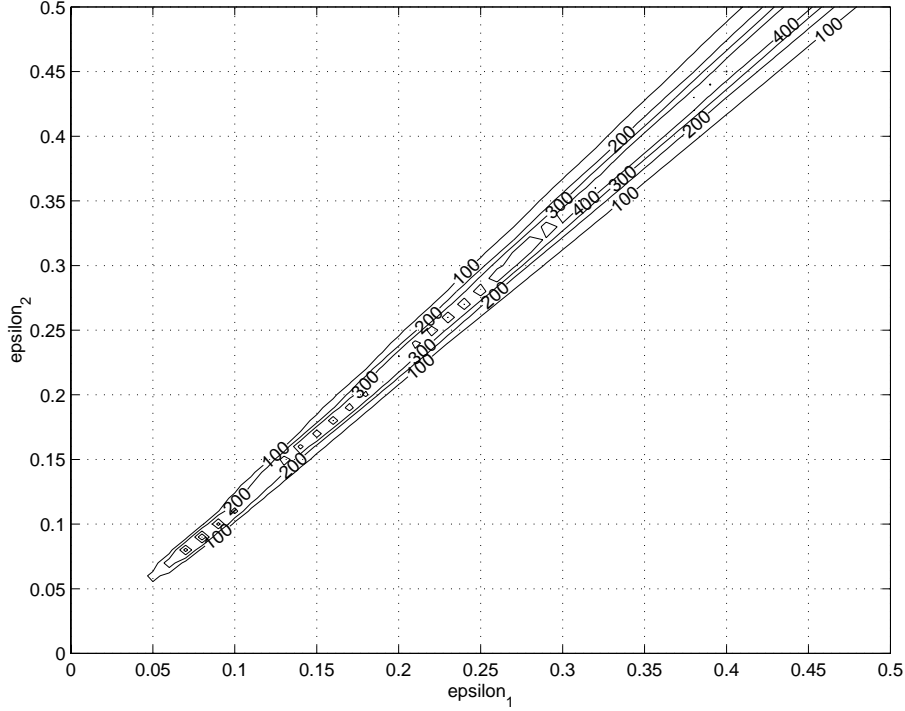


Figure 2.12: $R_{channel}$ dependence on the coupling coefficients ε_1 and ε_2 for $\alpha_H = 5.85$ and coupler phase mismatch $\Delta\varphi_1 = 20^\circ$. $E_{switch} = 0.1$ pJ, $E_{sat} = 10$ pJ, $T_b = 100$ ps, $T_c = 200$ ps, $T_{asym} = 12.5$ ps and $G = 1000$

Equally important is the influence of the gain on the system. In Fig. 2.13 the dependence of the channel extinction ratio on the gain and ratio between switch pulse energy and saturation energy is depicted. This has been done for non-optimal values for ε_1 and ε_2 to enhance visibility. Low gain allows a broad interval for the E_{switch}/E_{sat} where an acceptable channel extinction ratio can be obtained. When E_{switch}/E_{sat} is low a broad interval exists for the gain to obtain an acceptable extinction ratio. In addition, when the phase mismatch $\Delta\varphi_1$ deviates from $\Delta\varphi_1 = 20^\circ$ a larger area is available where switching is possible with a lower channel extinction ratio. A trade-off should be made between interval where the gain and the E_{switch}/E_{sat} ratio adopt values and the channel extinction ratio that is required. When designing a TOAD it is important to select a coupler that fits the parameters of the amplifier. The simulations in this section show that a non-ideal coupler is preferred. The amplifier should be adjusted in such a way that the parameters of the amplifier in combination with the parameters of the coupler result in high contrast switching i.e. a high channel extinction ratio. In Fig. 2.14 four different parameter sets of optical couplers have been drawn. For each parameter set the parameters G , E_{sat} and α_H of the amplifier are manually adjusted to optimise the channel extinction ratio. These parameters can be found in Table 2.2. When the

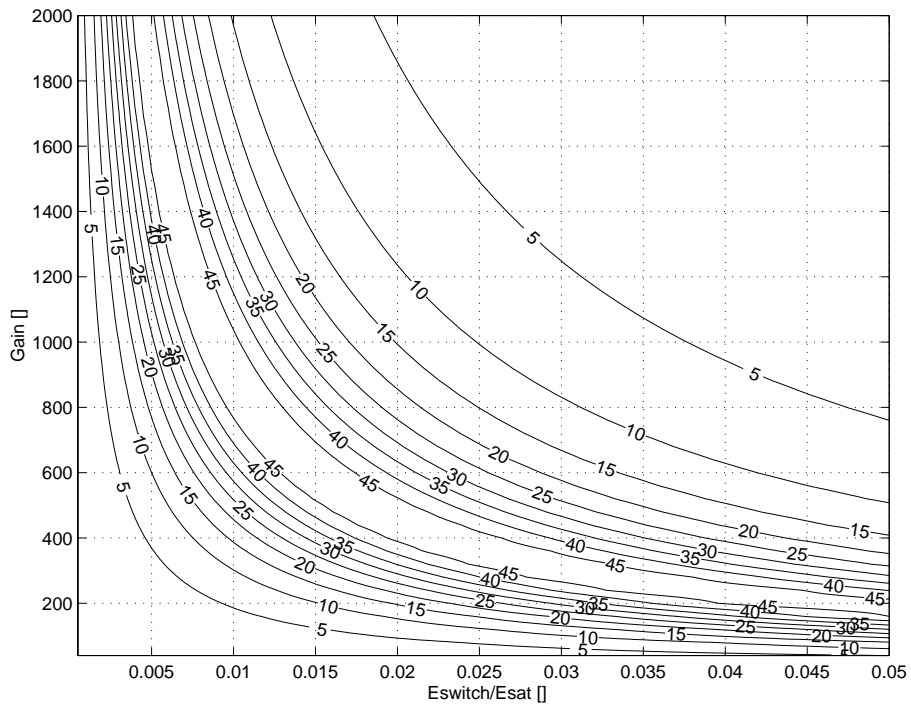


Figure 2.13: Dependence of $R_{channel}$ on the gain G and the ratio E_{switch}/E_{sat} for $\alpha_H = 5.85$ and coupler phase mismatch $\Delta\varphi_1 = 20^\circ$. $E_{switch} = 0.1 \text{ pJ}$, $E_{sat} = 10 \text{ pJ}$, $T_b = 100 \text{ ps}$, $T_c = 200 \text{ ps}$, $T_{asym} = 12.5 \text{ ps}$, $\varepsilon_1 = \varepsilon_2 = 0.4$

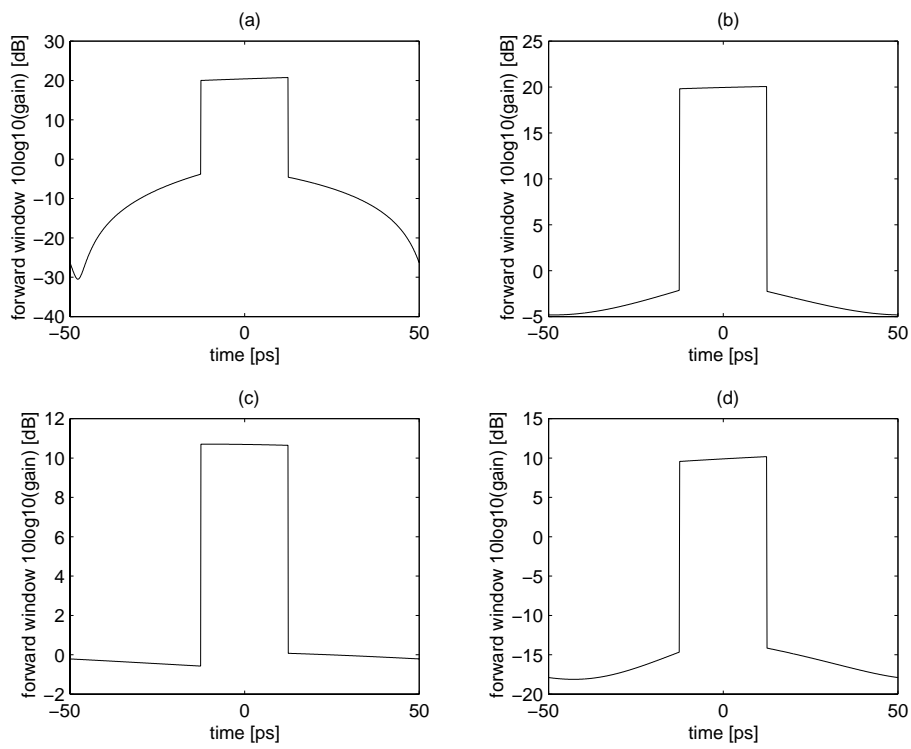


Figure 2.14: Optimised switching windows for four different sets of parameters of the coupler (see Table 2.2)

TOAD is realised the current and temperature of the amplifier determine G , E_{sat} and α_H . These parameters can not be controlled independently. If the properties of the coupler require amplifier parameters that cannot be reached by adjusting current and temperature than the TOAD will not perform optimally. A different coupler must be incorporated to which the amplifier can be adjusted.

2.5.2 Non-zero pulse width switching of a TOAD with zero length SOA

When Dirac delta pulses excite a saturable amplifier of zero length the response of the amplifier and the transfer window of the TOAD can be computed analytically. In practice, delta pulses cannot be generated. Pulses that can be generated exhibit a certain width which leads to an amplifier saturation process that continues as long as the pulse travels in the amplifier. In the case of a zero length amplifier the amount of time saturation takes place is equal to the duration of the pulse. Consequently, the window will not exhibit infinitely steep slopes. The leading and trailing edges of the window become less steep. The numerical scheme described by Eqs. 2.15 and 2.16 can be evaluated for a wide variety of pulse input shapes. The pulse shape that will be used in this section is the soliton pulse shape

$$P_{in}(\tau) = P_{switch} \operatorname{sech}^2\left(\frac{\tau}{\tau_0}\right) = \frac{E_{switch}}{2\tau_0} \operatorname{sech}^2\left(\frac{\tau}{\tau_0}\right), \quad (2.77)$$

where P_{switch} is the peak power of the pulse and E_{switch} the energy of the pulse. The centre of the pulse arrives at the SOA at $\tau = -\tau_{asym}$, in accordance with the excitation in Sec. 2.5.1. This saturation process is input to the model described in Sec. 2.5.1. Figure 2.15 (a) shows the difference in gain response between the delta pulse and soliton excitation. Figure 2.15 (b) shows that for the soliton case, in contrary to the delta pulse excitation, at two places, where the clockwise and counter clockwise signals intersect, a maximum of destructive interference in the forward direction and a constructive maximum in the backward direction occurs. From Fig. 2.15 (c) it can be seen that the full-width half-maximum time of the window has slightly decreased. In addition, at $\tau \approx -\tau_{asym}$ and $\tau \approx \tau_{asym}$ the output of the switch turns zero. The shape of the window has changed to an extent where the channels that should be suppressed experience close to $\tau = \pm\tau_{asym}$ higher gains. This results in a channel extinction ratio of $R_{channel} = 1.39$ which is lower than the $R_{channel} = 1.45$ for the delta pulse switched TOAD.

One way to compensate for the decrease in channel extinction ratio is to use a line signal that is composed of shorter optical pulses without increasing the bit rate, i.e. lowering the duty cycle. In the case of the window of Fig. 2.15 (c) narrower line pulses concentrate power around $\tau = 0$ where the gain is still high, however, they do have the disadvantage of occupying more bandwidth. A different approach is to decrease the asymmetry of the amplifier in the loop. Figure 2.16 displays for different values of the switch-signal pulse width and for the amplifier asymmetry the shapes of the forward gain windows.

Subplot (a) and (b) show that decrease of the amplifier asymmetry results in a higher channel extinction ratios. The main reason for this is that the ratio of the gain of the demultiplexed channel and the gain of the non-demultiplexed channels increases faster than the width of the

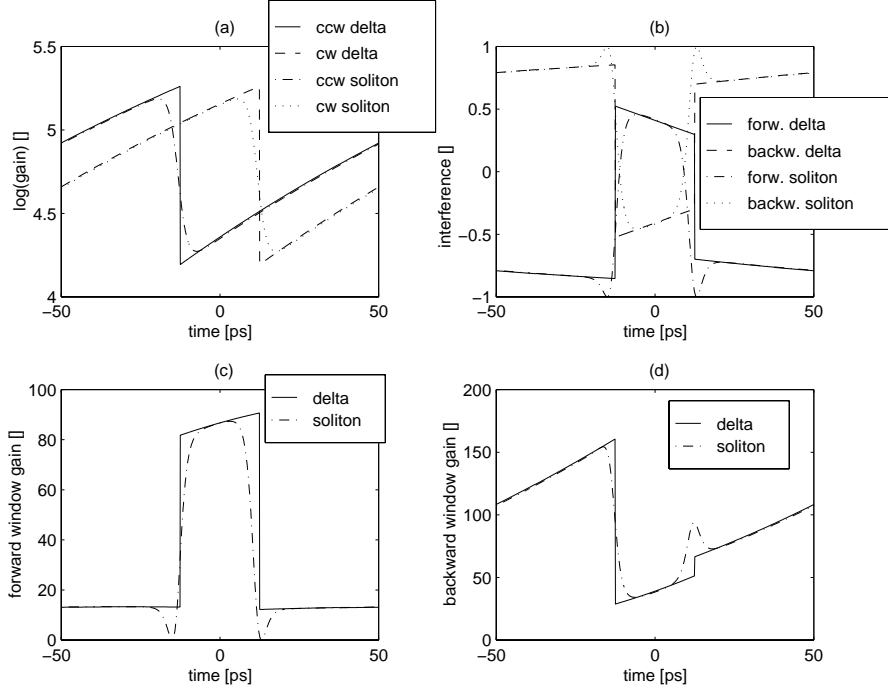


Figure 2.15: (a) Gain that is experienced by the counter clockwise travelling signal for the delta pulse excitation (solid and dashed curves) and for the soliton excitation (dashed-dotted and dotted curve). (b) The cosine term of Eqs. 2.72 and Eqs. 2.73 for the delta pulse excitation (solid and dashed curve) and for the soliton excitation (dashed-dotted and dotted curve), (c) Gain at the forward output (Eq. 2.72) for the delta (solid curve) and soliton (dashed-dotted curve) excitation, (d) Gain at the backward output (Eq. 2.73). $E_{switch} = 0.1$ pJ, $E_{sat} = 10$ pJ, $T_b = 100$ ps, $T_c = 200$ ps, $T_{asym} = 12.5$ ps, $G = 1000$, $\alpha_H = 5$, $\varepsilon_1 = \varepsilon_2 = 0$, $\varphi_1 = 0$ and $\varphi_2 = 90^\circ$. The pulse width of the soliton pulse amounted to 5 ps.

window decreases. When the switch pulses become too broad and the amplifier asymmetry too small as in subplot (c), larger widths of switch pulses can no longer be traded for a smaller amplifier asymmetry without losing gain. In subplot (d) this effect is even more prominent. This method does not require an input line signal containing narrower pulses though it is clear that when the window becomes smaller the pulse shape of the line signal pulses will become more distorted. Furthermore, if the window and the line signal pulses are too narrow the system becomes sensitive to synchronisation jitter between the switch signal and the line signal. If the pulses of the line signal are broad, i.e. large duty cycle, the jitter sensitivity is reduced. Unfortunately in this case not all of the input power to be demultiplexed will eventually be demultiplexed which is detrimental to the signal to noise ratio at the output.

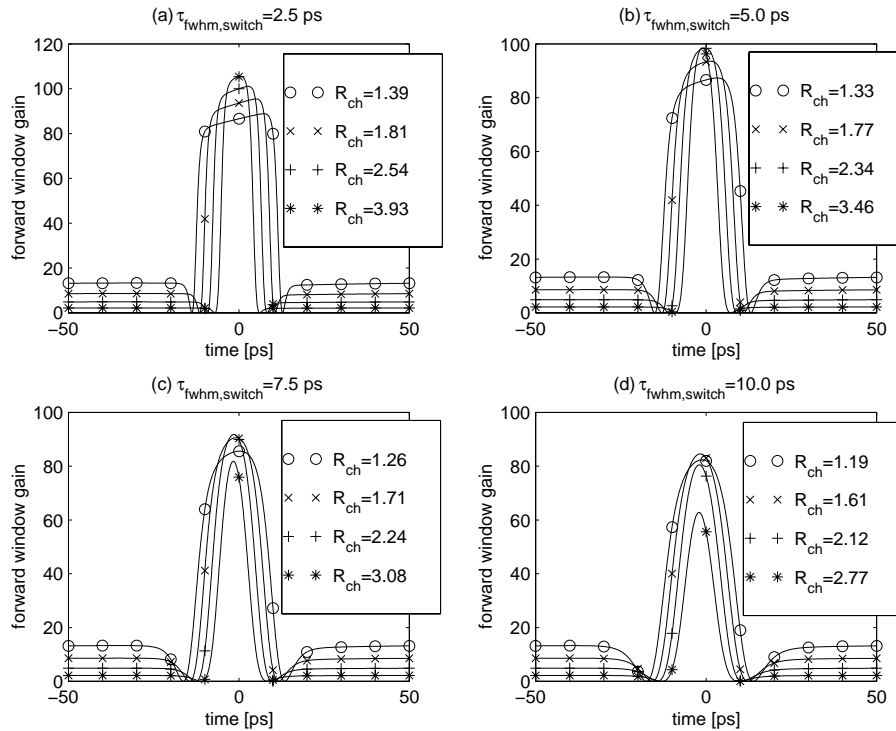


Figure 2.16: Graph (a) to (d) are plotted for amplifier asymmetries $\tau_{switch,fwhm} = 2.5$ ps, $\tau_{switch,fwhm} = 5$ ps, $\tau_{switch,fwhm} = 7.5$ ps, $\tau_{switch,fwhm} = 10$ ps. The values for the amplifier asymmetry equal 12.5 ps, 10 ps, 7.5 ps and 5 ps for the \circ , \times , $+$ and $*$ curves, respectively. The legends of the subplots contain values for $R_{channel}$. $E_{switch} = 0.1$ pJ, $E_{sat} = 10$ pJ, $T_b = 100$ ps, $T_c = 200$ ps, $T_{asym} = 12.5$ ps, $G = 1000$, $\alpha_H = 5$, $\varepsilon_1 = \varepsilon_2 = 0$, $\varphi_1 = 0$ and $\varphi_2 = 90^\circ$.

So far the behaviour has been discussed for an ideal coupler. In the preceding section cross talk in the coupler was demonstrated to improve the characteristics of the switch. For different values of the linewidth enhancement factor, α_H , and the cross-talk-induced phase mismatch in the coupler, $\Delta\varphi_1$, the channel extinction ratio is computed. Figure 2.20 displays a contour plot for $\tau_{switch,fwhm} = 5$ ps and $\tau_{asym} = 10$ ps. A channel extinction ratio of 25 can be obtained if the right line width enhancement factor and phase mismatch are realised. When different values for the width of the switch pulse and asymmetry of the amplifier are taken different values are found for the linewidth enhancement factor and the phase mismatch in the coupler for maximum channel extinction ratio. In summary, increasing pulse width of the switch signal results in a deteriorated switching contrast. A decrease of the amplifier asymmetry will counteract this but also reduces the width of the time window.

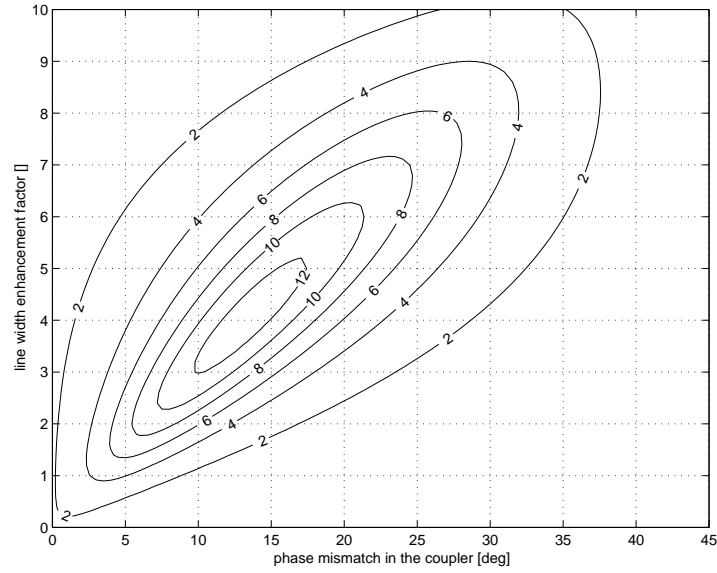


Figure 2.17: $R_{channel}$ versus α_H and $\Delta\varphi_1$ for $\tau_{switch, fwhm} = 2.5$ ps, $\tau_{asym} = 12.5$ ps. ($G = 1000$, $E_{switch} = 0.1$ pJ, $E_{sat} = 10$ pJ, $T_b = 100$ ps, $T_c = 200$ ps and $\varepsilon_1 = \varepsilon_2 = 0.4$)

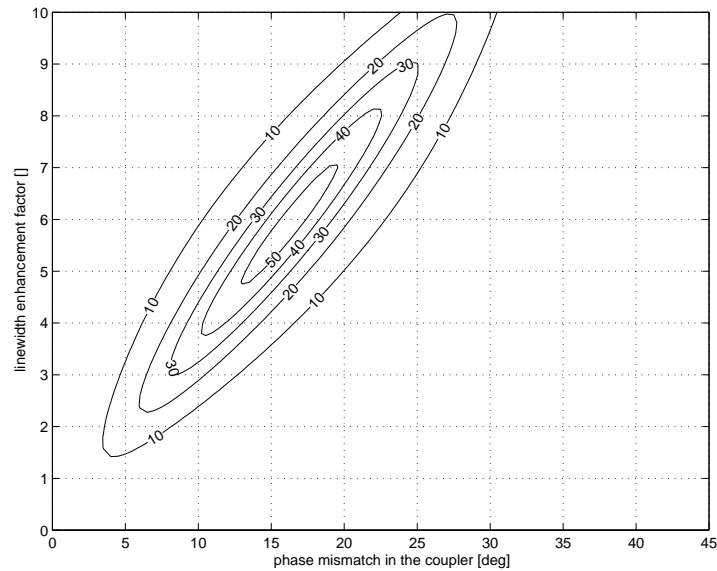


Figure 2.18: $R_{channel}$ versus α_H and $\Delta\varphi_1$ for $\tau_{switch, fwhm} = 2.5$ ps, $\tau_{asym} = 10$ ps. ($G = 1000$, $E_{switch} = 0.1$ pJ, $E_{sat} = 10$ pJ, $T_b = 100$ ps, $T_c = 200$ ps and $\varepsilon_1 = \varepsilon_2 = 0.4$)

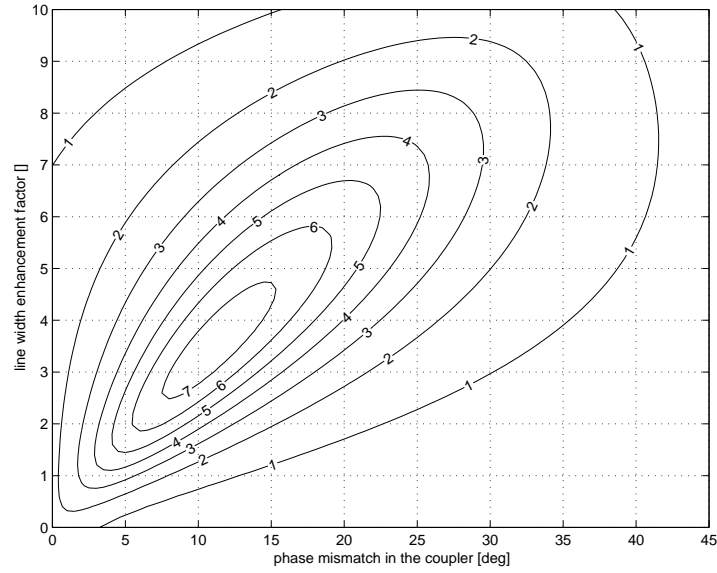


Figure 2.19: $R_{channel}$ versus α_H and $\Delta\varphi_1$ for $\tau_{switch, fwhm} = 5$ ps, $\tau_{asym} = 12.5$ ps. ($G = 1000$, $E_{switch} = 0.1$ pJ, $E_{sat} = 10$ pJ, $T_b = 100$ ps, $T_c = 200$ ps and $\varepsilon_1 = \varepsilon_2 = 0.4$)

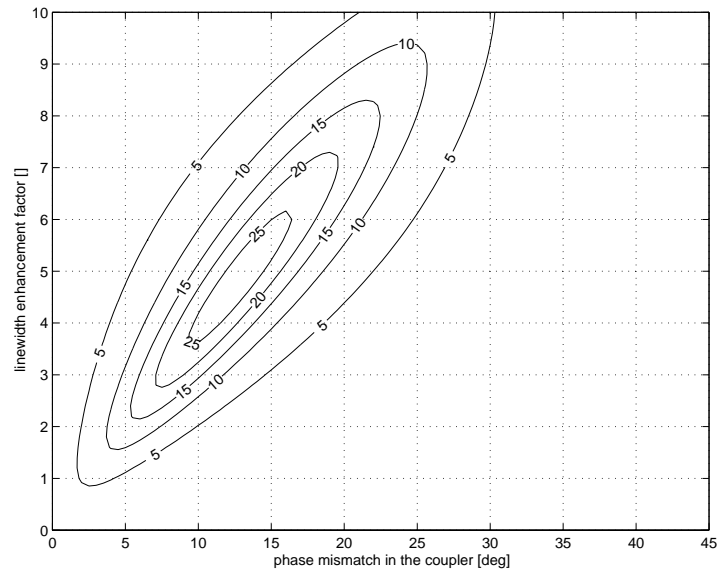


Figure 2.20: $R_{channel}$ versus α_H and $\Delta\varphi_1$ for $\tau_{switch, fwhm} = 5$ ps, $\tau_{asym} = 10$ ps. ($G = 1000$, $E_{switch} = 0.1$ pJ, $E_{sat} = 10$ pJ, $T_b = 100$ ps, $T_c = 200$ ps, and $\varepsilon_1 = \varepsilon_2 = 0.4$)

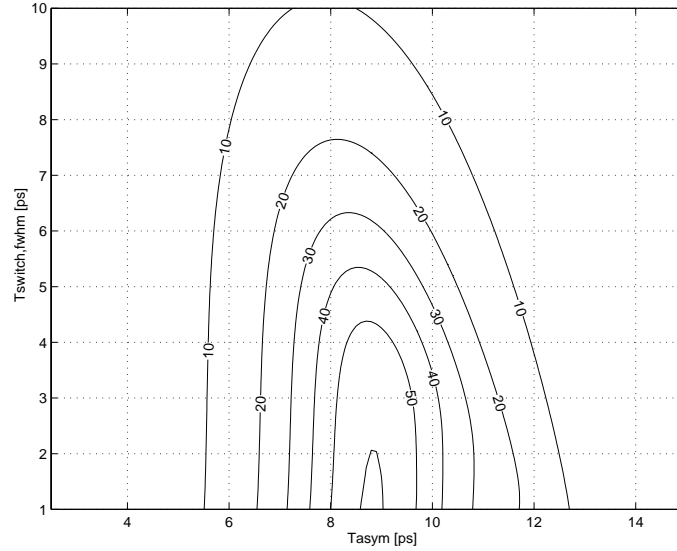


Figure 2.21: $R_{channel}$ contours as a function of τ_{asym} and $\tau_{switch,fwhm}$ for $\Delta\varphi_1 = 12.5^\circ$ and $\alpha_H = 5$. $E_{switch} = 0.1$ pJ, $E_{sat} = 10$ pJ, $T_b = 100$ ps, $T_c = 200$ ps, $G = 1000$ and $\varepsilon_1 = \varepsilon_2 = 0.4$

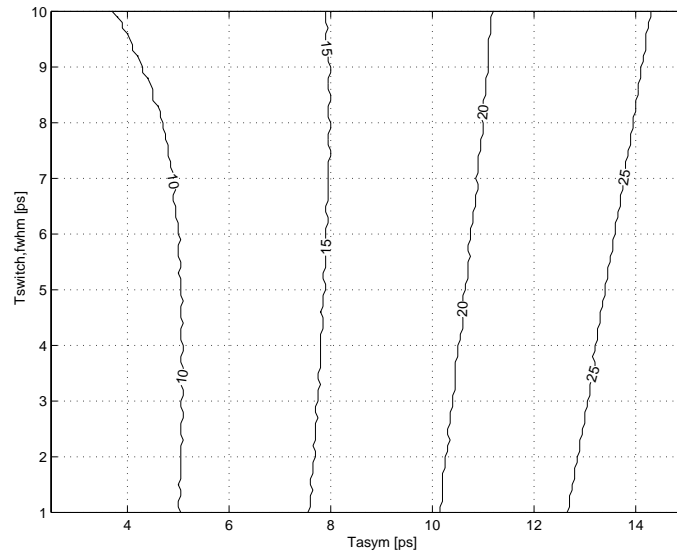


Figure 2.22: The width (fwhm) of the switching window as a function of τ_{asym} and $\tau_{switch,fwhm}$ for $\Delta\varphi_1 = 12.5^\circ$ and $\alpha_H = 5$. $E_{switch} = 0.1$ pJ, $E_{sat} = 10$ pJ, $T_b = 100$ ps, $T_c = 200$ ps, $G = 1000$ and $\varepsilon_1 = \varepsilon_2 = 0.4$

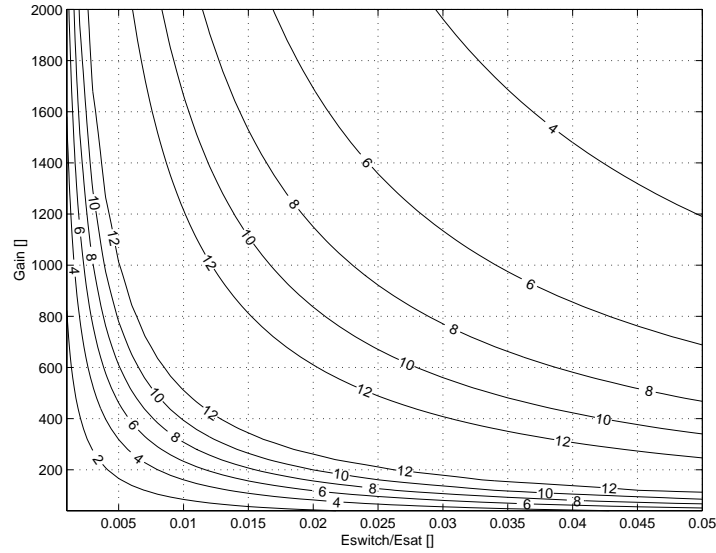


Figure 2.23: $R_{channel}$ versus gain, G , and E_{switch}/E_{sat} for $\tau_{switch, fwhm} = 2.5$ ps and $\tau_{asym} = 12.5$ ps. ($\alpha_H = 4.06$ and $\Delta\varphi_1 = 13.6^\circ$. $E_{sat} = 10$ pJ, $T_b = 100$ ps, $T_c = 200$ ps, and $\varepsilon_1 = \varepsilon_2 = 0.4$)

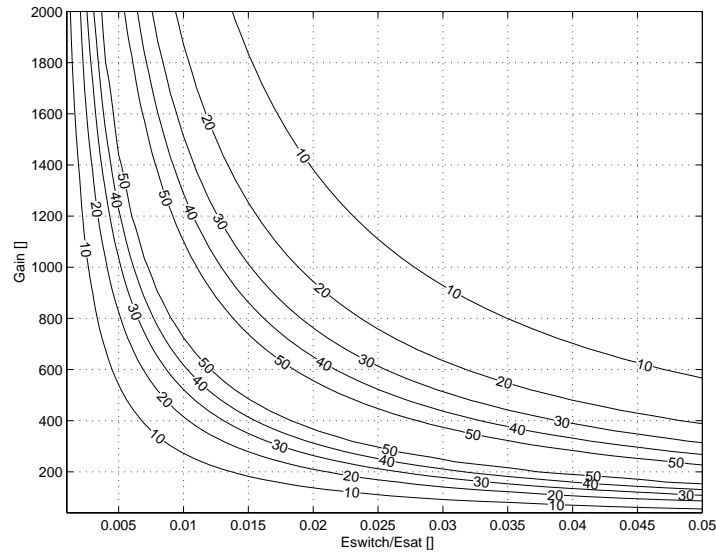


Figure 2.24: $R_{channel}$ versus gain, G , and E_{switch}/E_{sat} for $\tau_{switch, fwhm} = 2.5$ ps and $\tau_{asym} = 10$ ps. ($\alpha_H = 5.92$ and $\Delta\varphi_1 = 16.2^\circ$. $E_{sat} = 10$ pJ, $T_b = 100$ ps, $T_c = 200$ ps, and $\varepsilon_1 = \varepsilon_2 = 0.4$)

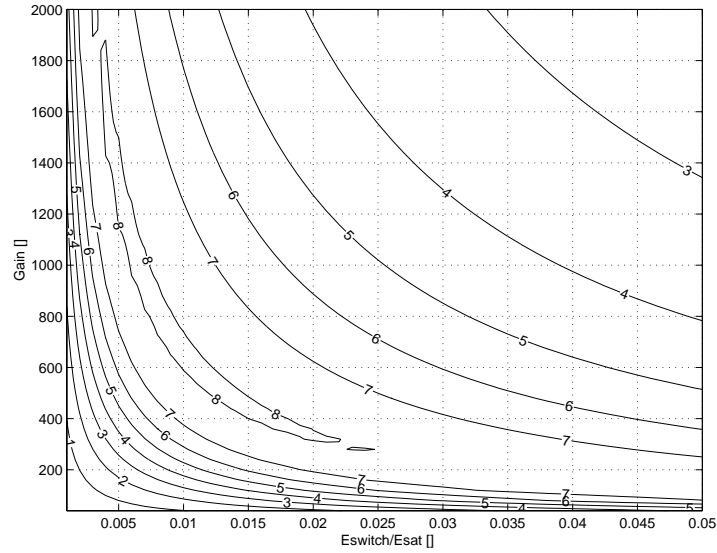


Figure 2.25: $R_{channel}$ versus gain, G , and E_{switch}/E_{sat} for $\tau_{switch, fwhm} = 5$ ps and $\tau_{asym} = 12.5$ ps. ($\alpha_H = 3.60$ and $\Delta\varphi_1 = 11.4^\circ$. $E_{sat} = 10$ pJ, $T_b = 100$ ps, $T_c = 200$ ps, and $\varepsilon_1 = \varepsilon_2 = 0.4$)

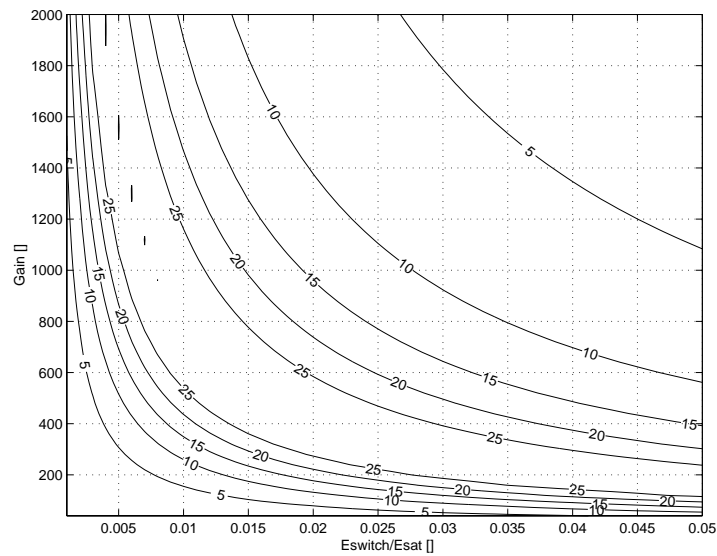


Figure 2.26: $R_{channel}$ versus gain, G , and E_{switch}/E_{sat} for $\tau_{switch, fwhm} = 5$ ps and $\tau_{asym} = 10$ ps. ($\alpha_H = 4.93$ and $\Delta\varphi_1 = 12.8^\circ$. $E_{sat} = 10$ pJ, $T_b = 100$ ps, $T_c = 200$ ps, and $\varepsilon_1 = \varepsilon_2 = 0.4$)

In Figure 2.21 the channel extinction ratio versus amplifier asymmetry and switching pulse width is plotted. This plot shows that decreasing the amplifier asymmetry results in an optimum channel extinction ratio. When that point is passed $R_{channel}$ will further deteriorate. Figure 2.22 depicts the width of the window for the same set of parameters as in Fig. 2.21. The contour lines in this plot cross the $\tau_{switch, fwhm} = 0$ for values of τ_{asym} equal to half the value of the contour line. This particular case corresponds to the delta pulse excitation. In addition, a certain value for τ_{asym} is to be expected where the width of the window and the channel extinction ratio show minimal dependence on the switch pulse width. This occurs at $\tau_{asym} \approx 6.5$ ps where a channel extinction ratio of 20 can be obtained.

In this case, it is interesting to observe the effects on the channel extinction ratio for different gains and ratio of pulse energy and saturation output power. Figs. 2.23-2.26 display the relation between the gain, ratio of E_{switch} and E_{sat} , and $R_{channel}$ for estimated values of α_H and $\Delta\varphi_1$ that give optimum channel extinction ratios in Figs. 2.17-2.20, respectively. An increase or decrease of the gains or of E_{switch} does not result in significant higher values for $R_{channel}$ once the optimum values for α_H and $\Delta\varphi_1$ have been determined. This appears to be independent of the values for $\tau_{switch, fwhm}$ and τ_{asym} . This supports the idea that finding an optimum α_H and $\Delta\varphi_1$ prevails over finding the optimum gain.

2.5.3 Non-zero pulsewidth switching of the TOAD with non-zero length SOA

Up till now the length of the amplifier has been assumed zero. In a physical realisation this will not be the case. An amplifier with length L will exhibit length dependent saturation because the optical intensity will be strongest at the end of the amplifier. Time and distance dependent saturation will be determined numerically using the model described in Sec. 2.3.3. A slightly different definition of τ_{asym} is used. Two times τ_{asym} is the delay between the clockwise and counter clockwise travelling signals in the loop for each signal to reach an input of the non-zero length amplifier. The propagation delay that is experienced by the clockwise and counter clockwise travelling signals in the amplifier is compensated so that the windows are centred around $\tau = 0$ and can easily be compared with the windows in the case where a spatially concentrated amplifier is used (see Fig. 2.27). Moreover, the switch pulse begins to saturate the amplifier at $\tau = -\tau_{asym}$ and can do this from the clockwise direction, counter clockwise direction and from both directions. Figure 2.28 displays the gain profiles and windows for a zero length amplifier and an 800 μm long amplifier. The switch pulse enters the amplifier from the counter clockwise direction. It can be seen that the slope of the trailing edge is less steep compared to the slope of the leading edge. Saturation of the amplifier occurs instantaneously and as a result the counter clockwise travelling signal causes a steep rising edge in the window. The clockwise travelling signal will see an amplifier where the first few micrometers are saturated. The last few micrometers of the amplifier have already started to recover.

For the clockwise travelling signal a different saturation profile exists and thus a different phase profile which, due to the partial recovery, results in a more slanted slope. Consequently, the time window will extend beyond the desired channel. The result is a worse channel extinction ratio. In addition, the gain that is experienced by the channels that are to be suppressed

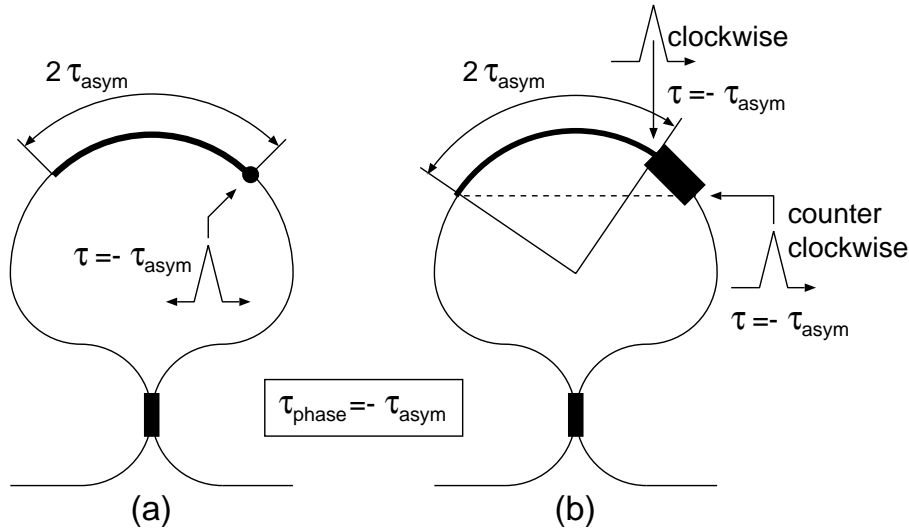


Figure 2.27: Graphical representation of the definition of τ_{asym} for (a) a zero-length amplifier, (b) non-zero length amplifier. The centre of the switch-pulse enters the SOAs at $\tau = -\tau_{asym}$

has increased considerably. Both factors contribute to a channel extinction ratio of only 1.05 compared to 1.39 for a zero-length amplifier and 1.45 for a delta pulse switched zero-length amplifier.

When the amplifier is saturated from the clockwise direction the trailing edge of the window remains steep and the leading edge becomes more slanted (Fig. 2.29). In this case the shape of the window has become narrower and of higher gain. The gain that is experienced by the channels to be suppressed has decreased. This results in an improved channel extinction ratio of 1.70. The third case covers both clockwise and counter clockwise excitation of the amplifier with half the switch pulse energy fed into each input. The gain profiles depicted in Fig. 2.30 show that in this case the gain has saturated more than in the other two situations. This is caused by the gain dependent nonlinear saturation process. When amplifiers become saturated the gain is reduced and additional saturation becomes more difficult. The power along the amplifier longitudinal direction increases non-linearly with the input power. When the amplifier is excited from both directions the two signals will both saturate the amplifier close to the level of saturation that one signal would cause. This mode of operation corresponds to the SLALOM configuration of Fig. 1.8 (c). The saturation occurs mainly in the first half of the amplifier and the pulses will see a fully saturated second half instead of a fresh second half when only one side of the amplifier is excited. This results in a lower overall gain and a twist in the gain curves. Subplot (c) of Fig. 2.30 shows that the forward gain is about the same for the not-demultiplexed channels but the window is smaller and narrower for the demultiplexed channel. The channel extinction ratio decreases to 1.20 which lies in between ratios of the cases where the amplifier is saturated from the clockwise and counter clockwise

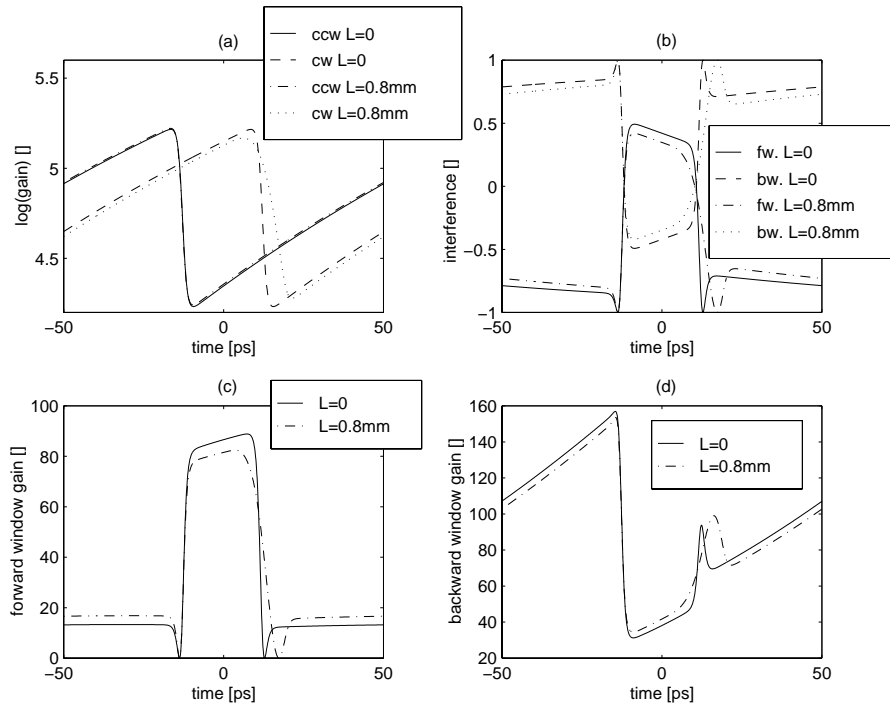


Figure 2.28: Counter clockwise excitation. (a) Gain of clockwise and counter clockwise travelling signal of a zero length (dashed and solid) and an $800\mu\text{m}$ long (dotted and dashed-dotted) amplifier. (b) The cosine of the total phase (including coupler) experienced by the forward (fw.) and backward (bw.) traveling signal of a zero length (dashed and solid curves) and an $800\mu\text{m}$ long (dotted and dashed-dotted) amplifier. (c) Forward gain of a zero length (solid) and an $800\mu\text{m}$ long (dashed-dotted) amplifier. (d) Backward gain. $E_{\text{switch}} = 0.1\text{ pJ}$, $E_{\text{sat}} = 10\text{ pJ}$, $T_b = 100\text{ ps}$, $T_c = 200\text{ ps}$, $T_{\text{asym}} = 12.5\text{ ps}$, $G = 1000$, $\alpha_H = 5$, $\varepsilon_1 = \varepsilon_2 = 0.5$, $\varphi_1 = 0$ and $\varphi_2 = 90^\circ$. The pulse width of the soliton pulse amounts to 5 ps .

direction. The influence of the length of the amplifier in combination with the asymmetry of the amplifier on the shape of the forward gain windows is investigated numerically. Forward gains are plotted in Fig. 2.31 (a-d) for $\tau_{\text{asym}} = 0$, $\tau_{\text{asym}} = 5\text{ ps}$, $\tau_{\text{asym}} = 10\text{ ps}$, $\tau_{\text{asym}} = 15\text{ ps}$, respectively and for $L_{\text{soa}} = 400\mu\text{m}$, $L_{\text{soa}} = 800\mu\text{m}$ and $L_{\text{soa}} = 1200\mu\text{m}$, indicated by the solid, dashed and dotted curve, respectively. When the amplifier is centred in the loop, a forward window is still visible with a large channel extinction ratio but a relatively low gain. A longer amplifier results in higher gain but a lower channel extinction ratio. In all the other graphs, where the amplifier is located asymmetrically in the loop, it can be observed that a longer amplifier results in a better channel extinction ratio and in a narrower window. In the preceding section it was shown that reducing the amplifier asymmetry resulted in a smaller window with better channel extinction ratio. The same occurs when the amplifier length is increased. An increase of amplifier length to $1200\mu\text{m}$ with an asymmetry of 12.5 ps gives

the same result as a decrease of amplifier asymmetry to 10 ps with a spatially concentrated amplifier. At this point it can be concluded that practical implementation of a non spatially concentrated amplifier can result in increased performance for non-zero width pulses. The phase deviation of the coupler from the ideal 90° determines whether the amplifier should be excited clockwise or counter clockwise in order to suppress the channels that are not intended to be demultiplexed.

When crosstalk in the coupler occurs the channel extinction ratio can be increased considerably. Similar to Figs. 2.17-2.20, Figs. 2.32-2.35 display the channel extinction ratio contour plots for an $800 \mu\text{m}$ long optical amplifier as a function of the linewidth enhancement factor and the phase mismatch in the coupler. The channel extinction ratio has significantly improved for lower α_H and a smaller phase mismatch in the coupler. Figures 2.36 and 2.38

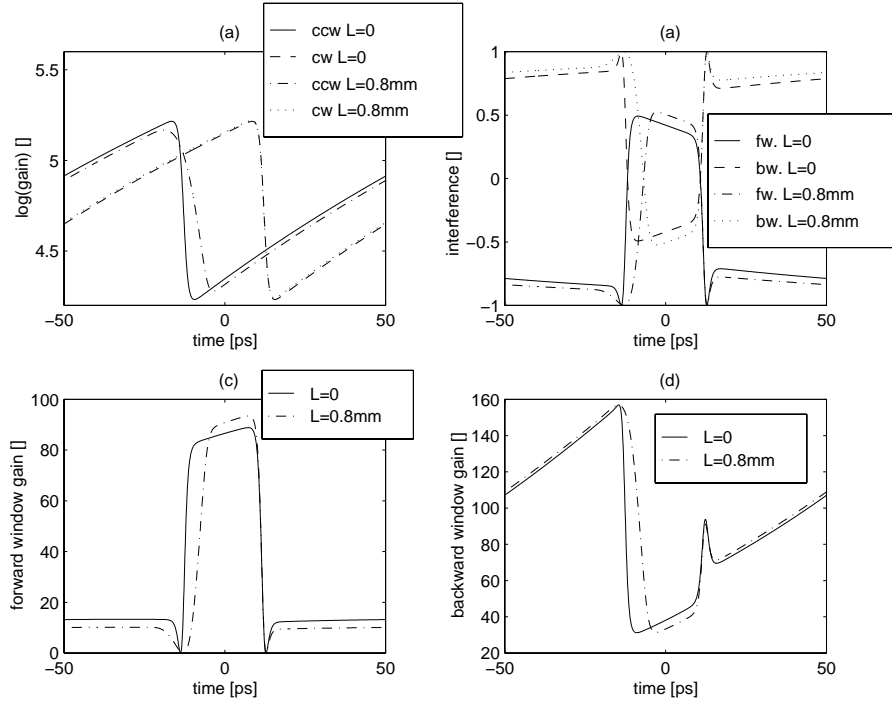


Figure 2.29: Clockwise excitation. (a) Gain of clockwise and counter clockwise travelling signal of a zero length (dashed and solid) and an $800 \mu\text{m}$ long (dotted and dashed-dotted) amplifier. (b) The cosine of the total phase (including coupler) experienced by the forward (fw.) and backward (bw.) traveling signal of a zero length (dashed and solid curves) and an $800 \mu\text{m}$ long (dotted and dashed-dotted) amplifier. (c) Forward gain of a zero length (solid) and an $800 \mu\text{m}$ long (dashed-dotted) amplifier. (d) Backward gain. $E_{switch} = 0.1 \text{ pJ}$, $E_{sat} = 10 \text{ pJ}$, $T_b = 100 \text{ ps}$, $T_c = 200 \text{ ps}$, $T_{asym} = 12.5 \text{ ps}$, $G = 1000$, $\alpha_H = 5$, $\epsilon_1 = \epsilon_2 = 0.5$, $\varphi_1 = 0$ and $\varphi_2 = 90^\circ$. The pulse width of the soliton pulse amounts to 5 ps.

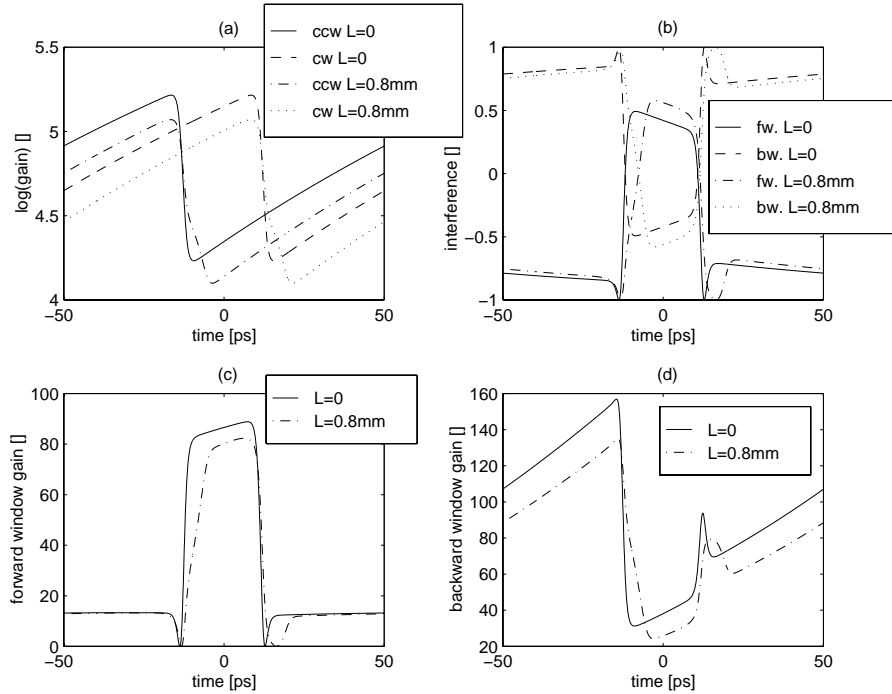


Figure 2.30: Clockwise and counter clockwise excitation. (a) Gain of clockwise and counter clockwise travelling signal of a zero length (dashed and solid) and an $800 \mu\text{m}$ long (dotted and dashed-dotted) amplifier. (b) The cosine of the total phase (including coupler) experienced by the forward (fw.) and backward (bw.) traveling signal of a zero length (dashed and solid curves) and an $800 \mu\text{m}$ long (dotted and dashed-dotted) amplifier. (c) Forward gain of a zero length (solid) and an $800 \mu\text{m}$ long (dashed-dotted) amplifier. (d) Backward gain. $E_{switch} = 0.1 \text{ pJ}$, $E_{sat} = 10 \text{ pJ}$, $T_b = 100 \text{ ps}$, $T_c = 200 \text{ ps}$, $T_{asym} = 12.5 \text{ ps}$, $G = 1000$, $\alpha_H = 5$, $\varepsilon_1 = \varepsilon_2 = 0.5$, $\varphi_1 = 0$ and $\varphi_2 = 90^\circ$. The pulse width of the soliton pulse amounts to 5 ps .

depict how the channel extinction ratio depends on the amplifier asymmetry and switch pulse width for a $400 \mu\text{m}$ and an $800 \mu\text{m}$ long amplifier, respectively. The pulse widths of the windows are displayed in Figs. 2.39 and 2.37 for both amplifier lengths. These plots are based on $\alpha_H = 5$ and a $\Delta\varphi_1 = 12.5^\circ$. For these values an increase in amplifier length from $L = 0$ (Fig. 2.22) to $L = 400 \mu\text{m}$ and $L = 800 \mu\text{m}$ results in decreasing optimal values for $R_{channel}$. These optimal values do occur for increased amplifier asymmetry. Apparently, it depends strongly on the values for α_H and $\Delta\varphi_1$ whether a longer amplifier improves the channel extinction ratio or not.

From Figs. 2.32-2.35, α_H and $\Delta\varphi_1$ are interpolated to provide near optimum channel extinction ratios. This data is used to compute the channel extinction ratio as a function of amplifier length for different ratios of the switch pulse energy and saturation output energy of

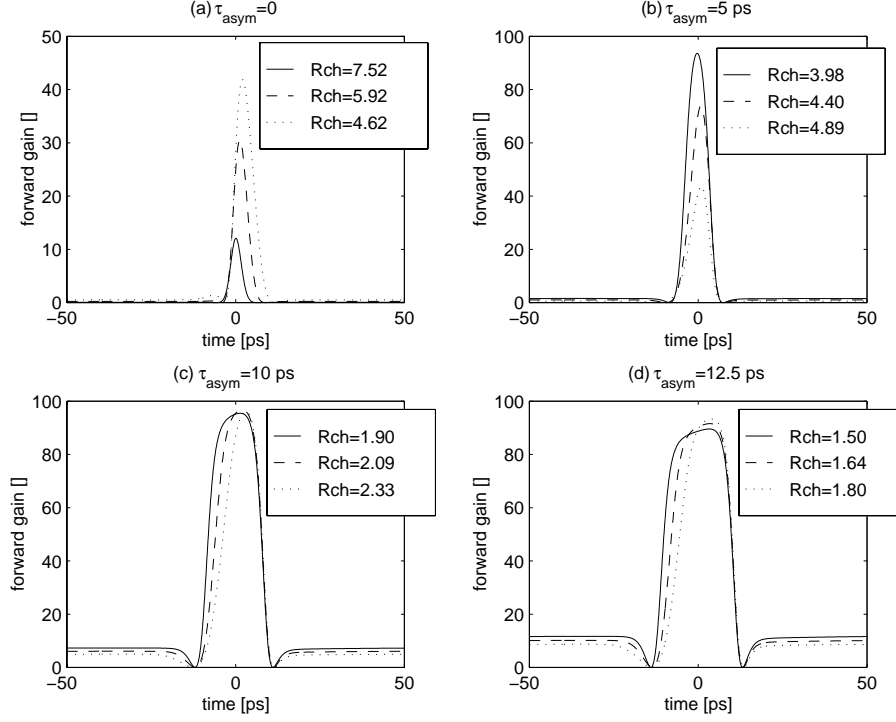


Figure 2.31: Subplot (a), (b), (c) and (d) depict the forward gain for $\tau_{asym} = 0$ ps, $\tau_{asym} = 5$ ps, $\tau_{asym} = 10$ ps and $\tau_{asym} = 12.5$ ps respectively for three amplifiers with length $L = 400 \mu\text{m}$ (solid), $L = 800 \mu\text{m}$ (dashed) and $L = 1200 \mu\text{m}$ (dotted) and clockwise excitation. $E_{switch} = 0.1$ pJ, $E_{sat} = 10$ pJ, $T_b = 100$ ps, $T_c = 200$ ps, $G = 1000$, $\alpha_H = 5$, $\varepsilon_1 = \varepsilon_2 = 0.5$, $\varphi_1 = 0$ and $\varphi_2 = 90^\circ$. The pulse width of the soliton pulse amounts to 5 ps.

the amplifier. This data is presented in Figs. 2.40-2.43. Common among these graphs is that for $E_{switch}/E_{sat} = 0.01$ around $L = 800 \mu\text{m}$ a maximum for $R_{channel}$ occurs. This is in agreement with expectations since these graphs are based on parameters of Figs. 2.32-2.35. These graphs also show that for different ratios of E_{switch} and E_{sat} a maximum occurs at a different amplifier length. If the other parameters, like $\Delta\varphi_1$, α_H and the gain are also changed a higher maximum can probably be achieved. In addition the channel extinction ratio is sensitive to variations in switch pulse energy. From Fig. 2.41 it can be seen that if the E_{switch} is divided by a factor three the channel extinction ratio decreases by a factor four. An increase of E_{switch} by a factor three results in an increase of $R_{channel}$ by a factor five.

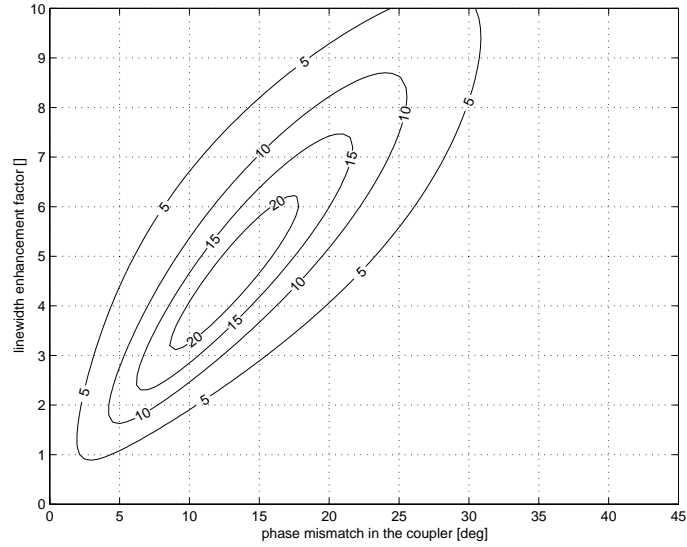


Figure 2.32: $R_{channel}$ versus α_H and $\Delta\varphi_1$ for $\tau_{switch, fwhm} = 2.5$ ps, $\tau_{asym} = 12.5$ ps. ($L = 800$ μm , $G = 1000$, $E_{switch} = 0.1$ pJ, $E_{sat} = 10$ pJ, $T_b = 100$ ps, $T_c = 200$ ps and $\varepsilon_1 = \varepsilon_2 = 0.4$ and clockwise excitation.)

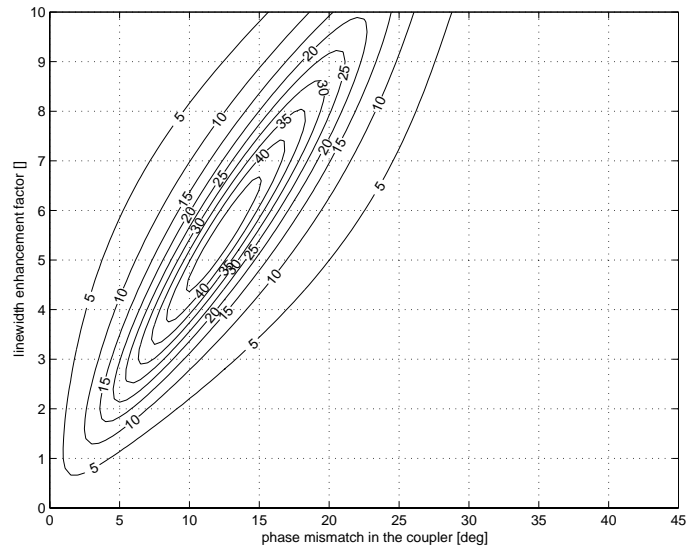


Figure 2.33: $R_{channel}$ versus α_H and $\Delta\varphi_1$ for $\tau_{switch, fwhm} = 2.5$ ps, $\tau_{asym} = 10$ ps. ($L = 800$ μm , $G = 1000$, $E_{switch} = 0.1$ pJ, $E_{sat} = 10$ pJ, $T_b = 100$ ps, $T_c = 200$ ps and $\varepsilon_1 = \varepsilon_2 = 0.4$ and clockwise excitation.)

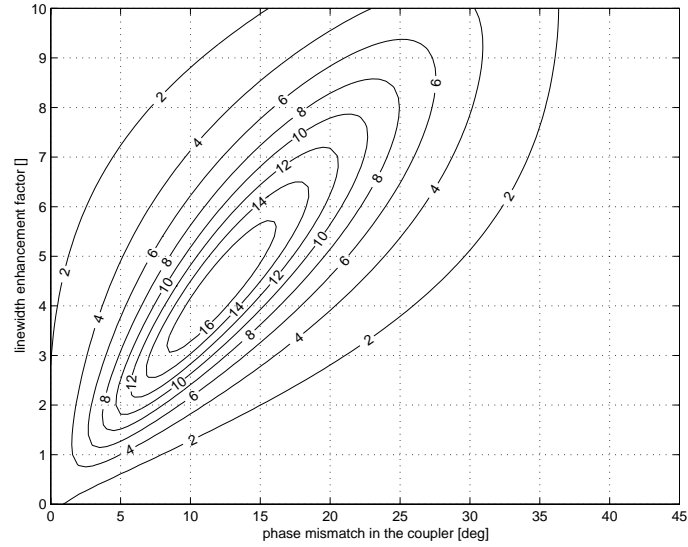


Figure 2.34: $R_{channel}$ versus α_H and $\Delta\varphi_1$ for $\tau_{switch, fwhm} = 5$ ps, $\tau_{asym} = 12.5$ ps. ($L = 800$ μm , $G = 1000$, $E_{switch} = 0.1$ pJ, $E_{sat} = 10$ pJ, $T_b = 100$ ps, $T_c = 200$ ps and $\varepsilon_1 = \varepsilon_2 = 0.4$ and clockwise excitation.)

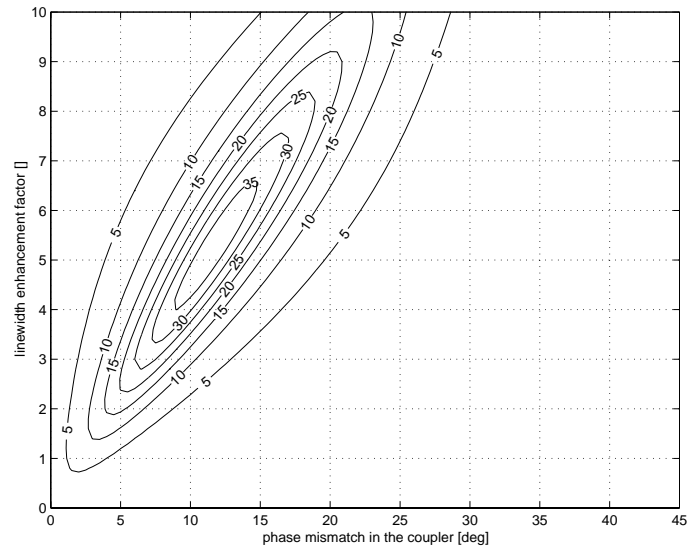


Figure 2.35: $R_{channel}$ versus α_H and $\Delta\varphi_1$ for $\tau_{switch, fwhm} = 5$ ps, $\tau_{asym} = 10$ ps. ($L = 800$ μm , $G = 1000$, $E_{switch} = 0.1$ pJ, $E_{sat} = 10$ pJ, $T_b = 100$ ps, $T_c = 200$ ps and $\varepsilon_1 = \varepsilon_2 = 0.4$ and clockwise excitation.)

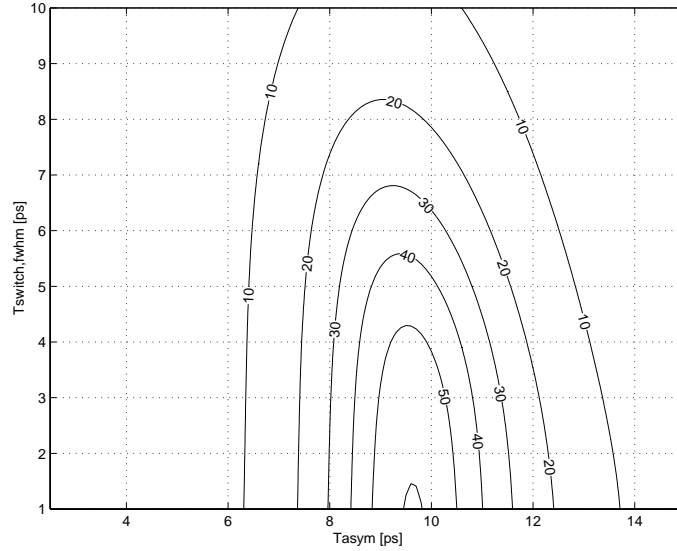


Figure 2.36: $R_{channel}$ contours as a function of τ_{asym} and $\tau_{switch,fwhm}$ for $\Delta\varphi_1 = 12.5^\circ$, $\alpha_H = 5$, $L = 400 \mu\text{m}$ and clockwise excitation. $E_{switch} = 0.1 \text{ pJ}$, $E_{sat} = 10 \text{ pJ}$, $T_b = 100 \text{ ps}$, $T_c = 200 \text{ ps}$, $G = 1000$ and $\varepsilon_1 = \varepsilon_2 = 0.4$

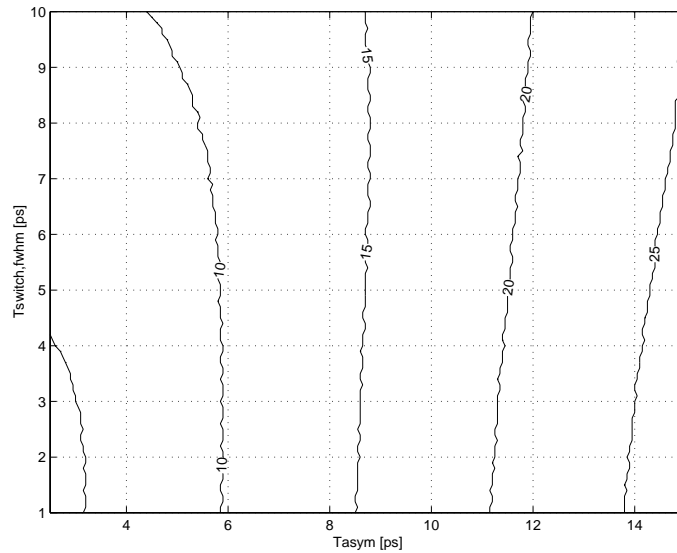


Figure 2.37: The width (fwhm) of the switching window as a function of τ_{asym} and $\tau_{switch,fwhm}$ for $\Delta\varphi_1 = 12.5^\circ$, $\alpha_H = 5$, $L = 400 \mu\text{m}$ and clockwise excitation. $E_{switch} = 0.1 \text{ pJ}$, $E_{sat} = 10 \text{ pJ}$, $T_b = 100 \text{ ps}$, $T_c = 200 \text{ ps}$, $G = 1000$ and $\varepsilon_1 = \varepsilon_2 = 0.4$

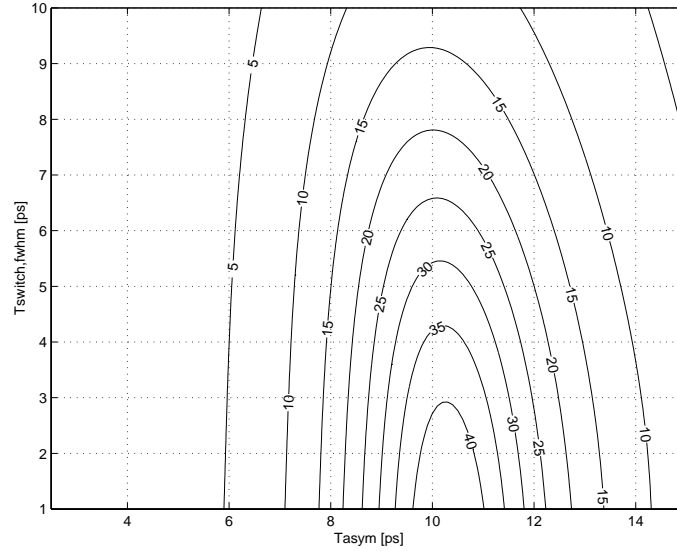


Figure 2.38: $R_{channel}$ contours as a function of τ_{asymp} and $\tau_{switch,fwhm}$ for $\Delta\varphi_1 = 12.5^\circ$, $\alpha_H = 5$, $L = 800 \mu m$ and clockwise excitation. $E_{switch} = 0.1 pJ$, $E_{sat} = 10 pJ$, $T_b = 100 ps$, $T_c = 200 ps$, $G = 1000$ and $\varepsilon_1 = \varepsilon_2 = 0.4$

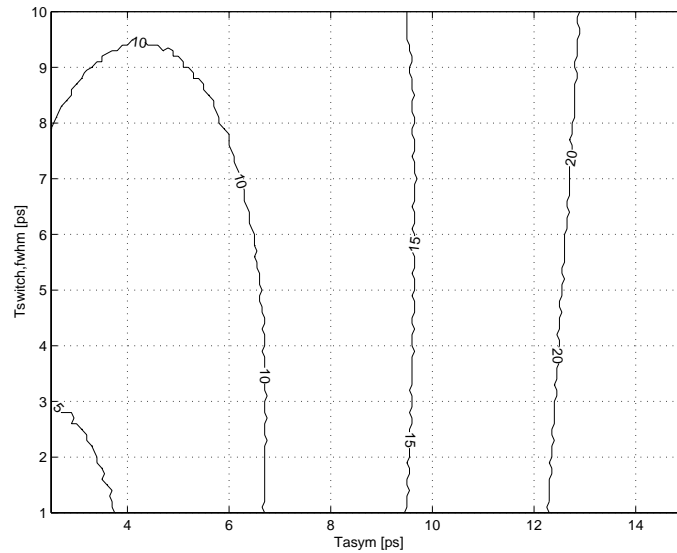


Figure 2.39: The width (fwhm) of the switching window as a function of τ_{asymp} and $\tau_{switch,fwhm}$ for $\Delta\varphi_1 = 12.5^\circ$, $\alpha_H = 5$, $L = 800 \mu m$ and clockwise excitation. $E_{switch} = 0.1 pJ$, $E_{sat} = 10 pJ$, $T_b = 100 ps$, $T_c = 200 ps$, $G = 1000$ and $\varepsilon_1 = \varepsilon_2 = 0.4$

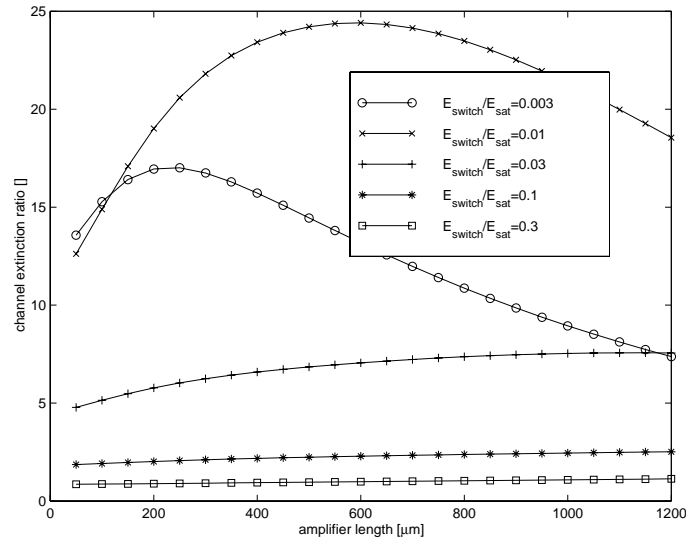


Figure 2.40: $R_{channel}$ versus amplifier length, L , for $\tau_{switch, fwhm} = 2.5$ ps, $\tau_{asym} = 12.5$ ps, different E_{switch}/E_{sat} and clockwise excitation. ($\alpha_H = 4.60$ and $\Delta\varphi_1 = 13.1^\circ$, $G = 1000$, $E_{sat} = 10$ pJ, $T_b = 100$ ps, $T_c = 200$ ps, and $\varepsilon_1 = \varepsilon_2 = 0.4$)

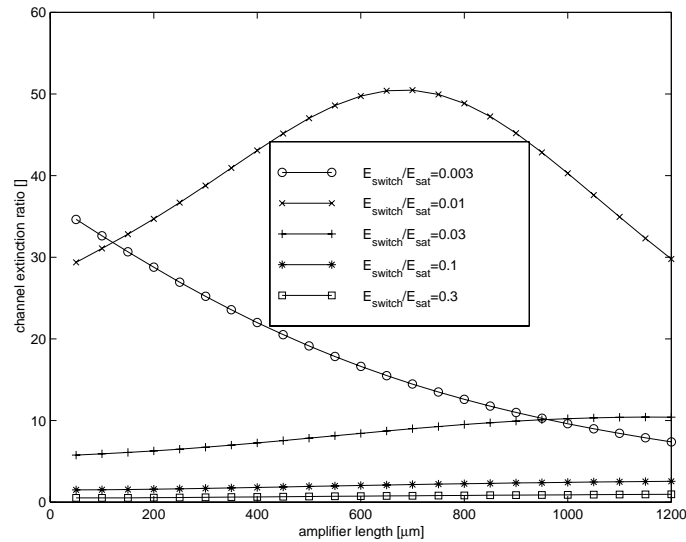


Figure 2.41: $R_{channel}$ versus amplifier length, L , for $\tau_{switch, fwhm} = 2.5$ ps, $\tau_{asym} = 10$ ps, different E_{switch}/E_{sat} and clockwise excitation. ($\alpha_H = 5.55$ and $\Delta\varphi_1 = 12.4^\circ$, $G = 1000$, $E_{sat} = 10$ pJ, $T_b = 100$ ps, $T_c = 200$ ps, and $\varepsilon_1 = \varepsilon_2 = 0.4$)

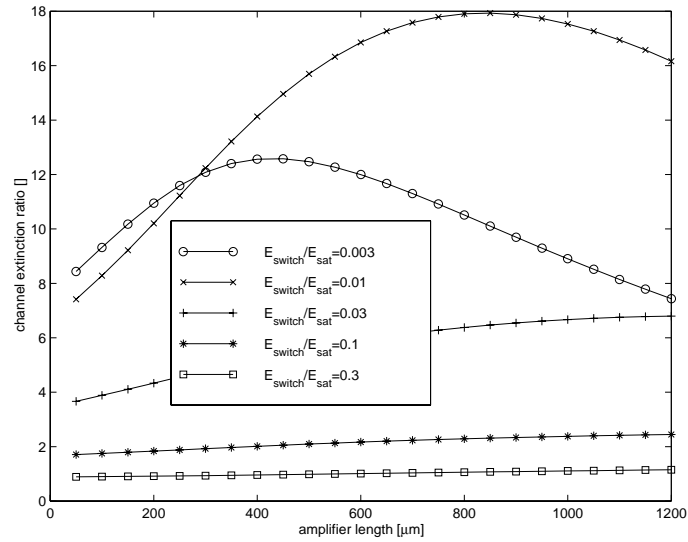


Figure 2.42: $R_{channel}$ versus amplifier length, L , for $\tau_{switch, fwhm} = 5$ ps, $\tau_{asym} = 12.5$ ps, different E_{switch}/E_{sat} and clockwise excitation. ($\alpha_H = 4.36$ and $\Delta\varphi_1 = 12.5^\circ$, $G = 1000$, $E_{sat} = 10$ pJ, $T_b = 100$ ps, $T_c = 200$ ps, and $\varepsilon_1 = \varepsilon_2 = 0.4$)

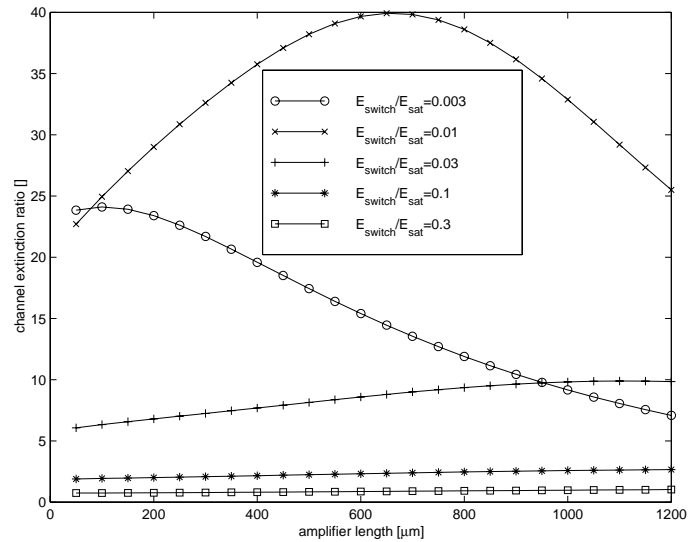


Figure 2.43: $R_{channel}$ versus amplifier length, L , for $\tau_{switch, fwhm} = 5$ ps, $\tau_{asym} = 10$ ps, different E_{switch}/E_{sat} and clockwise excitation. ($\alpha_H = 5.31$ and $\Delta\varphi_1 = 11.8^\circ$, $G = 1000$, $E_{sat} = 10$ pJ, $T_b = 100$ ps, $T_c = 200$ ps, and $\varepsilon_1 = \varepsilon_2 = 0.4$)

2.6 Summary

In this chapter three amplifier models have been derived and implemented in a TOAD-switch model. Simulations have been carried out which show that both qualitatively and quantitatively significant differences exist between the response of the models. A channel extinction ratio has been defined as the ratio of the energy in a window where the channel is located that is to be demultiplexed and the energy in the remaining channels which are to be suppressed, where a continuous-wave input signal is used. More than ten different parameters control the performance of this optical switch. Finding the maximum channel extinction ratio in a ten dimensional vector space is not within the scope of this thesis although simulation tools are available to verify the performance of a particular configuration. When a TOAD configuration is set up it has been found that the switch pulse should be as narrow as possible. The energy of the switch pulse should be accurate and stable. The non-zero length of the amplifier does not necessarily have a bad influence on the performance of the TOAD. The linewidth enhancement factor and the phase mismatch in the coupler are found to be key parameters in the fine tuning of the device. Moreover, it may very well be that a coupler in combination with an amplifier does not permit a channel extinction ratio large enough to obtain error free demultiplexing when the line signal includes significant noise. Optical gain can be exchanged for a different ratio between the energy of the switch pulse and saturation output power of the SOA.

References

- [1] R.J. Mears, L. Reekie, et al. Low-noise erbium-doped fibre amplifier operating at 1.54 μ m. Electronics Letters, 23:1026–1028, 1997.
 - [2] E. Desurvire. Erbium-doped fibre amplifiers: principles and applications, pages 98–114. John Wiley and Sons, Inc., 1994.
 - [3] A. Bjarklev. Optical fibre amplifiers: design and system applications. Artech House, Inc., 1993.
 - [4] K. Suto and J.-I. Nishizawa. Semiconductor Raman lasers. Artech house, Inc., 1994.
 - [5] S.V. Chernikov, J.R. Taylor, et al. High-power, compact, high-efficiency, fiber laser source around 1.24 μ m for pumping Raman amplifiers. In Technical Digest, OFC'97, Dallas, page 345, 1997.
 - [6] A.J. Stentz. Progress on Raman amplifiers. In Technical Digest of the OFC'97, Dallas, page 343, 1997.
 - [7] L.F. Tiemeijer. Optical properties of semiconductor lasers and laser amplifiers for fiber optical communication. PhD thesis, Delft University of Technology, 1992.
 - [8] G.P. Agrawal and N.A. Olsson. Amplification and compression of weak picosecond optical pulses by using semiconductor-laser amplifiers. Optics Letters, 14:500–502, 1989.
 - [9] Y. Yamamoto, S. Saito, and T. Mukai. AM and FM quantum noise in semiconductor lasers - Part II: comparison of theoretical and experimental results for AlGaAs lasers. IEEE Quantum Electronics, 19:47–58, 1983.
-

-
- [10] C.H. Henry. Theory of spontaneous emission noise in open resonators and its application to lasers and optical amplifiers. IEEE Journal of Lightwave Technology, 4:288, 1986.
- [11] L.F. Tiemeijer, P.J.A. Thijs, et al. Temperature dependence of a 1300 nm polarisation-insensitive multiple quantum well laser amplifier and its implications for the ultimate capacity of cascaded amplifier systems. IEEE Photonics Technology Letters, 6:1300–1302, 1994.
- [12] L.F. Tiemeijer, P.J.A. Thijs, et al. Noise figure of saturated 1310-nm polarization insensitive multiple-quantum-well optical amplifiers. IEEE Photonics Technology Letters, 8:873–875, 1996.
- [13] L.F. Tiemeijer, P.J.A. Thijs, et al. Polarisation resolved, complete characterization of 1310 nm fiber pigtailed multiple-quantum-well optical amplifiers. IEEE Journal of Lightwave Technology, 14:1524–1533, 1996.
- [14] L.F. Tiemeijer, P.J.A. Thijs, et al. Self-phase modulation coefficient of multiple-quantum-well optical amplifiers. IEEE Photonic Technology Letters, 8:876–878, 1996.
- [15] H. Dupont, M.J. Chawki, et al. Measurement of the effective phase-amplitude coupling factor α_{eff} of high speed semiconductor optical amplifier module. IEEE Photonics Technology Letters, 6:942–944, 1994.
- [16] H.A. Haus, E.P. Ippen, and K. Tamura. Additive-pulse modelocking in fiber lasers. IEEE Journal of Quantum Electronics, 30:200–208, 1994.
- [17] A.W. Snyder. Coupled-mode theory for optical fibers. Journal of the Optical Society of America, 62(11):1267–1277, 1972.
- [18] J.P. Sokoloff, P.R. Prucnal, et al. A terahertz optical asymmetric demultiplexer (TOAD). IEEE Photonic Technology Letters, 5:787–790, 1993.
- [19] M. Eiselt, W. Pieper, and H.G. Weber. SLALOM: Semiconductor laser amplifier in a loop mirror. Journal of Lightwave Technology, 13:2099–2112, 1995.
-

Chapter 3

Key components and system blocks

The optical transmission systems of today have become more complex as a result of transmission over longer distances and at higher bit rates. In Chapter 5 all-optical demultiplexing and regeneration is experimentally demonstrated. To this end a diversity of optical and electro-optical components have been utilised in a wide variety of optical geometries. In this chapter the building blocks that form the systems treated in Chapters 4 and 5 are examined. Some of these components are commercially available; others have been custom made.

3.1 Optical sources and modulators

3.1.1 DFB laser diode

Distributed feedback (DFB) laser diodes are common sources in optical transmission systems. In the research presented in this thesis a DFB laser diode is used to generate trains of narrow optical pulses that can be modulated by an external optical modulator to realise an optical data signal. A theoretical model is described that is implemented numerically to assess differences in performance between RZ formatted and NRZ formatted transmission systems in Chapter 4. The DFB laser that generates optical pulse trains for ≤ 10 Gb/s experiments is a broad-band research sample, manufactured by Uniphase Netherlands B.V. This buried heterojunction InGaAsP bulk laser diode operates at 1310 nm and has a typical fibre-coupled efficiency of $80 \mu\text{W}/\text{mA}$. A pulse pattern generator (PPG) is used to derive a 10 GHz sinusoidal signal. After amplification this signal is fed into the DC-biased DFB laser diode. Figure 3.1 (a) displays the measured temporal optical response with 60 mA bias current and excited by a 10 GHz, $120 \text{ mA}_{\text{peak-peak}}$ RF signal. It must be noted that due to reflections in the mount and package the active layer of the laser diode does not experience all of the RF power.

Carrier density fluctuations modulate the refractive index of the active layer and impose frequency chirp on the envelope of the optical pulses. Figure 3.1 (b) shows that transmission through 4.4 km of dispersion-shifted fibre compresses the output pulses of the laser diode to narrower optical pulses. When the laser is switched on from below threshold the laser is said to be gain switched. An increasing electrical signal raises the carrier concentration. Hence the optical gain increases. During this process spontaneously generated photons exist in the cavity. Once the optical gain exceeds a threshold level (given by cavity and mirror

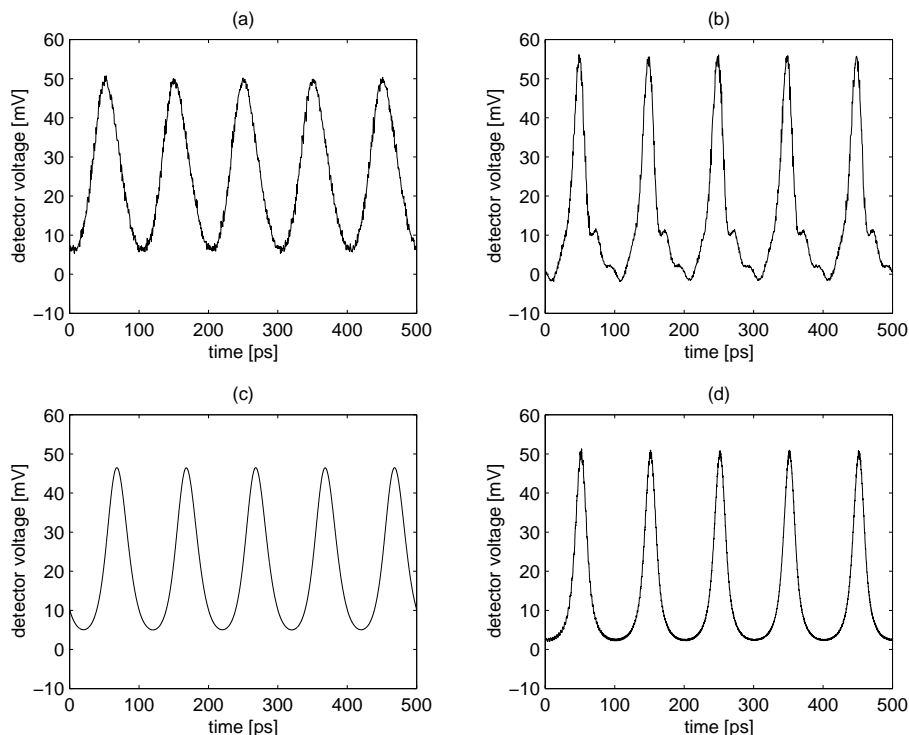


Figure 3.1: (a) Detected output power of a bulk DFB laser diode which is excited by a 120 mA_{pp} , 10 GHz sinusoidal signal and a bias current of 55 mA . (b) 4.4 km of DSF ($D = -19 \text{ ps}/(\text{km} \cdot \text{nm})$) at $\lambda = 1310 \text{ nm}$ is used to remove chirp of the pulses. As a result pulse compression occurs. (c) Computer simulation of the DFB laser in (a). $I_{DC} = 55 \text{ mA}$, $I_{AC} = 75 \text{ mA}_{pp}$, $\alpha_H = 3$, $n_g = 3$, $\epsilon_{comp} = 2.0 \cdot 10^{-17} \text{ cm}^3$, $\frac{\partial g}{\partial N} = 2.5 \cdot 10^{-16} \text{ cm}^2$, $\alpha_{loss} = 60 \text{ cm}^{-1}$, $R_F = 0.05$, $R_R = 0.3$, $L = 250 \mu\text{m}$, $w = 1.8 \mu\text{m}$, $d = 0.1 \mu\text{m}$, $\beta_{sp} = 30 \cdot 10^{-6}$, $\Gamma = 0.23$, $\tau_l = 1.8 \text{ ns}$, $N_0 = 1.0 \cdot 10^{-18} \text{ cm}^{-3}$, $B = 9.0 \cdot 10^{-11} \text{ m}^3 \text{ s}^{-1}$ and $C = 3.0 \cdot 10^{-29} \text{ m}^6 \text{ s}^{-1}$. (d) Computer simulation of the pulse compression in the 4.4 km of $D = -19 \text{ ps}/(\text{km} \cdot \text{nm})$ dispersive fibre. The optical response of the optical detector was taken $1 \text{ mV}/\text{mW}$.

losses), these spontaneously generated photons initiate stimulated radiative emission. While photons are generated, carriers are consumed at a faster rate than they are being generated by the electrical current. Consequently the optical gain reduces and the optical signal extinguishes. In the case of a gain-switched laser diode, the moment of ignition is determined by the random process of spontaneous emission of photons. This results in timing jitter. In Fig. 3.1 (a) the laser diode is not completely switched off between two optical pulses in order to reduce timing jitter. Consequently, a continuous signal manifests itself as a floor and decreases the extinction ratio. A choice must be made between either a reduced extinction ratio or an increased timing jitter that would limit performance. These compressed optical

pulses are employed in ≤ 10 Gb/s transmission and in 10 Gb/s to 2.5 Gb/s demultiplexing experiments.

A simplified model for a dynamic single-mode laser

If a DFB laser diode is properly modelled the lasing frequency is determined by the maximum net roundtrip gain. This maximum is determined by the gain profile, the frequency response of the grating that is etched near the active layer and the complex reflectivities of the mirrors. To find this optimum, coupled mode equations are solved to obtain the modal detuning of the propagation constant from the Bragg wavenumber that corresponds to the etched grating and the lasing frequency. From these values the threshold conditions can be determined for each mode. This model involves a complex numerical implementation which is beyond the scope of this thesis [1]. However, to be able to simulate the propagation of optical pulses in a fibre and to determine the performance of an RZ formatted transmission system a less complicated Fabry Pérot model is used where only one optical mode is considered: the lasing mode of the DFB laser diode [2], [3]. In addition, the Fabry Pérot model is not z-dependent and can therefore be evaluated efficiently. The carrier density in the active layer behaves according to the rate equation

$$\frac{\partial N}{\partial t} = \frac{I}{e \cdot wLd} - gS \frac{c_0}{n_g} - N \left(\frac{1}{\tau_c} + BN + CN^2 \right). \quad (3.1)$$

I is the current that flows through the active layer, e is the elementary charge, w , L and d are the width, length and depth of the active layer. S is the photon density and c_0 is the velocity of light in free space. The group refractive index is denoted by n_g . B and C are the radiative recombination and Auger recombination coefficients. τ_c is the carrier lifetime. The optical gain g satisfies

$$g = \frac{\partial g}{\partial N} (N - N_0) \frac{1}{1 + S \epsilon_{comp}}, \quad (3.2)$$

where $\frac{\partial g}{\partial N}$ is the linear gain parameter, N_0 is the carrier density at transparency and ϵ_{comp} is the gain compression coefficient. The photon density is governed by

$$\frac{\partial S}{\partial t} = gS \frac{\Gamma c_0}{n_g} - \frac{S}{\tau_s} + \Gamma \beta_{sp} B N^2. \quad (3.3)$$

Γ denotes the confinement factor. β_{sp} is the spontaneous emission coefficient which is the fraction of spontaneously emitted photons that goes into the lasing mode [4]. The photon lifetime, τ_s , is expressed as

$$\tau_s = \frac{n_g}{c_0} \frac{1}{\alpha_{loss} + \alpha_{mirror}}, \quad (3.4)$$

where α_{loss} is the internal cavity loss and α_{mirror} the mirror loss according to

$$\alpha_{mirror} = \frac{1}{2L} \log \left(\frac{1}{R_F \cdot R_R} \right). \quad (3.5)$$

R_F and R_R are the reflectivities of the front and rear mirrors, respectively. It is important to note that the mirror loss, α_{mirror} , can be related to the coupling strength, κ , of the grating etched in the proximity of the active layer of the DFB laser diode [5]. For example, an $\alpha_{mirror} \cdot L$ of 2.10 corresponds to $\kappa \cdot L$ of 1.88. The optical power that appears at the front facet emanates linearly from the photon density.

$$P_{out}(t) = \eta_{FF} \frac{hc_0^2}{\lambda n_g} \alpha_{mirror} \cdot wLd \cdot S(t). \quad (3.6)$$

with

$$\eta_{FF} = \frac{1}{1 + \sqrt{\frac{R_F}{R_R} \left(\frac{1-R_R}{1-R_F} \right)}}. \quad (3.7)$$

The temporal phase change of the optical field or frequency chirp amounts to

$$\frac{\partial \phi}{\partial t} = \frac{1}{2} \alpha_H \frac{c_0}{n_g} \frac{\partial g}{\partial N} (N - N_0), \quad (3.8)$$

where α_H is the line width enhancement factor. Euler's forward algorithm has been used to solve these rate equations. Figure 3.1 (c) and 3.1 (d) depict computer simulated pulses based on the laser diode model described in this section and the fibre model described in Sec. 3.2. This single wavelength Fabry P erot based model forms the basis of a numerical analysis of NRZ versus RZ formatted transmission presented in Chapter 4.

3.1.2 External-cavity tuneable mode-locked laser

In order to conduct > 10 Gb/s transmission and demultiplexing experiments an optical pulse source is required that generates high repetition rate, low jitter pulses of known pulse shape. But most of all the optical pulses should be narrow enough to be multiplexed to higher bit rates as is discussed in the introductory chapter. The geometry of the commercially acquired

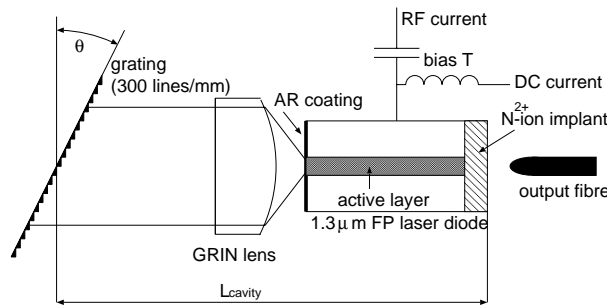


Figure 3.2: Commercially available external-cavity tuneable mode-locked laser (ECTMLL) after [6]

external-cavity tuneable mode-locked laser is depicted in Fig. 3.2 [6]. The laser diode is a

1.3 μm Fabry Pérot buried heterojunction type, 250 μm long. One side is antireflection coated and the other side is deliberately damaged by bombardment with N^{2+} ions. In this way a fast saturable absorber is created. A graded-index lens directs the laser output to a tilted grating. The optical wavelength can be tuned by adjusting the tilt angle, θ , of the grating. Light is coupled out of the cavity from the bombarded facet into a standard single-mode fibre (SSMF). This commercially purchased device is used to generate 10 GHz optical pulse trains. The wavelength of operation is tuneable from 1298 nm to 1314 nm. Within this interval the soliton shaped optical pulses have a typical width of 2.5 – 3.0 ps. The repetition rate can be tuned from 9.5 GHz to 10.5 GHz by varying the cavity length. The device is capable of passive (no RF signal is present) and active (RF signal determines repetition rate) mode-locking. The amount of RF power that needs to be supplied for active mode-locking ranges from 27 to 30 dBm and is generated by an 9 – 11 GHz power amplifier from the master clock of the pulse pattern generator. A DC bias current between 70 and 120 mA needs to be supplied. The output power equals –3 dBm. In the case of passive mode-locking the device can be synchronised to an external 10 GHz optical signal of different wavelength.

3.1.3 10 Gb/s optical modulator

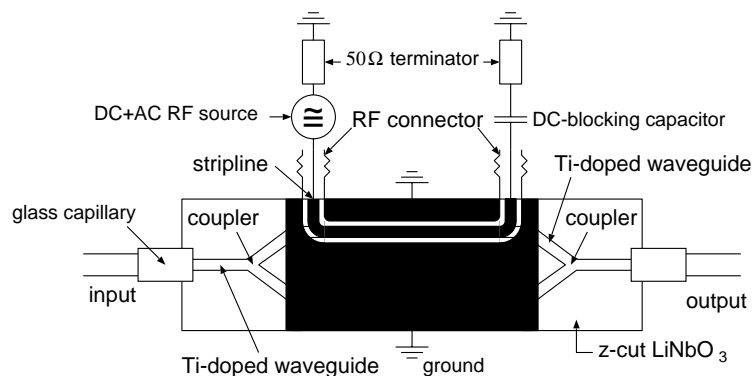


Figure 3.3: The Mach-Zehnder LiNbO_3 optical modulator

A LiNbO_3 optical intensity modulator imposes a data pattern on an optical continuous signal or on an optical pulse train. Figure 3.3 displays the schematic configuration of such a commercial modulator. The Ti-doped optical waveguides form a Mach-Zehnder interferometer. The operation of the modulator is based on the electro-optical properties of the LiNbO_3 . The optical signal travels in a Ti-doped waveguide and is split up into a upper and lower branch. In the upper branch, the optical signal experiences a change in phase that depends on an electric field that influences the refractive index of the LiNbO_3 . This electric field is induced by the co-propagating electrical modulation signal. In the lower branch no electro-optic effect is experienced. When the upper and lower branch recombine, differences in phase between the upper and lower branch are converted to differences in intensity. Hence, the intensity variations of the electrical modulation signals are transferred to variations in intensity of the

optical signal at the output. The corresponding transfer function satisfies

$$P_{out}(t) = P_{in}(t) \frac{\alpha_{loss}}{2} (1 + \cos(\frac{V_m(t)}{V_\pi} \pi + \Delta\phi)), \quad (3.9)$$

where $V_m(t)$ is the voltage of the modulation signal, V_π is the minimum voltage difference of the voltage needed for maximum output power and the voltage needed for minimum output power. $P_{in}(t)$ is the power of the optical input signal. $\Delta\phi$ is an offset in phase that is introduced by different lengths of the upper and lower branches. α_{loss} accounts for the optical excess loss. Generally, $V_m(t)$ is composed of a bias voltage, $V_{m,bias}$ and a voltage representing the data to be modulated, $V_{m,data}(t)$,

$$V_m(t) = V_{m,bias} + V_{m,data}(t). \quad (3.10)$$

$V_{m,data}$ is a signal that is generated by a NRZ pulse pattern generator. logical “1”s and “0”s are represented by a voltage of 2 V and 0 V, respectively. To obtain a maximum extinction ratio between the logical “1”s and “0”s at the output of the modulator, the optical power that represents a “0” must be minimised by properly adjusting $V_{m,bias}$ to values that equal

$$V_{m,bias} = V_\pi (2k - \frac{1}{2} - \frac{\Delta\phi}{\pi}), \quad (3.11)$$

where k is an integer. The commercially purchased optical modulator had a $V_\pi = 3.6$ V, an insertion loss of $\alpha_{loss} = 4.6$ dB and a $\Delta\phi = -145^\circ$ which requires a bias voltage of $V_{m,bias} = 1.1$ V. The pulse pattern generator is able to supply this bias voltage. A difficulty arises because the maximum output voltage of the PPG equals 2 V which is significantly smaller than V_π . Consequently the maximal output power according to Eq. 3.9 will not be reached. With these parameters an additional loss of 2.3 dB must be accounted for. The PPG generates pseudo-random bit sequences (PRBSs) which contain an equal amount of logical “1”s and “0”s. Since the “0”s are mapped to zero output power the output power of the modulator decreases by an additional 3 dB. Altogether, modulation reduces the optical power by ≈ 10 dB. The 3 dB electro-optical bandwidth of the modulator equals 19.9 GHz, large enough for the modulation of a 10 Gb/s NRZ formatted data signal on optical pulse trains. [7]

3.2 Optical fibre

Numerous text books have been written on the transmission properties of optical fibres e.g. [8], [9]. In Sec. 1.3 the nonlinear Schrödinger equation has been introduced. Equation 1.12 contains three parameters that describe the propagation of optical fields in optical fibre; the dispersion, the fibre nonlinearity and the attenuation. It has also been shown that in the absence of loss a pulse shape exists that remains unchanged as long as the dispersion and fibre nonlinearity act in opposite ways on the pulse. This pulse shape can be determined analytically and is called a soliton. In the case of a lossy fibre, soliton transmission is not supported and analytical expressions for the time and distance dependent pulse shape are generally not available. Theoretical evaluation of the propagation of optical signals in nonlinear dispersive lossy fibre requires the nonlinear Schrödinger equation to be solved numerically. The numerical procedure that is implemented is the split-step Fourier method which is described in the

literature [8]. In order to perform simulations of optical transmission or to study the behaviour of optical pulses in fibre it is necessary to determine the three parameters that control the nonlinear Schrödinger equation. Data sheets and literature were used to arrive at useful parameters that allow realistic simulations of nonlinear propagation in SSMF and DSF. The optical loss can be determined very accurately and easily with an optical source and a power meter. This in contradiction with the determination of the fibre dispersion and the fibre nonlinearity. Generally, the fibre nonlinearity and fibre dispersion depend strongly on the core geometry and composition. Many researchers have measured the nonlinear refractive index n_2 that forms the basis of the fibre nonlinearity γ ,

$$\gamma = \frac{2\pi n_2}{\lambda A_{eff}}, \quad (3.12)$$

where A_{eff} is known as the effective core area. Values for n_2 varying between $2 \cdot 10^{-20}$ and $4 \cdot 10^{-20} \text{ m}^2\text{W}^{-1}$ have been measured for SSMF. Numerical simulations in this thesis use $n_2 = 3.2 \cdot 10^{-20} \text{ m}^2\text{W}^{-1}$ and $A_{eff} = 35 \mu\text{m}^2$ at $\lambda = 1310 \text{ nm}$, which are common values in the literature [8], to arrive at a fibre nonlinearity of $\gamma = 4.4 \text{ W}^{-1}\text{km}^{-1}$. The in the literature more commonly used dispersion parameter D that is related to β_2 by

$$D = -\frac{2\pi c}{\lambda^2} \beta_2. \quad (3.13)$$

The zero dispersion wavelength is derived from measuring pulse broadening of low-power narrow optical-pulses in an SSMF fibre. The wavelength where pulse broadening is minimal is the zero dispersion wavelength, λ_D . At $\lambda_D = 1308 \text{ nm}$ minimal pulse broadening is observed. The dispersion slope at λ_D is approximated to be $0.1 \text{ ps}/(\text{nm}^2 \cdot \text{km})$. The average fibre loss aggregates to $0.36 \text{ dB}/\text{km}$. For the 4.4 km of dispersion-shifted fibre the same value for the fibre nonlinearity is assumed. The dispersion parameter equals $D = -19.5 \text{ ps}/(\text{nm} \cdot \text{km})$ at $\lambda = 1310 \text{ nm}$ with a slope of $0.084 \text{ ps}/(\text{nm}^2 \cdot \text{km})$. Fibre losses are determined to be $0.39 \text{ dB}/\text{km}$ [10].

3.3 Polarisation insensitive MQW amplifier modules

The polarisation insensitive amplifiers that are used as amplifying and nonlinear elements in the experiments described in Chapter 4 and 5 have been designed and manufactured by Uniphase Netherlands B.V. When the amplifiers are packaged they are referred to as amplifier modules and when they are implemented on a printed circuit board with network management they are called optical repeater units (ORUs). The first amplifier modules made available had polarisation insensitive optical isolators incorporated which reduced backward reflections of ASE and optical signals. In Table 3.1 at page 81 the amplifiers with serial numbers 27, 39, 47, 50, 56 and 57 are of this uni-directional type. The average values of these parameters have been used in the numerical transmission experiment of Sec. 4.1. The typical coupling loss of the in- and output fibres to the actual amplifier chip is estimated at $2.5 - 3.5 \text{ dB}$. These amplifiers have formed the basis of early experiments by Reid and Liedenbaum on soliton transmission [11], [12] and continue to do so in high speed all-optical demultiplexing and transmission experiments that are described in the remainder of this thesis. Today, the nearly polarisation insensitive amplifier modules do not contain built-in isolators but require external

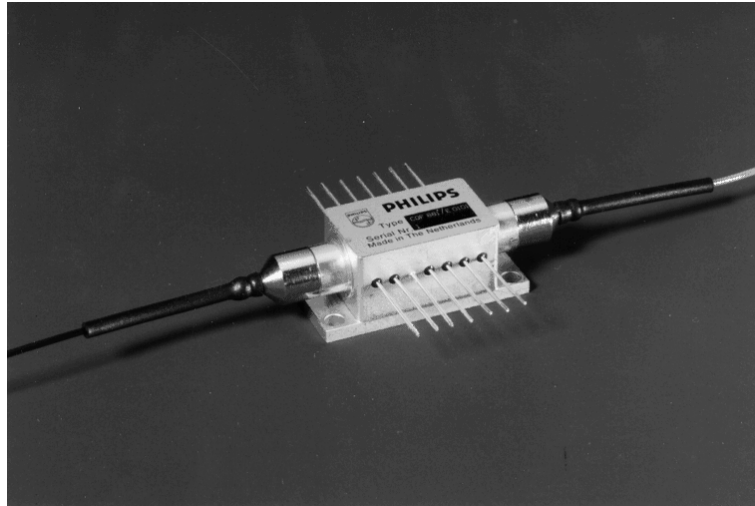


Figure 3.4: Close up of a multiple quantum well semiconductor optical booster amplifier.

optical isolators that are spliced onto both fibre pig-tails of the amplifier module. Figure 3.4 displays a close up of the package the amplifier chips are assembled in. In the exceptional case of a booster amplifier module two optical TE-wave isolators are implemented in the module. For implementation in a TOAD the amplifier must be bi-directional. Amplifier #5 is to be employed as the nonlinear element in the Sagnac based TOAD. Amplifier modules #251 to #258 are implemented in eight optical repeater units that were used in a field trial in the German fibre network, between the cities of Kassel and Hannover [13], and were later used for a 40 Gb/s all-optical time-domain multiplexed transmission laboratory experiment. Table 3.1 provides values for the numerical models developed in Chapter 2. L is the amplifier length, I is the bias current, T is the operating temperature, λ_p is the wavelength of the peak gain. G_p is the peak gain, BW is the -3 dB bandwidth, $P_{sat,p}$ is the saturation output power at 3 dB gain compression. G_{1310} and $P_{sat,1310}$ are the gain and saturation output power at $\lambda = 1310$ nm, respectively. NF is the noise figure and P_{ase} is the total ASE power that is measured at the output. For the gains, wavelengths and saturation output powers different values are available for TE and TM polarisation. Since the amplifiers are assumed to be polarisation insensitive the numerical models have not been adapted for TE and TM parameters. The assumption of a random state of polarisation justifies the utilisation of the average value of TE and TM data. Mostly, deviations between TE and TM parameters are limited to ± 1 dB. The relation between the saturation energy, E_{sat} , and the saturation output power at 3 dB gain compression, $P_{sat,3 dB}$, is described by

$$E_{sat} = \frac{\tau_c}{\log(2)} P_{sat,3 dB}. \quad (3.14)$$

To ensure stable operation, the amplifiers are temperature controlled using an internal Peltier element and thermistor combination.

Table 3.1: Parameters of the CQF88 (#27, #39, #47, #50, #56 and #57) [14], CQF881 (#1, #2 and #212) [15] and the CQF882 (#238, #251-258, #301, #322, #323)[16]. SOA #301 and #323 are polarisation insensitive strained bulk amplifiers.

SOA S/N #	L [μm]	I [mA]	T [$^{\circ}\text{C}$]	λ_p [nm]		G_p [dB]		BW [nm]		$P_{\text{sat,p}}$ [dBm]		G_{1310} [dB]		$P_{\text{sat},1310}$ [dBm]		NF [dB]	P_{ase} [dBm]
				TE/TM	TE/TM	TE/TM	TE/TM	TE/TM	TE/TM	TE/TM	TE/TM	TE/TM	TE/TM				
27	800	400	20	1294/1296	22.7/22.3	57/69	8.3/9.2	21.8/21.7	9.2/10.0	-	7.1						
39	800	400	20	1288/1288	21.7/21.9	61/63	10.6/10.6	20.3/20.6	11.4/11.4	-	5.3						
47	800	400	20	1300/1302	25.1/25.5	73/59	-/-	24.6/25.2	10.6/10.8	-	9.6						
50	800	400	20	1292/1290	24.6/25.4	73/61	-/-	24.0/24.3	11.0/10.5	-	9.2						
56	800	400	20	1307/1306	22.6/22.8	87/74	-/-	22.7/22.9	8.3/8.6	-	8.4						
57	800	400	20	1289/1290	24.8/24.3	81/67	-/-	24.2/23.3	11.2/10.4	-	9.2						
5	800	400	20	1321/1314	27.0/28.2	60/68	11.3/11.5	26.8/27.9	10.6/10.7	-	11.2						
1	800	400	20	1311	16.8	76	17.1	17.1	15.7	-	-6.1						
2	800	400	20	1310	16.5	63	16.8	16.8	14.0	-	-6.6						
238	500	350	20	1279/1307	22.7/19.4	79/67	9.6/-	20.9/19.5	11.5/-	7.4	2.5						
251	400	200	20	1288/1296	19.6/17.4	65/86	8.7/-	18.1/16.9	10.5/-	7.3	-0.9						
252	400	200	20	1289/1295	20.2/18.1	59/62	9.8/-	18.6/17.3	11.1/-	7.2	-0.7						
253	400	200	20	1279/1289	19.7/17.9	76/82	8.9/-	17.6/17.0	10.5/-	5.6	-1.5						
254	400	200	20	1274/1291	21.1/19.1	86/80	9.6/-	18.9/18.2	11.8/-	4.9	-0.6						
255	400	200	20	1291/1301	20.2/18.2	65/72	9.9/-	19.1/18.1	11.2/-	7.2	-0.3						
256	400	200	20	1283/1292	22.5/20.4	66/71	10.3/-	20.3/19.6	12.2/-	5.8	0.6						
257	400	200	20	1284/1298	19.1/17.1	78/76	10.7/-	17.7/16.7	12.3/-	6.2	-1.7						
258	400	200	20	1276/1294	19.8/17.5	85/83	10.0/-	17.7/16.9	12.2/-	5.8	-1.1						
301	650	325	24	1289/1283	17.4/17.3	78/71	10.0/-	16.5/15.4	11.6/-	8.8	0.1						
322	800	350	25	1299/1297	24.6/25.4	62/54	11.5/-	24.7/24.1	12.2/-	8.4	5.7						
323	700	350	24	1283/1283	23.3/24.7	80/60	10.6/-	22.1/21.8	12.0/-	8.6	5.7						

3.4 Optical detectors and receivers

3.4.1 PIN photodiode based detector

A commercially available 45 GHz PIN detector directly connected to a 50 GHz communications analyser (sampling oscilloscope) was used to monitor optical signals in the time domain. At $1.3 \mu\text{m}$ the opto-electronic conversion factor of the detector equals 0.57 mA/mW which corresponds to 13 mV/mW into a 50Ω load. This detector was used for temporal visualisation of high speed signals. It must be noted that for example a 2.5 Gb/s demultiplexed signal is considered high speed because the pulses are of the same width as the pulses of the multiplexed signal and therefore require an equal bandwidth.

3.4.2 2.5 Gb/s receiver

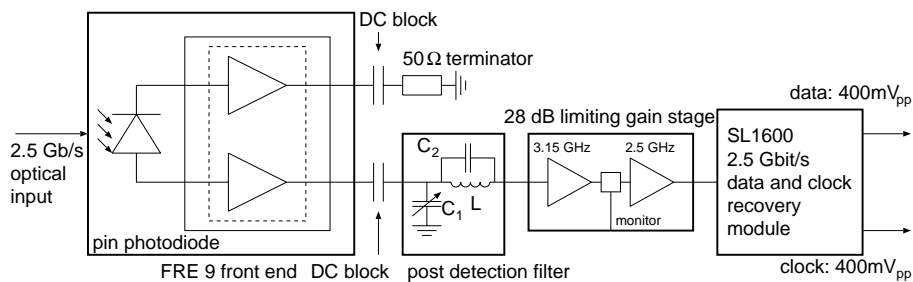


Figure 3.5: Schematic diagram of the 2.5 Gb/s receive path. The balanced optical front-end was developed by Uniphase Netherlands B.V.. The passive stop-band filter removes the 2.5 GHz spectral component. An amplifier stage and a limiting amplifier amplify the filtered signal to a level where an SL1600 chipset from Lucent Technologies recovers the clock and data pattern.

A preliminary experiment where a 10 Gb/s signal is demultiplexed to 2.5 Gb/s requires an optical receiver to measure its BER performance. Figure 3.5 displays the block diagram of how this receiver is realised. An experimental front-end, made available by Uniphase Netherlands B.V. performs the conversion from the optical domain to the electrical domain. One of the outputs of the balanced receiver is AC coupled to a 50Ω terminator while the other output is fed to a post detection filter. The signal that is to be detected is a RZ formatted PRBS data signal. The data and clock recovery module requires a NRZ formatted data signal. The main difference between the spectrum of an RZ PRBS signal and a NRZ PRBS signal is the absence of a spectral component located at the frequency that equals the bit rate in the spectrum of the NRZ formatted signal. To allow the clock and data recovery circuit to function properly the 2.5 Gb/s RZ signal is filtered with a linear filter that removes the 2.5 GHz spectral component. Figure 3.6 displays the transfer function of the post detection filter. It can be observed that the 2.49 GHz component is attenuated by more than 30 dB . The exact frequency is tuned by an adjustable capacitor. It must be noted that the exact bit rate agrees with the SDH-16 (standard digital hierarchy) standard of 2.488 Gb/s . The response of

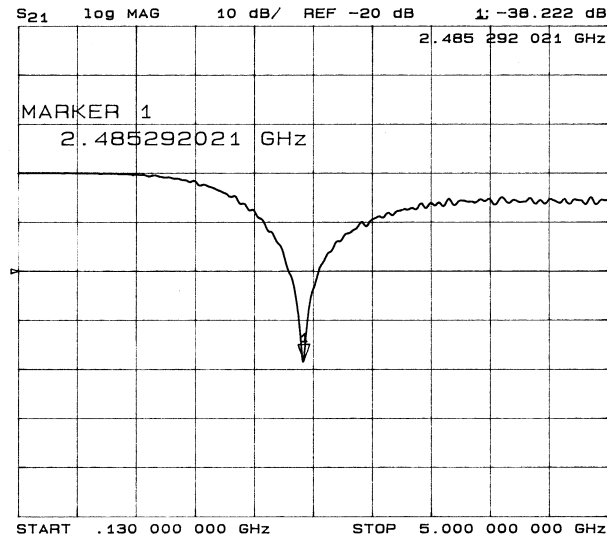


Figure 3.6: Frequency response of the post detection filter.

the front-end is measured and depicted in Fig. 3.7. The bandwidth of the receiver exceeds the 4 GHz with a responsivity of 20 mA/mW into 50 Ω . After the filter and limiting amplifier stage the frequency response of Fig. 3.8 shows that the bandwidth has been reduced to \approx 2.1 GHz and that the 2.49 GHz component remains suppressed. After the limiting amplifier stage the RZ data signal has transformed into a NRZ like data signal and is reconstructed in the clock and data recovering chipset. The output of this chipset is connected to 2.5 Gb/s bit error rate (BER) test equipment while at the input a $2^7 - 1$ PRBS, RZ signal is applied. The pulses are generated by the DFB-diode treated in Sec. 3.1.1 and modulated with the LiNbO₃ modulator introduced in Sec. 3.1.3. An adjustable optical attenuator attenuates the signal to a level where it can be fed into the receiver. Generally when the power at the input of the receiver (received power) is reduced system noise will result in wrong decisions made by the data recovery circuit. Consequently more errors occur. In other words, the system performance decreases. Figure 3.9 shows the bit error rate performance of the receiver versus received power for 27 ps and 16 ps wide pulses. At a BER of 10^{-9} a 2 dB power difference (power penalty) in received power exists between the 27 ps and the 16 ps pulses. It may be concluded that this RZ receiver is not ideal i.e. the performance depends on the pulse width of the data signal. The introduction of the post detection filter results in different propagation times for different spectral components of the detected signal. The spectral content of the 27 ps optical pulses deviates from the 16 ps optical pulses. For different pulse widths this will result in different “eye-closure” and bit error rate curves.

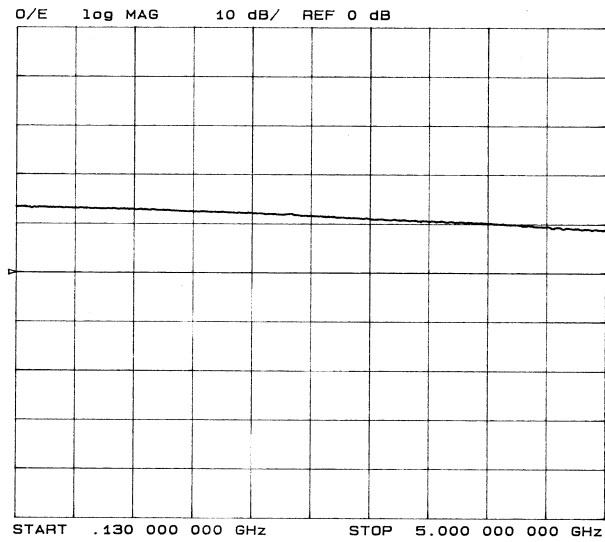


Figure 3.7: Spectral response of the FRE 09 optical front-end.

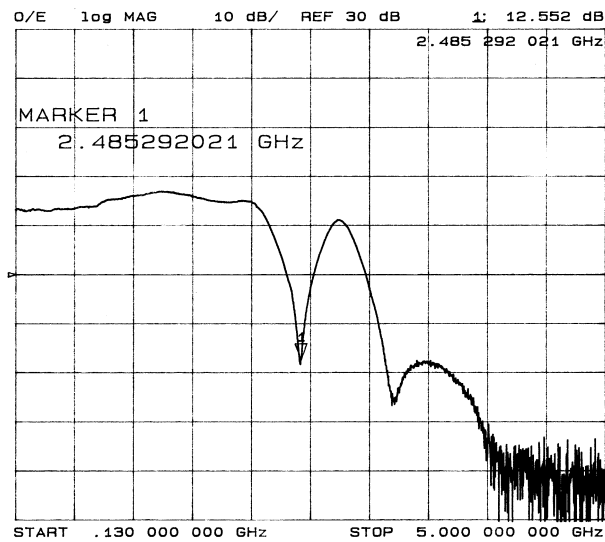


Figure 3.8: Spectral response measured after the limiting amplifier.

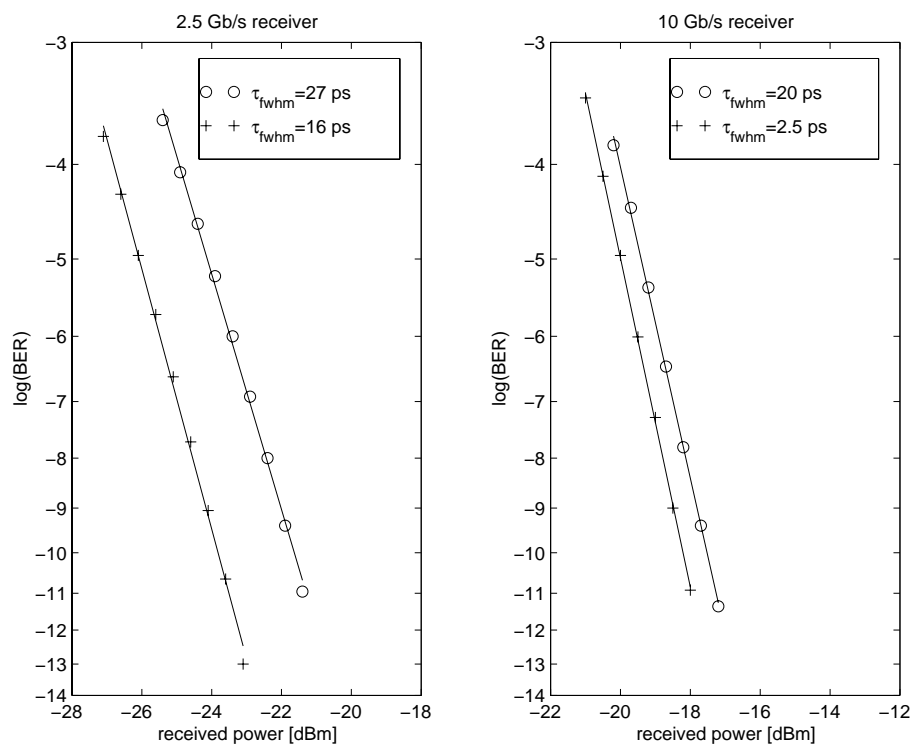


Figure 3.9: Bit error rate performance of the 2.5 Gb/s and the 10 Gb/s receiver.

3.4.3 10 Gb/s receiver

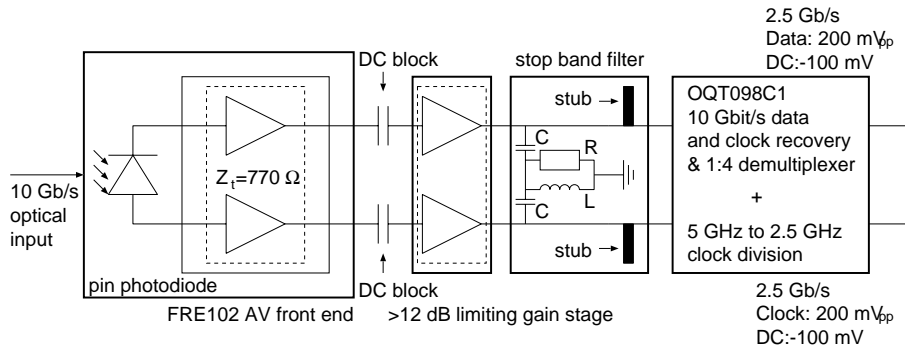


Figure 3.10: Schematic diagram of the 10 Gb/s receive path. The balanced optical receiver has been developed by Uniphase Netherlands B.V.. Lucent Technologies in Nürnberg designed and implemented a 10 Gb/s physical SDH interface around this front end. The passive RLC-microstrip filter removes the 10 GHz spectral component from the in amplitude limited signal after which the OQT098C1 chipset performs electrical clock and data recovery and demultiplexes the 10 Gb/s into four 2.5 Gb/s signals of which one signal is made available via an RF connector [17].

The receive path of the 10 Gb/s receiver is significantly different compared to that of the 2.5 Gb/s receiver. Instead of the utilisation of only one of the two balanced outputs, a fully balanced receiver is designed, similar to the receiver developed within the European ACTS project “Upgrade” [18]. The FRE 102 AV front end designed by Uniphase Netherlands B.V. exhibits an opto-electronic frequency response depicted in Figs. 3.11 and 3.12. The main advantage of employing a balanced receiver is that a flatter response is obtained and that the signal to noise ratio improves by approximately 3 dB. The opto-electronic frequency response of the receiver with limiting amplifier and post-detection filter is displayed in Figs. 3.13 and 3.14 for the single output and balanced output, respectively. In comparison with the response of the 2.5 Gb/s receiver the suppression of the before mentioned spectral component is clearly visible and of the same order of magnitude. As in the case of the 2.5 Gb/s receiver BER curves are measured (see Fig. 3.9). This has been done for $2^7 - 1$ PRBS data signals composed of 20 ps pulses from the DFB laser diode and for 2.5 ps pulses generated by the external-cavity tuneable mode-locked laser. In this case a difference in receiver sensitivity (for BER = 10^{-9}) of 0.7 dB exists which makes the receiver almost independent of the pulse width of the RZ pulses.

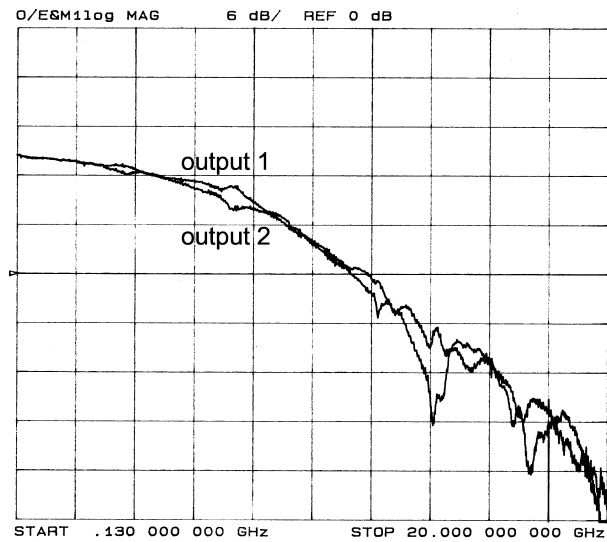


Figure 3.11: Frequency response of the unbalanced FRE 102 AV optical front-end.

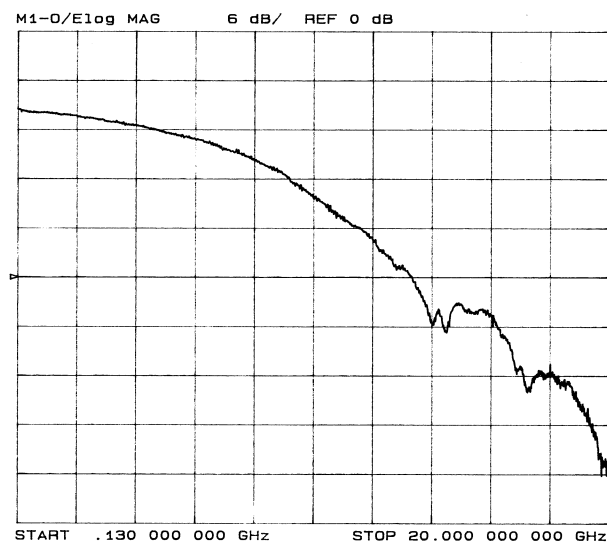


Figure 3.12: Frequency response of the balanced FRE 102 AV optical front-end.

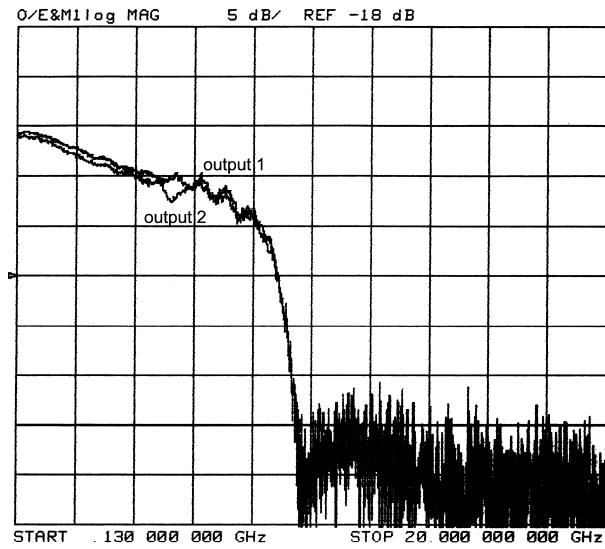


Figure 3.13: Frequency response of the unbalanced receiver, limiter and post detection filter [17]

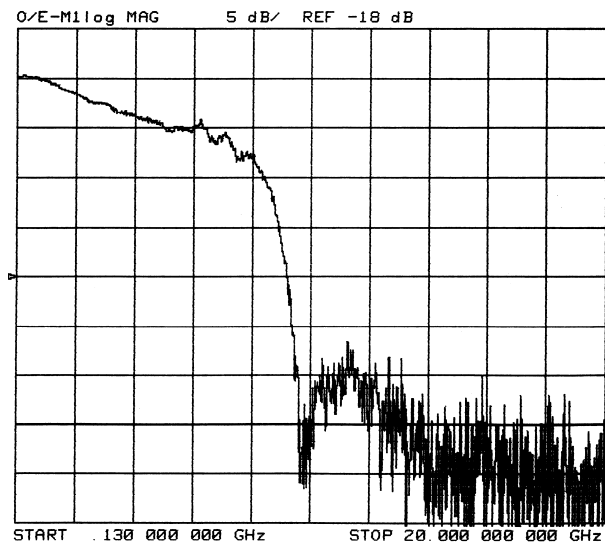


Figure 3.14: Frequency response of the balanced receiver, limiter and post detection filter [17]

3.4.4 Optically preamplified receiver

Semiconductor optical amplifiers can be placed before the input of the optical front-end to form an optically preamplified receiver. These optically preamplified receivers exhibit an improved receiver sensitivity as less power is required at the input of the amplifier to obtain the same power at the input of the photodiode. A typical configuration of an optically preamplified receiver is depicted in Fig. 3.15. Attenuator-1 attenuates the input signal so that

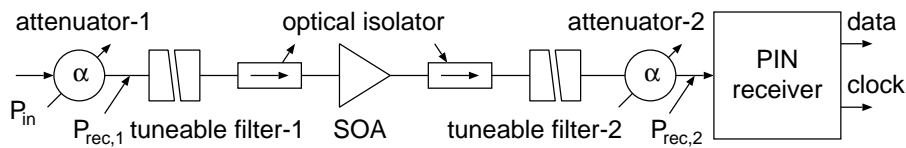


Figure 3.15: Optically preamplified receiver

the BER sensitivity on received signal power, $P_{rec,1}$, can be measured. The first optical filter eliminates the outband ASE added to the signal, e.g. by a cascaded amplifier link, after which the signal and inband noise are amplified by the SOA. Again, the optical signal is filtered to eliminate the outband noise introduced by the optical preamplifier. This signal is fed into the PIN receiver via attenuator-2. The main function of the second attenuator is to avoid over exposure of the photodiode. The performance of an optically preamplified receiver is limited by the noise figure of the SOA. Significant improvements of more than 10 dB in receiver sensitivity can be obtained. In Chapter 4 and 5 the performance of optically preamplified receivers is enhanced and improved BER performance is demonstrated in a variety of experiments.

3.4.5 Theoretical model of an optical receiver

In this section a receiver model is presented that describes the detection and determination of a bit error rate mathematically [19]. This model is implemented numerically and used to perform simulations that are presented in Sec. 4.1. Generally the input signal of the receiver contains a data signal that is to be received. This signal will be referred to as the line signal. In the case where an all-optical demultiplexer is used to reduce the bit rate of the line signal, the data signal is also referred to as the demultiplexed (line) signal. If SOAs are used to amplify the optical signal a broad-band ASE spectrum is present. An optical band-pass filter (OBPF) is inserted before the photodiode of the receiver to reduce the amount of ASE that lies outside the spectrum of the line signal. In this model the filter is assumed to have a square transfer function centred at $\lambda_{obpf} = \lambda_{line}$ and with a bandwidth of $\Delta\lambda_{obpf}$. The loss of the filter is denoted by α_{obpf} . Let $P_{line,in}(\tau)$ and $S_{ase,in}(\lambda, \tau)$ be the input line signal and the input ASE noise signal, respectively. The photocurrent for the line signal and noise signal can be expressed as

$$I_{line}(\tau) = \frac{\eta e \lambda_{line}}{c_0 h} \alpha_{obpf} P_{line,in}(\tau), \quad (3.15)$$

and

$$I_{ase}(\tau) = \frac{\eta e \lambda_{opbf}}{c_0 \hbar} \alpha_{opbf} \int_{\lambda_{opbf} - \frac{1}{2} \Delta \lambda_{opbf}}^{\lambda_{opbf} + \frac{1}{2} \Delta \lambda_{opbf}} S_{ase,in}(\lambda, \tau) d\lambda, \quad (3.16)$$

where η is the quantum efficiency of the detector. Furthermore, the receiver has also an electrical bandwidth $B_{rec,e}$. The optical bandwidth $\Delta \lambda_{opbf}$ in [m] is converted to [Hz] according to

$$B_{rec,o} = \frac{c}{\lambda_{opbf}^2} \Delta \lambda_{opbf}. \quad (3.17)$$

The electrical power of the signal is found by

$$S(\tau) = C \cdot I_{line}^2. \quad (3.18)$$

C is a constant that contains the impedance of the medium where the power is determined. The total noise power is composed of shot noise (N_{shot}), signal-spontaneous beat noise ($N_{sig,spont}$), spontaneous-spontaneous beat noise ($N_{spont,spont}$) and thermal noise (N_{therm}), thus

$$N(\tau) = N_{shot} + N_{sig,spont} + N_{spont,spont} + N_{therm}. \quad (3.19)$$

The noise components satisfy

$$N_{shot} = C \cdot 2B_e e (I_{line} + I_{ase}) \quad (3.20)$$

$$N_{sig,spont} = C \cdot 4I_{line} I_{ase} \frac{B_{rec,e}}{B_{rec,o}} \quad (3.21)$$

$$N_{spont,spont} = C \cdot I_{ase}^2 B_{rec,e} \frac{2B_{rec,o} - B_{rec,e}}{B_{rec,o}^2} \quad (3.22)$$

$$N_{therm} = C \cdot I_{therm}^2. \quad (3.23)$$

The noise power that is introduced by the amplifier of the optical front end is contained in N_{therm} . At this point the signal to noise ratio of the signal at the output of the front-end is determined. Between the output of the front-end and the input of the clock and data recovery usually a filter is situated. The data and clock recovery module sees the following input

$$S'(\tau) = S(\tau) \star p_{filt}(\tau) \star p_{filt}(-\tau) \quad (3.24)$$

and

$$N'(\tau) = N(\tau) \star p_{filt}(\tau) \star p_{filt}(-\tau), \quad (3.25)$$

where $p_{filt}(\tau)$ is the impulse response of the filter and the \star stands for a convolution. The shape of the filter can for example be square in which case an integrated dump receiver is simulated. Usually $p_{filt}(\tau)$ is the impulse response of a low pass filter. The filter does not add noise to the system. The data and clock recovery unit usually consists of a sample and hold circuit followed by a comparator to determine whether the output should be considered high or low i.e. a logical "1" or "0". To this end a threshold level, A_{thr} , and sample times, τ_{sample}

are defined. An analytical expression for the BER is found if the noise N is assumed to be Gaussian distributed. Under these circumstances the variation of the Gaussian distribution is equal to $N'(\tau)$. The bit error rate for an expected logical “0” equals

$$P_0 = \frac{1}{\sqrt{2\pi N'(\tau_{sample})}} \int_{A_{thr}}^{\infty} \exp\left(-\frac{(\rho - \sqrt{S'(\tau_{sample})})^2}{2N'(\tau_{sample})}\right) d\rho \quad (3.26)$$

and for a logical “1”

$$P_1 = \frac{1}{\sqrt{2\pi N'(\tau_{sample})}} \int_{-\infty}^{A_{thr}} \exp\left(-\frac{(\rho - \sqrt{S'(\tau_{sample})})^2}{2N'(\tau_{sample})}\right) d\rho. \quad (3.27)$$

In the case of a pseudo random bit sequence (PRBS) the amount of logical “0”’s approximates the amount of logical “1”. The total bit error rate can be expressed as

$$\text{BER} = \frac{1}{2}P_0 + \frac{1}{2}P_1. \quad (3.28)$$

The sample moments $\tau_{sample} + nT_b$ are periodic with the bit rate. For different values for $\tau_{sample} = [0, T_b]$ and different values for $A_{thr} = [S'_{min}, S'_{max}]$ the average bit error rate can be calculated over all the bits that form the PRBS signal.

3.5 Miscellaneous components

3.5.1 Tuneable optical filters

In the experiments treated in this thesis optical tuneable filters have three different functions. First, semiconductor optical amplifiers generate wide band ASE. During transmission, the line signal is flooded with this ASE. At the receiver the line signal is detected preferably without the ASE. In this case a tuneable filter passes the line signal and rejects the ASE. Secondly, at the output of an all-optical demultiplexer an optical filter discriminates the demultiplexed signal from the switch signal. Thirdly, the optical clock-recovery circuit treated in Sec. 5.2 and the all-optical cross-gain modulated ring laser discussed in Sec. 5.1 require a tuneable optical filter that determines the wavelength of operation. In the case of the all-optical clock-recovery circuit the bandwidth of the filter determines the width of the recovered clock pulses. Except for one self assembled tuneable filter all tuneable filters were commercially acquired. The filters are composed of multiple layers of thin films. Operation of the filters is based on interference of transmitted beams which leave the thin films after repeated reflection at the interfaces of the thin multilayers that form the filter. The wavelength for which constructive interference occurs in the forward direction (pass band) depends on the angle of incidence. Hence, rotation of a substrate with thin film layers deposited on it allows the selection of a wavelength that is passed to the output. The bandwidth of an optical filter must be adjusted to the bandwidth of the optical data signal that is filtered.

Pulses that are generated by the DFB laser diode are filtered with a 1 nm wide optical filter. Pulses that are generated by the 10 GHz external-cavity mode-locked laser (see Sec. 3.1.2) are passed through a 2.5 nm wide filter. The insertion loss of the 2.5 nm wide filter cassettes

is below 0.5 dB and the loss of the collimator module in which the filter-cassettes are inserted lies below 0.4 dB. The two 1 nm wide filter cassettes have insertion losses below 1.5 dB. An additional filter cassette has a bandwidth of 0.8 nm and an insertion loss of 0.5 – 2.0 dB. The home made filter has an insertion loss of 2.0 dB and a bandwidth of 2 nm. All filters are tuneable from 1290 nm to 1330 nm. Polarisation dependent losses are below 0.5 dB [20].

3.5.2 Adjustable optical delay lines

Optical delays are inserted when a signal needs to be delayed with respect to other signals. Commercially available adjustable optical delays are employed in the all-optical demultiplexing experiments [21]. Two 0 – 200 ps, and a 0 – 300 ps adjustable delays are available. The insertion loss of the two 0 to 200 ps optical delays varies between 1.44 and 1.62 and between 1.61 and 2.13 dB, respectively. The 0 to 300 ps delays exhibit an insertion loss of 0.85 to 1.95 dBm. Polarisation dependent losses are less than 0.06 dB. Furthermore, home made optical delay lines are constructed by aligning two collimating lens ferules at a certain distance and fasten them with a clip. The lens ferules have an anti-reflective coating. The insertion loss of these delays depends strongly on the 0 to 120 ps delay. The maximum insertion loss amounts to 3 dB. Polarisation dependent loss was not observed.

References

- [1] L.M. Zhang and J.E. Carroll. Large-signal dynamic model of the DFB laser. IEEE Journal of Quantum Electronics, 28:604–611, 1992.
 - [2] K. Petermann. Laser diode modulation and noise, pages 5–58. Kluwer Academic Publishers, 1991.
 - [3] G.P. Agrawal, N.K. Dutta, and S. Mitra. Long-wavelength semiconductor lasers, pages 287–321. Van Nostrand Reinhold, New York, 1986.
 - [4] G.P. Agrawal, N.K. Dutta, and S. Mitra. Long-wavelength semiconductor lasers, pages 224–227. Van Nostrand Reinhold, New York, 1986.
 - [5] K. Petermann. Laser diode modulation and noise, pages 50–51. Kluwer Academic Publishers, 1991.
 - [6] R. Ludwig and A. Ehrhardt. Turn-key ready wavelength, repetition rate and pulsewidth-tunable femtosecond hybrid modelocked semiconductor laser. Electronics Letters, 31:1165–1167, 1995.
 - [7] Sumitomo Osaka Cement Co., LTD., 1, Kanda Mitoshiro-cho, Chiyoda-ku, Tokyo 101, Japan. LiNbO₃ optical modulators, operation manual and inspection pass sheet model T.MZ 1.3-20, MZ4-134-8-4561.
 - [8] G.P. Agrawal. Nonlinear Fiber Optics. Optics and Photonics. Academic Press, New York, second edition, 1995.
 - [9] A. Hasegawa and Y. Kodama. Solitons in optical communications. Oxford University Press, Oxford, 1995.
 - [10] Plasma Optical Fibre B.V., Zwaanstraat 1, 5651 CA Eindhoven, The Netherlands. Data sheets of BF10961B dispersion shifted fibre.
-

-
- [11] J.J.E. Reid, C.T.H.F. Liedenbaum, et al. Realisation of 20 Gbit/s long haul soliton transmission at 1300 nm non standard single mode fibre. In Proceedings of ECOC'94, volume 4, pages 61–64, 1994.
- [12] C.T.H.F. Liedenbaum, J.J.E. Reid, et al. Experimental long haul 1300 nm soliton transmission on standard single mode fibres using quantum well laser amplifiers. In Proceedings of ECOC'94, volume 1, pages 233–236, 1994.
- [13] A. Mattheus, H. Gruhl, J.J.E. Reid, et al. Final report on link for technical exhibition. “Upgrade” Deliverable D6221 AC045-tzd-ams-DS-P-025-b1, European Commission, Advanced Communications Technologies & Services, Brussels, Belgium, 1997.
- [14] Uniphase Netherlands B.V., Prof. Holstlaan 4, 5656AA Eindhoven, The Netherlands. Datasheets of CQF88 MQW polarisation insensitive isolated semiconductor optical amplifier modules #27, #39, #47, #50, #56 and #57.
- [15] Uniphase Netherlands B.V., Prof. Holstlaan 4, 5656AA Eindhoven, The Netherlands. Datasheets of CQF881 MQW semiconductor optical booster amplifier modules #1, #2 and #212.
- [16] Uniphase Netherlands B.V., Prof. Holstlaan 4, 5656AA Eindhoven, The Netherlands. Datasheets of CQF882 MQW semiconductor optical amplifier modules , #5, #238, #251-258, #301, #322 and #323.
- [17] Lucent Technologies Germany, Thurn-und-Taxis-Str. 10, D-90411 Nürnberg, Germany. Manual of 10 Gb/s RZ receiver.
- [18] C. Schulien, B. Teichmann, and J.J.E. Reid. Specification of NRZ/RZ conversion for STM-64 transmission. “Upgrade” Deliverable D5111 AC045-att-csn-DS-R-005-b1, European Commission, Advanced Communications Technologies & Services, Brussels, Belgium, 1996.
- [19] N.A. Olsson. Lightwave systems with optical amplifiers. Journal of Lightwave Technology, 7:1071–1082, 1989.
- [20] Tecos GmbH, Scheibenstr. 47, 40479 Düsseldorf, Germany. Datasheets of tunable optical filters, K-403, KC-057, KC-069, KC-106, KC-107, KD-071, KD-086, KD-151, KD-197, KD-208 and KD-209.
- [21] Santec Corporation, Micom Valley Tohkadai, Kamisue, Komaki, Aichi 485-0822, Japan. Datasheets of adjustable optical delay lines (ODL300/ODL320) 96141, 97191, 98052.
-

Chapter 4

10 Gb/s transmission experiments

The choice of a NRZ or RZ data format depends on the possibilities for multiplexing a NRZ or RZ signal and on the transmission properties and performance of NRZ and RZ modulated signals in SOA cascaded links. In Sec. 4.1 computer simulations are presented that show the BER performance of an optically repeatered transmission system employing SOA modules for RZ and NRZ formatted data [1]. Numerical results are obtained from the models introduced in Chapter 2 and 3. The performance of an RZ formatted transmission system is experimentally investigated for a long-haul optically repeatered and unrepeatered link. Section 4.2 provides experimental data that gives insight into the optimum performance of two SOA based transmission systems [2], [3]. Key components and system blocks that are utilised in these experiments have been described in Chapter 3. At $1.3 \mu\text{m}$, Raman amplification provides an alternative means of loss compensation. Section 4.3 treats a distributed Raman amplifier based transmission experiment [4]. The transmission experiments discussed in Sec. 4.2 employed a sinusoidally modulated DFB laser diode. In Sec. 4.4 this source is replaced by the external-cavity mode-locked tuneable laser of Sec. 3.1.2. For different wavelengths and link input powers the transmission performance is investigated of a four section 200 km link with high gain SOA modules. Data obtained from this experiment is used to improve the transmission link to allow successful transmission of a 40 Gb/s OTDM signal in Chapter 5.

4.1 RZ (soliton) versus NRZ formatted transmission

Pages 96-99 display material presented at the IEEE Third Symposium on Communications and Vehicular Technology in the Benelux on a numerical investigation of the performance of NRZ and RZ (soliton) based SOA cascaded transmission systems [1].

4.2 Repeatered and unrepeatered RZ transmission

Pages 100-103 contain published material in the System Technologies volume of the Trends in Optics and Photonics Series of 10 Gb/s long-haul transmission experiments [2], [3].

10 Gbit/s Long Haul Soliton versus NRZ Optical Transmission in the 1300nm Window

Robert C.J. Smets, Jean G.L. Jennen

Eindhoven University of Technology, Building EH 12.25, P.O. Box 513, 5600 MB Eindhoven, The Netherlands

Abstract—We have compared the operation and applicability of soliton transmission systems versus NRZ (Non Return to Zero) transmission systems for the 1300nm optical window. For a different number of in-line amplifiers the BER (Bit Error Rate) curves of both transmission systems have been simulated. For both systems the same fibre dispersion and attenuation has been assumed and all amplifier gains have been chosen so that the fibre losses are compensated for. In case of the soliton system an extra dispersion shifted fibre has been located directly after the laser diode to unchirp and compress the laserpulses. With respect to the BER simulations, soliton and NRZ transmission systems are expected to be competitive. Transmission exhibiting an error probability below 10^{-9} is attainable for both systems. Under equal circumstances, we conclude from our simulations that soliton systems show better BER performance than NRZ systems beyond 450 km. Owing to the dispersion compensating properties soliton transmission systems are advantageous when long haul transmission is considered. However, NRZ transmission is both a well established and relatively simple technique and can be more readily implemented.

I. INTRODUCTION

Since the introduction of standard single mode fibre (SSMF) more than 55 million kilometers has been installed. At present 2.5 Gbit/s data transmission has become a commercial standard. In the near future the increasing demand for more network capacity can be satisfied by introducing 10 Gbit/s transmission systems. The very low dispersion in the 1300 nm window of SSMF makes a 10 Gbit/s system attractive. Considering the recently achieved progress in the development and use of quantum-well laser amplifiers (QWLAs) [1], [2], [3], attenuation of over 50 km of SSMF can be easily compensated for, making repeaters superfluous. Recently, more and more promising experimental results are being published on NRZ [4] [5] as well as soliton transmission. Even 20 Gbit/s soliton transmission over 200 km [6] has been realised as well as 2×10 Gbit/s wavelength division multiplexed NRZ transmission over 63.5 km [5]. As solitons can be multiplexed easily in the time domain it is more likely that for higher bitrates (i.e. ≥ 40 Gbit/s) soliton systems will be preferred to NRZ systems whose maximum bitrate is limited by the maximum achievable electrical bandwidth in current electronics. Although the literature available on soliton as well as NRZ systems is extensive, theoretical study on long

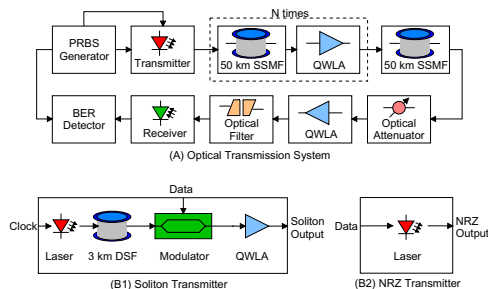


Figure 1: Optical Transmission System (A), Soliton Transmitter (B1), NRZ Transmitter (B2)

haul transmission systems with cascaded QWLAs is not yet complete. The effects of amplifier saturation, ASE and timing jitter on system performance still need investigation. In this paper we compare the performance between a 10 Gbit/s NRZ system [4], [5] and a 10 Gbit/s soliton system theoretically by means of computing bit error rate (BER) curves.

II. TRANSMISSION MODEL

Figure 1 shows the NRZ and soliton transmission system. In the case of NRZ transmission the laser diode is directly modulated with the PRBS signal. The soliton system requires a more complex transmitter. Chirped near-soliton pulses are generated by gain switching of the laser diode and unchirped and compressed in the dispersion shifted fibre after which the optical modulator modulates the data on the soliton train. Finally, the power is boosted by a QWLA up to a level where nonlinear effects compensate dispersion effects in the SSMF. Both soliton and NRZ transmission systems are built up out of eight different components figure 1, namely QWLAs, fibres, a laserdiode, a photodiode, a PRBS generator, a BER detector, a filter and an attenuator. The soliton system needs an additional modulator. Therefore nine models are needed for a theoretical description of both systems.

QWLA model

The model used to describe the QWLAs is based upon the rate equations in [7] and [8], where the z-dependence has been eliminated by integration over the amplifier length L . The ASE is wavelength dependent [4], namely:

$$P_{out}(\tau, \lambda) = P_{in}(\tau, \lambda)e^{h(\tau, \lambda)} + h \frac{c^2}{\lambda^3} \frac{NF}{2} e^{h(\tau, \lambda)} d\lambda \quad (1)$$

with

$$h(\tau, \lambda) = \int_0^L g(z, \tau, \lambda) dz, \quad (2)$$

$$\varphi_{out}(\tau, \lambda) = \varphi_{in}(\tau, \lambda) - \frac{1}{2} \alpha_H h(\tau, \lambda) \quad (3)$$

and

$$\frac{\partial h(\tau, \lambda)}{\partial \tau} = -\frac{h(\tau, \lambda) - g_0(\lambda)L}{\tau_c} - \frac{\sum_{\lambda_i} \frac{\lambda_i}{\lambda} P_{in}(\tau, \lambda_i) / P_{sat}(\lambda)}{\tau_c} \cdot (e^{h(\tau, \lambda)} - 1), \quad (4)$$

where τ_c is the carrier lifetime, $P_{sat}(\lambda)$ represents the $1/e$ saturation output power, $g_0(\lambda)L$ represents the small signal amplifier gain, $h(\tau, \lambda)$ is the time dependent amplifier gain, α_H is the linewidth enhancement factor, $d\lambda$ is the wavelength discretisation stepsize, h is Planck's constant, c stands for the velocity of light, NF is the fibre coupled noise figure, and $P_{in}(\tau, \lambda_i)$ represents the total input power to each amplifier, i.e. the sum of input signal power and ASE originating from the previous amplifiers. τ is the reduced time with respect to a reference plane moving with the signal ($\tau = t - \frac{z}{v_g}$, with v_g the group velocity). The amplifier is assumed to have zero reflecting input/output facets and to be polarization independent. The gain is assumed to have a Gaussian shaped spectrum. The equations are numerically solved using *Euler forward* iteration.

Fibre model

Propagation in the fibre is described by the nonlinear Schrödinger equation [9],

$$\frac{\partial A}{\partial z} = -\frac{\alpha}{2} A - \frac{i}{2} \beta_2 \frac{\partial^2 A}{\partial \tau^2} + i\gamma |A|^2 A, \quad (5)$$

where A is the slowly varying envelope of the optical signal, α represents the losses in the fibre, γ is the non-linearity parameter and $\beta_2 = -D \frac{\lambda^3}{2\pi c}$ is the dispersion parameter. D is the dispersion. Eq. 5 is numerically solved using the *split-step Fourier* method.

Laser diode model

The model employed is a simple Fabry Perot model

where the z-dependence has been eliminated [10]. Laser pulses are generated by gain switching of the laser diode. After transmission through a dispersion shifted fibre, the pulses closely resemble soliton pulses. In the case of NRZ modulation the signal shows an extinction ratio and slopes equal to experimentally observed values.

Photodiode model

The optical signal is converted to the electrical domain by the photodiode as described by [11]. A quantum efficiency of 0.8 is taken. The model includes shot noise, signal-spontaneous beat noise, spontaneous-spontaneous beat noise and thermal noise. The electrical bandwidth is 10.2 GHz and the thermal noise is adjusted, so that the receiver has a sensitivity of -13.7 dBm at 10 Gbit/s NRZ and a BER of 10^{-9} , in agreement with measured data (figure 2).

Optical filter

The optical filter is assumed to be square and sufficiently broad with respect to the signals bandwidth. The optical filter reduces the ASE by allowing only a small fraction of the ASE spectrum to pass. The effective bandwidth of the filter is 2 nm and the filter introduces a loss of 2 dB.

Optical attenuator

The optical attenuator is used primarily to attenuate the signal in order to compute BER values for different receiver input powers.

Optical modulator

The optical modulator has only functionality in the soliton system. Its purpose is to modulate the soliton train. When the modulator is excited by a logical one, a raised-cosine window is opened letting a soliton pass. When a logical zero is applied, a window of smaller amplitude is opened, attenuating the soliton. The optical modulator introduces a loss of 5 dB. The roll-off factor of the raised cosine function is $\beta = T_b/2$, with T_b the bit time. The extinction ratio i.e. the ratio between the peak power of a logical one and a logical zero is equal to $ER = 20$.

PRBS generator and BER detector

The PRBS generator generates a $2^7 - 1$ pseudo-random bit sequence. The BER detector computes the optimum BER for a number of detection thresholds and sampling times, assuming a gaussian distribution for all noise sources. The BER is obtained by averaging over all $2^7 - 1$ bits. We emphasize that the clock of the PRBS generator is used to sample the received data and that there is no clock recovery at the receiver.

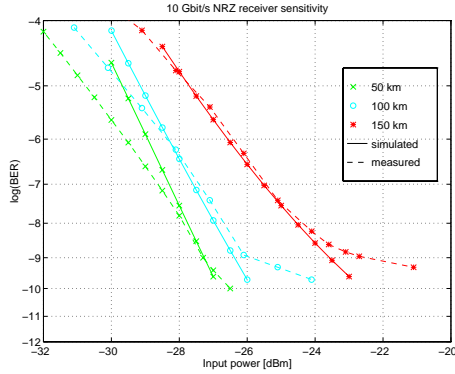


Figure 2: Measured and simulated BER curves in absence of clock recovery, $ER = 6$

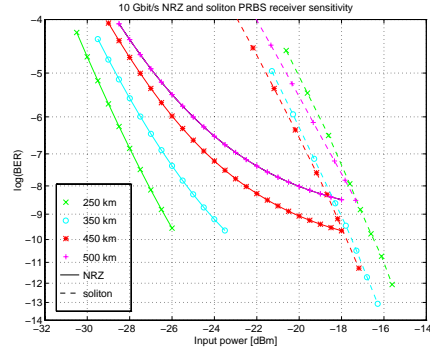


Figure 3: Simulated NRZ and soliton BER curves in absence of clock recovery, $ER = 20$

III. COMPUTER SIMULATIONS

At 1300 nm the 50 km SSMF sections exhibit a loss of $\alpha = 0.4$ dB/km and a dispersion of $D = 0.6$ ps/km/nm and a nonlinearity parameter of $\gamma = 2.1$ W/km. The 3 km dispersion shifted fibre exhibits a loss of $\alpha = 0.4$ dB/km and a dispersion of $D = -17$ ps/km/nm. The QWLAs are adjusted to a gain of 22.5 dB at the signal wavelength of $\lambda = 1310$ nm, almost equal to the loss of the 50 km fibre span. A 60 nm gain bandwidth was assumed. The fibre to fibre noise figure of the amplifier was estimated at 9 dB. For the 3 dB saturation output power $P_{sat,3dB} = 10$ dBm was assumed. The linewidth enhancement factor was estimated at $\alpha_H = 5$. For the gain-recovery time $\tau_c = 200$ ps was taken. Using the NRZ or soliton transmitter a power of 2 dBm or 6 dBm respectively, is launched into the first fibre section. All computer simulations were carried out with the same algorithms. The only difference between the NRZ and soliton simulations is the number of sample points per bit. Because the phase of the solitons is of major importance, 256 sample points per bit were used for soliton simulations while 20 sample points sufficed in the case of NRZ simulations. Figure 2 shows measured and simulated NRZ BER-curves with an extinction ratio of $ER = 6$. The good agreement between the measured and theoretical curves validates our model.

IV. DISCUSSION

Figure 3 depicts the simulated BER-curves for NRZ and soliton transmission over 150 km and 200 km. The higher receiver input power of the soliton sig-

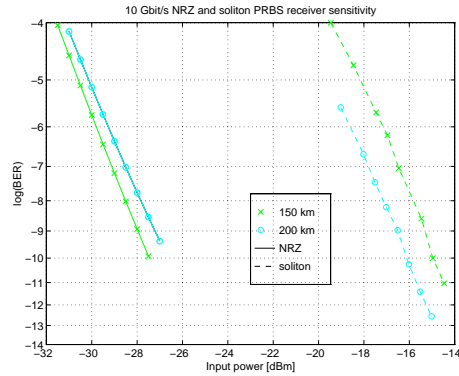


Figure 4: Simulated NRZ and soliton BER curves in absence of clock recovery, $ER = 20$

nal is due to the amplifier in the soliton transmitter, therefore better BER performance is expected. Additional simulations reveal that this different behaviour can be explained by the absence of clock recovery. As solitons are sensitive to timing jitter caused by saturation and soliton interaction, timing jitter is expected to be the most likely cause. In contrary to NRZ transmission it can be clearly seen that in the case of soliton transmission at 200 km a better BER is obtained with less input power than at 150 km. The same result is obtained for longer transmission links, presented in figure 4. However, after 450 km no further improvement is observed. Additional simulations show that the improvement of the soliton signal could be explained by lesser non-linear effects in the fibre

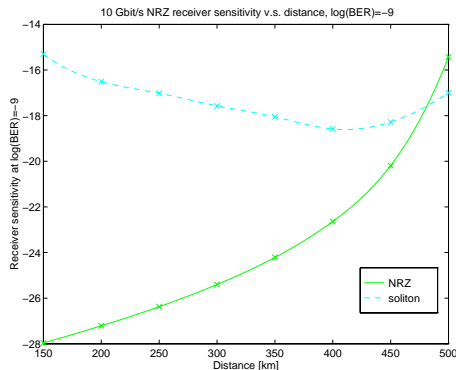


Figure 5: Receiver sensitivity versus transmission distance at $BER = 10^{-9}$

caused by saturation of the amplifiers resulting in a broadened pulse which is less sensitive to timing jitter, resulting in a better BER. The degradation after 450 km is probably caused by less dispersion compensation due to diminishing output power caused by saturation of the amplifier by ASE. By placing an additional ASE-filter at 450 km we expect to increase the maximum transmission distance at a $BER = 10^{-9}$. In contrary to NRZ transmission soliton transmission simulations did not reveal BER floors however. Figure 5 shows that the receiver sensitivity of the NRZ system at $BER = 10^{-9}$ in contrary to the soliton system is strongly dependent on the transmission distance due to built up ASE. Only after 450 km the soliton system shows a better sensitivity. When a BER of 10^{-12} is required, a soliton system is preferred when more than 350 km needs to be bridged.

V. CONCLUSION

A transmission model has been presented for simulation of NRZ and soliton systems. With respect to the simulated BER curves we expect soliton transmission to be superior to NRZ when long haul transmission systems beyond 450 km are considered. Timing jitter caused by soliton interaction and saturation of the QWLAs is expected to seriously degrade the performance of soliton transmission systems and therefore needs further investigation. The relatively complex transmitter makes NRZ systems preferable to soliton systems.

VI. ACKNOWLEDGEMENT

This article is part of the Ph.D. work of R.C.J. Smets which is supported by Philips Research Laboratories

and the Ph.D. work of J.G.L. Jennen which is supported by STW (Dutch Technology Foundation) in close cooperation with Philips Optoelectronic Centre.

REFERENCES

- [1] L.F. Tiemeijer, et al., "Polarization Insensitive Multiple Quantum Well Laser Amplifiers for the 1300 nm Window," *Applied Physics Letters*, vol. 8, pp. 826-828, February 1993.
- [2] L.F. Tiemeijer, et al., "33 dB Fiber to Fiber Gain +13 dBm Fiber Saturation Power Polarization Independent 1310 nm MQW Laser Amplifiers," in *Technical Digest Topical Meeting on Optical Amplifiers and Applications, Post-deadline*, pp. 1-5, June 1995.
- [3] L.F. Tiemeijer, *Optical Properties of Semiconductor Lasers and Laser Amplifiers for Fiber Optical Communication*. PhD thesis, Delft University of Technology, The Netherlands, December 1992.
- [4] J.G.L. Jennen et al., "Performance of Cascaded 1300 nm QW Laser Amplifiers in 10 Gbit/s Long Haul NRZ Transmission," in *Technical Digest Topical Meeting on Optical Amplifiers and Applications*, pp. 123-126, June 1995.
- [5] H. de Waardt, *High Capacity 1300 nanometer Optical Transmission*. PhD thesis, Delft University of Technology, The Netherlands, September 1995.
- [6] J.J.E. Reid, C.T.H.F. Liedenbaum et al., "Realisation of 20 Gbit/s Long Haul Soliton Transmission at 1300 nm on Standard Single Mode Optical Fibre," in *Proceedings 20th European Conference on Optical Communication / Post-deadline Papers*, pp. 61-64, September 1994.
- [7] G.P. Agrawal and N.A. Olsson, "Self-Phase Modulation and Spectral Broadening of Optical Pulses in Semiconductor Laser Amplifiers," *IEEE Journal of Quantum Electronics*, vol. 25, pp. 2297-2306, November 1989.
- [8] G.P. Agrawal and N.A. Olsson, "Amplification and Compression of Weak Pico Second Optical Pulses by Using Semiconductor-Laser Amplifiers," *Optics Letters*, vol. 14, pp. 500-502, May 1989.
- [9] G.P. Agrawal, *Nonlinear Fiber Optics*. Academic Press, Inc., 1989. ISBN 0-12-045140-9.
- [10] G.P. Agrawal and N.K. Dutta, *Long-Wavelength Semiconductor Lasers*. Van Nostrand Reinhold Company Inc., 1986. ISBN 0-442-20995-9.
- [11] N.A. Olsson, "Lightwave Systems with Optical Amplifiers," *IEEE Journal of Lightwave Technology*, vol. 7, pp. 1071-1082, July 1989.

114 km Repeaterless and 437 km Repeated, 10 Gbit/s Transmission at 1310 nm
Using an RZ Format

Robert C.J. Smets, Jean G.L. Jennen, Huug de Waardt,
Eindhoven University of Technology, Den Dolech 2, Eindhoven 5616 AZ, The Netherlands.

Bernd Teichmann, Claus Dorschky, Roland Seitz,
Lucent Technologies, Thurn-und Taxisstr. 10, Nürnberg 90411, Germany.

John J.E. Reid, Luuk F. Tiemeijer,
Philips Optoelectronics Centre, Prof. Holstlaan 4, Eindhoven 5656 AA, The Netherlands.

Andre J. Boot,
Royal PTT Nederland, KPN Research, P.O. Box 421, Leidschendam 2260 AK, The Netherlands.

Abstract

Both repeaterless and repeated, 10 Gbit/s, return to zero (RZ), optical transmission systems were investigated experimentally using the same receiver and laser source (1310 nm). Repeaterless transmission over a record 114 km of standard single mode fiber (SSMF) with an unprecedented maximum power budget of 45 dB at a bit error rate (BER) of 10^{-9} was achieved. An optimum receiver sensitivity of -33.8 dB was obtained due to the combination of good receiver characteristics and the performance of a polarization insensitive semiconductor optical amplifier. In the case of the repeated system we found that the maximum number of in-line amplifiers for error free operation was restricted to ten. The experimentally obtained maximum error free transmission distance was 437 km. Accumulation of in-band amplified spontaneous emission was found to cause this limitation.

Keywords

Pulse propagation and solitons, Semiconductor optical amplifiers, Optical communications.

Introduction

With the advent of optical amplification, some 100 million kilometers of already installed SSMF may be upgraded to higher bitrates for transmission over longer distances, particularly at 1300 nm where chromatic dispersion is minimal. Today, optical losses in the 1300 nm wavelength domain can be compensated for by means of optical amplification using either praseodymium-doped fluoride-fiber amplifiers (PDFAs), Raman amplifiers or semiconductor optical amplifiers (SOAs). Research has resulted in commercially available polarization insens-

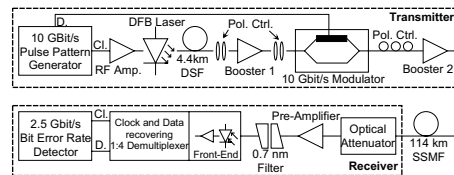


Figure 1. 114km Repeaterless transmission system setup

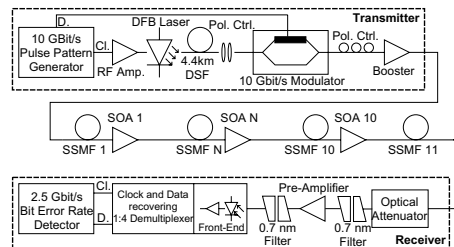


Figure 2. 437 km Repeated transmission system setup

itive, high gain, and high output power semiconductor optical amplifiers which are compact, less complex and far more power efficient than other proposed optical amplifiers for this window [1], [2].

In [3] 10 Gbit/s, non return to zero (NRZ) repeaterless transmission over 102 km was reported using a booster SOA, placed directly after the transmitter, and a polarization insensitive SOA, configured as a preamplifier to increase receiver sensitivity. Reference [4] describes 110.8 km transmission using a PDFa as a booster and an avalanche photo detector at the receiver. In this paper we investigate the transmission performance of a non repeated link using RZ data modulation

Table 1. Fiber and SOA parameters of each section. The fiber to fiber gain, G_{ff} , and the output power, P_{out} , is inclusive of isolator losses. The booster is denoted by B. Note that SOA 11 is preceded by an optical filter with an insertion loss of 2.7 dB.

N	Length [km]	Att. [dB]	Gff [dB]	Bias [mA]	Temp. [°C]	Pout [dBm]
B				350	17	+0.6
1	37.977	14.6	12.1	100	35	-1.9
2	38.339	14.0	12.8	130	35	-3.1
3	38.421	14.1	12.6	130	35	-4.6
4	38.370	14.7	15.0	160	35	-4.3
5	38.037	14.7	15.8	200	25	-3.2
6	38.460	14.0	13.5	200	25	-3.7
7	38.454	14.2	14.3	200	25	-3.6
8	38.352	14.5	16.3	200	25	-1.8
9	38.850	14.9	17.9	400	25	+2.8
10	38.480	15.6	14.2	400	25	+1.4
11	53.330	19.6				
		+2.7	18.6	350	31	-2.3

instead of NRZ.

At 2.5 Gbit/s, a 516 km link was bridged at 1550 nm by [5] using polarization sensitive SOAs. For each amplifier the input polarization had to be controlled. In [6] the use of polarization insensitive SOAs resulted in 420 km error free transmission at 10 Gbit/s using non gain-switched RZ pulses of 40 ps at full width half maximum (FWHM). The maximum number of in-line amplifiers was limited by the amplified spontaneous emission noise buildup. Here we describe a similar experiment with gain switched pulses of 18 ps at FWHM.

Prior to describing the experiments we give a short description of the multiple quantum well laser amplifiers (QWLAs) which we used as SOAs in the experiments. After the results and discussion section we will indicate what can be achieved with presently available SOAs today.

Multiple Quantum Well Laser Amplifiers

In the experiments we used two kinds of SOAs, polarization sensitive booster amplifiers and polarization insensitive amplifiers. Both types feature a multiple quantum well, angled stripe semi-insulating planar buried heterostructure.

The booster amplifier contains four InGaAsP compressively-strained quantum wells providing gain for TE polarized light. For this type of amplifier 17 dB fiber to fiber gain, 18 dBm fiber output power (3 dB gain saturation) and a fiber to fiber noise figure of 6 dB has been reported [2]. Due to a high saturation output power this device is used as a power booster before the data signal is launched into the SSMF.

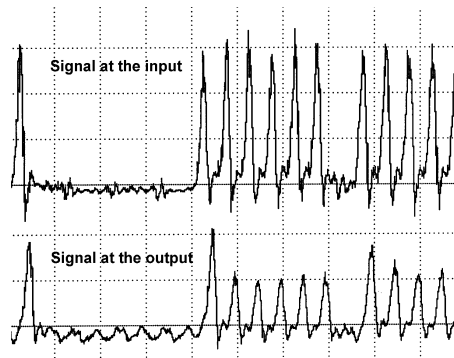


Figure 3. 10 Gbit/s data signal at the input and output of the 437 km cascaded amplifier link. The pulses at the output broadened slightly due to the dispersion of the last fiber section.

The polarization insensitive (< 0.5 dB) SOA contains an active layer composed of four compressively strained wells and three tensile strained wells, equally amplifying the TE- and TM-component of the incident light. The total fiber to fiber gain of this amplifier exceeds 30 dB, the 3 dB saturated fiber output power is better than 13 dBm and the fiber to fiber noise figure is better than 8 dB [1]. The latter device is used for both in-line amplification and preamplification prior to detection.

Experiments

Repeaterless System

Figure 1 depicts the repeaterless transmission system schematically. A DFB laser diode operating at 1310 nm was gain switched at 10 GHz to produce chirped RZ pulses of 30 ps at FWHM that were subsequently compressed to 18 ps at FWHM using 4.4 km of dispersion shifted fiber thus effectively removing the chirp. As gain switched pulses closely resemble soliton pulses we can expect these pulses to evolve to solitons within the fiber. After boosting the 10 GHz pulse train up to 10 dBm, the pulse train was modulated with a 10 Gbit/s, $2^{31}-1$ pseudo random bit sequence (PRBS) by the LiNbO₃ electro-optic modulator with an extinction ratio (ER) of 15 dB. Finally the signal is boosted up to 12 dBm and launched into 114 km of SSMF (zero dispersion at 1309 nm) with a total attenuation of 42.9 dB. The signal at the output did not show any pattern effects. A 400 mA bias current was applied to each of the two boosters. Booster 1 and 2 exhibited a fiber to fiber gain of 13.6 dB and 15.4 dB

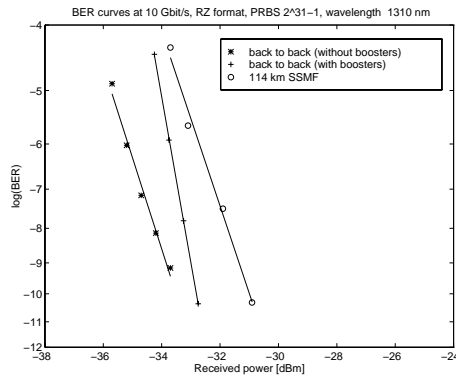


Figure 4. BER performance of the 114 km repeaterless system

and a 3 dB saturation output power of 16 dBm and 13 dBm, respectively.

In the optical front-end the optical RZ signal was converted into an electrical NRZ-like signal. After clock recovery and demultiplexing of the 10 Gbit/s NRZ signal into a 2.5 Gbit/s NRZ signal bit error rate curves were measured. The 10 Gbit/s BiCMOS clock and data recovering 1:4-demultiplexer is described in more detail in [7]. The receiver sensitivity without optical preamplification amounted to -17.3 dBm for a BER of 10^{-9} . A polarization insensitive SOA with 27.8 dB fiber to fiber gain including isolator losses and a noise figure of 8 dB was used to improve the sensitivity to -33.8 dBm for a BER of 10^{-9} . Prior to detection most of the amplified spontaneous emission (ASE) was suppressed using an optical band pass filter with 0.7 nm bandwidth and 2.7 dB insertion loss.

Repeatered System

Figure 2 shows the system setup of a repeatered system. In this case the transmitter contains only one booster and the receiver is equipped with an additional optical filter of 0.7 nm bandwidth and an insertion loss of 2.8 dB. The link contains ten sections of 38 km of SSMF followed by an optical amplifier. Finally the last amplifier is connected to 53 km of SSMF. The in-line amplifiers are of the same type as the preamplifier. Table 1 shows the exact length and attenuation of each fiber and the gain, bias current, temperature and output power of each SOA. The current and temperature were experimentally determined to give optimum signal to noise ratio at the output of each SOA taking into account that no significant pulse broadening should occur.

Figure 3 shows the signal at the input and output of the

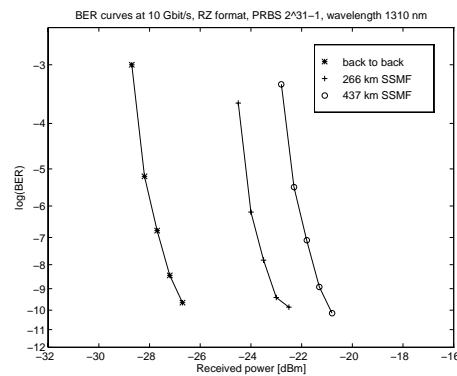


Figure 5. BER performance of the 437 km repeatered system

link. The slight pulse broadening that can be observed occurred in the last fiber section. After each amplifier output we measured the optical spectrum and we measured the bit error rate with the fiber of the next section installed. In the repeatered system a different preamplifier was used. This amplifier exhibited a poorer performance compared to the preamplifier in the repeaterless system. A 2.7 dB insertion loss of the second optical filter and a 3 dB penalty due to the badly performing preamplifier accounts for the difference of about 6 dB in the back-to-back receiver sensitivities of both systems.

Results and Discussion

Repeaterless System

Figure 4 shows the BER curves for the receiver sensitivity without booster amplifiers (*), back to back with booster amplifiers (+) and after insertion of 114 km SSMF (o). The introduction of the booster amplifiers resulted in a penalty of 0.8 dB for a BER of 10^{-9} due to extinction ratio degradation caused by the ASE contribution of both booster amplifiers. An optimum receiver sensitivity of -33.8 dBm has been obtained with a bias current of 170 mA for the preamplifier and without booster amplifiers [8]. It can be clearly seen that the penalty after 114 km of SSMF transmission is smaller than 1.7 dB at a BER of 10^{-9} and that no error floors are present. The 1.7 dB penalty might be explained by the non-ideal soliton character of the pulses. Due to fiber non-linearity, near soliton pulses launched into the 114 km SSMF evolve into solitons as they radiate dispersive waves containing non-soliton components. These waves deteriorate the extinction ratio and manifest themselves as an additional beat-noise source.

Repeatered System

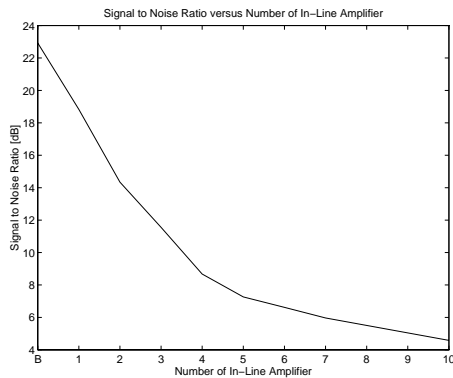


Figure 6. Signal to noise ratio degradation versus number of in-line amplifier. Spectral resolution of the optical spectrum analyzer was 2nm

Figure 5 shows the bit error rate performance back to back (*), after six in-line amplifiers (266 km of SSMF) (+) and after ten in-line amplifiers (437 km of SSMF) (o). After six sections we found a penalty of 4.1 dB and the penalty after 437 km amounted to 5.8 dB. The insertion of the eleventh in-line amplifier and an additional 25 km of fiber resulted in an optimum BER of $5 \cdot 10^{-10}$.

The penalty observed is caused by extinction ratio degradation due to pattern effects caused by saturation of the amplifiers and the buildup of ASE noise. Figure 6 depicts the signal to noise ratio versus the number of in-line amplifiers where we can see that the S/N ratio decreases rapidly. There are two reasons for this degradation. First, ASE accumulation results in a higher noise level and second, the peak wavelength of the saturated ASE spectrum shifts to higher wavelength due to wavelength dependent saturation. This means that less gain and output power is available for the remaining sections. Eventually error free transmission can no longer be achieved.

Conclusions

With respect to the point to point system we report to our knowledge the first successful repeaterless 10 Gbit/s, RZ transmission over a record 114 km at 1310 nm without in-line amplification. The unequalled power budget of 45.0 dB for the 1310 nm window has been enabled by the good receiver characteristics. In the case of the cascaded system we have found that a maximum of 10 in-line amplifiers can be cascaded without introducing errors and that the penalty is caused by in-band ASE accumulation. The maximum error free

transmission distance amounted 437 km which is just above the 420 km obtained by [6]. This work was performed within the framework of the European ACTS project UPGRADE and supported by the Dutch Technology Foundation (STW).

References

- [1] L.F. Tiemeijer, et al., "Polarization resolved, complete characterization of 1310 nm fiber pigtailed multiple-quantum-well optical amplifiers," *J. Light. Tech.*, Vol. 14, Iss. 6, June 1996, pp. 1524-33.
- [2] L.F. Tiemeijer, et al., "High-output-power (+15 dBm) unidirectional 1310-nm multiple-quantum-well booster amplifier module," *Phot. Tech. Lett.*, Vol. 7, No.12, December 1995, pp. 1519-21.
- [3] L.F. Tiemeijer, et al., "102 km 38.6 dB budget 10 Gbit/s NRZ Repeaterless Transmission at 1310 nm using Semiconductor Booster Amplifier Module and a Semiconductor Preamplifier Module," in *Proceedings Volume 1 of the European Conference on Optical Communication 1995* (IMEC, Gent, 1995), pp. 275-8.
- [4] M. Shimizu, ed., "Highpower, low-noise praseodymium-doped fluoride-fiber amplifiers," in *Technical Digest of the Conference on Optical Fiber Communications 1995* (Optical Society of America, Washington DC, 1995), pp. 110-1.
- [5] S. Yamamoto, et al., "516 km, 2.4 Gbit/s Optical Fiber Transmission Experiment using 10 Semiconductor Laser Amplifiers and Measurement of Jitter Accumulation," in *Technical Digest Volume 5 of the Conference on Integrated Optics and Optical Fiber Communication 1989* (Optical Society of America, Washington DC, 1989), paper 20PDA-9.
- [6] P.I. Kuindersma, et al., "10 Gbit/s RZ Transmission at 1309 nm Over 420 km Using a Chain of Multiple Quantum Well Semiconductor Optical Amplifier Modules at 38 km Intervals," in *Proceedings Volume 2 of the European Conference on Optical Communication 1996* (Telenor R&D, Kjeller, 1996), pp. 165-8.
- [7] J.Hauenschild, et al., "A 10 Gbit/s BiCMOS clock and data recovering 1:4-demultiplexer in a standard plastic package with external VCO," in *Digest of Technical Papers of the 1996 IEEE International Solid-State Circuits Conference* (IEEE, New York, 1996), pp. 202-204.
- [8] B. Mikkelsen, et al., "High performance semiconductor optical amplifiers as in-line and pre-amplifiers," in *Proceedings Volume 2 of the European Conference on Optcial Communication 1994* (Istituto Internazionale delle Comunicazioni, Genova, 1994), pp. 709-13.

4.3 Distributed Raman amplification

In addition to semiconductor optical amplification, Raman amplification has always been an option for compensation of losses in optical fibre. The availability of high output power pump lasers at $\lambda = 1.24 \mu\text{m}$ [5] allowed practical implementation of these lasers into a Raman fibre amplifier [6]. Figure 4.1 displays the geometry of the distributed Raman amplifier. The

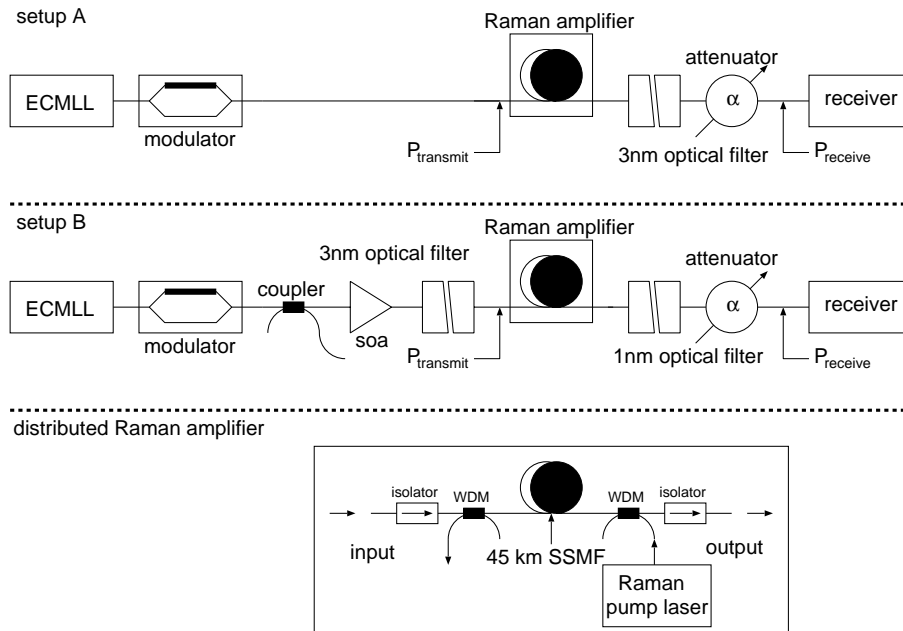


Figure 4.1: Setup A: implementation of a 45 km distributed Raman amplifier excited by $P_{transmit} = -12.7 \text{ dBm}$ low input power. Setup B: excitation of a Raman amplifier with $P_{transmit} = 1.6 \text{ dBm}$ high input power signal. The Raman amplifier is pumped in the counter-propagating direction of the signal.

Raman pump laser operates at $1.24 \mu\text{m}$ and delivers a maximum of 1.3 W into the 45 km of standard single-mode fibre via a WDM coupler. In this way 27 dB of optical gain at $\lambda = 1300 - 1310 \text{ nm}$ is achieved, where the gain compensates the 19 dB loss of the fibre, WDM couplers and isolators. An excess gain of 8 dB remains. Reduction of the pump power to $\approx 700 \text{ mW}$ eliminates the excess gain. Two transmission experiments have been conducted. In the first experiment the input of the distributed Raman amplifier is connected directly to the output of the modulator (see Fig. 4.1, setup A). A -12.7 dBm strong 10 Gb/s data signal ($P_{transmit}$) is launched into the 45 km of SSMF. A 3 nm broad optical band-pass filter removes possible reflections of the pump. Subsequently the signal is attenuated, detected and tested for errors. Figure 4.2 summarises the bit error rate performance graphically. The introduction of 45 km of SSMF with Raman gain has had no influence on the performance of the system. Error free performance is demonstrated over 45 km of lossless fibre. The second

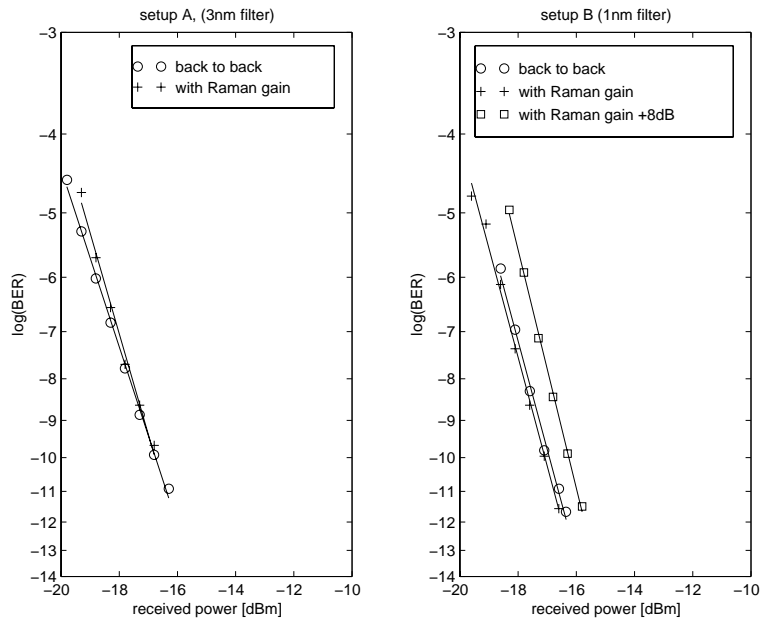


Figure 4.2: BER performance of measurement setups A and B

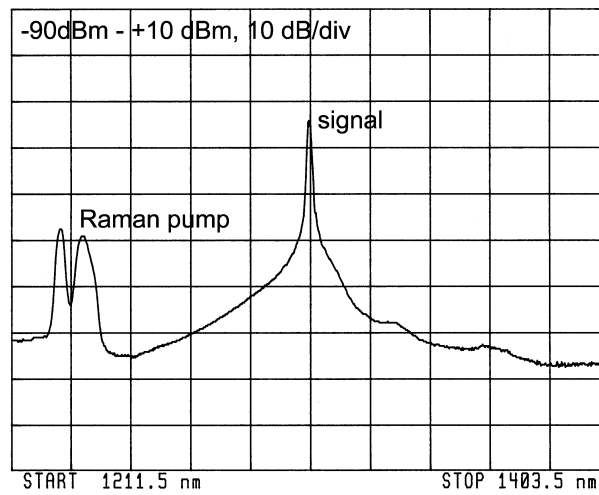


Figure 4.3: Spectrum of the Raman pump and the 10 Gb/s signal. The spectrum is measured with a co-propagating pump.

experiment involves a semiconductor optical amplifier which increases the input power of the distributed Raman amplifier to 1.6 dB. A 1 nm broad optical band-pass filter is placed after the Raman amplifier (a 3 nm broad filter is preferred but was not available). Bit error rate curves are measured for three different conditions: back to back, with 45 km of transparent optical fibre inserted and with 45 km of SSMF with 8 dB excess gain. The BER curves are plotted in Fig. 4.2 and display a slight improvement between the back to back curve and the curve measured after 45 km of transparent SSMF. Introduction of 8 dB of excess gain causes a penalty of ≈ 0.7 dB. This power penalty is likely to have been caused by self-phase modulation in the optical fibre. The pulse width of the optical pulses was reduced from 2.4 ps to 1.7 ps while the optical spectrum broadened proportionally to a point where the 1 nm broad filter distorts the data signal and BER performance deteriorates. In addition, no power penalties occur if the gain is set to solely compensate the fibre losses. Compensation of fibre losses is independent of the amount of input power to the link. Figure 4.3 displays the spectrum of the data signal and the Raman pump power. The data signal absorbs power from the pump signal at a wavelength which lies ≈ 80 nm below the wavelength of the data signal. The spectrum of the pump power is wide enough to support signals of higher bit rates. These experiments prove the applicability of in line distributed Raman amplification for long-haul RZ transmission.

4.4 Wavelength and input power dependent transmission

4.4.1 Introduction

In Secs. 4.1 and 4.2 the performance of the systems is limited by extinction ratio degradation caused by gain saturation of the SOAs. For a given wavelength of operation and transmitted power, the in-line SOAs were adjusted to provide a maximum transmission distance of 437 km that was bridged error free. These experiments, together with early experiments conducted within the European ACTS project “Upgrade”, provided disenchanting results with respect to the performance of the investigated transmission systems. In these experiments pulses in the order of 40 ps were used. The depressed cladding SSMF fibre has a zero-dispersion point at 1305 nm and a dispersion slope of $0.1 \text{ ps}/(\text{nm}^2 \cdot \text{km})$. Initially dispersion was thought to be the limiting factor but it turned out that amplified spontaneous emission caused deterioration of performance. These early experiments were conducted with 800 μm long high gain amplifiers. These amplifiers saturate easily, especially for high input powers. In Chapter 5 of this thesis ≥ 200 km, 40 Gb/s transmission experiments are conducted. For these experiments an external cavity mode-locked tuneable laser source is used (see Sec. 3.1.2). This source produces pulses with pulse widths lying between 2.5 and 4 ps. The objective of the experiments conducted in this section was to investigate the possible applicability of the 800 μm long isolated polarisation insensitive MQW SOAs in the 40 Gb/s transmission line. 10 Gb/s transmission experiments are performed for different wavelengths and input powers to the periodically amplified link. In addition, bit error rate performance, pulse broadening, optical spectral and temporal behaviour are measured as a function of transmitted distance. The pulse shape of the 10 Gb/s signal is the same as the pulse shape of the 40 Gb/s signal, as treated in Chapter 5. Recommendations are made on possible changes in

system geometry and components for improved transmission at 40 Gb/s. [7]

4.4.2 Experimental setup

Figure 4.4 displays the experimental setup with four sections of 50 km of SSMF. The tunable pulse source generates 10 GHz pulse trains at one of the five wavelengths: 1302.6 nm, 1304.9 nm, 1307.2 nm, 1309.4 nm and 1311.3 nm. These optical pulse trains pass the polarisation controller which matches the state of polarisation to the state required by the modulator. In this experiment the optical modulator imposes a $2^{23} - 1$ PRBS data pattern on these pulses for bit error rate measurements and a $2^7 - 1$ PRBS pattern for measuring the temporal envelope of the signal along the link. A second polarisation controller matches the polarisation of the optical signal to the booster amplifier where the signal is amplified to a level of 1 dBm. The maximum power that is to be launched into the four cascaded fibre-amplifier sections has been set to +3 dBm. To achieve this the signal is attenuated and amplified by SOA-1 to a level of +5 dBm. A second attenuator allows the link input power, $P_{transmit}$, to be set to either +3dBm, 0 dBm, -3 dBm or -6 dBm. The 200 km transmission link consists of four sections of 50 km of SSMF and four polarisation insensitive MQW SOAs to compensate for the fibre losses. SOA-5 is the heart of the optically preamplified receiver. After transmission of a multiple of 50 km of fibre the line signal is attenuated by attenuator-3 after which a band-pass filter removes the accumulated outband ASE. SOA-5 amplifies this signal. A second band-pass filter removes the outband ASE added by SOA-5. Via attenuator-4 the preamplified line signal is guided into the 10 Gb/s receiver. The signal power at the output of attenuator-3 is the received power, $P_{receive}$, for which the BER at the 2.5 Gb/s output of the receiver is measured. The input of attenuator-3 can also be connected to fibre-3, -2 and -1 so that the system performance is measured after 150 km, 100 km and 50 km, respectively. Back to back BER curves are measured once the input of attenuator-3 is connected to the

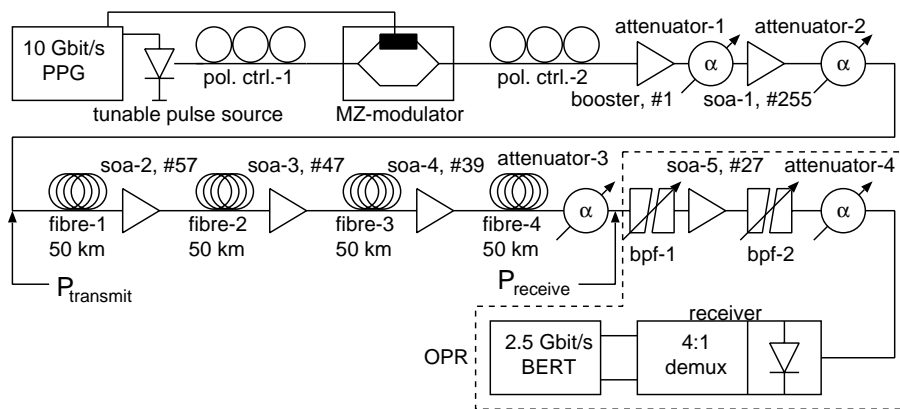


Figure 4.4: Experimental setup of the 200 km transmission system. The setup is configured for BER measurements using an optically pre-amplified receiver (OPR). Optical spectra, autocorrelation traces and temporal envelopes can also be measured for different input powers and distances.

output of attenuator-2, i.e. without fibre. In addition to BER measurements, autocorrelation traces were measured using a lithiumniobate based background-free intensity autocorrelator. From these curves the full-width half-maximum widths are determined which provide insight into the amount of pulse broadening. Optical spectra are measured to give an indication as to whether the pulse narrowing or broadening is amplifier-chirp induced or adiabatic via the SPM in the fibre. A 45 GHz photodiode connected to a 50 GHz digital-sampling oscilloscope provides limited-time resolution envelope measurements of the optical line signal. All SOAs except SOA-1 are 800 μm long and are driven by 400 mA. SOA-1 is 400 μm long and is pumped at 200 mA. The temperature of the SOAs is set to 20°C. After each section of fibre the BER curves, autocorrelation traces, optical spectra and temporal envelopes of the received signal are measured for each one of the five wavelengths and for the four different link input powers, $P_{transmit}$.

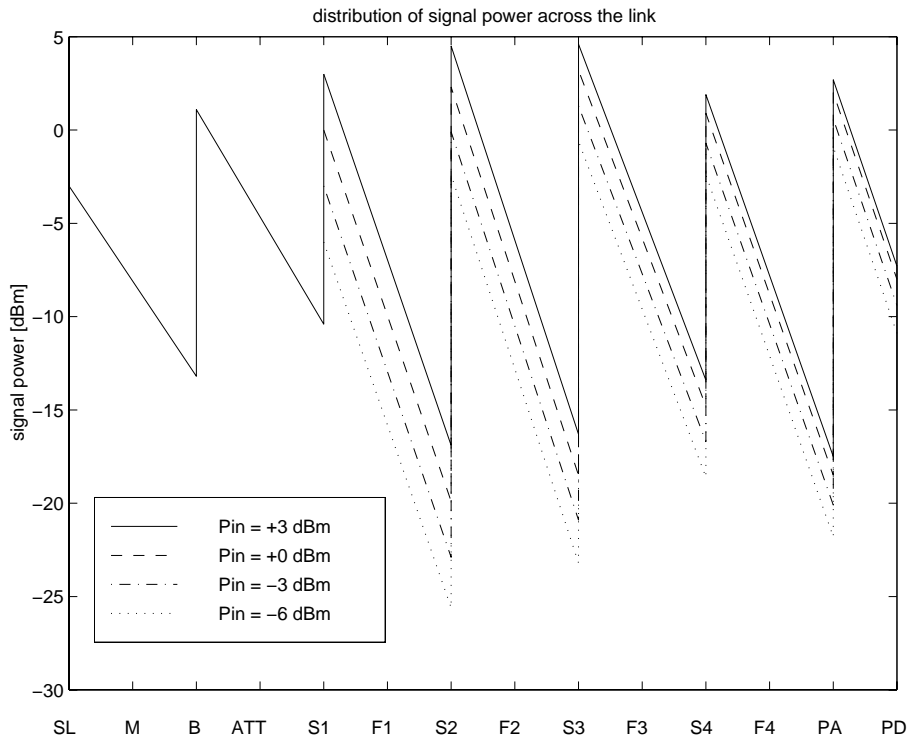


Figure 4.5: Power map of the 200 km experiment. SL stands for the soliton laser, the source, M is the modulator, B is the booster amplifier and ATT stands for attenuator-1. Fibre-X is denoted by FX and SOA-Y is denoted by SY. PA and PD indicate the pre-amplifier and photodiode of the receiver. The power map has been measured at $\lambda = 1307.2$ nm and for four different link-input powers.

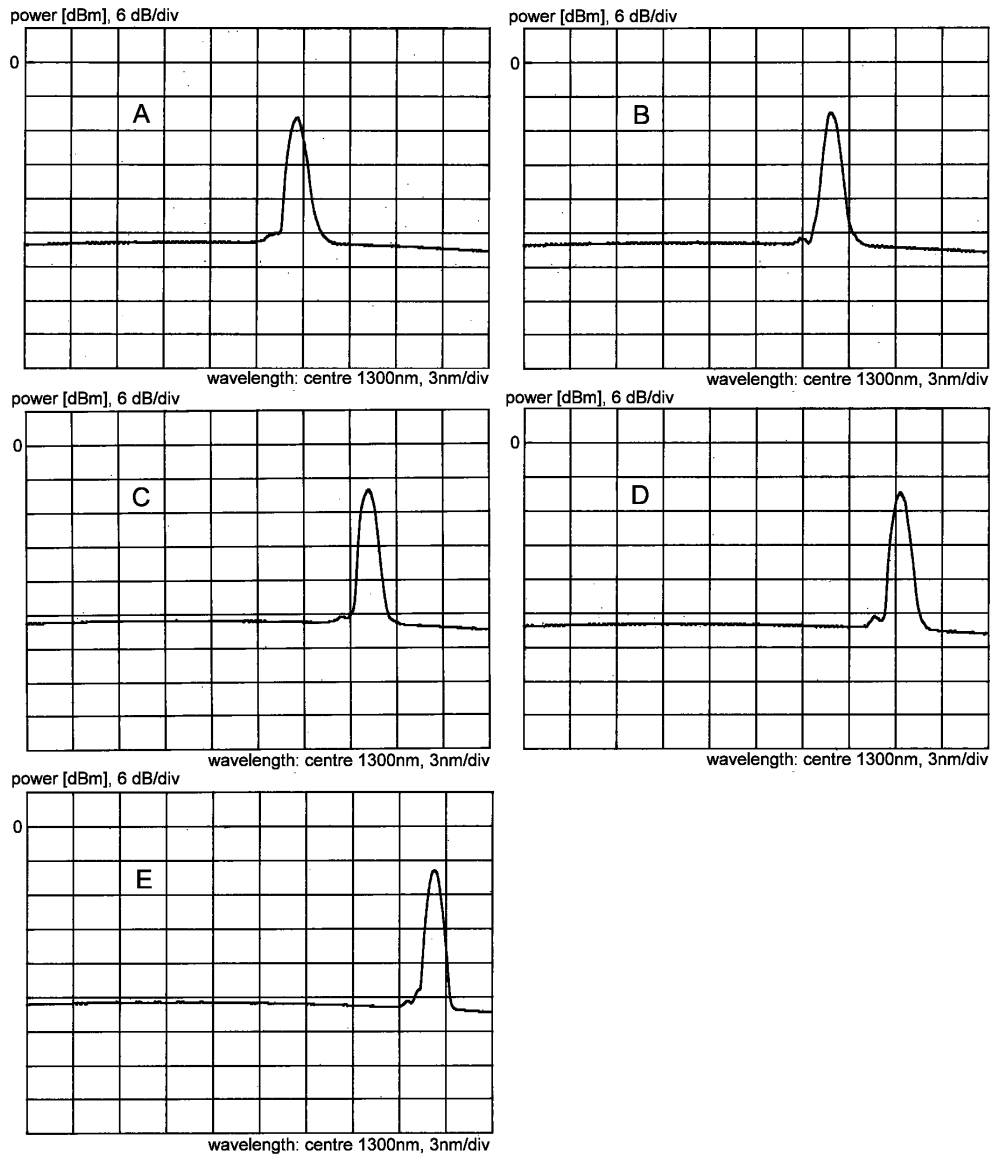


Figure 4.6: Optical spectra for the five different wavelengths at 0 km. Subplots A, B, C, D and E correspond to the 1302.6 nm, 1304.9 nm, 1307.2 nm, 1309.4 nm and 1311.3 nm channels, respectively.

4.4.3 Experimental results and interpretation

Figure 4.5 displays the power distribution across the link for different link input powers. At point S1 (0 km) the differences between $P_{transmit}$ amount to 3 dB. At 200 km these dif-

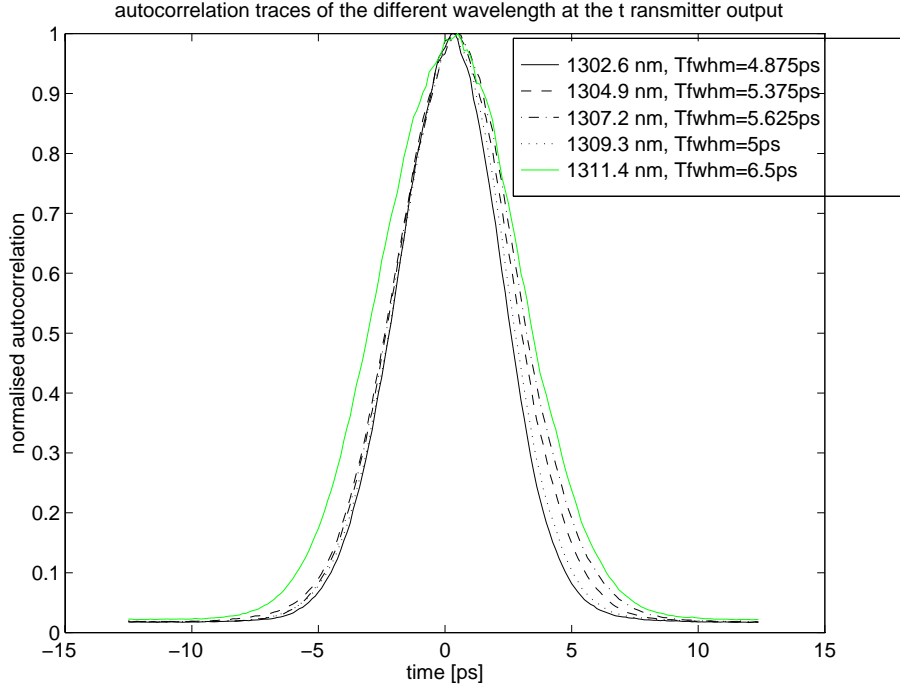


Figure 4.7: Back to back autocorrelation traces. The transmitted pulses are narrow compared to the 100 ps bit time. At longer wavelengths the pulses are slightly broader. This is due to differences in DC bias of the pulse source. The values displayed in the frame are the full-widths half-maximum times of the autocorrelation traces.

ferences have gradually decreased to 0.7 dB for the highest input powers and 1.5 dB for the lowest input powers. If the average loss of 21 dB per section and the average unsaturated gain of more than 24 dB per section is taken into account, it is evident that the SOAs are heavily saturated for all four input powers after 200 km of transmission. Figure 4.6 displays the spectra of all five wavelengths at the input of the link. At this point the pulses are already chirped by gain saturation of SOA-1. Without dispersion this will not be of great influence to the temporal envelope of the line signal. All spectra appear as non distorted. Figure 4.7 displays the autocorrelation traces of the five wavelengths at the output of the transmitter. The width of the traces is proportional to the actual width of the pulses. The factor of proportionality depends on the shape of the pulses that enter the autocorrelator. In the case of soliton shaped pulses the relation between the width of the autocorrelation trace and the width of the soliton equals

$$\tau_{fwhm,soliton,R_{xx}} = 1.5428 \cdot \tau_{fwhm,soliton}. \quad (4.1)$$

According to Fig. 4.7 all of the pulses are approximately of the same width. Figure 4.8 displays the temporal behaviour of the middle channel of a $2^7 - 1$ PRBS pattern. The ringing indicates that the pulses are narrower than the limiting 12 ps full-width half-maximum time of

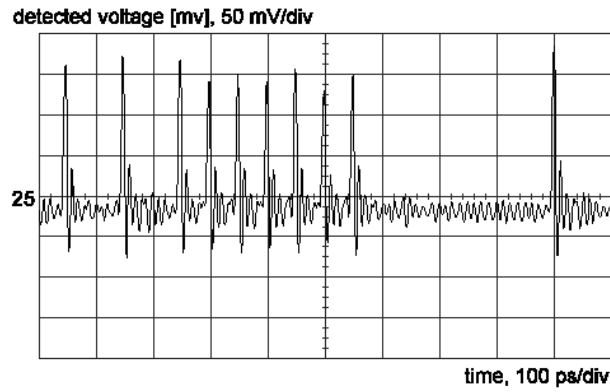


Figure 4.8: Temporal envelope of the 1307.2 nm channel. The “01010111111000000100” sequence from the $2^7 - 1$ PRBS pattern is clearly visible.

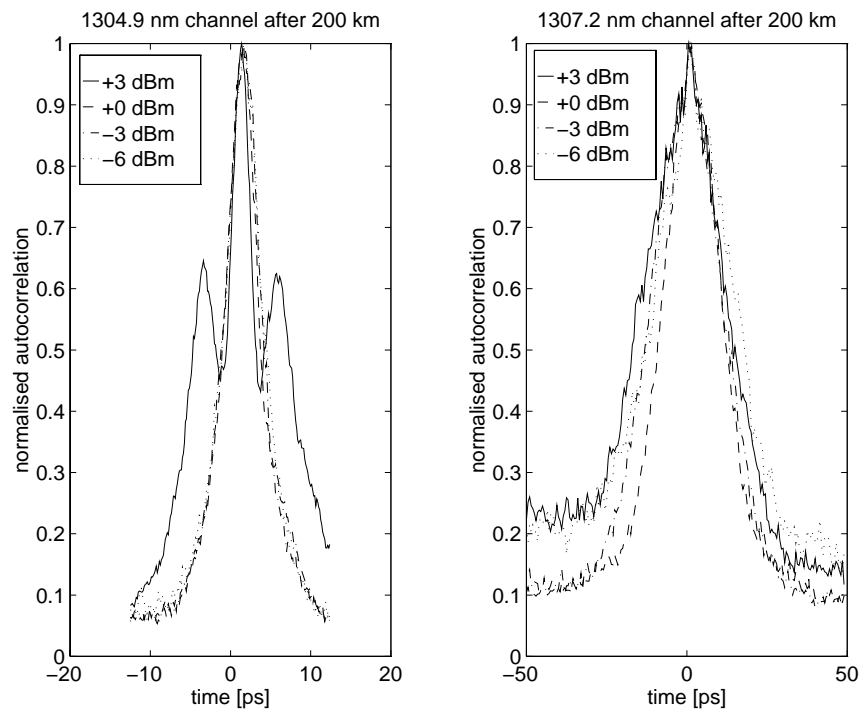


Figure 4.9: Autocorrelation traces after 200 km

the photodetector. This is in correspondence with the autocorrelation traces. The interaction of the optical pulses with the SOAs and optical fibres can be interpreted from observations

of the autocorrelation traces, power density spectra, temporal responses and bit error rates. For example, if pulse narrowing occurs (this can be measured with an autocorrelator) and the optical spectrum broadens (this can be determined from the optical power density spectrum) then SOA induced chirp is not likely to influence the interaction between dispersion and the fibre nonlinearity. In this example, if a BER measurement reveals a power penalty then ASE build up is the most likely cause of system degradation. The emphasis in this experiment does not lie in the optimisation of the link to obtain a record performance. It lies in understanding whether the 800 μm long, high-gain, SOAs are suitable for 200 km transmission at 40 Gb/s, knowing that more power is needed for 40 Gb/s transmission while the saturation output power of the SOAs remains unchanged. Therefore no system parameters are optimised or re-adjusted. From the measured BER curves the receiver sensitivity at a BER of 10^{-9} is computed for the different input powers and wavelengths of operation. The autocorrelation traces depicted in Fig. 4.9 show that around zero dispersion ($\lambda_D = 1305$ nm) pedestals have grown once the transmitted power exceeds 0 dB. In the case of lower input powers the autocorrelation traces do not deviate from normally expected behaviour. In contrary to the absence of abnormalities in the autocorrelation traces, the optical spectra, depicted in Fig. 4.10, show input power dependent distortion. For both channels (1304.9 nm and 1307.2 nm) dispersion is minimal. Therefore four wave mixing is likely to cause the “breaking up” of the spectrum. The power map (Fig. 4.5) shows that at certain points along the link the power increases to levels of $\approx +5$ dBm which strongly supports fibre nonlinearities such as self-phase modulation and four wave mixing.

Figure 4.11 displays the signal response after 200 km with +3 dBm link input power. Significant pulse broadening is visible. The 1302.6 nm channel lies in the normal dispersion regime. In the case of anomalous dispersion (1309.4 nm channel) pulse broadening occurs. For wavelengths that lie close to the zero dispersion point the detector response is distorted by ringing effects; though in the case of the 1307.2 nm channel an anomaly can be seen at the trailing edges. The ringing seems to be inverted which could indicate a second optical pulse close to the main pulse. This pulse does not appear on the autocorrelation trace because the time scales do not correspond. The leading edges of the 1307.2 nm and 1309.4 nm channels (anomalous dispersion) show also an anomaly which manifests most clearly at the leading edge of the last pulse in subplot D of Fig. 4.11. Due to the amplification process the leading edge of the pulse envelope becomes “blue” chirped which propagates faster in the anomalous dispersion regime and becomes separated from the pulse. In the normal dispersion regime the leading edge has become steeper. The “blue” chirped parts of the pulse envelope travel slower than the non-chirped parts and travel to the center of the pulse where they increase the power around the peak of the pulse. This results in increased SPM which in turn causes pulse broadening (normal dispersion regime of the fibre). The chaotic shapes of the optical spectra do support the existence of these small pulses. In addition, a small irregularity is also present at the foot of the leading edges and is also visible at 1309.4 nm. Figure 4.12 summarises the broadening of the pulses as a function of wavelength for different link input powers and transmission distances.

Generally, it is not possible to separate the amplifier nonlinearity from the fibre nonlinearity as they both affect the optical spectrum and require interaction with dispersion before they become visible in the time domain. The system that is investigated uses amplifiers with more gain than is needed for the compensation of optical losses. If the optical input signal is too

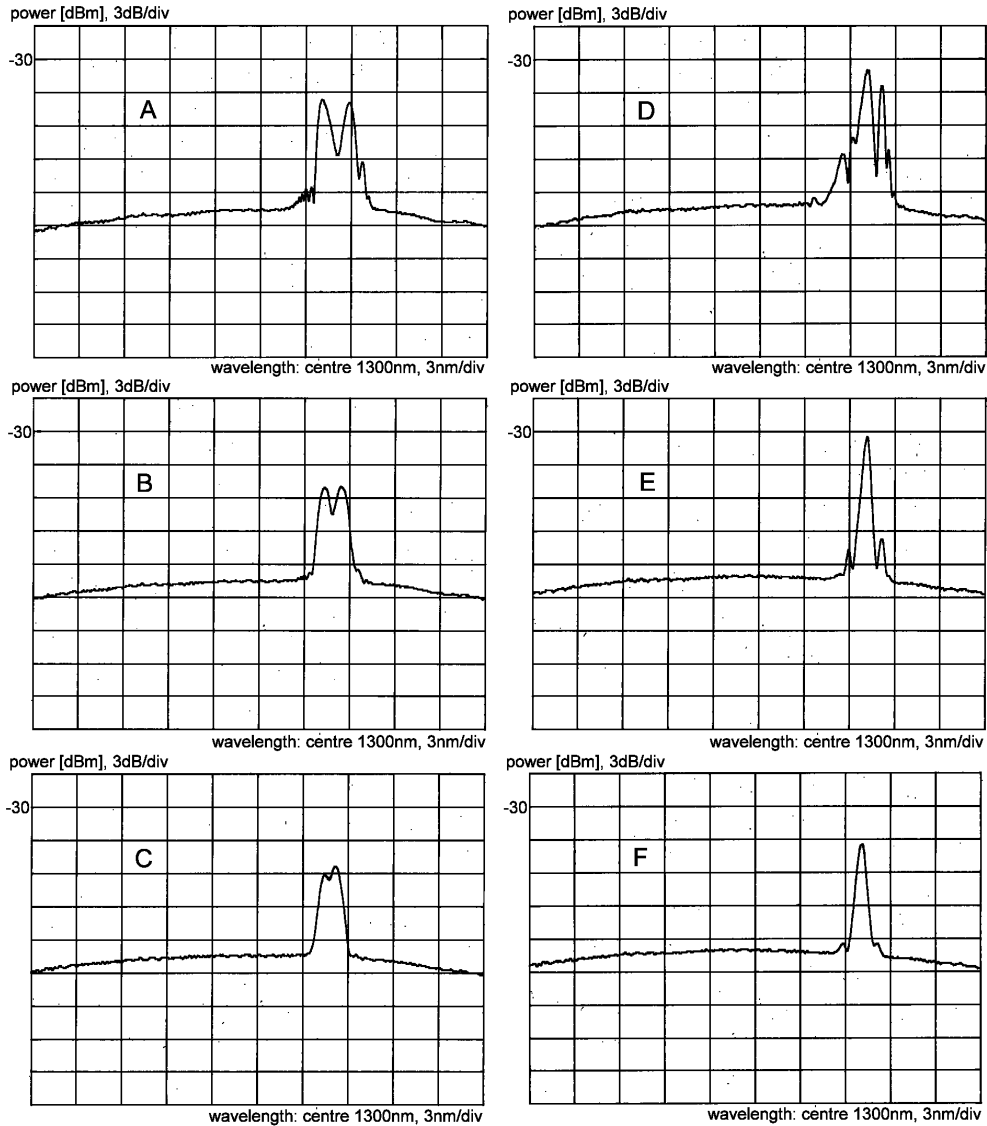


Figure 4.10: Optical spectra of the 1304.9 nm channel for link input powers of +3, 0 and -3 dBm depicted in A, B and C, respectively and for 1307.2 nm for the same powers as in D, E and F, respectively.

small outband ASE build up causes the saturation of the amplifier instead of the optical signal. Higher input powers will therefore reduce the ASE build up but will cause severe pulse shape distortion (pattern effects) and phase modulation (chirp) on the signal due to self-phase modulation in the saturable SOAs. This chirp manifests itself as amplitude distortions once

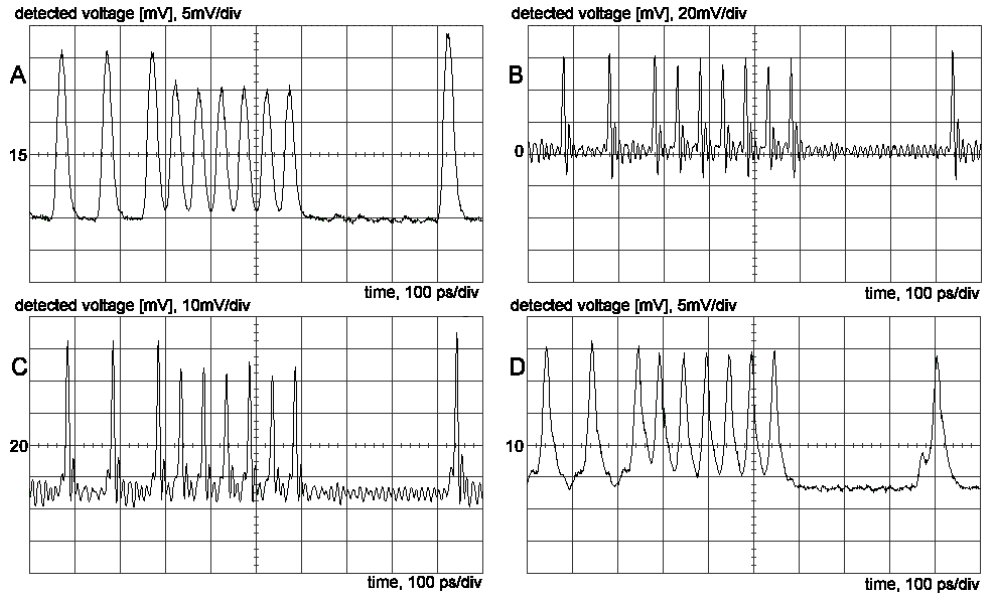


Figure 4.11: Temporal envelope of the 1302.6 nm, 1304.9 nm 1307.2 nm and 1309.4 nm channel after 200 km for +3 dBm link input power (subplot A, B, C and D, respectively).

it interacts with dispersion in the optical fibre. Possible reduction of the drive current of the amplifier reduces the gain and the amount of ASE. However, with the decrease of pump current the saturation energy of the amplifier decreases which detrimentally influences system performance. Figure 4.13 displays the receiver sensitivity of the system as a function of distance for different wavelengths and link input powers. These values are obtained by interpolation of measured BER versus received power curves. Increase of input power from 0 dBm to +3 dBm does not result in improvement of the receiver sensitivity after 200 km. Although significant pulse broadening occurs (Fig. 4.12) the 1302.6 nm channel shows unexpectedly good performance (Fig. 4.13). Together with the 1307.2 nm channel the full 200 km link is bridged for link input powers between -3 dBm and +3 dBm. The 1304.9 nm channel does not reach the 200 km error free. Transmission at 1307.2 nm gives rise to the formation of a second optical pulse near the leading and to a lesser extent near the trailing edges. The position of this pulse can be responsible for increased “eye-closure” or “eye-opening” at the input of the decision circuit in the data recovery circuit of the receiver. Consequently the receiver sensitivity will degrade for an “eye-closure” or improve for increased “eye-opening”. This explains why the BER curves make a rather unpredictable first impression.

4.4.4 Conclusions and recommendations

The main conclusion is that this transmission link performs unsatisfactorily because it is not possible to obtain error free transmission and maintain pulse widths that agrees with pulse widths needed for 40 Gb/s transmission (≤ 8 ps). The causes lie in the high gain of the

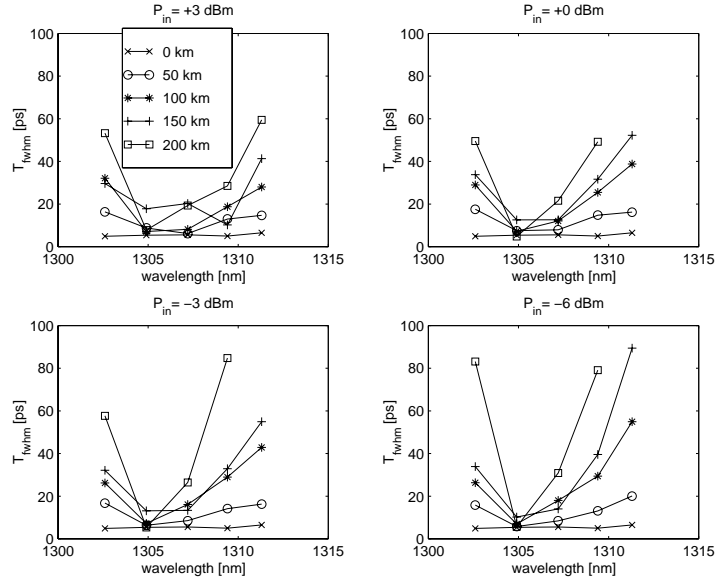


Figure 4.12: Width of the autocorrelation traces as a function of wavelength for different transmission lengths and different link input powers.

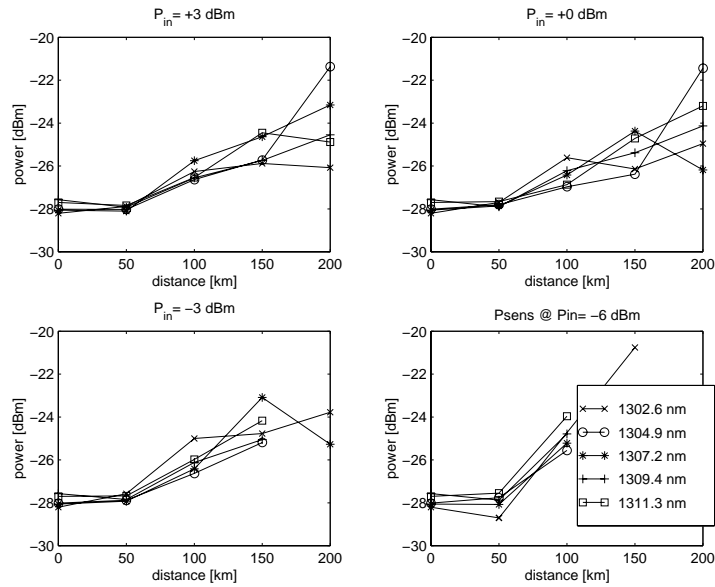


Figure 4.13: Receiver sensitivity at a BER of 10^{-9} as a function of transmitted distance for different wavelengths and different link input powers.

amplifiers resulting in either distorted pulses or in too much ASE. Transmission around the zero dispersion point is only possible if the link input power is kept low to reduce nonlinearities. Soliton transmission is not supported in this configuration because amplifier-induced phase modulation distorts the uniform phase of the soliton. If 40 Gb/s transmission is to be performed successfully, smaller sections of fibre must be used, the pulse energy should be lower (especially if the link is operated close to the zero dispersion point) and an amplifier with less gain and a higher saturation energy must be used. Shorter amplifiers will exhibit improved saturation output power under low-gain conditions. Further investigation could provide more insight into possible reduction of FWM by amplifier-induced phase modulation.

References

- [1] R.C.J. Smets and J.G.L. Jennen. 10 Gbit/s long haul soliton versus NRZ optical transmission in the 1300 nm window. In Proceedings of the IEEE Third Symposium on Communications and Vehicular Technology in the Benelux, pages 187–190, 1995.
 - [2] R.C.J. Smets, J.G.L. Jennen, et al. 114 km, repeaterless, 10 Gbit/s transmission at 1310 nm using an RZ data format. In Technical Digest of the OFC'97, Dallas, volume 6, pages 114–115, 1997.
 - [3] R.C.J. Smets, J.G.L. Jennen, et al. 114 km repeaterless and 437 km repeatered, 10 Gb/s transmission at 1310 nm using an RZ format. In Trends in Optics and Photonics Series, System Technologies, volume 12, pages 416–419. Optical Society of America, 1997.
 - [4] S.V. Chernikov, M.J. Guy, D.V. Gapontsev, J.R. Taylor, R.C.J. Smets, J.G.L. Jennen, H. de Waardt, et al. 10 Gbit/s error free transmission of 2 ps pulses over a 45 km span using distributed raman amplification at 1300 nm. In Technical Digest, OFC'98, San Jose, pages 31–32, 1998.
 - [5] S.V. Chernikov, J.R. Taylor, et al. High-power, compact, high-efficiency, fiber laser source around $1.24\mu\text{m}$ for pumping Raman amplifiers. In Technical Digest, OFC'97, Dallas, page 345, 1997.
 - [6] J. Reid, M. Tamburrini, H. de Waardt, R. Smets, S. Chernikov, et al. Final report on devices for all-optical multiplexing and demultiplexing, all-optical functionality at in-line nodes and raman amplification. “Upgrade” Deliverable D4131 AC045-uni-jjr-DS-P-029-b1, European Commission, Advanced Communications Technologies & Services, Brussels, Belgium, 1998.
 - [7] J. Reid, H. de Waardt, R. Smets, et al. Final report on the suitability of optical soliton transmission for high bitrate data transport in the european network. “Upgrade” Deliverable D4231 AC045-eut-hdw-DS-P-030-b1, European Commission, Advanced Communications Technologies & Services, Brussels, Belgium, 1998.
-

Chapter 5

All-optical signal processing systems

This chapter deals with the physical implementation of a number of all-optical signal processing circuits. More specifically, optical switches based on the TOAD configuration, [1] and [2], employing MQW SOAs have been realised, tested and integrated as a part of an all-optical time-domain multiplexed transmission system. To this end, additional pulse sources need to be realised. They supply the all-optical switch with a continuous stream of narrow optical pulses. Section 5.1 describes a jitter free source that has been designed for 10 Gb/s down to 2.5 Gb/s demultiplexing experiments which are treated in Sec. 5.3. The 10 Gb/s to 2.5 Gb/s demultiplexing experiment was performed to gain more insight into the operation and performance of the all-optical time-domain demultiplexer. Section 5.4 deals with an equivalent configuration for the demultiplexing of a 40 Gb/s to a 10 Gb/s signal. A transmission experiment with all-optical demultiplexing requires a clock recovery circuit in order to obtain synchronisation with the incoming data signal. Section 5.2 treats a 10 Gb/s all-optical clock recovery circuit that provides narrow optical switch pulses for the optical switch. This optical demultiplexer with optical clock recovery is implemented in a 216 km transmission system (Sec. 5.5). Finally all-optical signal regeneration is demonstrated in Sec. 5.6. In Chapter 2 the channel extinction ratio was introduced as a quantitative measure for the performance of the optical switch. In this chapter where the optical switch is investigated experimentally it is not possible to measure this channel extinction ratio due to the limited resolution in the time domain of measurement equipment. Therefore bit error rate (BER) measurements are used for the determination of the performance of this all-OTDM based (transmission) system.

5.1 All-optical cross gain-switched ring laser

5.1.1 Introduction

Before 10 Gb/s to 2.5 Gb/s demultiplexing experiments can be conducted, a 10 Gb/s signal is required and a 2.5 GHz pulse train must be generated which acts as the eventual switch signal. The 10 Gb/s signal is generated using the DFB laser diode, dispersion-shifted fibre and an external modulator as described in Chapter 3. Chapter 2 showed theoretically how fast the channel extinction ratio decreases when switch pulses broaden. Therefore it is important

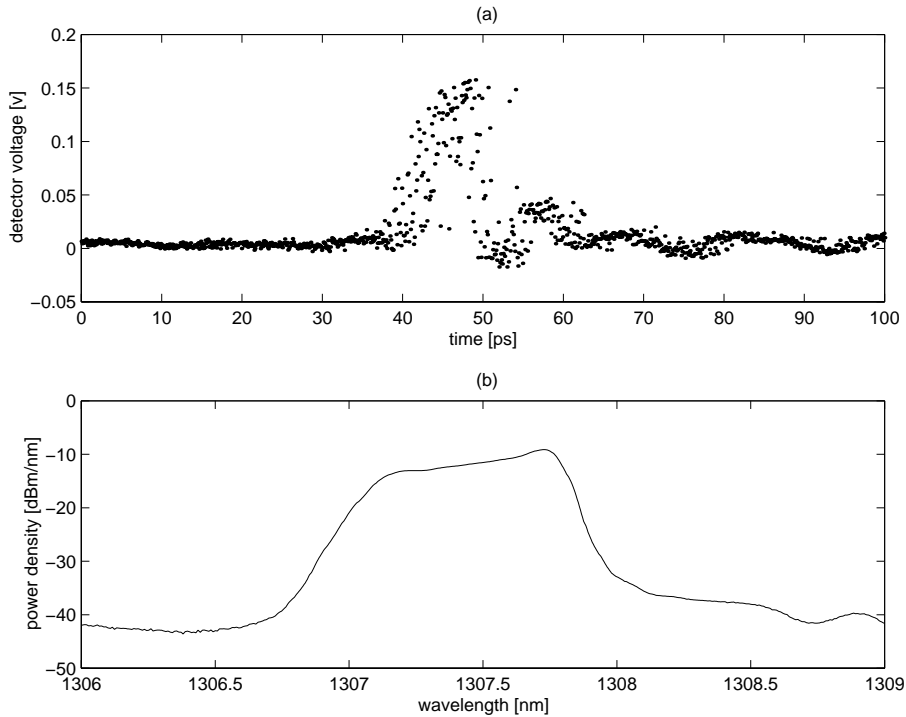


Figure 5.1: (a) Temporal response of a 2.5 GHz gain-switched DFB laser diode after 4.4 km of DSF. (b) The corresponding optical spectrum (0.05 nm resolution bandwidth). $I_{bias,DC} = 35$ mA, $I_{bias,AC} = 80$ mA_{pp}

to use switch pulses that are as narrow as possible or at least as narrow as the pulses of the signal to be demultiplexed. The rise and fall times of the edges of the temporal window that is formed by the optical demultiplexer strongly depend on the width of the optical switch pulses (see Sec. 2.5.2). If a DFB laser diode is used to obtain 20 ps wide pulses at a repetition rate of 2.5 GHz the laser diode must be switched off for about 95 % of the 400 ps period. Figure 5.1 (a) displays the temporal response of the output of a 2.5 GHz sinusoidally modulated DFB laser diode that is operated below threshold, i.e. gain-switched. Subplot (b) depicts the optical spectrum. The spectrum clearly displays chirp that is caused by variations in carrier density during the process of on and off switching. The time jitter, ≈ 10 ps, that is visible in Fig. 5.1 is of the same order as the pulse width. In addition to the time jitter, the laser diode may occasionally omit the generation of a pulse if the carrier inversion induced by the bias current and the modulation current does not result in a roundtrip gain larger than one. This was also observed in a pulse train generation experiment (Sec. 3.1.1) where the laser diode was biased below threshold and modulated by a 10 GHz sine wave. Instead of a 10 GHz pulse train a 5 GHz pulse train was observed (the temporal envelope is not displayed). If this occurs in a demultiplexing configuration the optical switch will not open and certain bits shall not appear at the output. Consequently, the performance of an on this source based demultiplexer

was far from ideal as its bit error rate performance was limited by a $\text{BER} \leq 10^{-7}$. A different type of source must be utilised. Section 5.1.2 elaborates theoretically on the origin of this time jitter and shows that internal feedback and external modulation of the optical gain medium by an optical field is able to reduce time jitter.

5.1.2 Theory

Time jitter in gain-switched pulses is caused by the random generation of photons in the active layer of laser diodes. As long as a laser diode is driven above threshold, stimulated emission dominates the spontaneous emission. An increase in current results in a fast increase of the number of photons e.g. a higher output power. If the number of photons is small, the laser operates below threshold, a stochastic process, or spontaneous emission, is responsible for starting the stimulated emission. This causes the stochastic distribution in the turn-on time of the laser diode. The laser diode model described in Sec. 3.1.1 does not incorporate such a random process. Therefore, in Eq. 3.3 the photon density, S , around threshold conditions should be interpreted as the average photon concentration. In this case the repetition time of 400 ps is large enough to allow the photon concentration in the laser diode to quench before a new electrical pulse supplies carriers for the ignition of the next optical pulse. Compared to Eq. 3.3, Eq. 5.1 contains a stochastic term that describes the random fluctuations in the photon number [3], [4] and [5].

$$\frac{\partial S}{\partial t} = gS \frac{\Gamma c_0}{n_g} - \frac{S}{\tau_s} + \frac{c_0}{n_g} n_{sp} g + F_S(t). \quad (5.1)$$

In addition to deterministic chirp a stochastic chirp exists. The randomly generated photons exhibit a random phase.

$$\frac{\partial \phi}{\partial t} = \frac{1}{2} \alpha_H \frac{c_0}{n_g} G(N - N_0) + F_\phi(t). \quad (5.2)$$

$F_S(t)$ and $F_\phi(t)$ are Langevin functions [6] describing the stochastic processes. The term $\frac{c_0}{n_g} n_{sp} g$ in Eq. 5.1 represents the average spontaneous emission. At this point it is important to see that each spontaneously generated photon will change the optical field with random phase [7]. The second order moments of $F_S(t)$ and $F_\phi(t)$ are

$$\langle F_S(t) F_S(t') \rangle = 2S(t) \epsilon_{ase} B N^2 \delta(t - t') \quad (5.3)$$

and

$$\langle F_\phi(t) F_\phi(t') \rangle = \frac{1}{2S(t)} \epsilon_{ase} B N^2 \delta(t - t') \quad (5.4)$$

$F_S(t)$ and $F_\phi(t)$ are uncorrelated. ϵ_{ase} is the enhancement factor of spontaneous emission as defined in Ref. [4]. Although a single-mode laser is considered, the Langevin functions are uncorrelated for multiple modes. This has the consequence that for DFB laser diodes spontaneously generated photons outside the gain band of the DFB laser diode do not contribute to the ignition process. DFB laser diodes exhibit therefore an increased turn-on time jitter compared to multimode laser diodes [4]. The generation of a spontaneously emitted photons,

$F_S(t)$, results in the annihilation of electron-hole pairs. In addition, electron-hole pairs are randomly generated, $F_N(t)$. Therefore, the rate equation for the carrier density (Eq. 3.1) expands with two terms to

$$\frac{\partial N}{\partial t} = \frac{I}{e \cdot wLd} - gS \frac{c_0}{n_g} - N \left(\frac{1}{\tau_c} + BN + CN^2 \right) + F_N(t) - F_S(t), \quad (5.5)$$

with

$$\langle F_N(t)F_N(t') \rangle = \frac{2}{wLd} N \left(\frac{1}{\tau_c} + BN + CN^2 \right) \delta(t - t'). \quad (5.6)$$

Again, $F_N(t)$ is a Gaussian stochastic process with zero average. Around threshold the deterministic terms in the rate equations are close to zero and the stochastic terms take control. If a known external signal is fed into the active layer the deterministic term is raised well above zero. When the laser is turned on, i.e. the active layer is pumped, the stochastic term is no longer responsible for the ignition of the laser. This external signal is often referred to as the optical seed. Usually, the seed signal is a continuous signal, [8]. Seeding where part of the generated signal is fed back into the cavity is also demonstrated to reduce time jitter [9]. This method is called self seeding. Unfortunately this theory could not be implemented in a commercial, packaged laser diode because the available laser diodes were equipped with internal isolators which prevent injection of the seed. A laser with a ring structure operates in a similar way as a self seeded laser. Such a laser was designed and is described in Sec. 5.1.3.

5.1.3 Experimental setup

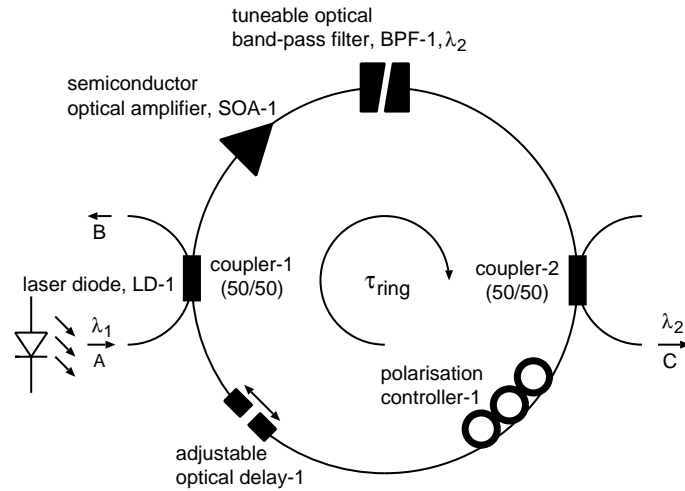


Figure 5.2: Geometry of the all-optical cross gain-switched tuneable ring laser. SOA-1 is equipped with internal isolators as a result of which the ring operates unidirectionally.

To allow feedback of the generated periodically pulsed signal into a resonator with an amplifying medium a fibre ring laser is constructed. A MQW SOA, SOA-1, provides optical gain

in the clockwise direction and should be modulated to periodically switch the ring laser on and off. Modulation can be performed either electrically or optically. In the case of MQW SOA modules the device has not been designed and packaged for high speed modulation. In contrast to the modulation of SOA-1 with an electrical signal an optical signal may be used. This results in a relatively faster modulation of the SOA module. Controlled saturation of the device allows manipulation of the optical gain. Figure 5.2 displays such a ring configuration where provisions have been made for optical modulation of the semiconductor optical amplifier. Via coupler-1 the modulation signal, generated by laser diode LD-1 at $\lambda = \lambda_1$, is injected into SOA-1. The tuneable optical band-pass filter, BPF-1, prevents the ring laser from lasing at the wavelength of this switch signal. Instead the ring laser will oscillate at the wavelength determined by the optical filter (λ_2). In conventional injection seeded DFB lasers oscillation at the wavelength of the seed is prohibited by the gain spectrum, internal losses and the transfer function of an etched grating. Coupler-2 is located directly after the filter to extract power from the ring cavity. A polarisation controller minimises the roundtrip polarisation rotation. Different states of polarisation per roundtrip result in different propagation constants and different roundtrip times. This would result in time jitter. Adjustable optical delay-1 is inserted to be able to tune the length of the ring to a sub-harmonic frequency of 2.5 GHz. The optical control signal is generated by a commercially available 2.5 Gb/s DFB laser diode (LQF92D). Via coupler-1 this signal controls the roundtrip gain of the ring cavity by saturating semiconductor optical amplifier-1. LD-1 is temperature controlled and biased with a current between 20 and 100 mA. Furthermore the current is modulated sinusoidally with a maximum swing of 120 mA.

5.1.4 Experimental results and discussion

Figure 5.3 displays the output power of the ring laser versus drive current of SOA-1 for different input powers of a continuous control signal, $P_{control}$. The threshold current with no control signal present equals 65 mA and increases to 210 mA for 3 mW input power at point A in Fig. 5.2. An input power of 4 mW inhibits lasing of the ring laser. The modulation signal injected in the loop is sinusoidally shaped. Consequently, the gain of SOA-1 is periodically modulated. If the drive current of SOA-1 is set, for example, to 100 mA (in absence of the control signal the laser operates well above threshold) the periodic modulation of the total roundtrip gain (SOA gain minus cavity losses) exceeds the factor one for a small period of time. During this time the optical field inside the cavity is amplified. Outside this interval the optical field that passes the amplifier is not amplified strong enough to compensate for the encountered losses in the previous roundtrip. With a properly adjusted optical delay this occurs N times within one roundtrip time. Between these excess gain intervals an optical field remains present in the cavity. Every 400 ps the SOA is being saturated by the modulation signal to a gain level which is too small to compensate the losses of the cavity, after which the amplifier recovers and optical gain is added to the ring where all pulses have advanced to the former position of their predecessor. Every 400 ps optical pulses are located at the same position in the ring. In other words: the ring laser is never switched off. This is contrary to the gain switched DFB laser diode where the cavity volume is so small that all photons have disappeared between two successive periods of excitation. When optical gain is available again, the optical field does not have to be built up from spontaneous but from stimulated emission. Therefore, the ring cavity laser is said to be self seeding. Moreover, both the optical

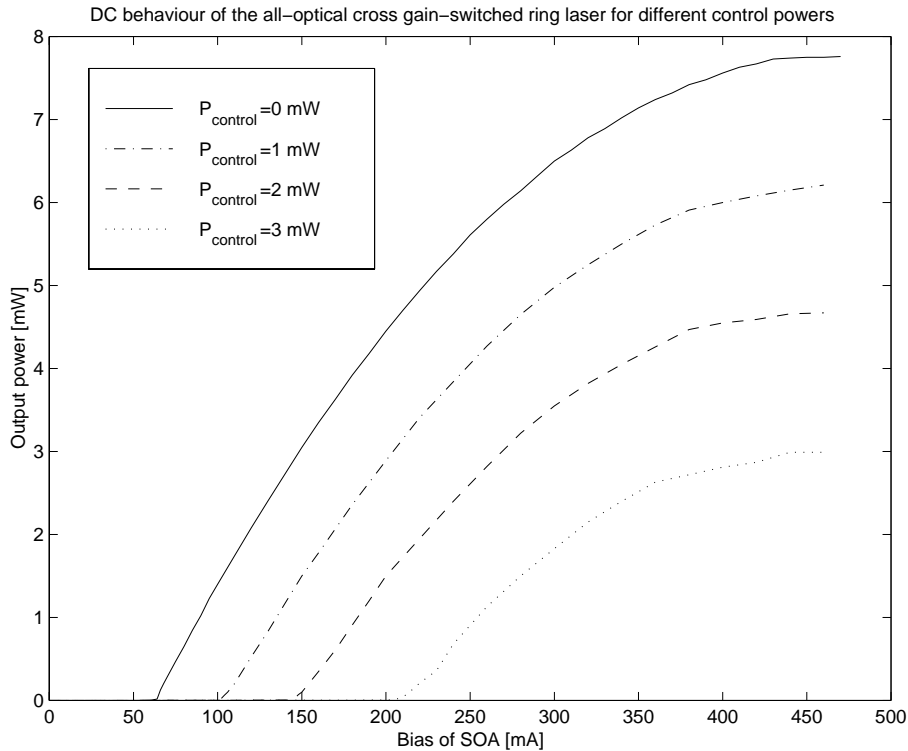


Figure 5.3: A continuous control signal controls the output power of the ring laser. $\lambda_1 = 1307 \text{ nm}$, $\lambda_2 = 1310 \text{ nm}$.

control signal and the gain of SOA-1 are deterministic because SOA-1 always operates above threshold.

Figure 5.4 displays the dynamic response to a sinusoidally modulated control signal. The tuneable filter was tuned between 1280 nm and 1330 nm in steps of $\approx 10 \text{ nm}$. Wavelengths within 3 nm of λ_1 should not be selected. The smallest full-width half-maximum time of the pulses amount to $\approx 12 \text{ ps}$ which should suffice for the system requirements mentioned in Sec. 5.1.1. The power of the control signal amounts to -4.2 dBm which results in -7.4 dBm at the input of the SOA. Some of the pulses in Fig. 5.4 (a) exhibit a small amount of ringing at the trailing edge. The ringing is believed to be caused by the limited frequency response of the detector which agrees with the observation that broad pulses show almost no ringing while narrower pulses show increased ringing. SOA-1 is, dependent on the wavelength of operation, electrically biased between 75 mA and 115 mA at 20° C . The cavity losses are estimated to be 11.8 dB. The output power of the pulses amounts to -7.0 dBm . The exact frequency of operation corresponds to the SDH-16 standard of 2.488 GHz. Deviations of $\pm 20 \text{ MHz}$ are tolerated.

No bit error rate measurements are performed to determine the performance of the all-optical cross gain-switched ring laser. Connection to the optical demultiplexer (see Sec. 5.3) as

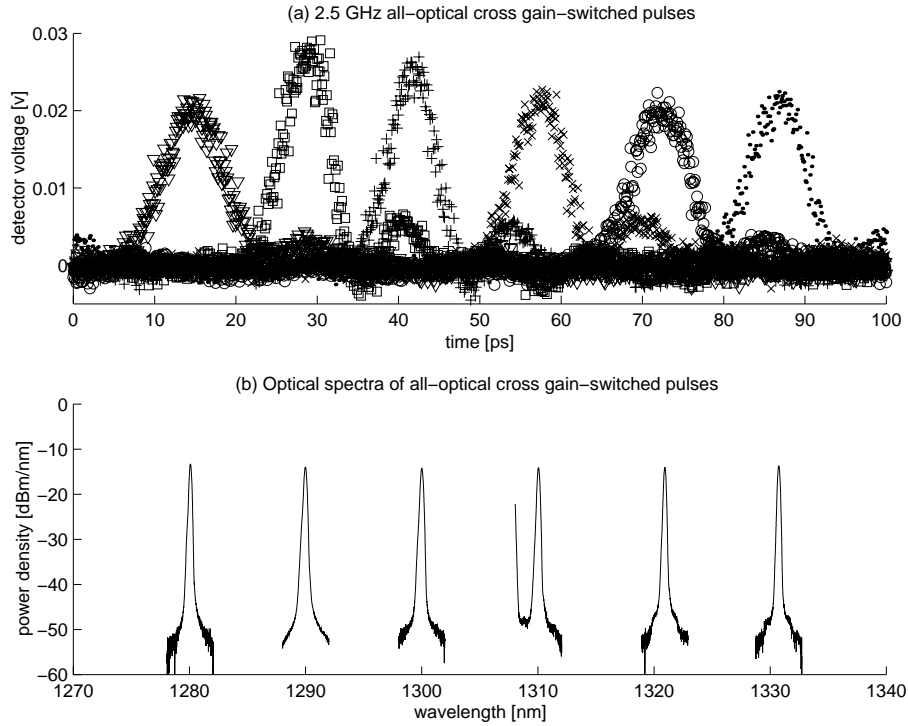


Figure 5.4: (a) Temporal response of the ring cavity to the sinusoidally shaped control signal for six different wavelengths. (b) The six spectra of the temporal responses plotted in (a). Responses are plotted directly above the optical spectra and can be distinguished by the six different plot symbols.

provider of the switch signal resulted in error free operation of the entire system. The pulse shape of the output can be changed by varying either the gain of SOA-1 and/or the DC and AC current of LD-1. If the DC current of the laser diode is increased a roundtrip gain > 1 exists for a smaller period of time. This results in a narrower pulse and a lower output power. Reduction of the gain of SOA-1 has the same result.

5.1.5 Conclusions and recommendations

Spontaneous emission causes random ignition of optical pulses in a gain-switched DFB laser diode to an extent where a gain-switched DFB laser diode was no longer appropriate to serve as a switch signal source for an all-optical demultiplexer (TOAD). Time jitter can be eliminated by preventing spontaneous emission to control the pulse generation process. An optical source has been realised that provides ≤ 20 ps narrow switch pulses for the 10 Gb/s to 2.5 Gb/s demultiplexing experiment. The source is based on an optically cross gain-switched ring laser employing self seeding to reduce time jitter. The laser is tuneable from 1280 to 1330 nm so that at all times switch signal and line signal overlap can be avoided in the all-

OTDM applications. In addition to the work described in Ref. [8] and [9] a new way of reducing time jitter has been demonstrated. The number of optical components in and out the ring is large, making it expensive and therefore not very practical. Additional research into the interaction of the external control signal with the internal optical field in SOA-1 and the ring is advisable.

5.2 10 Gb/s all-optical clock recovery

5.2.1 Introduction

Similar to the required 2.5 GHz optical switch signal for the 10 Gb/s to 2.5 Gb/s demultiplexing experiment (Sec. 5.3) a 10 GHz optical pulse train must be generated to control the 40 Gb/s to 10 Gb/s demultiplexer of Sec. 5.4. The 216 km transmission experiment, that will

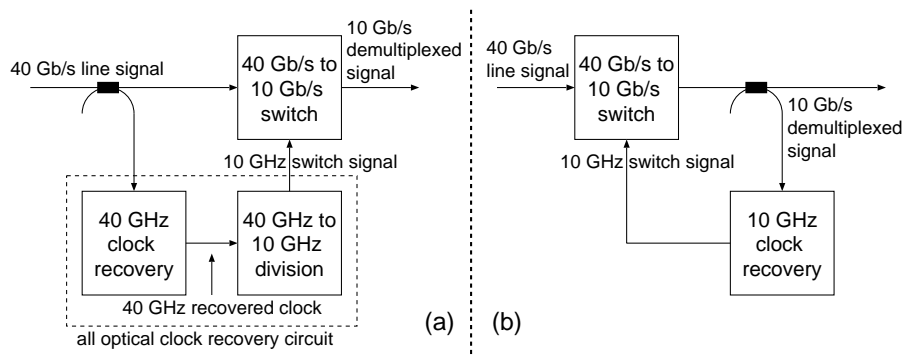


Figure 5.5: (a) All-optical clock recovery from the high-speed line signal with all-optical clock division to the bit rate of the four demultiplexed channels. (b) Clock recovery from the output of the demultiplexer. In this configuration all-optical clock division is not required.

be described in Sec. 5.5, requires an optical switch signal that is recovered from the transmitted line signal. The recovered switch pulses must be as narrow as possible so as to avoid deterioration of the channel extinction ratio as demonstrated theoretically in Chapter 2. Figure 5.5 displays two possible implementations of all-optical clock recovery circuits which should provide the optical switch with a suitable switch signal. Figure 5.5 (a) displays the classical way of all-optical clock recovery. Part of the line signal is guided into a clock recovery circuit that operates at the bit rate of the line signal. Depending on the number of channels the repetition rate of the recovered clock signal must be divided by the number of channels. Although this configuration is straightforward, practical realisation is difficult because of the extremely high clock recovery rate and the demand for narrow optical pulses. In addition, realisation of this configuration demands many optical components. An alternative scheme is depicted in Fig. 5.5 (b). Here the clock recovery unit is located after the optical switch where the demultiplexed signal is available. Clock recovery takes place at this much lower bit rate. Essential in this configuration is that the clock recovery must be started externally because without a clock signal the optical switch remains closed and a demultiplexed channel

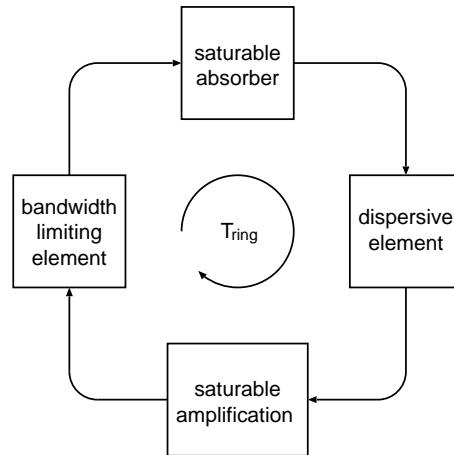


Figure 5.6: Passively mode-locked ring laser employing a saturable absorber and a saturable amplifier. The block “dispersive element” represents the total dispersion in the ring and “bandwidth limiting element” contains the frequency limitation of the optical gain, optical absorption and optical cavity losses.

will not be available. To this end a special procedure must be followed to start the all-OTDM system (see Sec. 5.4). Most electrical clock recovery circuits are based on either a cavity that resonates on or on a phase locked loop (PLL) that locks to the frequency equal to the bit rate for an RZ or half the bit rate for a NRZ data signal. Most all-optical clock recovery circuits are constructed around a passively mode-locked laser, i.e. an optical cavity. The advantages of a passively mode-locked laser are the small pulse width of the generated pulses, the high repetition rates and the uniformity of the generated pulses i.e. a high stability. Passively mode-locked lasers can roughly be divided into two categories: mode-locking based on fibre nonlinearity induced pulse narrowing interacting with dispersion induced pulse broadening and mode-locking based on the interaction between saturable absorption and saturable amplification in semiconductor materials. The first category is compatible with erbium-doped fibre amplification to provide gain to the cavity of the mode-locked ring laser. Once the optical field increases, modulation instabilities occur. The fibre nonlinearity and the presence of anomalous dispersion excite the natural mode of propagation in the fibre i.e. form a soliton shaped pulse. EDFAs do not introduce chirp on the envelope of the pulses because there is no phase-amplitude coupling. In the $1.3 \mu\text{m}$ wavelength domain optical amplification is achieved with SOAs which do impose chirp on the amplified optical pulses. This complicates the formation of chirp free optical pulses in e.g. a ring laser. Amplifier induced chirp impedes the ability of optical solitons to obtain a constant phase distribution. Moreover when this chirp interacts with dispersion the pulses will broaden. This effect is larger than can be compensated for by self-phase modulation pulse narrowing. To this end a saturable absorber can be introduced in the cavity of mode-locked lasers to narrow the optical pulses more efficiently. The external-cavity tuneable mode-locked laser (ECTMLL) treated in Sec. 3.1.2 belongs to this category. A schematic description of a passively mode-locked ring laser em-

ploying saturable absorption and amplification is depicted in Fig. 5.6. Passively mode-locked lasers have the characteristic that they produce self-sustaining pulses. Injection of a low powered data signal that modulates e.g. an amplifier or absorber, synchronises the free running ring laser to this signal under the condition that the cavity length is matched to the bit time of the synchronising data signal.

5.2.2 Theory

Theory of mode-locking is treated extensively in the literature, e.g. [10], [11] and [12]. In this section an insight is provided into the mode-locking mechanism. Most theoretical treatments start with differential equations of the slow amplification, $h_g(\tau)$, and slow absorption, $h_a(\tau)$,

$$\frac{dh_g(\tau)}{d\tau} = \frac{h_{g,0} - h_g(\tau)}{\tau_g} - \frac{|p(\tau)|^2}{E_{g,sat}} (\exp(h_g(\tau)) - 1) \quad (5.7)$$

and

$$\frac{dh_a(\tau)}{d\tau} = -\frac{h_{a,0} - h_a(\tau)}{\tau_a} - \frac{|p(\tau)|^2}{E_{a,sat}} (\exp(h_a(\tau)) - 1). \quad (5.8)$$

$h_g(\tau)$ ($h_a(\tau)$) describes amplification (absorption) of the amplifier (absorber), integrated over its length. $p(\tau)$ is the pulse shape of the mode-locked pulse, $E_{g,sat}$ and $E_{a,sat}$ the saturation energies of the gain and absorption media, respectively. τ_g and τ_a indicate the carrier lifetimes of the amplifier and absorber respectively. Finally, $h_{g,0}$ and $h_{a,0}$ are the small signal integrated gain and absorption. Under the assumption that the width of pulse $p(\tau)$ is small such that the amplifier and absorber do not recover while saturation takes place, the gain and absorption satisfy

$$h_g(\tau) = h_{g,i} \exp\left(-\frac{E_p(\tau)}{E_{g,sat}}\right) \quad (5.9)$$

and

$$h_a(\tau) = h_{a,i} \exp\left(-\frac{E_p(\tau)}{E_{a,sat}}\right), \quad (5.10)$$

with $h_{g,i}$ and $h_{a,i}$ the gain and absorption before the pulse enters the amplifier and absorber, respectively. $E_p(\tau)$ is the total amount of energy of the mode-locked pulse that has entered the saturable structure and satisfies

$$E_p(\tau) = \int_{-\infty}^{\tau} |p(\tau')|^2 d\tau'. \quad (5.11)$$

The dispersive element is modelled as far as second order dispersion. Thus

$$h_d(\tau) = -j\beta_1 + j\beta_2 \frac{\partial^2}{\partial \tau^2}. \quad (5.12)$$

The bandwidth limiting element represents the wavelength (frequency) dependence of the entire cavity. In literature often a Lorentzian profile is assumed. Here a Gaussian profile is

assumed. A Gaussian profile is more conservative with respect to the operation of the ring laser because the chirp induced shift of the optical spectrum will have a larger impact on a filter with steep edges (Gaussian) than on a filter with smooth edges (Lorentzian). The time dependent response of the second order approximation of the Gaussian filter equals

$$h_f(\tau) = 1 + \frac{1}{(\Delta\omega)^2} \frac{\partial^2}{\partial\tau^2}. \quad (5.13)$$

$\Delta\omega$ is the bandwidth of the filter. In one roundtrip the pulse shape changes to

$$p_{n+1}(\tau) = \exp\left[\frac{1}{2}\{(1 - j\alpha_g)h_g(\tau) - (1 - j\alpha_a)h_a(\tau) - h_f(\tau) + 2h_d(\tau) - \alpha_{loss}\}\right]p_n(\tau), \quad (5.14)$$

which is known as the mode-locking equation [12]. The integer n is the round trip number and α_{loss} is the linear cavity loss. For stable operation the pulse shape after each roundtrip is not allowed to change. However, a shift in time, $\Delta\tau$, is allowed as this will result in a slightly longer or shorter cavity length without effecting the shape of $p(\tau)$, thus for stationary operation

$$p_{n+1}(\tau) = p_n(\tau + \Delta\tau) = p_n(\tau) + \Delta\tau \frac{\partial p_n(\tau)}{\partial\tau}. \quad (5.15)$$

Substitution of Eq. 5.15 into Eq. 5.14 gives the differential mode-locking equation

$$\Delta\tau \frac{\partial p(\tau)}{\partial\tau} = \exp\left[\frac{1}{2}\{(1 - j\alpha_g)h_g(\tau) - (1 - j\alpha_a)h_a(\tau) - h_f(\tau) + 2h_d(\tau) - \alpha_{loss}\} - 1\right]p(\tau). \quad (5.16)$$

Solutions of this equation are usually obtained by substituting an ‘‘Ansatz’’ for $p(\tau)$. Evaluation and linearisation of the mode-locking equation followed by separation of variables result in a set of equations for the parameters of the system. Solutions of this equation determine the parameter boundaries for $p(\tau)$ -shaped mode-locked pulses [12], [13]. This method is efficient in analytical determination of the boundary conditions for mode-locking under the assumption that the pulse shape is known. For different $p(\tau)$, different parameter settings can be obtained. In this section the model for the saturable absorber is based on a semiconductor structure.

In the next section a saturable absorber is treated that is based on a semiconductor optical amplifier that is placed in a Sagnac interferometer. Although this configuration can be modelled by Eq. 5.8 the physical mechanism behind the pulse narrowing can not be attributed to generation of electron-hole pairs but rather to an interferometric mechanism. Implementation of this interferometric mechanism into the mode-locking equation, Eq. 5.16, is not straightforward. Transformation of the parameters of the Sagnac based saturable absorber to $h_{a,i}$, $E_{sat,a}$, α_a and τ_a provides a first order alternative to a substantially more difficult expression of the mode-locking equation.

A Sagnac interferometer based saturable absorber

As stated in Sec. 5.2.2 the main task of the slow saturable absorber is to narrow the pulses in the cavity. Saturable absorbers can be realised in a number of ways. Proton bombardment

or ion implantation of part of a laser or amplifier will cause lattice defects that can absorb photons. Moreover, a semiconductor laser diode or optical amplifier operated under conditions of reverse bias can act as a saturable absorber which is often employed in multisection lasers [14]. Figure 5.7 displays a saturable absorber based on a SOA that is asymmetrically

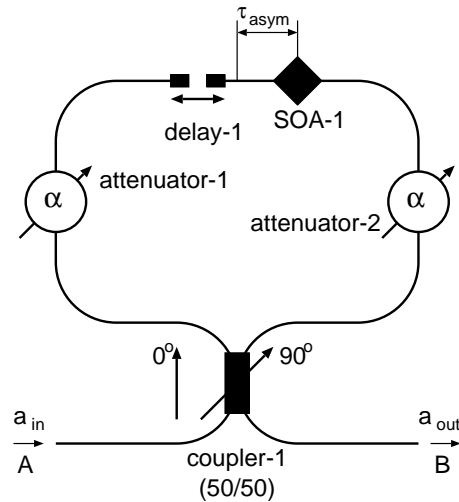


Figure 5.7: Geometry of the Sagnac interferometer based saturable absorber. The loss of the left and right branch can be adjusted independently. Not drawn is a polarisation controller that matches TE and TM states of polarisation of the signals upon their return in the coupler.

placed in a Sagnac interferometer. An optical pulse that is injected into the Sagnac interferometer is split up into a clockwise and counter clockwise travelling pulse. At a certain point both pulses will enter the amplifier. Optical attenuators allow adjustment of the input power of the clockwise travelling signal and the counter clockwise travelling signal. A difference in time of arrival of both pulses at the bidirectional SOA-1 can be set by adjustable optical delay-1. Once the signals have passed the amplifier they recombine in coupler-1. A polarisation controller (not drawn) matches the TE and TM state of polarisation when the signals recombine in the coupler. Both clockwise and counter clockwise pulses saturate the amplifier. The chirp imposed on the clockwise and counter clockwise travelling pulses can be influenced by controlling the input powers to the amplifier and the position of the amplifier in such a way that the temporal phase difference between both pulses can be varied. This saturation process imposes phase changes (chirp) on both pulses in such a way that when the clockwise and counter clockwise travelling pulses recombine in the coupler, significant constructive interference occurs for the centre region of the pulse and mostly destructive interference for the leading and trailing edges of the pulse. For specific settings of the attenuators and the optical delay line optimum pulse compression can be achieved. This pulse compression depends on the pulse width and pulse power. To investigate this the zero-length, bi-directional amplifier model of Chapter 2 is incorporated into a Sagnac interferometer. For different settings of the attenuators and amplifier asymmetry, amplifier gain and saturation

output power the temporal and spectral response of the absorber to a soliton shaped pulse can be computed. The saturable absorber model of Eq. 5.8 has also been implemented into a computer program. Figure 5.8 (a) displays the action of the Sagnac based saturable absorber

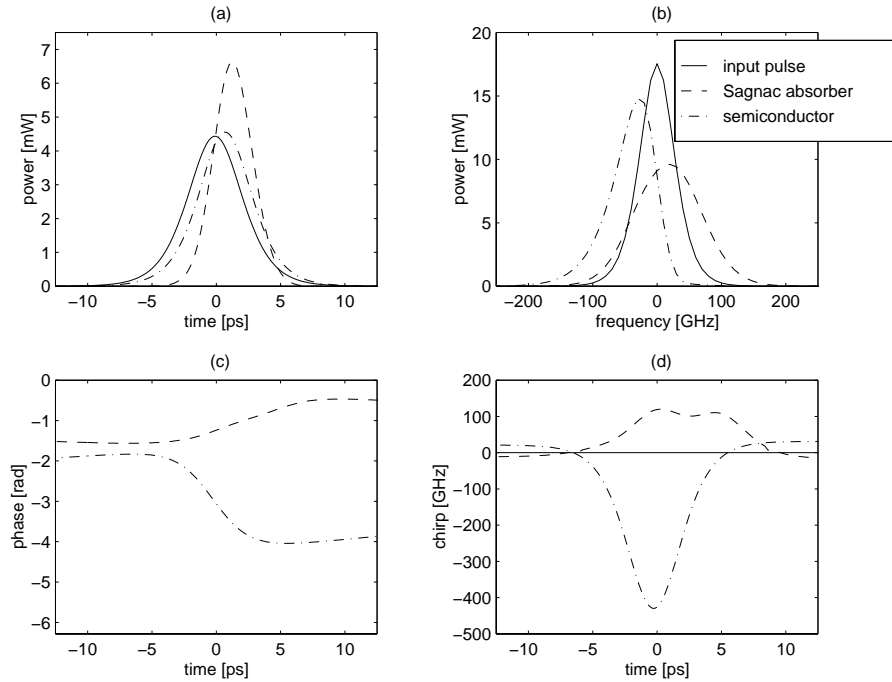


Figure 5.8: Response of the Sagnac based saturable absorber (dashed line) and the semiconductor saturable absorber according to Eq. 5.10 (dashed-dotted line) to a 5 ps, -6 dBm optical pulse at a repetition time of 100 ps (solid line). (a) The temporal power response with pulse widths of 5 ps, 4.9 ps, 3.6 ps for the three above mentioned curves. (b) The envelope of the spectral responses. (c) the temporal phase that is imposed on the input signal. (d) The frequency chirp that is responsible for the shift of the spectra in subplot (b). The gain of the amplifier amounted to 23 dB, $E_{sat} = 10$ dBm, $\alpha_H = 8$, $\tau_c = 200$ ps. The small signal absorption of the semiconductor model equals -23 dB. The amplifier asymmetry amounts to 2.5 ps and the loss of the attenuators equals 3 dB and 13 dB for the left and right branch of the Sagnac interferometer, respectively. An ideal 3 dB coupler is assumed.

and the semiconductor absorber model of Eq. 5.10 on a -6 dBm strong, 5 ps optical pulse train with a repetition rate of 100 ps. The average power of the input and output pulses in the graph is set equal for reasons of comparison. This way pulse broadening (narrowing) results in a lower (higher) peak power. Significant pulse compression takes place for the Sagnac based absorber while the pulse compression of the semiconductor absorption model is, with the given parameters, relatively small. For stronger input powers or lower $E_{a,sat}$ the pulse compression in the semiconductor absorber will become stronger. The optical spectra

are given in subplot (b). As is to be expected, the spectrum of the pulses at the output of the Sagnac interferometer based absorber have broadened. Due to saturation effects a time dependent phase is imposed on the envelope of the output pulses. For the semiconductor model it can be seen that a red shift occurs while the Sagnac based absorber is shifted to the blue side of the spectrum. The amplifier asymmetry and asymmetric loss in the left and right branches determine the amount of pulse compression and the symmetry of the output pulse. Not demonstrated here is the possibility of steepening the leading or trailing edges of the pulse by adjusting the attenuation and/or the amplifier asymmetry. This configuration is implemented in the ring laser as the absorbing element.

Numerical simulation of the ring laser

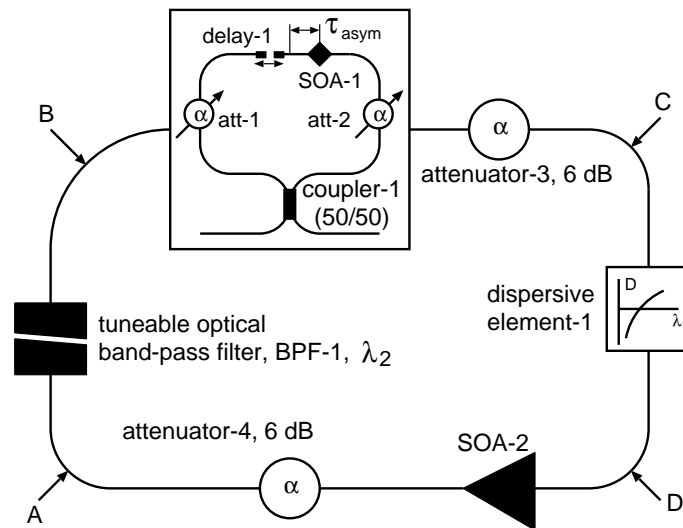


Figure 5.9: Setup for the simulation of the ring laser with the Sagnac interferometer based saturable absorber.

To investigate the operation and stability of the ring laser, the scheme depicted in Fig. 5.9 was simulated. The optical band-pass filter, BPF-1, is assumed to have a Gaussian transfer function. At point A a low powered relatively broad optical pulse is inserted and the response to each following component is computed until one roundtrip has been completed. This way an arbitrary number of roundtrips can be calculated. At points A, B, C and D the pulse shapes are stored for later inspection. Computation times are reduced and numerical stability is enhanced by employing spatially concentrated amplifier models. At two points two 6 dB attenuators are inserted which account for cavity losses. Coupler-1 has a splitting ratio of 3 dB. The phase difference between the output ports equals 90° . Figure 5.10 displays stable operation of the ring laser. The pulse shapes after the first 60 roundtrips are depicted. A constant time shift, $\Delta\tau$ is observed which is in agreement with Eq. 5.15. After ≈ 20 roundtrips the ring laser achieves stationary operation. More than 1000 roundtrips were

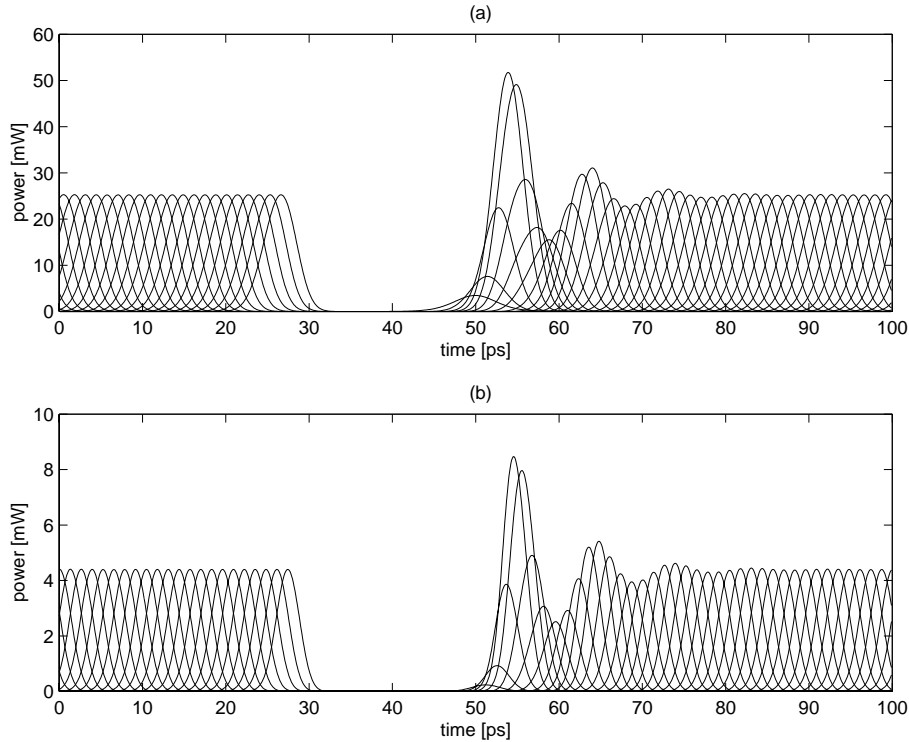


Figure 5.10: Stable operation of the ring laser. At $\tau = 50$ ps a pulse is launched into the ring and for the first 60 roundtrips the pulses are depicted in the same figure. Subplot (a) contains the pulse shapes at point B. Subplot (b) contains the pulses at point C. The bandwidth of the filter equals 240 GHz. The settings of the Sagnac based absorber equal the settings of Fig. 5.8. The amplifier has a gain of 23 dB, $P_{sat} = 16$ dBm, $\alpha_h = 5$ and $\tau_c = 200$ ps.

computed and instabilities were not observed. Figure 5.11 displays unstable operation of the ring laser. This was achieved by increasing the amplifier asymmetry in the absorber to 10 ps. The pulse shapes after the first 60 roundtrips are depicted. Although stable operation appears eventually to be reached, the system exhibits an instability. This instability repeats itself periodically even beyond a 1000 roundtrips. In addition it can be observed that the pulse shapes of the low amplitude pulses in Fig. 5.11 (b) have become asymmetrical compared to the stable pulses in Fig. 5.10 (b). This should also be attributed to the increased amplifier asymmetry. Figure 5.12 displays the evolution and power of the pulse widths for each roundtrip time for stable and unstable operation. Another important parameter is the width of the optical filter. A broad filter passes more 10 GHz spaced modes while a narrow filter reduces the number of modes. Therefore a broad filter is expected to give narrow pulses and a narrow filter broad pulses. Numerical simulations have been carried out to verify this. Figure 5.13 displays the dependence of the pulse widths and pulse power as a function of the bandwidth of the filter. Both at point B and C of Fig. 5.9 the pulse width and pulse power have been evaluated.

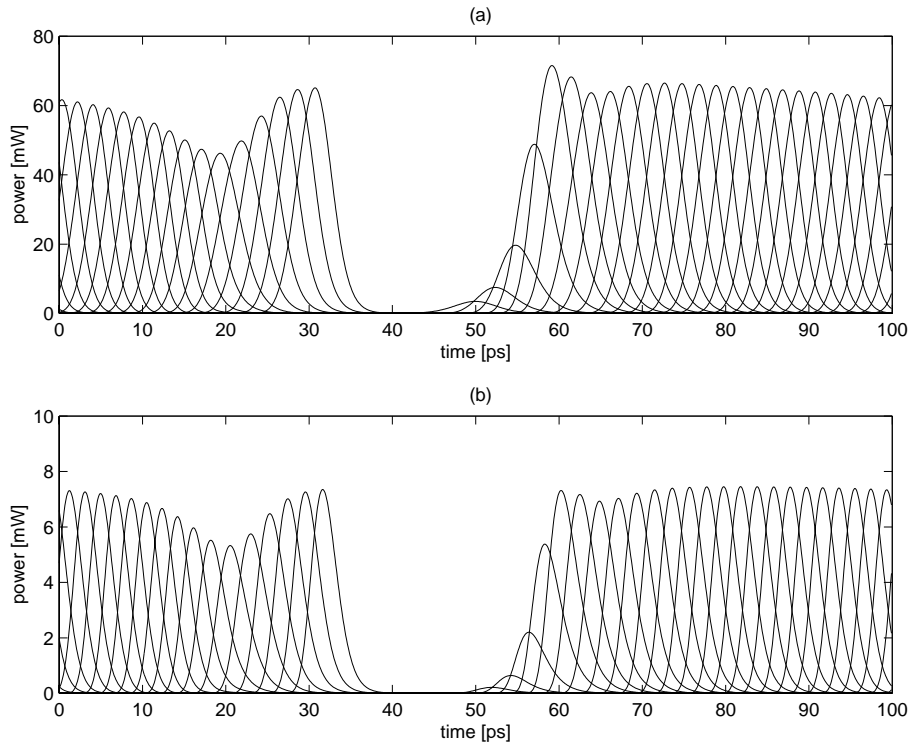


Figure 5.11: Unstable operation of the ring laser. The settings equal the settings in Fig. 5.10, except for the amplifier asymmetry in the Sagnac loop which is set to 10 ps.

In accordance with expectations, it can be observed that a broader filter results in narrower pulses. Broader filters also allow for more power in the cavity. The amplifiers are driven into saturation resulting in more chirp and less efficient use of the available bandwidth. As a result pulses exhibit less narrowing than is to be expected when the bandwidth of the filter is increased. In comparison with a semiconductor optical absorber, the chirp that is encountered in the Sagnac based saturable absorber is of the opposite sign as the chirp encountered in the semiconductor optical absorber. In the case of a semiconductor saturable absorber based ring laser the chirp encountered in the semiconductor optical absorber is of the opposite sign as the chirp encountered in the saturable amplifier. Consequently, detuning is more severe in the case of implementation of the Sagnac based saturable absorber in a ring laser. In combination with the Gaussian filter detuning demands more of the total roundtrip gain because the detuning together with the Gaussian filter characteristics manifests itself as an additional loss. This also explains why chirp free, Fourier limited, pulses will not be generated. In the case of the semiconductor saturable absorber the encountered chirp can be counteracted by the experienced chirp in the optical amplifier because their chirp is of the opposite sign.

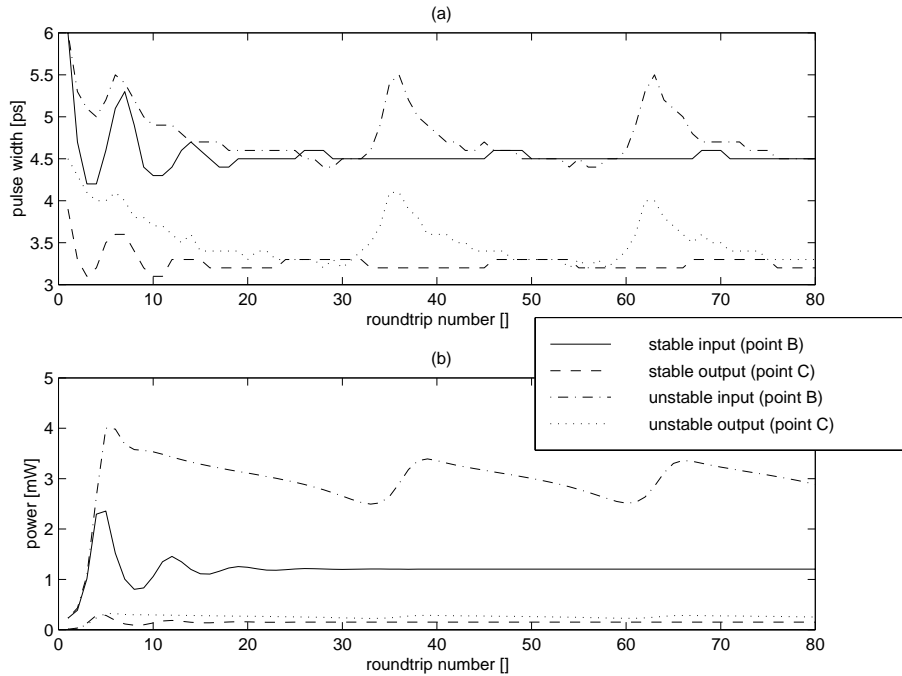


Figure 5.12: Pulse width (a) versus roundtrip number and pulse power (b) versus roundtrip number for stable operation, simulated at point B in Fig. 5.9 (solid curve) and C in Fig. 5.9 (dashed curve), respectively and unstable operation, simulated at point B (dashed-dotted curve) and C (dotted curve), respectively. The same parameters were used as in Figs. 5.10 and 5.11.

5.2.3 Experimental setup

The optical clock recovery circuit is schematically depicted in Fig. 5.14. If the input is connected to a 10 Gb/s RZ data signal at $\lambda = \lambda_1$ then at the output a 10 GHz pulse train at $\lambda = \lambda_2$ is expected. The gain and saturation output power of the amplifiers are controlled by a bias current. The temperature of both amplifiers was set to $\approx 20^\circ\text{C}$. An intensity autocorrelator is used to give an indication of the width of the pulses. In addition a 45 GHz PIN photodetector connected to a 50 GHz digital sampling oscilloscope which can be triggered to either the pattern trigger or clock trigger of the pulse pattern generator, provides the temporal power envelope of the pulses. An optical spectrum analyser is used to monitor the signal in the wavelength domain. At points B and C in Fig. 5.14 signals are measured.

Figure 5.15 displays the practical realisation in the form of a photograph. In the background the sampling oscilloscope is visible. Connected to it is the high-speed PIN-detector (lower trace) and a < 10 GHz amplified detector (upper trace). The lower trace is the eye diagram of the 10 Gb/s data signal at the input and the upper trace is the 10 GHz component of the recovered clock. This trace is used to optimise the settings of the clock recovery circuit as it provides information on possible pattern effects that are imposed on the recovered pulses by

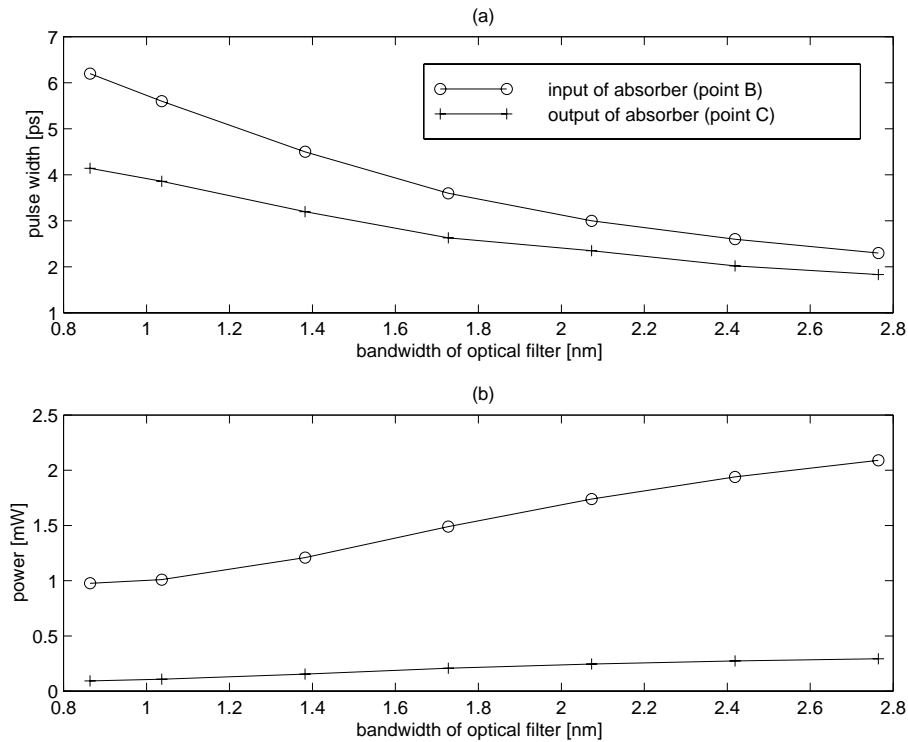


Figure 5.13: Pulse width (a) versus filter bandwidth and pulse power (b) versus filter bandwidth, simulated at point B (\circ) and C (+) in Fig. 5.9. Same parameters are used as in Fig. 5.10.

the data signal. The trace gives a visual indication of timing and jitter, amplitude fluctuations, noise, and output power.

5.2.4 Results and discussion

The configuration depicted in Fig. 5.14 has been realised using fibre pig-tailed components. A -9 dBm, PRBS modulated, 10 Gb/s signal at $\lambda = 1304.5$ nm is fed into the passively mode-locked ring laser which locked to this signal. Initially the wavelength of the recovered clock was set to 1313.5 nm. It was found that for a broad range of parameter settings stable clock recovery takes place. The controls effect the stability, wavelength of operation, pulse width, sensitivity to the input signal, the output power, and locking range. Stable clock recovery could be reproduced any time with the notable exception that the control settings differed each time the circuit was re-synchronised to the same 10 Gb/s input signal. This is caused by the interdependence of parameters, the random behaviour of the state of polarisation in the loop and the dependence on mechanical and temperature induced strain in optical fibre. This polarisation walk off can be corrected by periodically re-adjusting the state of polarisation in

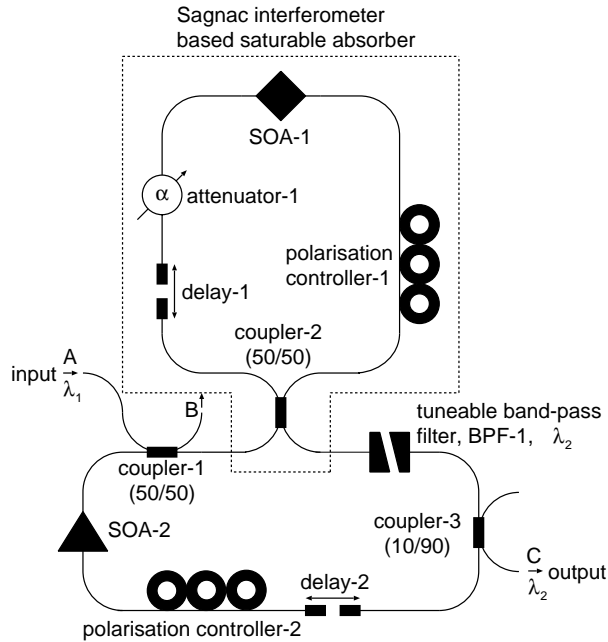


Figure 5.14: Geometry of the all-optical clock recovery circuit

Table 5.1: Settings for stable locking of the optical clock recovery of Fig. 5.14. P_{input} and P_{output} refer to the measured input and output signal powers.

parameter	min.	average/typical	max.	notes
I_{SOA-1}	170 mA	212 mA	300 mA	$T = 20^\circ \text{C}$
I_{SOA-2}	180 mA	326 mA	350 mA	$T = 20^\circ \text{C}$
delay-1	142 ps	145 ps	149 ps	137 ps \leftrightarrow SOA-1 centred
delay-2	63 ps	67 ps	72 ps	
α_{left}	4.0 dB	9.6 dB	13.8 dB	loss of att.-1 and delay-1
α_{right}	1.5 dB	1.5 dB	1.5 dB	loss of pol. ctrl.-1
P_{input}	-12.4 dBm	-9.0 dBm	3.0 dBm	
P_{output}	-15.4 dBm	-13.2 dBm	-9.6 dBm	

the loop. Residual polarisation sensitivity of the components requires either re-adjustment of amplifier gains and of the attenuation in the left branch of the Sagnac interferometer based saturable absorber. Table 5.1 displays an overview of values for different parameters for which the clock recovery operates.

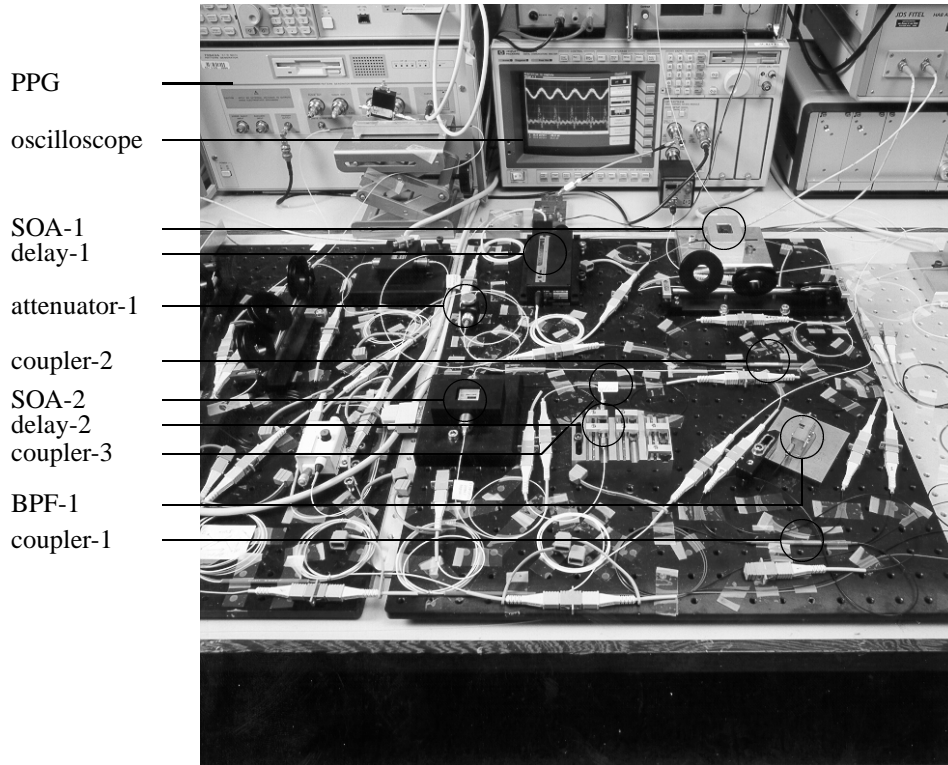


Figure 5.15: Realisation of the optical clock recovery circuit using fibre pig-tailed components taped to a rigid back plane. The names of the components correspond to the names in Fig. 5.14.

Temporal response

Figure 5.16 displays the temporal response at point C of the clock recovery circuit to the -9 dBm data signal. The signal has been coded with a $2^{31} - 1$ PRBS data pattern. The 1304.5 nm input pulses have a width of 3.1 ps. SOA-1 and SOA-2 are biased at 212 mA and 258 mA, respectively. Optical delay-1 has been set to 144 ps which corresponds to an amplifier asymmetry of 3.5 ps. The attenuation of the left branch amounts to 11.3 dBm. BPF-1 is set to 1313.5 nm. The output power of the generated pulse train amounts to -13.6 dBm. The ringing suggests that the pulse width is smaller than the limiting 12 ps response of the 45 GHz photodiode. To investigate possible pattern effects on the recovered clock signal the sampling scope was triggered with a trigger signal synchronised to the repetition rate of a $2^7 - 1$ PRBS pattern. The measured temporal response is depicted in Fig. 5.17. For these power levels the measured temporal envelope does not display any evidence of possible pattern effects or discontinuities. BER measurements on an all-OTDM system, incorporating this optical clock recovery circuit, performed in Sec. 5.4 will show that the performance of

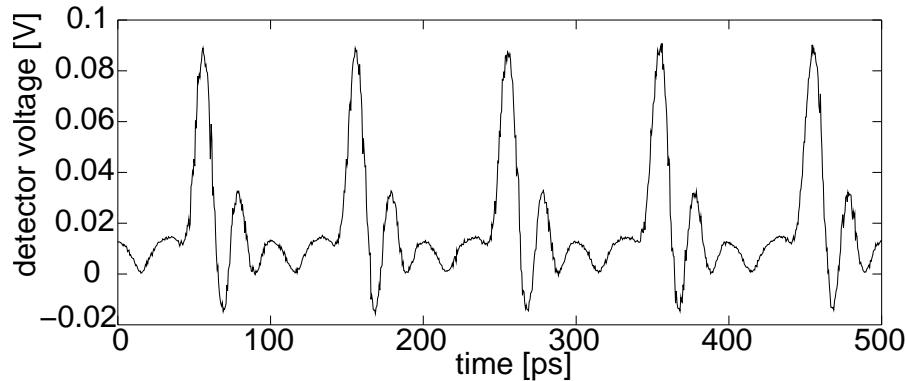


Figure 5.16: Recovered clock pulses from a $2^{31} - 1$ PRBS return to zero data signal

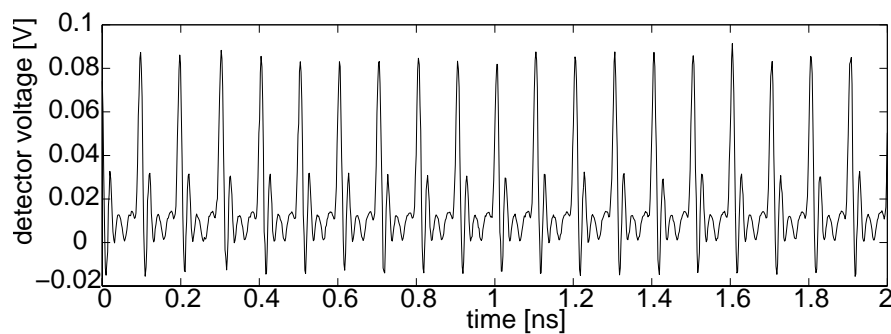


Figure 5.17: Recovered clock pulses from a $2^7 - 1$ PRBS return to zero data signal.

the optical clock recovery is satisfactory as error free demultiplexing is demonstrated.

Spectral response

Figure 5.18 and 5.19 display the optical spectra of the output of the clock recovery and of the input of the Sagnac based saturable absorber, respectively. The left signal in the spectrum of Fig. 5.19 is the 10 Gb/s data signal while the right signal is the spectrum of the recovered clock. The power of the recovered clock is more than a factor 10 larger than the power of the data signal. This masks pattern effects imposed by the data signal on the recovered clock signal. Figure 5.20 displays autocorrelation traces of the data signal and recovered clock signals for filter bandwidths of 2 nm (standard) and 3 nm. The recovered optical pulses are pedestal free which is essential for a unambiguously defined temporal window formed by the optical demultiplexer (TOAD). If a 3 nm filter is used the recovered pulse train displays pulses of approximately the same width as the input pulses of the data signal. If the bandwidth of the filter is decreased to 2 nm the recovered pulses broaden according to theoretical predictions

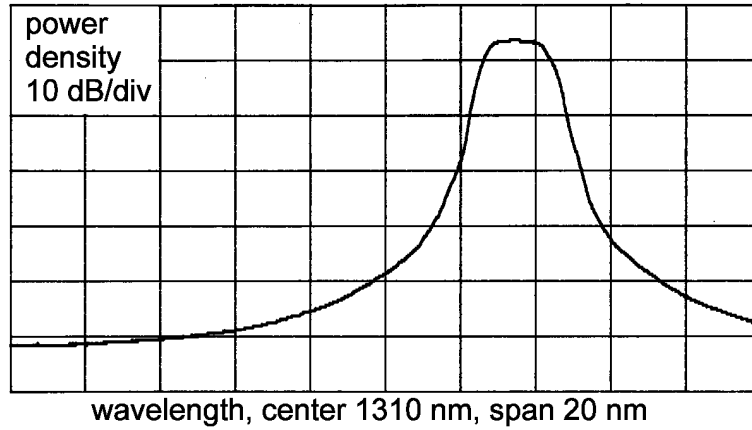


Figure 5.18: Optical spectrum of the recovered clock from the $2^{31} - 1$ PRBS modulated data signal, measured at point C in Fig. 5.14

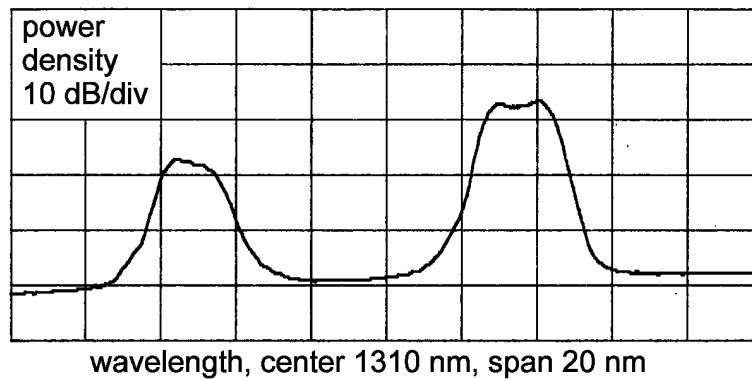


Figure 5.19: Optical spectrum of the recovered clock from the $2^{31} - 1$ PRBS modulated data signal, measured at point B in Fig. 5.14. The left signal is the 10 Gb/s data signal which lies approximately 10 dB below the recovered 10 GHz clock signal.

of Fig. 5.13. In this case fewer modes contribute to the mode-locking, which results in a broader pulse.

The full-width half-maximum time of the intensity autocorrelation traces of soliton shaped pulses relates to the width of the soliton pulses as

$$\tau_{fwhm,soliton,R_{xx}} = 1.5428 \cdot \tau_{fwhm,soliton}. \quad (5.17)$$

In the case of the 2 nm filter and under the assumption that the recovered pulses are soliton shaped, the width of the recovered clock pulses is 4.76 ps. For a 3 nm band-pass filter the width of the pulses equals to 3.2 ps. These values are of the same order of magnitude but

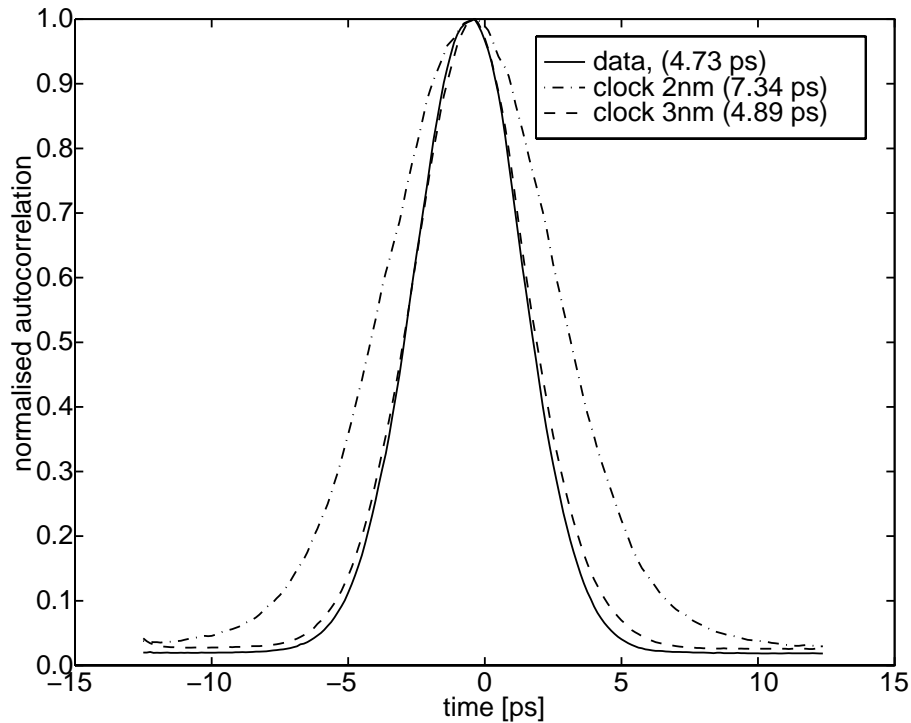


Figure 5.20: Autocorrelation traces of the 10 Gb/s data signal and the recovered clock signal at the output (point B) of Fig. 5.14 for a 2 nm optical filter and a 3 nm optical filter.

larger than predicted by Fig. 5.13. The 4.8 ps pulses have optical spectra that are slightly broader than the 3.1 ps pulses coming from the ECTMLL. This indicates that the recovered pulses are chirped. This corresponds with the theory discussed in Sec. 5.2.2. Pulse trains with a width of ≤ 5 ps are suitable for use as a switch signal for 40 to 10 Gb/s all-OTDM applications (see Chapter 2).

Tuneability of the clock recovery

The insertion of a tuneable optical band-pass filter allows selection of the wavelength of the recovered pulses. Figure 5.21 displays optical spectra and autocorrelation traces of the recovered clockpulses at $\lambda = 1284$ nm and $\lambda = 1333$ nm. The autocorrelation traces of subplots (c) and (d) show the introduction of a small pedestal, visible from the hump on the leading and trailing edges. For this experiment the 2 nm optical filter was operated beyond its specification which might have caused the formation of the pedestals. Also dispersion is known to cause pedestal problems in mode-locked ring lasers. The clock recovery circuit is tuneable over a 50 nm wide interval.

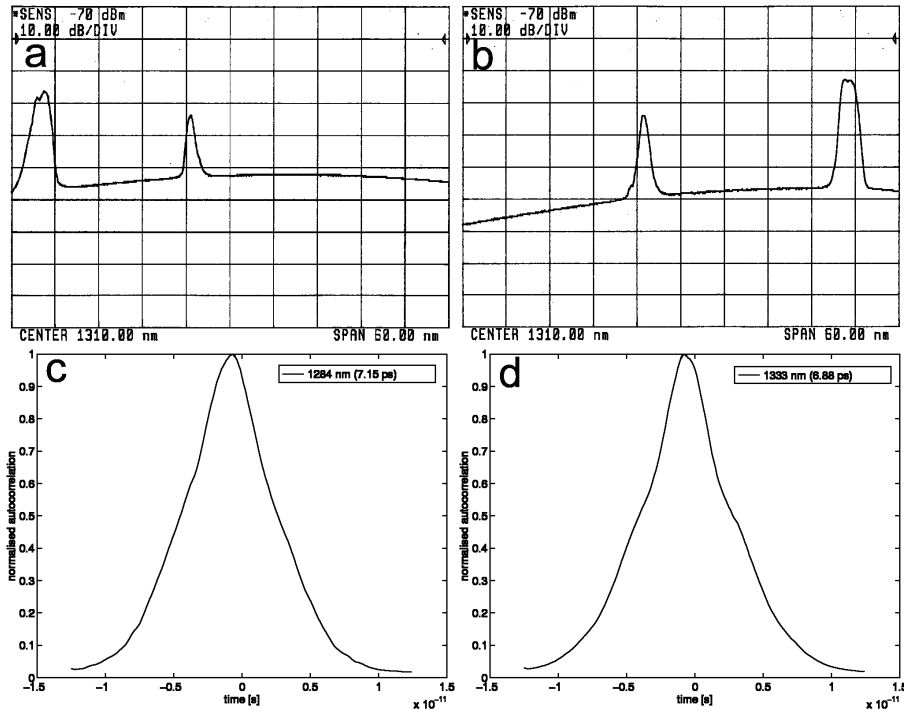


Figure 5.21: (a) and (b) optical spectra measured at point A of Fig. 5.14 for $\lambda = 1284$ nm and $\lambda = 1333$ nm, respectively. (c) and (d) show the corresponding autocorrelation traces.

Polarisation sensitivity and locking range

Significant polarisation sensitivity of the recovered clock signal to the input data signal was not observed. Variations of the input polarisation state caused the output power of the clock recovery circuit to vary less than ± 0.4 dB. This is in accordance with expectations. The synchronisation depends on the saturation of polarisation insensitive SOA-1 in the Sagnac based saturable absorber. The typical polarisation sensitivity of SOA-1 amounts to ± 1 dBm. The cavity roundtrip length amounted to 9.2 m. Assuming a refractive index of 1.5 for the optical fibre the ground frequency equals 21.6 MHz. The ring laser is therefore operated at approximately the 458th. harmonic. This will put severe limitations on the locking bandwidth of the clock recovery circuit. This bandwidth is experimentally determined by increasing (decreasing) the frequency of the clock of the pulse pattern generator. For small changes in frequency, the output of the ECTMLL remains unchanged. At certain points the clock recovery will stop oscillating. The difference between the upper and lower frequency where this happens gives the locking bandwidth. The bandwidth of the clock recovery circuit was determined using this technique and amounted to 184 KHz for a $2^{31} - 1$ PRBS data pattern. Within this bandwidth optical clock recovery is observed while outside this bandwidth optical clock recovery stopped abruptly.

5.2.5 Conclusion and recommendation

An all-optical clock recovery circuit (OCR) has been built which is capable of providing 3.1 ps pulses for ≥ 10 Gb/s all-optical signal processing applications. The OCR is based on a passively mode-locked ring laser employing a novel configuration where a saturable amplifier is inserted into a Sagnac interferometer to act as a saturable absorber. The wavelength of the recovered clock is tuneable over a 50 nm wide range. The bandwidth of the optical filter determines the pulse width. By tuning the currents of both amplifiers, and by proper adjustment of the amplifier asymmetry, the length of the cavity and the attenuator in the Sagnac interferometer, it is possible to minimise the pulse width. Chirp and pattern effects can be further reduced. Additional analytical and numerical investigation to the dependence of the amplifier asymmetry and the difference between left and right branch attenuation on the generated pulse shape is recommended. To this end a simulation tool has already been developed. The clock recovery circuit is expected to perform well in combination with the all optical switch, bearing in mind that the locking range of the clock recovery is limited to ≈ 200 KHz.

5.3 10 Gb/s to 2.5 Gb/s all-OTDM

5.3.1 Introduction

In this section experiments are described on a 10 Gb/s to 2.5 Gb/s optical demultiplexer as a first trial before effort is put into a 40 Gb/s to 10 Gb/s optical demultiplexer. Transmission experiments were not conducted as no optical fibre was available at the time of this particular experiment. During the last five years electrical demultiplexers have become available that also operate at 10 Gb/s. Therefore this all-optical technology is not likely to be implemented in practical systems at these relatively low speeds. However the experiments described in this section do provide insight into the operation and performance of the all-optical switch because at these low speeds visualisation of signals is relatively easy.

5.3.2 Experimental setup

Figure 5.22 displays the scheme of the OTDM setup under investigation. In this setup the switch signal is not recovered from the data signal but generated from the auxiliary 2.5 GHz clock output of the pulse pattern generator. Strictly speaking there is no all-optical clock recovery. However, the switch signal is obtained from an all-optical circuit, the cross gain-switched ring laser of Fig. 5.2. Therefore the setup does belong to the category of all-optical demultiplexers.

From the 10 GHz electrical clock a 10 Gb/s return to zero data signal is obtained using the sinusoidally modulated laser diode, LD-1, discussed in Chapter 3. Dispersion-shifted fibre, DSF-1, compresses these chirped pulses after which a desired data pattern is superimposed via LiNbO₃ modulator, MZ mod-1.

The PRBS data patterns generated by the pulse pattern generator have the property that each consecutive fourth bit forms a PRBS sequence of the same order. Therefore the 2.5 Gb/s demultiplexed pattern is equal to the pattern of the 10 Gb/s data signal. In addition, four patterns at 2.5 Gb/s contain all the bits of a single pattern at 10 Gb/s.

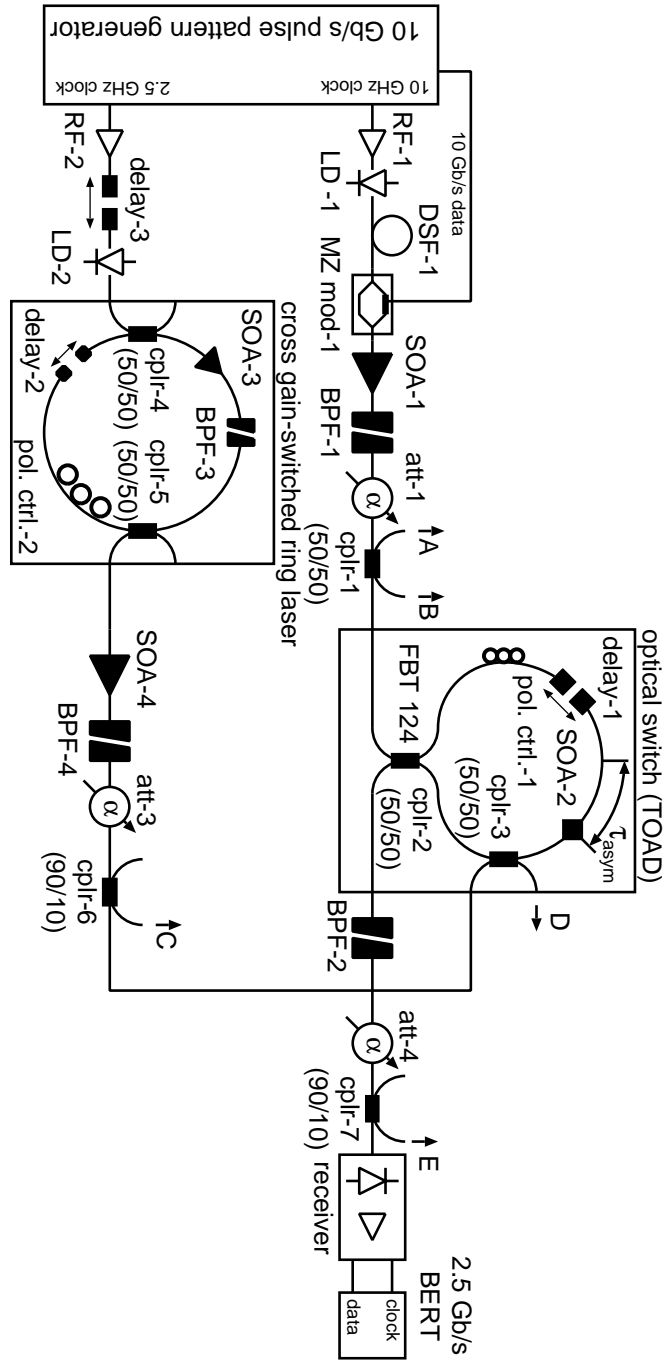


Figure 5.22: Experimental setup of the 10 Gb/s to 2.5 Gb/s all-OTDM experiment

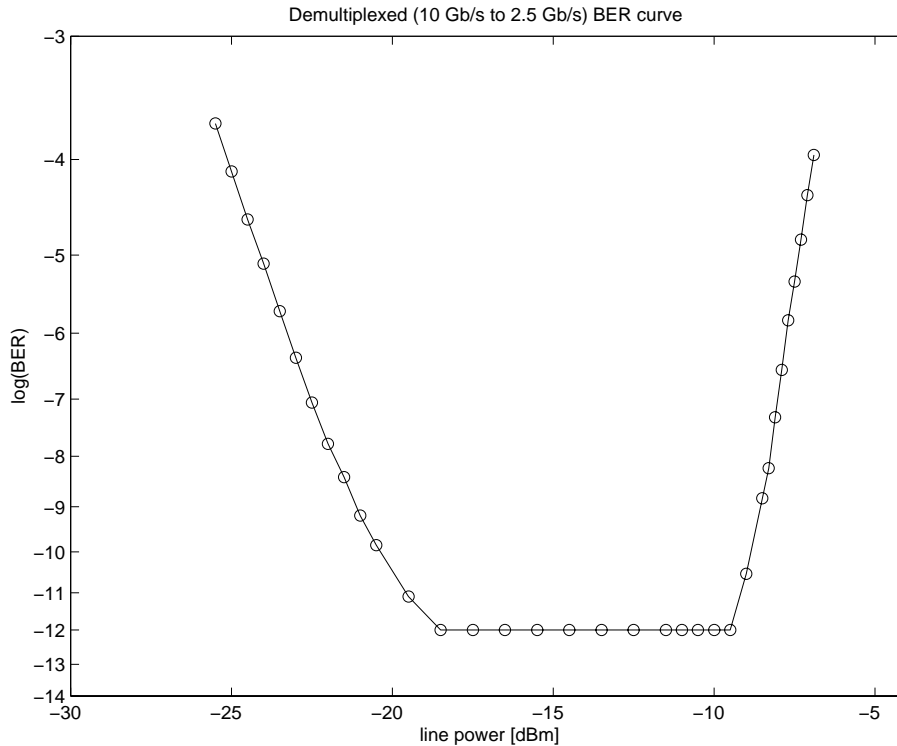


Figure 5.23: Bit error rate versus input power of the TOAD (point B). The amplifier asymmetry amounted to $\tau_{asym} = 25$ ps. τ_{delay} was set to 10 ps. The power of the switch signal equals to $P_{switch} = -3$ dBm. $I_{SOA-2} = 100$ mA.

The data signal is amplified in SOA-1 and stripped from outband ASE by the 1 nm broad optical band-pass filter-1. Attenuator-1 controls the input power to the optical switch which varies from -3.0 to -25.0 dBm. The wavelength and pulse width of this signal is 1311 nm and 20 ps, respectively.

The amplified 2.5 GHz sinusoidal clock signal modulates laser diode, LD-2, biased above threshold. LD-2 is a standard 2.5 Gb/s, $1.3 \mu\text{m}$ communication DFB laser diode. A sinusoidally modulated optical signal is obtained that controls the cross gain-switched ring laser. The output of the cross gain-switched ring laser is amplified and stripped of outband ASE. Attenuator-3 adjusts the switch signal input power to the optical switch in between the $+1.0$ and -15.0 dBm. Electrical delay-3 adjusts the delay between the 10 Gb/s data signal and the 2.5 GHz switch signal over a maximum range of 120 ps.

Both signals are fed into the TOAD based optical switch. At point D the delay is measured between the 10 Gb/s data signal and the 2.5 GHz switch signal with a digital sampling oscilloscope that visualises the power envelope of the switch and line signal as a function of time. The delay time τ_{delay} is defined as the smallest difference between the values of the time base belonging to the peak of the 10 Gb/s signal and the 2.5 GHz switch signal that follows

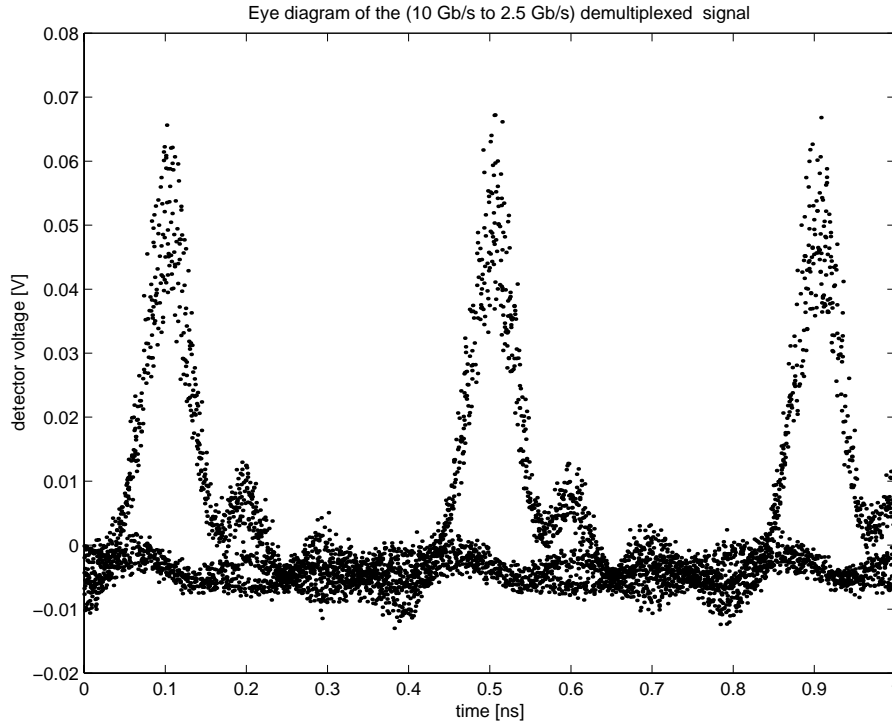


Figure 5.24: Eye diagram at the photodiode of the receiver for $P_{line} = -13$ dBm. The amplifier asymmetry amounted to $\tau_{asym} = 25$ ps. τ_{delay} was set to 10 ps. $I_{SOA-2} = 100$ mA. The power of the switch signal equals $P_{switch} = -3$ dBm.

directly behind.

τ_{asym} is set according to the following procedure. First adjustable delay-1 and polarisation controller-1 are adjusted such that in absence of the switch signal and with a high powered 10 Gb/s signal the output power at point E is minimal. In this position the amplifier is located in the centre of the polarisation insensitive Sagnac interferometer. Alteration of the delay results in an amplifier asymmetry, τ_{asym} , of half the read-out of the change of adjustable delay-1.

The optical band-pass filters, BPF-1 and BPF-2, are tuned to the wavelength of the 10 Gb/s data signal while BPF-3 and BPF-4 tune the switch signal to a different wavelength. In this configuration all optical band-pass filters have a -3 dB bandwidth of 1 nm.

At point E the forward directed or transmitted output of the demultiplexer can be measured. At point A the backward directed or reflected output signal of the demultiplexer can be measured. Points B and C are used to observe or measure the power of the 10 Gb/s line signal and the 2.5 GHz switch signal, respectively. All amplifiers are operated at 20° C. The pump current of SOA-1 and SOA-4 is set to 400 mA and 350 mA, respectively.

The cross gain-switched ring laser is adjusted as described in Sec. 5.1. At the output of the 2.5 Gb/s receiver the bit error rate can be determined for different input powers, delays, and

amplifier currents. In these experiments no autocorrelation traces or optical spectra were measured. The necessary equipment was not available at the time this experiment was carried out. Temporal responses are measured using a 45 GHz PIN-photodetector connected to a 50 GHz digital sampling oscilloscope for monitoring the 10 Gb/s input signal at point B and for determination of τ_{delay} at point D. A second digital sampling oscilloscope with a built in opto-electronic converter measured the transmitted or reflected output at points E and A, respectively. The wavelength of the switch signal is determined by an optical wavelength meter at point C.

5.3.3 BER performance versus input powers

An important parameter is the dependence of the performance of the demultiplexer on the amount of input power to the optical switch. Figure 5.23 displays the bit error rate curve as a function of input power to the optical switch. The amplifier asymmetry amounted to $\tau_{asym} = 25$ ps. The switch pulses, with a power $P_{switch} = -3$ dBm, followed the pulses of the channel to be demultiplexed after $\tau_{delay} = 10$ ps. The current of SOA-2 was set to 100 mA. If the power of the line signal becomes too low the demultiplexed signal at the output of the TOAD is covered with noise to an extent where error free detection is no longer possible. In other words, if the TOAD input is regarded as the receiver input the power of the line signal has dropped below the sensitivity of the optical demultiplexer which is part of the receiver. If the intensity of the line signal is too high the line signal will saturate the amplifier along with the switch pulse. Severe distortions will occur resulting in an increasing BER. For $P_{line} = -13$ dBm (four channels) the eye diagram of the signal at point E is depicted in Fig. 5.24.

It can be observed that a 2.5 Gb/s signal is available and that the eye is open. The ringing at the trailing edges of the pulses is a side effect resulting from the modulation of LD-1. Under these conditions the system ran stationary and error free for more than six hours.

In addition to the single curve of Fig. 5.23 similar BER curves have been measured for a variety of switch signal input powers and currents for SOA-2. At the same time the output power of the TOAD was measured. This way a clear picture is obtained for the dependence on the power of both line and switch signals. The results are displayed graphically in Fig. 5.25-5.28. For each BER measurement τ_{delay} , and the input power incident on the photodiode of the receiver have been optimised. BER measurements below 10^{-10} (error free) are mapped to 10^{-10} and BER above 10^{-3} are mapped to 10^{-3} . At this point it can be seen from the area where the BER is better than 10^{-10} that there exists an optimal amplifier current equal to 100 mA.

For low currents the amplifier does not provide enough gain for error free demultiplexing. Increasing currents result in more gain and a rising TOAD output power. At this point relatively large input powers are required to obtain error free demultiplexing. Once the current is set above 75 mA a broad area exists where demultiplexing is supported. Beyond the 125 mA the performance degrades independently from the power of the switch signal. When I_{SOA-2} reaches the 200 mA demultiplexing can no longer be observed. Figure 5.26 and 5.28 display an ever increasing TOAD output power with line power and amplifier current. There is no correlation between the BER performance of the demultiplexer and the output power. It is important to note that when the switch signal power decreases the amplifier becomes less saturated and the gain increases. As a result the output power of the TOAD is expected to

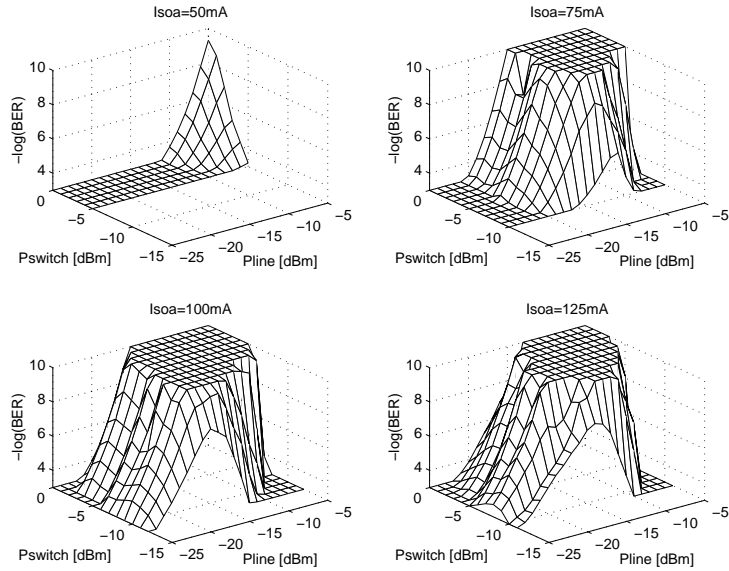


Figure 5.25: Bit error rate versus switch and line power of the TOAD (point B). The amplifier asymmetry amounted to $\tau_{\text{asym}} = 25$ ps. For each $P_{\text{switch}} = \text{constant}$ curve τ_{delay} is optimised.

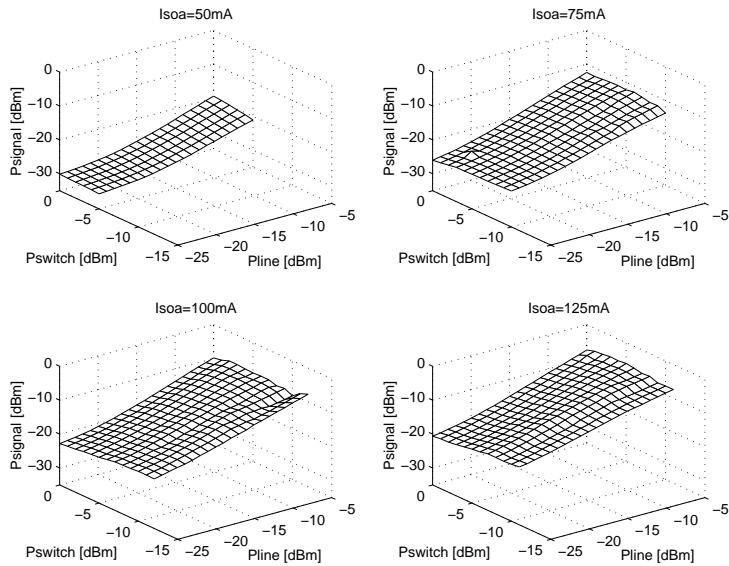


Figure 5.26: TOAD output power versus switch and line power. Conditions of Fig. 5.25 apply.

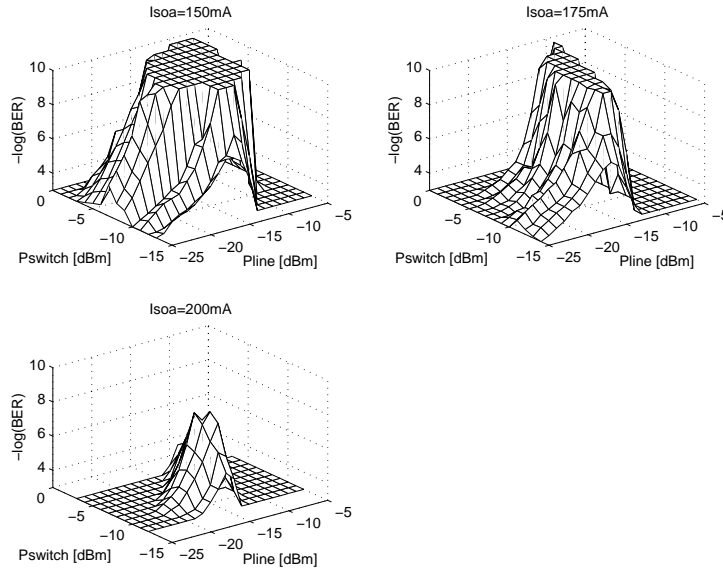


Figure 5.27: Bit error rate versus switch and line power of the TOAD (point B). The amplifier asymmetry amounted to $\tau_{\text{asym}} = 25$ ps. For each $P_{\text{switch}} = \text{constant}$ curve τ_{delay} is optimised.

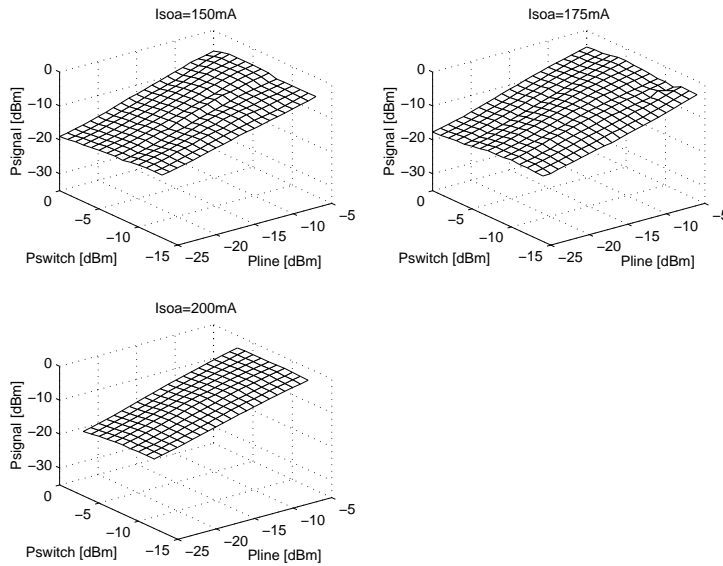


Figure 5.28: TOAD output power versus switch and line power. Conditions of Fig. 5.25 apply.

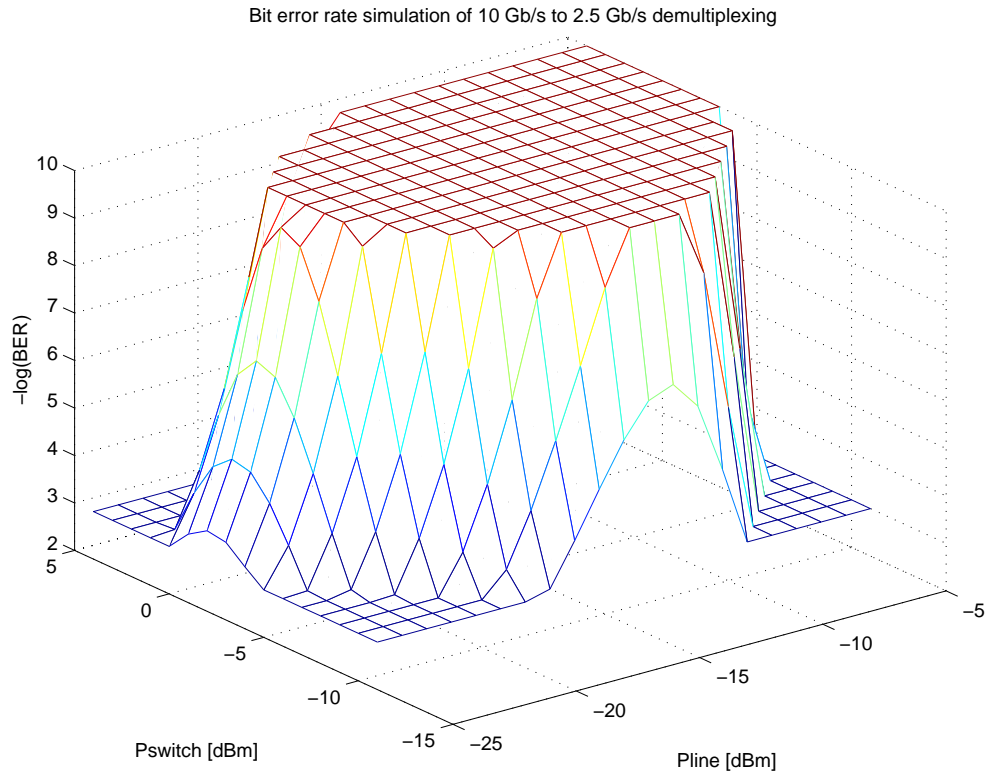


Figure 5.29: Simulated BER performance for different input powers and switch signal powers. $\lambda_{peak, SOA-1} = \lambda_{line} = 1310 \text{ nm}$, $\lambda_{switch} = 1320 \text{ nm}$, $BW_{SOA-1} = 60 \text{ nm}$, $BW_{line} = 1 \text{ nm}$, $G_{on \text{ chip}, SOA-1}(\lambda_{peak}) = 700$, $E_{sat, on \text{ chip}, SOA-1}(\lambda_{peak}) = 6 \text{ pJ}$, $E_{sat, on \text{ chip}, SOA-1}(\lambda_{switch}) = 7 \text{ pJ}$, $L_{SOA-1} = 800 \text{ }\mu\text{m}$, $v_g = 1 \cdot 10^8$, $\tau_c = 200 \text{ ps}$, $\alpha_H = 5$, $NF_{on \text{ chip}, SOA-1} = 6.5 \text{ dB}$. The coupling losses of the amplifier amount to 2.5 dB. Ideal couplers are assumed. Loss in the left and right branch amount to 4 dB. $\tau_{asym} = 25 \text{ ps}$, $\tau_{delay} = 10 \text{ ps}$. The quantum efficiency of the detector amounts to 0.8, the electrical bandwidth equals 2.5 GHz, the optical bandwidth amounts to 1 nm. The thermal noise current of the receiver for these parameters amounts to 2.1 μA .

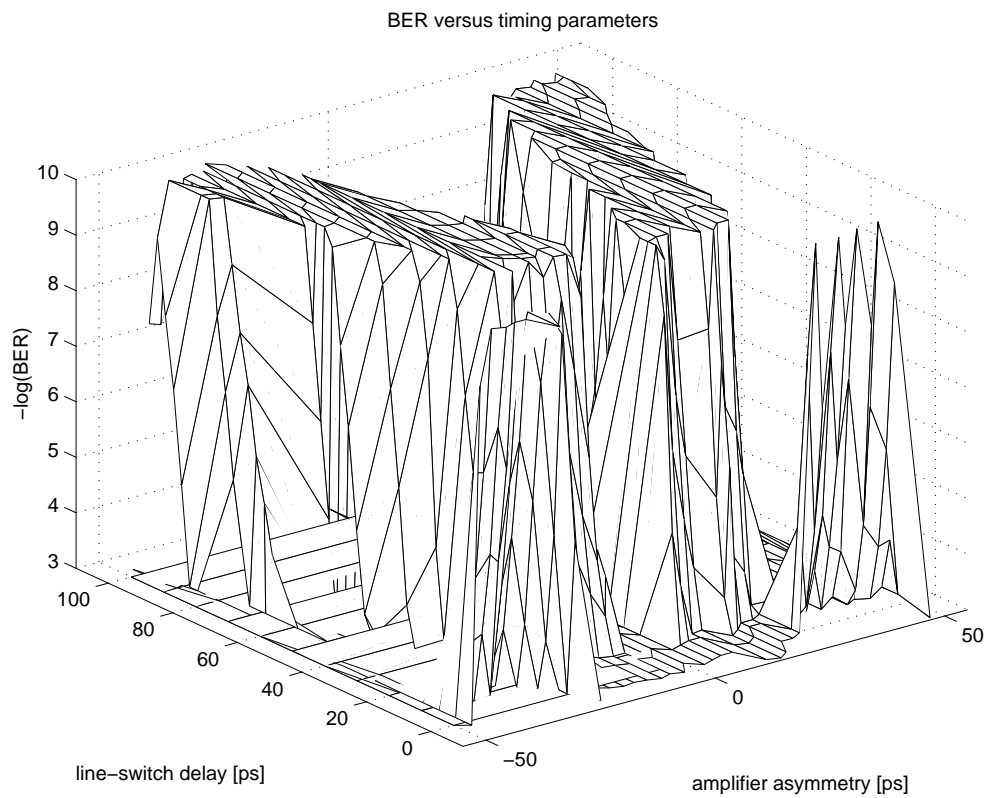


Figure 5.30: Bit error rate versus amplifier asymmetry, τ_{asym} , and line-switch signal delay, τ_{delay} , of the TOAD. $P_{line} = -13$ dBm, $P_{switch} = -6$ dBm and $I_{SOA-2} = 100$ mA.

rise. However, less switch power results in switching with a lower contrast, caused by a reduction of the 180° phase difference between the clockwise and counter clockwise travelling signal. This results in a smaller gain of the temporal window formed by the optical demultiplexer. This counteracts the increase of gain due to the reduced saturation of SOA-2. The slope of the surface for varying line power and constant switch power is not exactly as was to be expected if the line signal does not saturate the amplifier. These measurements show that the line signal does saturate the amplifier. This is expected as high gain amplifiers were implemented. Saturation of SOA-1 by the line signal does not compromise error free performance as long as the intensity of the switch signal is approximately 6 dB larger than the intensity of the TOAD input signal.

Figure 5.29 displays a numerical simulation of this experiment. The amplifier model introduced in Sec. 2.3.3 has been incorporated in this simulation to enable the computation of bit error rates. The signal to be demultiplexed is a 10 Gb/s, $2^7 - 1$ PRBS modulated soliton shaped signal with a full-width half-maximum pulsewidth of 20 ps at 1310 nm. The 2.5 GHz switch signal pulses also have a width of 20 ps and a wavelength of 1320 nm. The parameters of SOA-1 were matched to the practical case of a 100 mA biased SOA. In addition to differences in parameters between the experimental setup and the numerical simulation, τ_{delay} has been adjusted for optimum BER performance during the experiments which was not the case for the numerical simulation. Despite these differences the measured and simulated surfaces show good agreement.

5.3.4 BER performance versus time delays

In addition to the power dependence of the demultiplexer performance of Sec. 5.3.3 correct timing of the system is also of great importance. Generally, the performance of the system is largely determined by the amplifier asymmetry and the delay between the line and switch signals. Figure 5.30 displays the dependence of the bit error rate on the above mentioned asymmetry, τ_{asym} , and delay, τ_{delay} as defined in Chapter 2. For positive amplifier asymmetries τ_{delay} is defined as the smallest positive difference between a pulse of the line signal and the switch pulse arriving τ_{delay} later. This delay is measured and monitored at point D. For negative amplifier asymmetries the delay is recalculated as if coupler-3 were in the left branch.

For amplifier asymmetries with $|\tau_{asym}| \leq 50$ ps a line-switch delay can be found for which error free demultiplexing is achieved. For amplifier asymmetries ranging between ± 15 and ± 30 ps variations in a line-switch delay of more than 50 ps are allowed for error free demultiplexing. This indicates that the configuration is insensitive to time jitter. The structure of Fig. 5.30 is line symmetric in $\tau_{asym} = 0$. This was expected as a result of the coupler specifications in Chapter 2. If coupler-2 had a significant deviation from 90° then the surface plot should not have been symmetric.

5.3.5 Miscellaneous experiments

Incorrectly set demultiplexing parameters

Optimisation of the performance of the demultiplexer can not be performed by solely observing the output power. From the temporal envelope of the outputs one can obtain information that can be related to incorrectly set parameters. Malfunctioning of the demultiplexer is

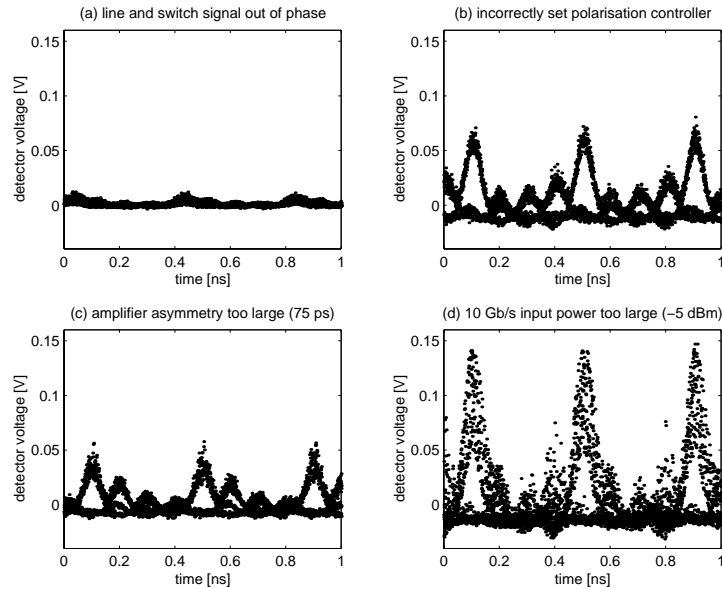


Figure 5.31: Eye diagrams of the demultiplexed signal can provide insight into incorrectly set parameters.

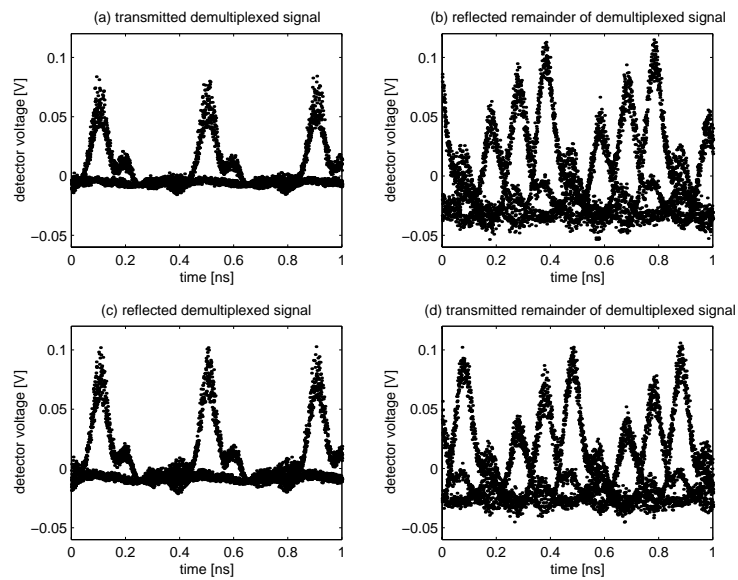


Figure 5.32: Eye diagrams of the demultiplexed signal that can either be transmitted to the forward directed output (point E) or be reflected to the backward directed output (point A).

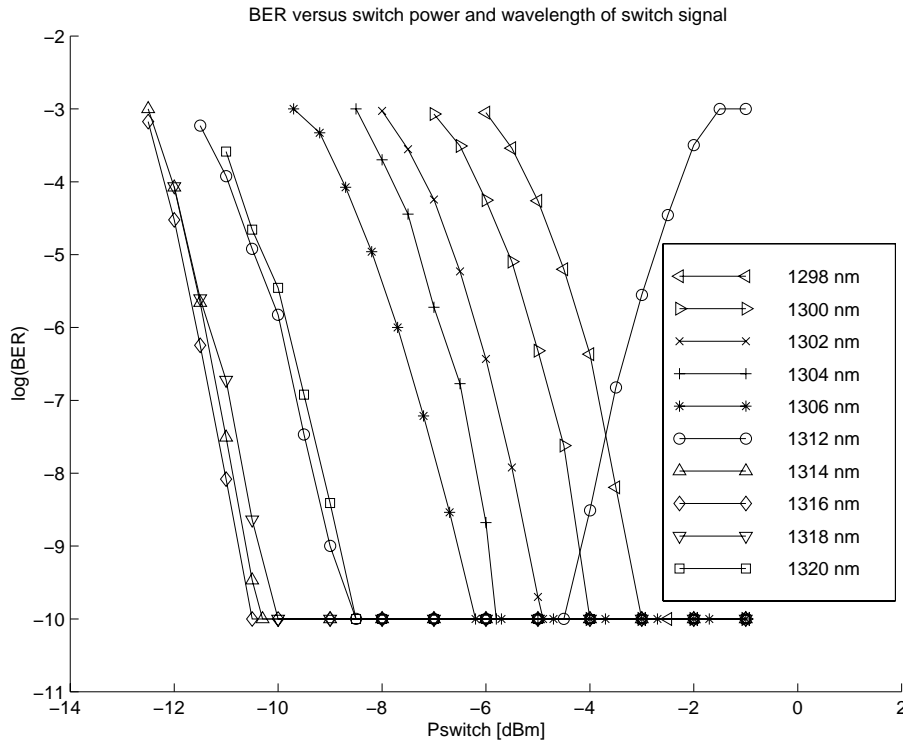


Figure 5.33: BER performance on wavelength and power of the switch signal. $P_{line} = -16$ dBm, $\tau_{asym} = 25$ ps, $\tau_{delay} = 10$ ps and $I_{SOA-2} = 100$ mA.

usually caused by a wrongly set line-switch signal delay, an incorrectly set polarisation controller, an amplifier asymmetry that is too large or an input power that exceeds a maximum. Figure 5.31 displays eye diagrams of different demultiplexed signals where one system parameter was not adjusted correctly. In subplot (a) the delay between the line and data signal is set incorrectly. As a result the window in time is located between two 2.5 Gb/s channels resulting in zero output power. Subplot (b) displays the eye diagram for a polarisation mismatch in the loop. This results in parasitic eyes of increasing power with time. If the amplifier asymmetry is too large the window extends beyond the channel to be demultiplexed (c). Additionally, in this case parasitic eyes exist, but now of decreasing power with time until the next demultiplexed pulse appears. If the input power is too large (d) the signal switches itself resulting in what appears as a significant eye closure and parasitic eyes. In all the cases (a) to (d) a BER of $\geq 10^{-3}$ was measured. Except for the wrongly set system parameters the same settings as in Sec. 5.3.3 were used. Observation of the eye diagram at the output of the all-optical demultiplexer allows the determination of wrongly set parameters and of the action that should be taken to improve performance.

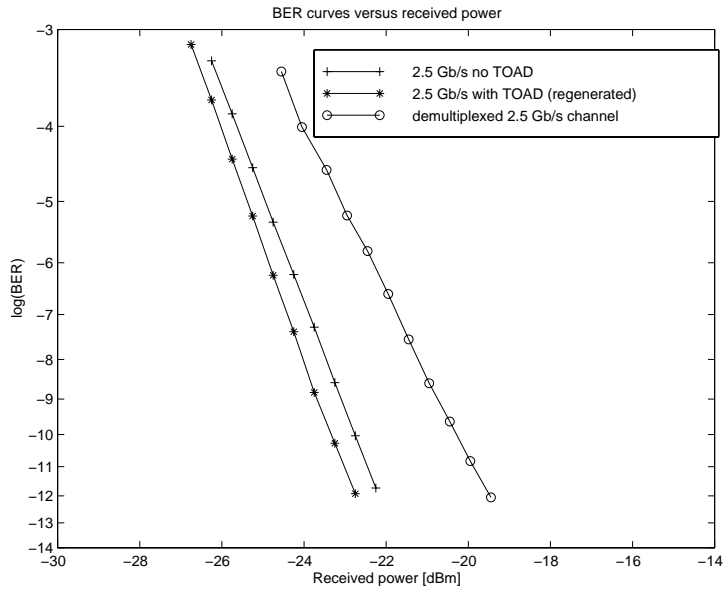


Figure 5.34: Penalties of the all-optical demultiplexer configuration

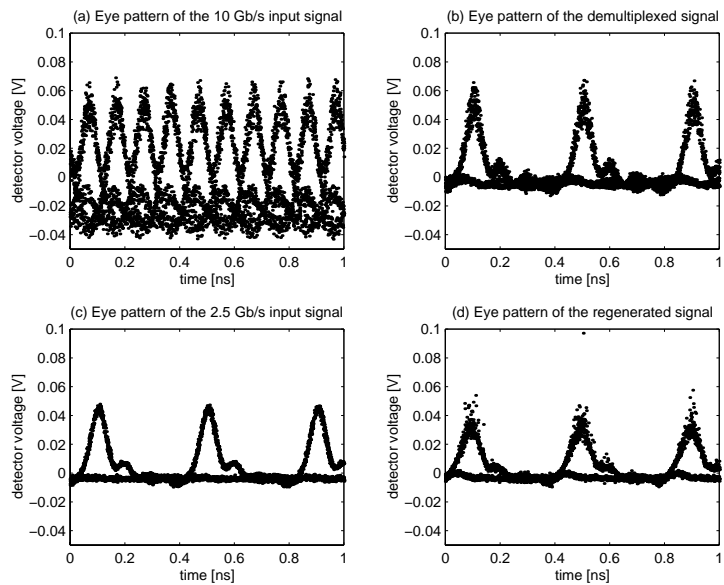


Figure 5.35: (a) Eye diagram of the 10 Gb/s line signal. (b) Eye diagram of the demultiplexed signal. (c) Eye pattern of the 2.5 Gb/s input signal. (d) The regenerated eye diagram.

Reversed operation of the TOAD

The polarisation controller 1 in the loop is set in such a way that an additional phase shift of 180° is added. The demultiplexed signal will, instead of being transmitted, be reflected. Figure 5.32 displays the eye diagrams of the demultiplexed signal for normal operation (subplots (a) and (b)) and for operation where the polarisation controller adds 180° phase (subplot (c) and (d)). In both cases the remainder of the demultiplexed signal contains the eye diagrams of the remaining three channels. These three eyes are of different power as a result of the periodic (2.5 GHz) gain saturation.

Performance dependence on the switch signal wavelength

In the previous experiments the wavelength of the switch signal was set to 1320 nm, shifted far away from the wavelength of the line signal. For different wavelengths the bit error rate was measured as a function of switch signal input power. The input power of the line signal was set to -16 dBm. This way even for low switch powers the saturation of SOA-2 is not influenced by the line signal. Figure 5.33 displays the dependence. Around $\lambda_{switch} = 1316$ nm the TOAD reaches its maximum sensitivity to the switch signal power. Less than -10 dBm of optical switch power is required to obtain error free demultiplexing. If the wavelength is decreased to shorter wavelengths more power is required for error free operation. At 1312 nm the wavelength of the switch signal lies too close to the wavelength of the line signal and severe cross talk limits performance for higher powers of the switch signal. This experiment displays the advantage of using a switch signal of longer wavelength.

Polarisation sensitivity

The polarisation sensitivity of the TOAD based demultiplexer has been determined by placing a polarisation controller at the input of the TOAD. For future planned transmission experiments it is of the utmost importance that the polarisation sensitivity is small. Rotation of the wheels of the polarisation controller resulted in power variations of less than 0.7 dB at the input of the 2.5 Gb/s receiver. The implication to the BER performance depends on the amount of input power to the optical switch and the receiver. If the line input power is between the maximum and minimum allowed power no deterioration in BER performance is perceived. If the line input power corresponds to a value on a BER slope variations in BER are observed. Experimentally observed variations in the BER correspond to BER variations following from these power fluctuation mapped to Figs. 5.25-5.28.

Penalties

Insertion of an optical demultiplexer generally causes a reduction in performance. To measure this the 10 GHz pulse train at the transmitter side is modulated with a 10 Gb/s PRBS signal where every second, third and fourth bit are set to zero. This is done for a $2^7 - 1$ PRBS sequence. This pattern is programmed four times at bit level into the memory of the pulse pattern generator. As the size of this memory is limited, only short PRBS sequences fit. The input level of the line signal to the optical demultiplexer is set to -13 dBm and the switch power to -6 dBm. The input power to the photodiode of the receiver is varied with an optical attenuator and for different input powers the BER is measured. This is done for three different

situations. First a 2.5 Gb/s signal is generated and fed into the receiver. Figure 5.34 displays this curve (+) which is the reference or back to back BER curve. Secondly the TOAD switch and cross gain-switched ring laser are inserted and a BER curve is measured. In Fig. 5.34 this curve is referred to as the regenerated curve (*). Finally a 10 Gb/s signal is applied to the TOAD and a BER measurement is performed on the 2.5 Gb/s demultiplexed signal (o). With respect to the base line the demultiplexed curve displays a power penalty of 2.3 dB at a BER of 10^{-9} . The regenerated BER curve displays a negative penalty of 0.6 dB at a BER of 10^{-9} . The eye diagrams of the signals involved are depicted in Fig. 5.35. Although the eye diagram of the regenerated 2.5 Gb/s signal (subplot (d)) looks more distorted than the 2.5 Gb/s input signal the bit error rate curve indicates a small improvement. This discrepancy can be explained from the sensitivity of the 2.5 Gb/s receiver to the pulse width of the received signal. As stated in Chapter 3 the 2.5 Gb/s receiver is sensitive to the spectral content of the detected signal. The spectral content of the regenerated signal will be different from the 2.5 Gb/s line signal because of the interaction with the nonlinearity of the optical demultiplexer. This was not experimentally confirmed. The 2.3 dB penalty of the demultiplexed 2.5 Gb/s signal is most likely caused by channel cross talk which manifests itself through degrading BER performance when in-band ASE is present. In addition, pattern effects due to amplifier saturation contribute for a minor part to this penalty.

5.3.6 Discussion and Conclusions

From the results presented in the previous subsections some important parameters are indicated and conclusions are drawn. The difference between the minimum input line power and the maximum line power before the BER exceeds the 10^{-9} error margin can be defined as the dynamic range of the demultiplexer and should be as large as possible. The maximum dynamic range obtained in this experiment is 13 dB. It is the dynamic range that enables the demultiplexer to compensate for power penalties that occur once a transmission link is added to the system and dispersion and noise deteriorate the received line signal. The polarisation sensitivity should be subtracted from this figure to obtain a more realistic value. The minimum switch signal power has been measured to be ≈ -10 dBm. Low switch powers result in a SOA that is not unnecessarily saturated and will therefore exhibit a high gain. This is important because the demultiplexer will also function as an optical preamplifier in OTDM transmission systems. The adjustment of the parameters can be made by optimising the BER or by observing the eye diagram of the demultiplexed signal. Analysis of the eye diagram is preferred as it allows more direct adjustment and control of essential system parameters. An automated management system could be realised by using digital (image) processing technology. Successful 10 Gb/s to 2.5 Gb/s demultiplexing is demonstrated using a purposely designed cross gain-switched ring laser. With respect to future 40 Gb/s to 10 Gb/s demultiplexing experiments there is no reason not to use these long MQW SOAs as was the case for in-line use. A decrease of dynamic range and an increased sensitivity to time jitter (smaller intervals for τ_{asym} and τ_{delay}) could pose as possible system performance limiting factors.

5.4 40 Gb/s to 10 Gb/s all-OTDM

5.4.1 Introduction

The realisation of the TOAD based optical switch in combination with a 10 GHz optical clock recovery circuit that provides the narrow optical switch pulses allows the realisation of a 40 Gb/s to 10 Gb/s demultiplexer. In the next subsection the experimental configuration required for implementation is detailed. Section 5.4.3 deals with the performance of this configuration. Limited BER measurements have been performed compared to Sec. 5.3 because the introduction of the optical clock recovery in a feedback configuration with the optical switch does not improve the mechanical stability of the entire system. In Sec. 5.4.6 the results are discussed. Conclusions are drawn and directed towards 40 Gb/s transmission experiments discussed later.

5.4.2 Experimental setup

Figure 5.36 displays the optical scheme of the 40 Gb/s to 10 Gb/s all-optical demultiplexer. The 10 Gb/s pulse pattern generator provides a 10 GHz clock for the external-cavity tuneable mode-locked laser (ECTMLL) generating a 3 ps wide optical pulse train. A 10 Gb/s NRZ pattern is superimposed on this pulse train via the modulator. A booster amplifier, booster-1, is inserted to compensate for the intrinsic modulator loss. After this amplifier a 10 Gb/s RZ signal is available to the input of the optical multiplexer.

The optical multiplexer is a passive functional unit built up around splitter-1 and -2 and adjustable optical delays-1, -2, -3 and -4. Each delay consists of a length of optical fibre to achieve a coarse delay between the channels and to decorrelate the phase and state of polarisation of the individual channels. An adjustable optical delay allows fine tuning of the position of each 10 Gb/s channel in the 40 Gb/s data signal (delay 1-4). The four time delayed replicas of the 10 Gb/s signal are re-joined by using splitter-2. The delays of channel 2, 3 and 4 to channel 1 amount to 2150.3 ps, 4500.8 ps and 6675.5 ps, respectively. The insertion loss amounts to 9.3 dB of which 6 dB is due to the second splitter. Connector losses, excess loss of the splitters and losses in the lens ferrule based adjustable delays account for the remaining 3.3 dB loss. The four branches do not contain polarisation-maintaining fibre or polarisation controllers. Therefore the polarisation of each channel is random. This will not degrade the performance of the demultiplexer or the transmission link (Sec. 5.5) because any polarisation dependent saturation of the amplifiers will further be reduced, although it might result in small differences in performance between individual channels. After the optical multiplexer and attenuator-1, SOA-1 amplifies the signal to a level where it can be launched into e.g. an optical link.

Filter, BPF-1, is used to remove out-band ASE from the 40 Gb/s signal that is incident to the optical demultiplexer. Figures 5.37 and 5.38 display the physical realisation of the transmitter and optical multiplexer, respectively. The construction of the TOAD based switch is similar to the one constructed in Sec. 5.3 with the exception that coupler-1 (FBT 124) was replaced by another coupler (FBT 118). This coupler had less than ideal properties with respect to the 90° phase shift between the output ports (See Chapter 2). Following the numerical simulation results of Chapter 2, implementation of this non-ideal coupler can improve the performance of the demultiplexer. The output of the TOAD is filtered (BPF-2) such that the switch signal

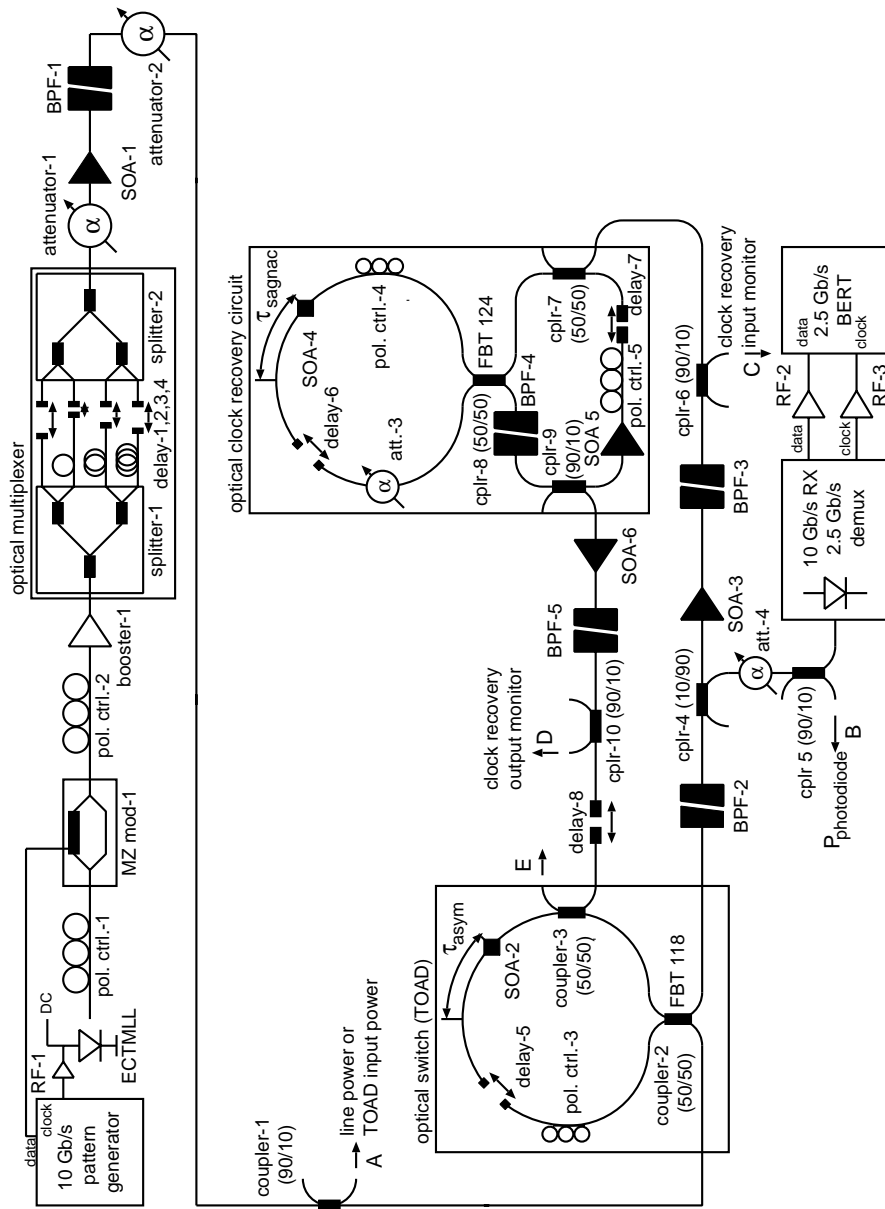


Figure 5.36: Experimental setup of the 40 Gb/s to 10 Gb/s all-OTDM system.

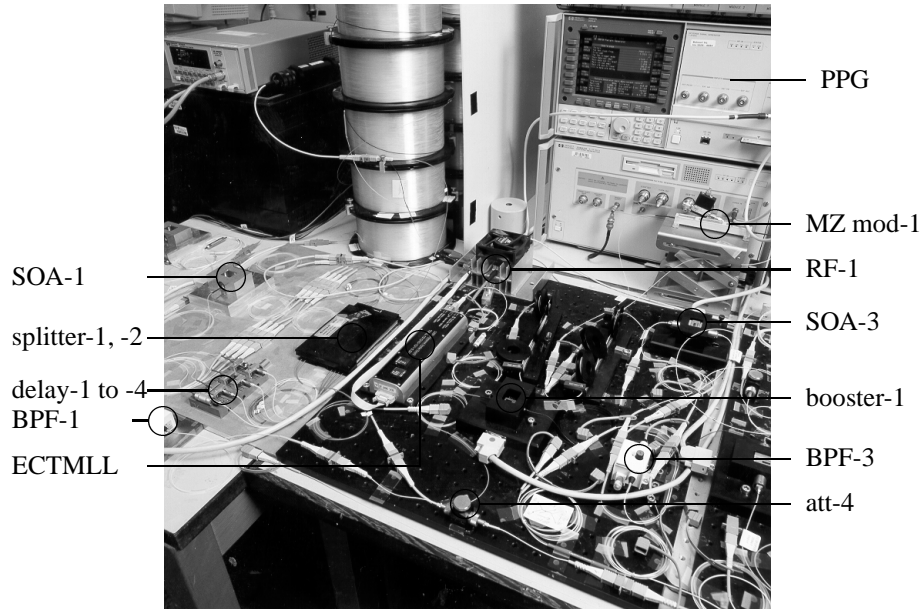


Figure 5.37: Experimental realization of the transmitter and optical multiplexer

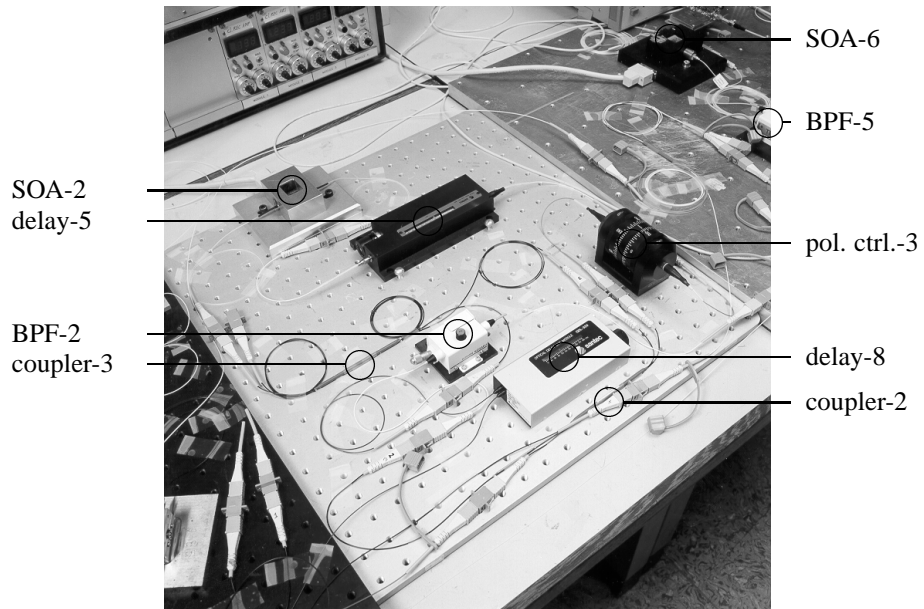


Figure 5.38: Experimental realization of the optical switch (TOAD)

is removed. The remaining demultiplexed signal is partly injected into the receiver and partly amplified (SOA-3) after which it is fed into the optical clock-recovery circuit. Couplers-1, -3, -5, -6 and -10 are used for monitoring purposes. The output of the clock recovery is amplified (SOA-6), filtered (BPF-5) and delayed in an adjustable delay (delay-8) for controlling the phase between the line and switch signals.

Before measurements are performed, the system is started by transmitting only one highly powered channel. This channel is fed into the demultiplexer in absence of the switch signal. The unsaturated TOAD amplifier (SOA-2) exhibits a high gain and saturates on this signal. Despite a distorted appearance of the channel at the output of the TOAD, the clock recovery circuit will lock upon the 10 GHz component of this signal and a train of recovered pulses becomes visible. These pulses are fed into the switch signal input of the TOAD. Under the assumption that the amplifier asymmetry and line-switch signal delay are set correctly, the signal at the output improves in such a way that operation of the clock recovery circuit improves further. After optimisation with respect to the BER of all the controls the remaining channels are switched on one by one. Once all the settings are optimised the system remains stable for ≈ 30 minutes after which readjustment is required to keep the system synchronised.

5.4.3 BER performance versus input powers

The performance of the OTDM transmission systems depends strongly on the amount of power variation that is allowed at the input of the optical switch in Fig. 5.36. In Fig. 5.39 the bit error rate is measured for different input powers of the optical switch. This is done for all four channels. The dynamic input range, at a BER of 10^{-9} , equals 7.1, 7.2, 6.9 and 6.9 dB for channel 1, 2, 3 and 4, respectively. The average sensitivity of the demultiplexing receiver is achieved for $P_{line} = -15.6$ dBm. If the input power increases to -8.4 dBm no error free (BER = 10^{-9}) demultiplexing is observed. The maximum difference in receiver sensitivity exists between channel four and channel two and amounts to 0.9 dB at a BER of 10^{-9} . These four curves have been measured for $P_{switch} = 0$ dBm, $\tau_{asym} = 8$ ps, τ_{delay} and $P_{photodiode}$, the power incident on the photodiode of the receiver, are all optimised for each data point. The current of SOA-2 equals 175 mA. The currents of SOA-3 and SOA-6 are adjusted such that the experimental conditions are met with respect to P_{switch} . SOA-4 and SOA-5 are adjusted such that stable clock recovery takes place and variations of attenuator-3 can be as large as possible while maintaining stable clock recovery. Attenuator-3 and polarisation controllers-4 and -5 are adjusted such that the 10 GHz component of the recovered clock signal that is available as a trace on the digital sampling oscilloscope exhibits minimal amplitude and timebase related fluctuations. Delay-7 is adjusted such that the roundtrip time is a multiple of 100 ps. Delay-6 is adjusted such that the amplifier is located between the centre of the loop and the position where the system locks up which occurs for $\tau_{asym} \approx 10$ ps. This adjustment is an iterative process where no unique settings exist. This is due to the interdependence of parameters and the limited ways of observing and assessing the quality of the recovered clock and the demultiplexed signals (BER and temporal envelope from the digital sampling oscilloscope). Fig. 5.40 has been likewise measured with the exception that the input power to the switch equals $P_{line} = -13$ dBm and P_{switch} is varied by adjusting the gains of SOA-6 and SOA-3. Under these conditions an averaged swing over the four channels of 4.6 dB in P_{switch} guaranties error free demultiplexing. The differences in sensitivity to fluctuations

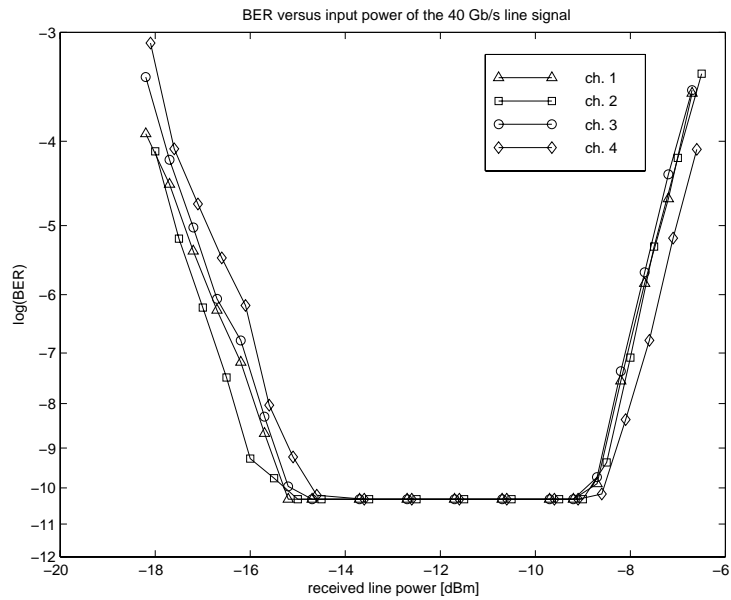


Figure 5.39: BER performance of the all-optical demultiplexer for different 40 Gb/s line signal input powers.

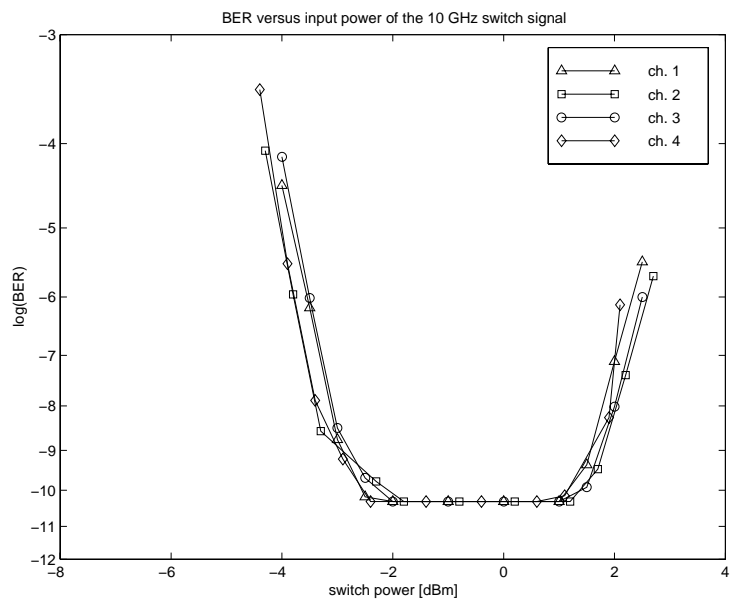


Figure 5.40: BER performance of the all-optical demultiplexer for different 10 GHz switch signal input powers.

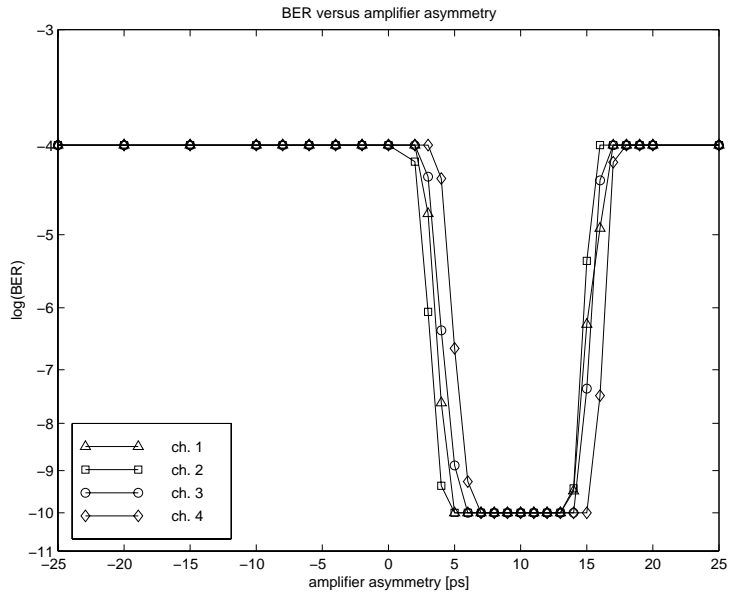


Figure 5.41: BER performance of the all-optical demultiplexer for different amplifier asymmetries.

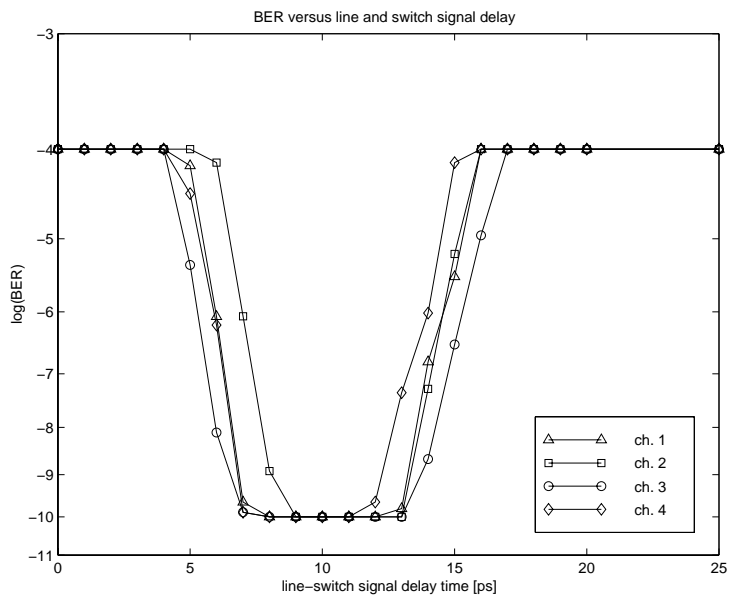


Figure 5.42: BER performance of the all-optical demultiplexer for different line-switch signal delay.

in P_{switch} between individual channels is limited to ≈ 0.8 dB at a BER of 10^{-9} .

5.4.4 BER performance versus time delays

Equally important as the line and switch signal input power dependent performance of the demultiplexer is the effect of amplifier asymmetry and line signal to switch signal delay on the BER performance. For $P_{line} = -13$ dBm and $P_{switch} = 0$ dBm the BER has been measured for different amplifier asymmetries. Fig. 5.41 displays the results graphically. For channel 1, 2, 3 and 4 the allowable amplifier asymmetry varies between 4.6 – 14.1 ps, 4.0 – 14.1 ps, 5.1 – 14.3 ps and 5.9 – 15.4 ps, respectively. From the graph it is observed that the amplifier should be located 10 ± 2 ps from the centre of the loop. However, when implemented after a transmission link possible dispersion induced pulse broadening requires a smaller time window and therefore a smaller amplifier asymmetry. An amplifier asymmetry of 8 ps is therefore more realistic. In addition the BER curves in Fig. 5.41 are not symmetrical in $\tau_{asym} = 0$. Demultiplexing is only observed for positive amplifier asymmetries. This is in stark contrast with Fig. 5.30 where the BER performance is line symmetric with respect to $\tau_{asym} = 0$. The main reason for this lies in the fact that a different coupler is used compared to the 10 Gb/s to 2.5 Gb/s demultiplexer. The phase difference between the output ports of this coupler deviates from the ideal 90° . From Chapter 2 this automatically has consequences for the channel extinction ratio which improves for $\tau_{asym} > 0$ but deteriorates for $\tau_{asym} < 0$. Moreover, performance will depend strongly on τ_{asym} because of its influence on the residual phase shift between the clockwise and counter clockwise travelling time intervals that correspond to the channels not demultiplexed. This phase shift from 90° should preferably match twice the deviating phase between the output ports of the coupler. For amplifier asymmetries beyond 15 ps the time window becomes too broad and neighbouring channels interfere. This is interesting because in this case the window is larger than the 25 ps bit time. In addition to the amplifier asymmetry the delay between the line and switch signal is also of importance. To this end under the same conditions with $\tau_{asym} = 8$ ps the delay between the line signal and switch signal is varied and the BER measured. This is done for all four channels. Fig. 5.42 displays the result. Optimum performance for all four channels is achieved if the switch pulse travels 8 – 12 ps behind the pulses of the channel to be demultiplexed.

5.4.5 Miscellaneous experiments

In this section outcomes and findings of additional experiments are presented. In contrary to Sec. 5.3 eye diagrams are not presented here but in Sec. 5.5 where a 216 km transmission experiment is performed.

Polarisation sensitivity

Similar to the 10 Gb/s to 2.5 Gb/s OTDM experiment the sensitivity of the experimental setup to polarisation rotations at the input of the optical switch is investigated. To this end a polarisation controller was placed before the input of the optical switch. The polarisation controller consisted of a quarter-wave plate and a half-wave plate which allows variation between all states of polarisation. Power fluctuations within 0.4 dB are observed and are

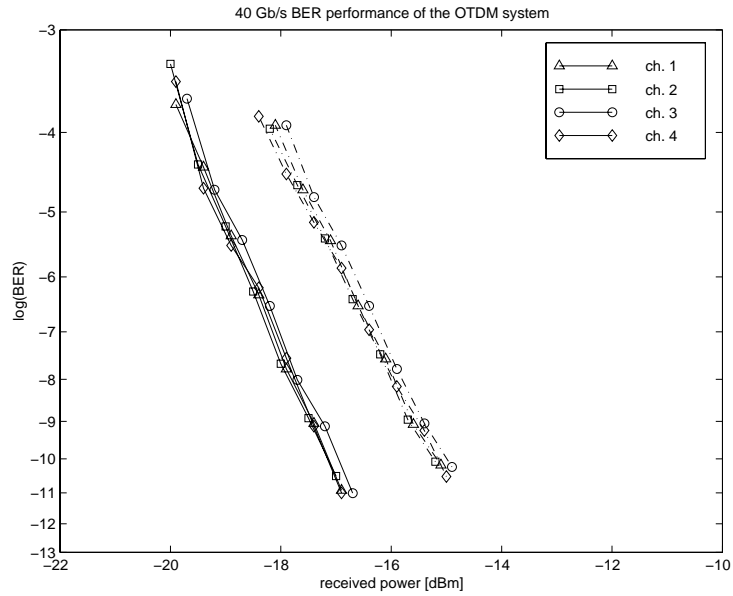


Figure 5.43: BER performance of the all-optical demultiplexer (solid line: without all-OTDM, dashed-dotted line with all-OTDM)

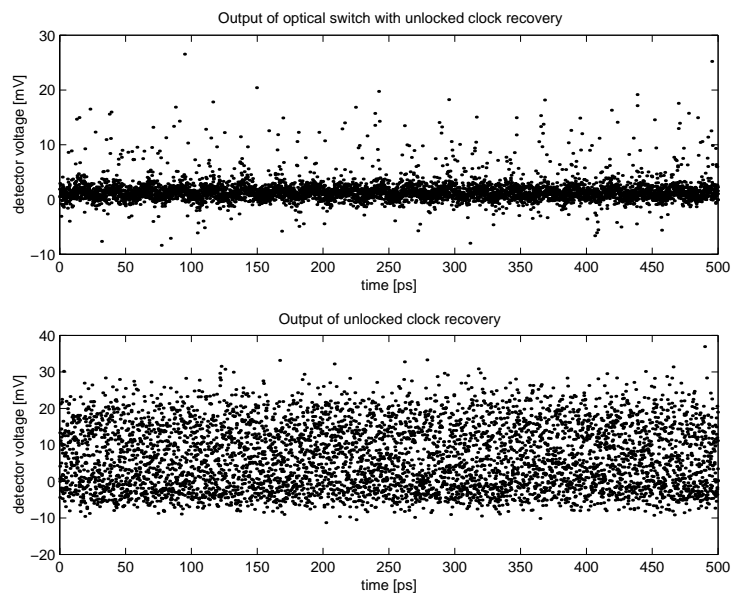


Figure 5.44: Typical eye diagrams of the TOAD output and clock recovery output when the system has crashed

uncorrelated with readouts of both indicator rings of the wave plates. For all states of polarisation the system remains locked to the relevant demultiplexed channel. In this experiment the TOAD amplifier is saturated more severely than in the lower bit rate experiment (higher switch energies and higher gains). This explains partly the improved insensitivity to changes in the state of polarisation at the input compared to the 0.7 dB of the low speed demultiplexer. The implementation of a different coupler with different residual polarisation sensitivity also changes the polarisation sensitivity.

Penalties

For all four channels the bit error rate performance is investigated. First, back to back BER measurements are performed where the BER is measured as a function of signal power incident to the photodiode, $P_{photodiode}$. Next, the multiplexer and optical demultiplexer are inserted. BER measurements are performed for each channel with the other channels present. Figure 5.43 displays the four BER curves with and without the OTDM system. The average power penalty introduced by the OTDM system is 1.9 dB. As the BER measurement time increases beyond ≈ 30 minutes, alignment and control of the polarisation controllers and delay lines was needed to keep the system operational. The experimental conditions are: $P_{line} = -13$ dBm, $\tau_{asym} = 8.5$ ps, $P_{switch} = -3$ dBm, $\lambda_{line} = 1305.5$ nm, $\lambda_{switch} = 1312.8$ nm, $2^{23} - 1$ PRBS pattern. The current of SOA-2 equals 175 mA. The amplifiers of the all-optical clock recovery unit are biased as described in Sec. 5.2. The delay between the line and switch signal (controlled by delay-8) varied between 7 ps and 12 ps. Similar to the 10 Gb/s to 2.5 Gb/s demultiplexing experiment, the penalty is mainly caused by channel crosstalk while pattern effects are believed to have a minor influence on this penalty.

Instabilities

Already mentioned in this section is the occasional lock-up of the system. If this occurs the output of the clock recovery and optical switch typically resemble the image shown in Figure 5.44. From this state the system can be brought back into service by switching off all but one of the channels and at the same time by increasing the input power to the optical switch or by obstructing the recovery of the switch signal. This way a 10 GHz component appears at the output of the optical switch on which the optical clock recovery circuit can lock. Careful adjustment of parameters postpones this seizure but eventually the system seizes up as readjustments can no longer be made or have been made in the wrong direction. As stated before without corrections made every 10 to 15 minutes the system operates for a maximum of ≈ 30 minutes. With periodic readjustments it is possible to keep the system running for times exceeding the 2 hours which is long enough to measure a BER curve. The instabilities are believed to be caused by either mechanical vibrations and/or temperature induced divergence of critical lengths of e.g. the cavity length of the clock recovery circuit. Adjustment of amplifier currents result in changing refractive indices and thus in shorter or longer propagation delays that can either compensate or strengthen variations in cavity length. Also variations in optical power can stop system operation. For example, higher input powers result in a stronger input signal to the clock recovery circuit. Besides pattern effects on the recovered clock the amplitude of the recovered clock can decrease because amplifiers in the

clock recovery circuit become more heavily saturated. A weaker switch signal will cause less saturation of the amplifier in the optical switch which rises the gain of that amplifier. Consequently the output of the optical switch rises which in turn decreases the power of the recovered clock pulses. This process continues until either the clock recovery locks up or the output of the optical switch is distorted to a degree where bit error rate measurements can no longer be performed. The system can be made less sensitive to power fluctuations by driving amplifiers into saturation. This way the output of the amplifiers becomes less sensitive to power fluctuations at the input. The system can also be adjusted such that a decrease in switch signal power results in a smaller forward gain of the window that fits the demultiplexed channel. This reduction in forward gain could compensate the gain increase due to lesser gain saturation.

5.4.6 Discussion and conclusions

In this section two functional blocks successfully interact with each other to form an all optical demultiplexer with all optical clock recovery. The combination is able to demultiplex a 10 Gb/s channel out of a 40 Gb/s line signal. The introduction of 10 to 40 Gb/s optical multiplexing and demultiplexing from 40 back to 10 Gb/s results in an average power penalty of 1.9 dBm. The behaviour of all channels is approximately identical. The maximum deviation in receiver sensitivity between two channels amounts to 0.5 dB. Despite the periodically required readjustment of specific controls this system was used in a ≥ 200 km, 40 Gb/s transmission experiment.

During the measurements it was found that the configuration is sensitive to mechanical vibrations and temperature induced fluctuations of the state of polarisation. This results in polarisation mismatch in the Sagnac based absorber and the TOAD based demultiplexer. If not corrected, eventually the performance of these subsystems deteriorates and the system will go off-line. Small BER optimising re-adjustments made every 10 to 15 minutes ensure long term operation. The re-adjustments should be made carefully as a strong re-adjustment in the wrong direction (degrading BER) may cause the system to crash. If this happens the recovered clock and data signal can only be restored by following the procedure of Sec. 5.4.2. The BER curves have been measured by optimising between individual BER measurements (data points) but with the restriction that if the system crashes the BER curve is re-measured from the beginning. Temperature and stress induced polarisation rotations in the optical clock recovery circuit require periodic readjustment of the adjustable delay lines to compensate for polarisation dependent roundtrip times. Adjustment of this delay line causes deviations in the line to switch signal delay time. Although this deviation can be compensated for by re-adjusting delay line-8, large scale BER versus amplifier asymmetry and line-switch signal delay measurements are impractical.

5.5 216 km, 40 Gb/s transmission using SOAs

5.5.1 Introduction

The OTDM setup of Sec. 5.4 has only relevance if it can be incorporated into a long-haul transmission system. In this section a ≥ 200 km transmission experiment is performed. The acquired experience recorded in earlier sections of this thesis on the implementation of SOAs

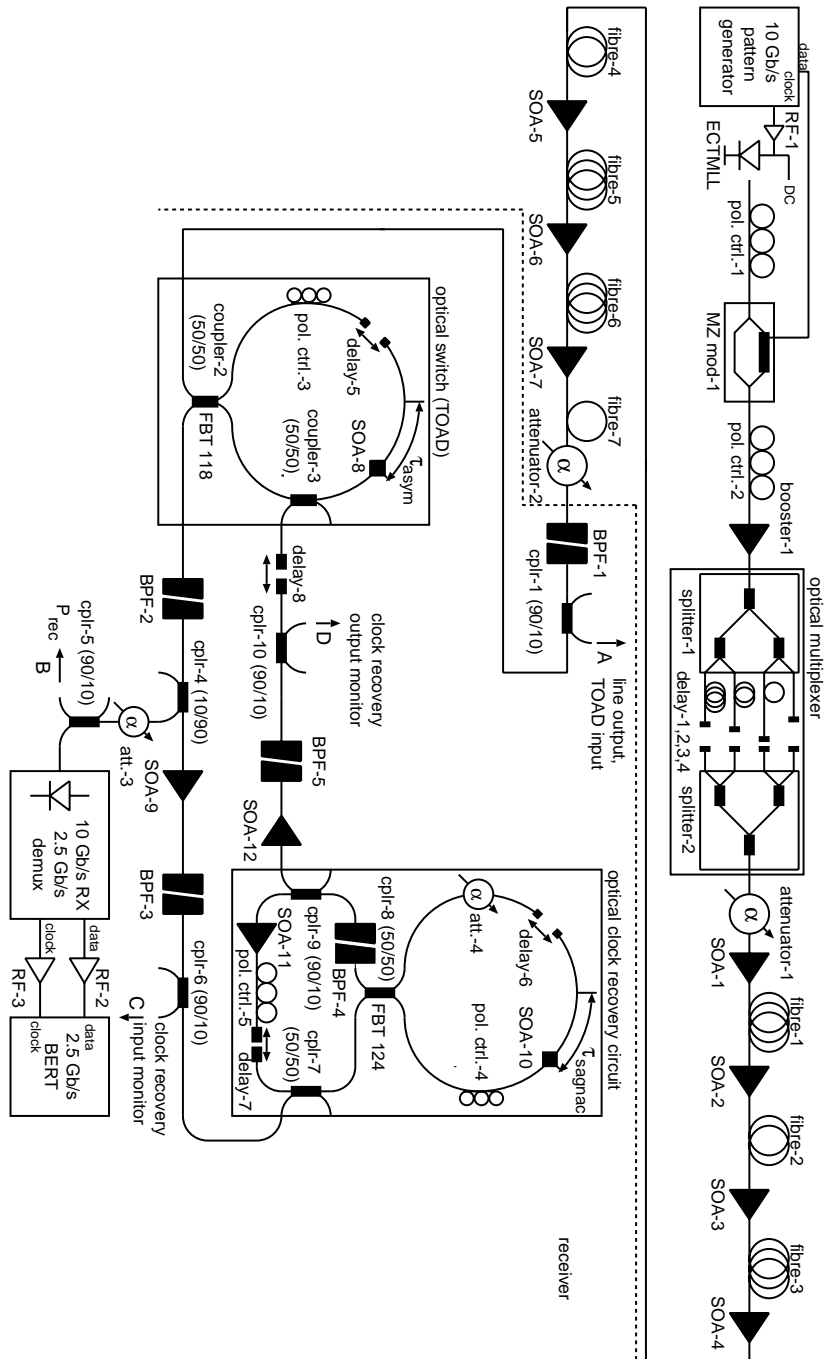


Figure 5.45: Experimental setup of the 40 Gb/s, 216 km transmission system employing all-OTDM technology

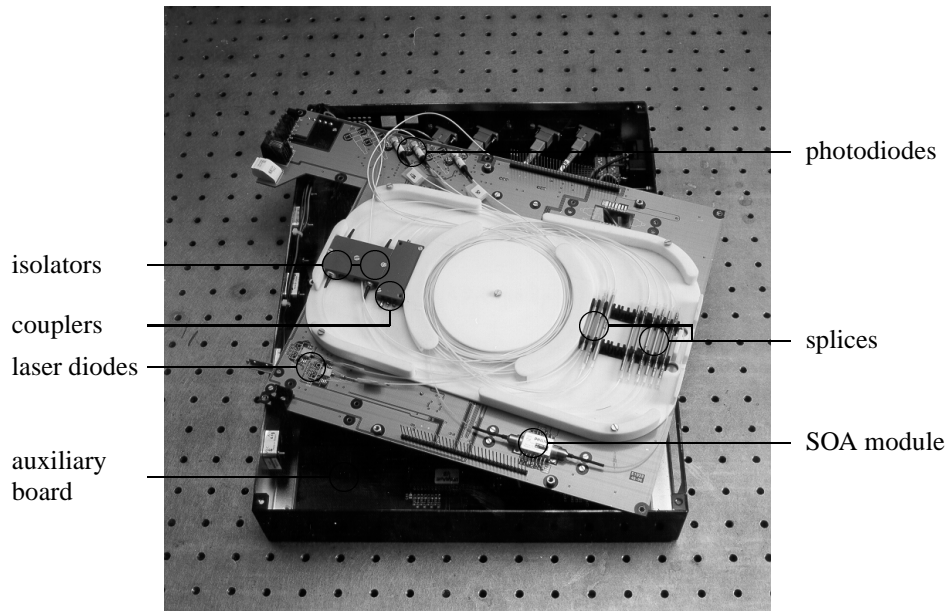


Figure 5.46: Interior of an ORU which has been used in the European ACTS Project Upgrade



Figure 5.47: The 216 km transmission link. SOA-2 to -6 are ORUs.

in transmission links and on all-optical demultiplexers has led to a revised view on in-line amplification and a fully operational all-optical demultiplexer with all-optical clock recovery. New ideas on in-line SOA-based amplification have led to the replacement of long (800 μm) amplifiers with short (400 μm) amplifiers.

5.5.2 Experimental setup of the 216 km transmission system

Figure 5.45 displays the experimental setup of the 40 Gb/s transmission experiment. The transmitter and receiver are the same as described in Sec. 5.4.

Between the transmitter and receiver a transmission link has been established containing six in-line SOAs, SOA-2 to -7, and 216 km of SSMF divided into seven segments, fibre 1-7, of 37.9, 27.7, 36.5, 27.2, 37.3, 36.3, 12.8 km, respectively. SOA-2 to -6 have been implemented in optical repeater units (ORUs) that were also used in a 10 Gb/s field trial between the cities of Kassel and Hannover in Germany for the European ACTS Project “Upgrade” [15]. In Chapter 4 it was demonstrated that using high gain in-line SOAs reduces the maximum transmission distance by either too much gain (ASE noise limits performance) or by too low a saturation output power (pattern effects limit performance). Implementation of shorter amplifiers provides a higher saturation output power because amplifier generated ASE will not saturate the amplifier and exhibit a lower gain that results in less generation of ASE. The amplifiers in the ORUs are 400 μm long. The ORUs provide 11 to 15 dB gain. ORUs with less gain are implemented after short sections while ORUs with high optical gain are used to compensate loss of larger sections of fibre. This way excess gain in the system is avoided. The 400 μm long amplifiers are operated at 20°C and driven by a 200 mA current by means of temperature and current stabilising controllers. Figure 5.46 displays the interior of an optical repeater unit. The printed circuit board contains the optical amplifier (bottom-right), isolators, WDM couplers, lasers and photodiodes for the management system used to control the amplifier current and monitor the input and output powers. The service channel of the management system operates at 1510 nm and is controlled from the head-end ORU by a personal computer. Additional fibre provides the return link for the service channel. The link is terminated by an adjustable attenuator (attenuator-2) to determine the bit error rate sensitivity to changes in received line power by the TOAD-switch. Optical band-pass filter, BPF-1, eliminates out-band ASE. The optical link is depicted in Fig. 5.47. In the foreground five ORUs are visible. To the right of the ORUs SOA-7 is visible which is not equipped with a link management system. The bottom right depicts two of the 17 fibre spools, each coiled up with an average of 12.7 km of SSMF. The amount of power that is launched into the link equals 3 dBm (−3 dBm per channel). The power distribution in the link is depicted in Figure 5.48. After fibre-7 a maximum of −3 dBm of optical power is available. The ORUs with SOA-2 to -6 have output powers below 3 dBm, while the input powers lie above −12 dBm. If the insertion loss of the management system at the output of the SOA (2.1 dBm typical) is accounted for the output powers of the actual modules lie below \approx 5 dBm. The insertion loss of the management system at the input of the amplifier amounts to 2.9 dBm (typical). The actual input powers of SOA-2 to -6 lie therefore above −14.9 dBm [16]. These values are in agreement with the input and output powers of SOA-1 which does not have this insertion loss. High-gain SOA-7 does experience a much lower input power and a comparable output power. The 114 km unrepeated experiment reprinted in Chapter 4 utilised a high-gain SOA for optical preamplification. Although SOA-7 is followed by fibre section-7 the

Table 5.2: Settings for error free demultiplexing after 216 km

parameter	min.	average/typical	max.	notes
I_{SOA-9}	256 mA	318 mA	345 mA	$T = 20^\circ\text{C}$
I_{SOA-12}	350 mA	385 mA	400 mA	$T = 20^\circ\text{C}$
τ_{delay}	8.0 ps	9.5 ps	11.5 ps	0.5 ps resolution
P_{switch}	-1.3 dBm	0.3 dBm	1.5 dBm	
P_{rec}	-13.9 dBm	-10.3 dBm	-9.0 dBm	

original setup assigned SOA-7 as an optical pre-amplifier. In that case fibre section-7 was intended to be situated before SOA-5. This configuration did not satisfy because error free operation could not be achieved.

5.5.3 Results and discussion

BER performance

The same measurement procedures have been applied in this section as in Sec. 5.4 for obtaining BER information. Figure 5.49 displays the bit error rate performance of the transmission link. The solid lines are the back to back curves while the dashed-dotted lines are the BER curves after 216 km. The power along the horizontal axis is the power at the input of the TOAD-switch.

For decreasing TOAD input powers the BER increases as the signal to noise ratio in the decision circuit of the receiver decreases. For larger TOAD input levels the BER eventually increases because the line signal is so strong that it will start switching the TOAD instead of being switched by the switch signal. Back to back, the dynamic range amounts to 7.6 dB which is considerably smaller than the 13 dB of the 10 Gb/s to 2.5 Gb/s demultiplexer. The dynamic range after 216 km has reduced to 4.2 dB. The total average penalty caused by the transmission over 216 km of SSMF amounts to 4.0 dB. Error free transmission is observed for all channels. The differences between the channels are likely to be caused by small differences in power and channel separation occurring in the optical multiplexer at the transmitter side. This makes one channel more susceptible to ASE than other channels. Also differences in state of polarisation between the four channels contribute to these differences, despite the fact that in the eight SOAs averaging with respect to residual polarisation sensitivity of the SOAs occurs. SOA-8 is set to 175 mA, $\tau_{asym} = 8$ ps. τ_{delay} and P_{switch} are optimised to obtain optimum BER performance by respectively adjusting delay-8 and the current of SOA-12. The optical clock recovery is operated as described in Sec. 5.2. For each BER measurement the clock recovery is fine-tuned from visual observations of the 10 GHz component at point D. If fine tuning accidentally leads to a system lock-up, the entire BER curve is remeasured. The current of SOA-9 is adjusted such that the input power to the clock recovery is minimal. Attenuator-3 is adjusted such that the power incident on the photodiode of the 10 Gb/s receiver is not the BER limiting factor.

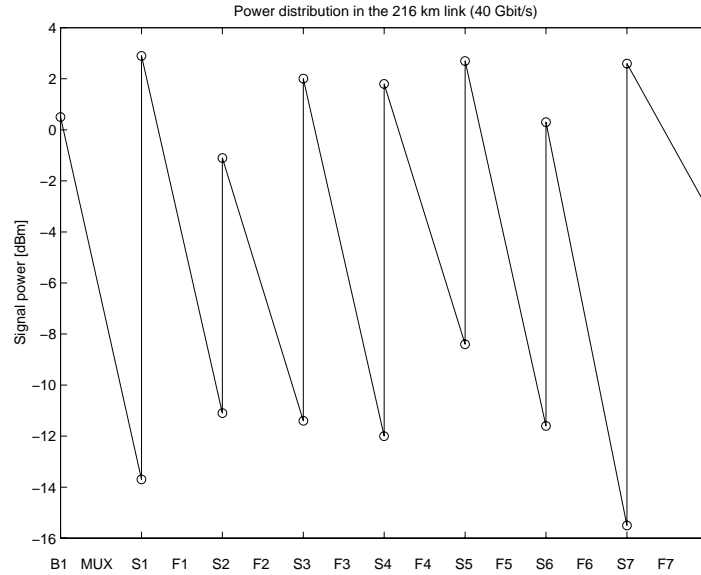


Figure 5.48: Power map of the 216 km, 40 Gb/s transmission experiment. B1 indicates the booster amplifier, MUX indicates the optical multiplexer, Sx and Fy refer to in-line SOA-x and fibre section-y.

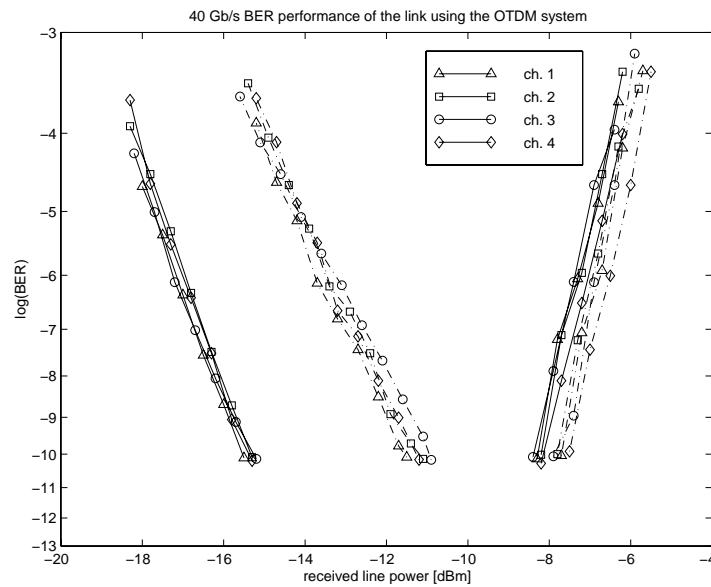


Figure 5.49: BER performance of the 216 km transmission link. The received power is measured at the input of the TOAD based optical switch (solid lines: back to back, dashed-dotted lines: after 216 km).

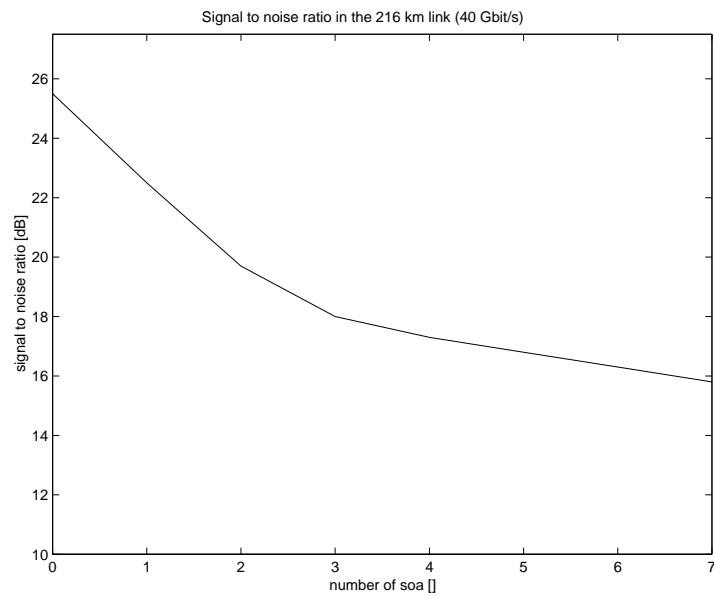


Figure 5.50: Signal to noise ratio after each amplifier (0 indicates the booster amplifier)

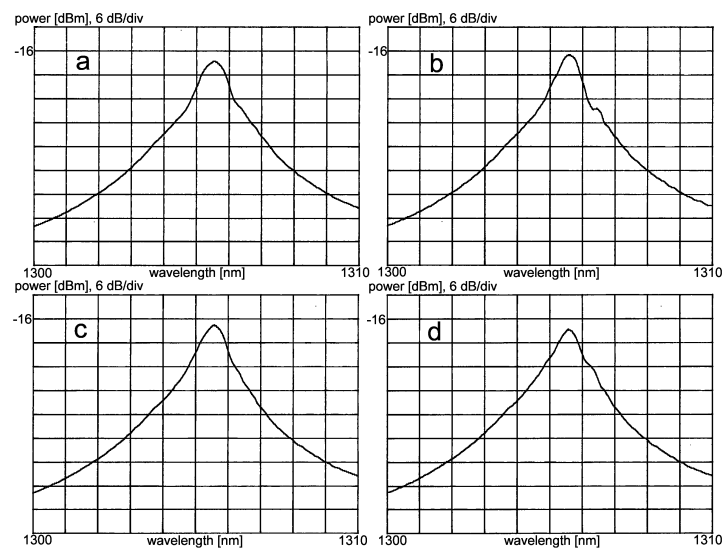


Figure 5.51: Optical spectra of the demultiplexed signals measured at point C for each of the four channels.

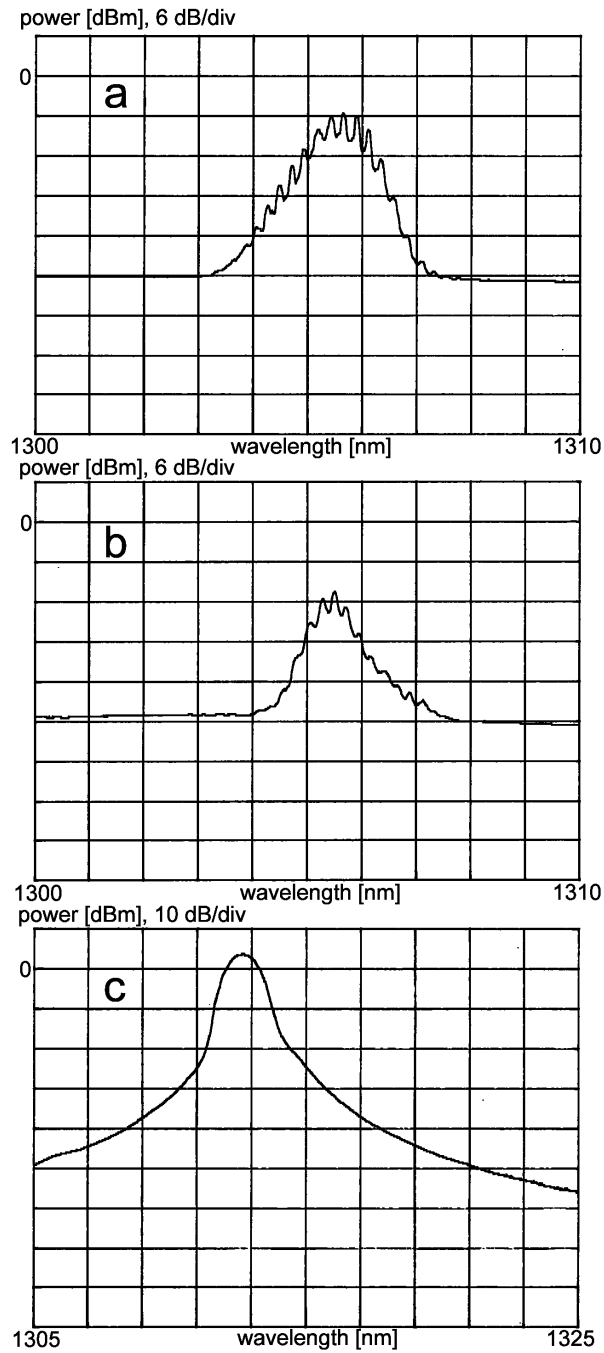


Figure 5.52: Spectra of the 40 Gb/s signal that is launched into the link (a), the 40 Gb/s signal after 216 km (b) and the spectrum of the recovered clock (c).

Spectral behaviour

Figure 5.50 displays the decrease of the signal to noise ratio as a function of transmission distance. Data is obtained from the optical spectra that have been measured after each amplifier. It can be seen that the signal to noise ratio gradually decreases. After SOA-7 the signal to noise ratio is ≈ 16 dB. In the beginning of the link the signal to noise ratio decreases rapidly while after SOA-3 the deterioration of the signal to noise ratio per SOA progresses at a slower rate.

Figures 5.51 and 5.52 display the demultiplexed spectra of the four channels at point C, the spectra of the link input and output signal and the spectrum of the recovered clock. The 40 Gb/s link input and output spectra show the individual modes which are spaced 0.23 nm from each other corresponding to ≈ 40 GHz. The exact wavelength of the signal is 1305.7 nm. The spectrum of the received signal has narrowed considerably. This indicates possible pulse broadening. The optical spectra of the four 10 Gb/s channels do not show any abnormality. The signal to noise ratio could not be measured as BPF-2 and -3 hide the noise level outside the bandwidth of the signal. In addition, it can be observed that the 40 GHz spaced spectral components have disappeared.

Temporal behaviour

Figure 5.53 displays part of a $2^7 - 1$ PRBS, 40 Gb/s signal at the output of the transmitter and after 216 km of SSMF. Although ringing of the detector distorts the pattern, logical ones and zeros can be distinguished quite clearly. Figure 5.54 displays the averaged temporal response of a demultiplexed signal after transmission of 216 km of SSMF. There is no visual evidence of significant channel cross talk. One channel is clearly visible. The remaining three channels are suppressed. However, some pattern effects have become visible that result from encountered amplifier saturation in the link or in the optical demultiplexer. These effects do not appear to be severe. The lower subplot contains the unaveraged temporal envelope of the recovered clock of a $2^{23} - 1$ PRBS signal. Compared to Fig. 5.16 the recovered clock pulses are subject to noise and time jitter. Despite the noise and jitter individual clock pulses are clearly distinguishable. The signals are measured using a digital sampling oscilloscope that is pattern triggered by the PPG at the transmitter side. Figure 5.55 displays the eye diagrams of the 40 Gb/s line signal after 0 km (a) and 216 km (b). The ringing of the photodiode is responsible for the eye closure. Most of the noise is introduced by the PIN photodetector and sampling stage of the digital sampling oscilloscope. Figure 5.56 displays the eye diagrams of the four demultiplexed channels after 216 km of transmission (BER of 10^{-9}). The formation of an open eye is visible. The relatively large amplitude fluctuations in the peaks of the eyes can be explained from multiple causes such as pattern effects that have already been made visible in Fig. 5.54 (a). Recovered clock pulses that exhibit time jitter and/or pattern effects can have a negative impact on the shape and position of the time window which can lead to amplitude fluctuations of the demultiplexed signal.

Finally autocorrelation traces have been measured to provide insight into possible broadening due to dispersion. Figure 5.57 displays the autocorrelation traces of the 40 Gb/s signal that is launched into the link and is received after 216 km. Significant pulse broadening is observed. The width of the autocorrelation trace after 216 km of transmission has doubled compared to the width after 0 km. Under the assumption that the pulse shape at the output is not changed significantly with respect to the pulse shape at the input of the link, the width of the received

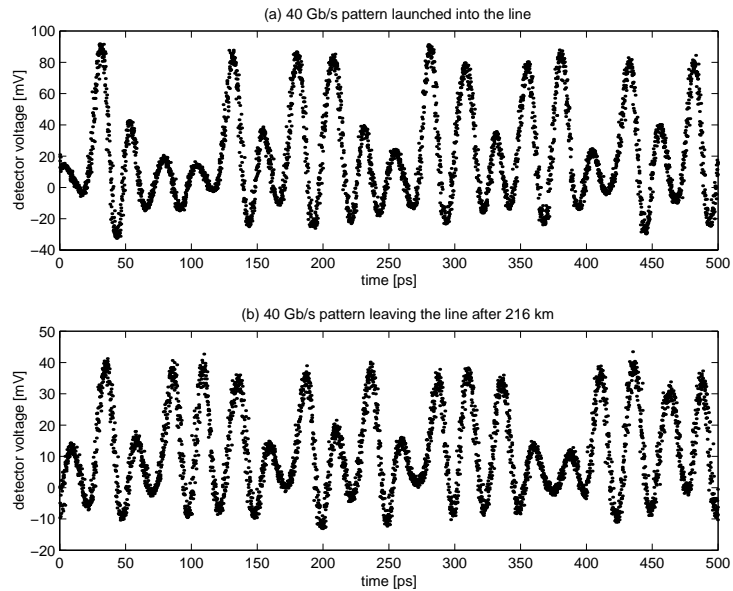


Figure 5.53: Part of the $2^7 - 1$ PRBS, 40 Gb/s data signal at the input (a) and output (b) of the 216 km link (time averaged).

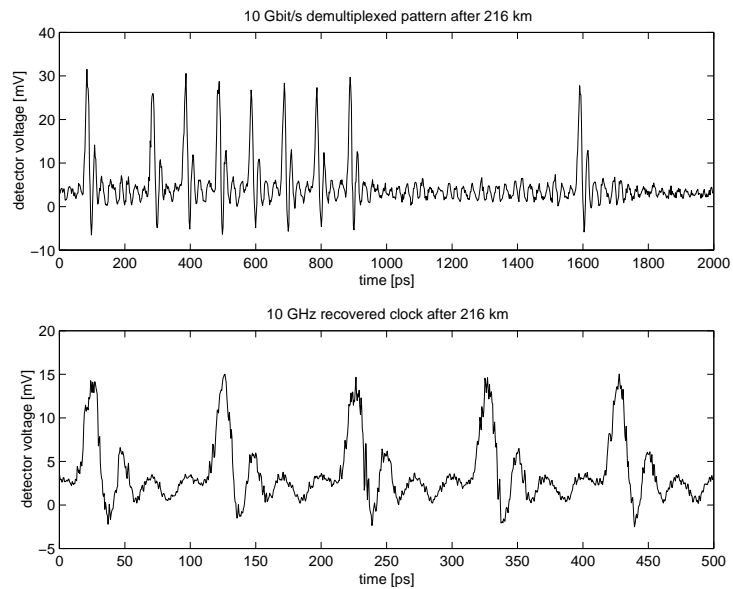


Figure 5.54: (a) Part of a $2^7 - 1$ PRBS demultiplexed channel at the output of the TOAD (averaged). (b) Temporal response of the recovered clock output (unaveraged).

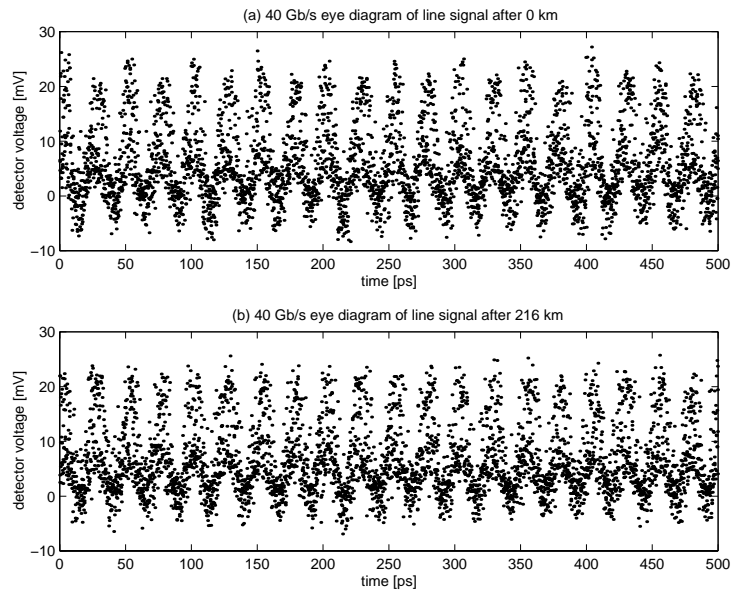


Figure 5.55: (a) 40 Gb/s eye diagram after 0 km. (b) 40 Gb/s eye diagram after 216 km.

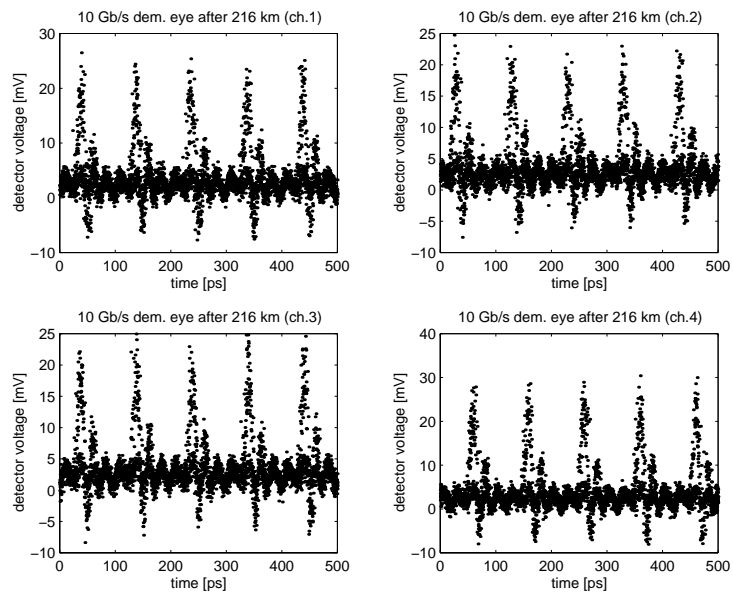


Figure 5.56: Eye diagrams of the four from the 40 Gb/s line signal demultiplexed channels after 216 km at a BER of 10^{-9} .

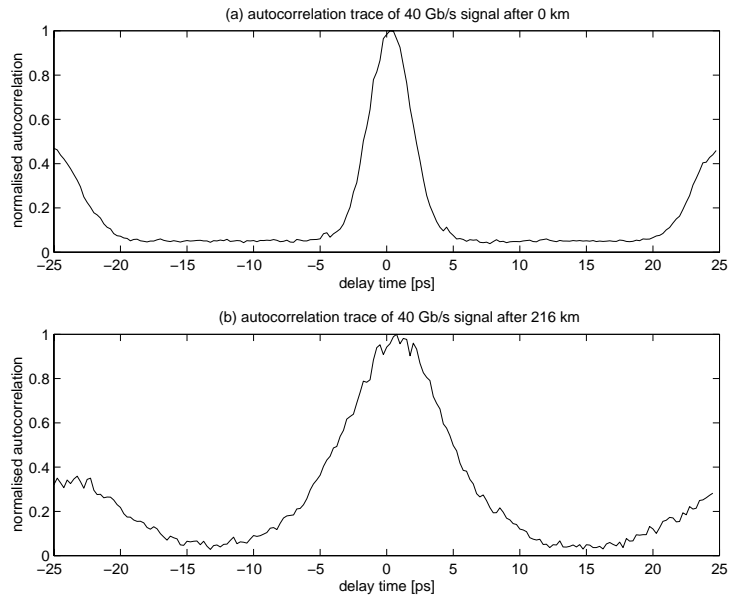


Figure 5.57: (a) 40 Gb/s autocorrelation trace after 0 km. (b) 40 Gb/s autocorrelation trace after 216 km.

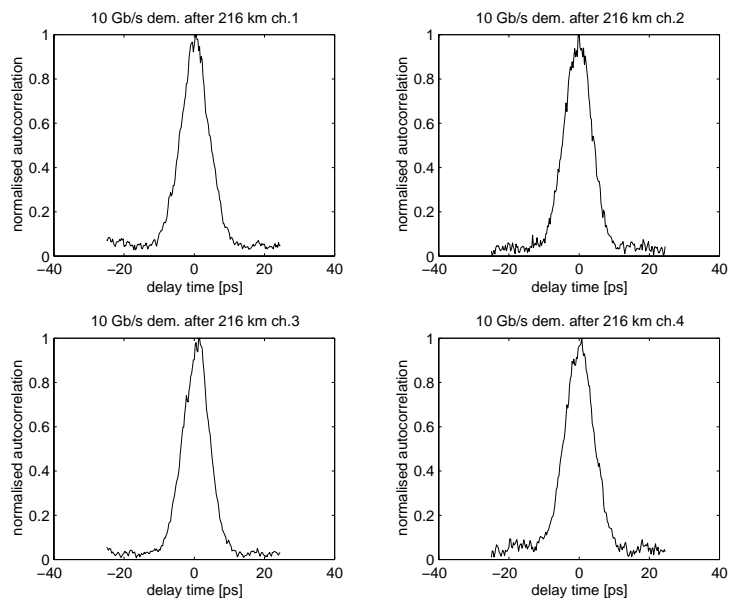


Figure 5.58: Autocorrelation traces of each of the four 40 Gb/s line signal demultiplexed channels after 216 km.

Table 5.3: Saturated and unsaturated gains of the in-line ORUs and amplifier modules. SOA-2 to SOA-6 are ORUs with 400 μm long amplifier modules. SOA-1 and SOA-7 are modules of 400 μm and 800 μm length, respectively.

in-line number	serial number	current [mA]	in-line gain [dB]	small signal gain [dB]	gain compression [dB]
SOA-1	255	150	16.6	17.1	0.5
SOA-2	258	200	10.0	10.5	0.5
SOA-3	251	200	13.4	13.8	0.4
SOA-4	256	200	13.8	14.2	0.4
SOA-5	257	200	11.1	11.0	-0.1
SOA-6	253	200	11.9	12.1	0.2
SOA-7	322	175	18.1	20.2	2.1

pulses is estimated as 6 ps. With a pulse separation of 25 ps inter symbol interference (ISI) can be neglected. Figure 5.58 displays the autocorrelation traces of the four demultiplexed channels. The 10 Gb/s autocorrelation traces are in agreement with the 40 Gb/s autocorrelation trace of the received signal depicted in Fig. 5.57.

Gain compression in the 216 km link

Pattern effects and noise are the main sources of power penalties in semiconductor optical amplified transmission systems. Pattern effects are caused by the inability of semiconductor amplifiers to maintain a constant inversion during amplification of rapidly fluctuating input powers. The carrier lifetime of SOAs is ≈ 200 ps which is short compared to a long sequence of logical ones at bit rates of even up to 100 GHz. Therefore saturation effects will be localised in time intervals in the order of the carrier lifetime. Consequently when the amplifier is saturated, the average gain will be lower with respect to the unsaturated small signal gain. This has been measured for the seven in-line amplifiers of the 216 km link (See Table 5.3). The gains of the amplifiers when inserted in the link is listed in the fourth column. The unsaturated gains are listed in the fifth column under “small signal gain”. The difference between these two columns is called the gain compression and is listed in the last column. All amplifiers except SOA-7 (#322) are 400 μm long. SOA-7 has a length of 800 μm . From Table 5.3 it becomes clear that the short amplifiers of the ORUs and SOA-1 exhibit limited saturation. An average gain compression of 0.3 dB per amplifier should be accounted for. SOA-7 is a high gain, 800 μm long amplifier module similar to the ones used in Sec. 4.4. SOA-7 is on its own directly responsible for a gain compression of the same order as the already accumulated gain compression of all the other amplifiers. Fortunately SOA-7 is the only 800 μm long amplifier in the link (At the time of measurement, only six 400 μm long SOAs were available).

5.5.4 Conclusions and recommendations

216 km has been bridged error free at a bit rate of 40 Gb/s. All-optical multiplexing and demultiplexing with all optical clock recovery technology has been incorporated successfully.

A penalty of 4.0 dB is observed which is caused mainly by the build up of ASE. In combination with an increased fluctuation of extinction ratios between individual pulses makes this ASE noise build up the main cause of this penalty. Pulse broadening is observed but is not responsible for the penalty. Pattern effects have been reduced by using short amplifiers that exhibit a higher saturation output power. The length of each section of fibre is matched to the gain of a specific ORU. In addition the input power of the ORUs is chosen such that the ORUs operate in the linear regime while at the same time it is ensured that amplified spontaneous emission build up does not deteriorate the signal beyond the border of error free detection. It is strongly recommended that future OTDM transmission experiments utilise an improved or optimised version of the TOAD. This allows more specific BER measurements with respect to variations in input powers and delay settings. Automation of a future setup is strongly recommended.

5.6 All-optical regeneration at 10 Gb/s

5.6.1 Introduction

In Chapter 4 experiments were performed with a 200 km link comprising high gain semiconductor optical amplifiers. These SOAs provided so much excess gain (if a high saturation output power is required) that the ASE level increased after four cascades to a level where error free transmission becomes challenging. Higher signal input powers were able to compensate for this rising ASE floor. However, increased signal levels lead to more pattern effects

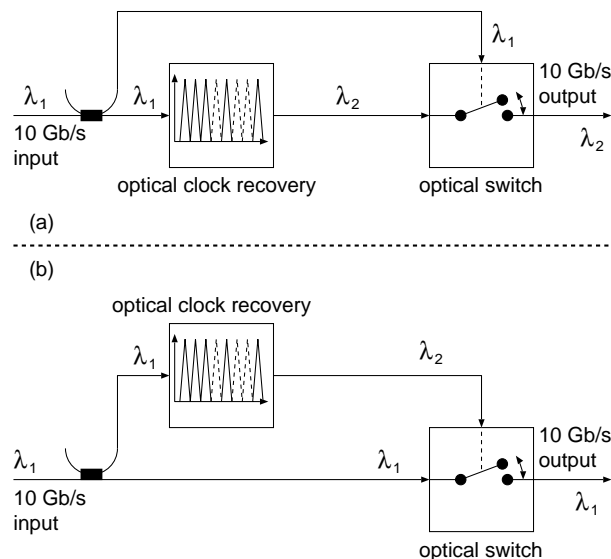


Figure 5.59: (a) Optical regeneration with wavelength conversion. (b) Optical regeneration without wavelength conversion.

and more chirp. Together with fibre nonlinearity induced self-phase modulation this led to the breaking up of the spectra and the formation of pedestals. This occurred typically around the zero dispersion point where third-order dispersion is dominant. In this section it will be shown that the TOAD based optical switch in combination with the all-optical clock recovery circuit is able to improve an optical signal that has travelled through the before mentioned system.

Most optical regenerators assume the configuration depicted in Fig. 5.59 (a) [17], [18]. In this configuration the signal, at λ_1 , to be regenerated controls a clock recovery circuit that generates a pulse train at a different wavelength, λ_2 . This pulse train is modulated by the signal to be regenerated. The shape of the new signal is fully determined by the characteristics of the clock recovery circuit and is free of noise, pattern effects and time jitter. If conversion to a different wavelength is undesirable then a possible solution is depicted in Fig. 5.59 (b) where the signal with noise and pattern effects is resampled and reshaped.

In this case the clock is recovered from the input signal. Even though Fig. 5.59 (b) displays a configuration where the clock recovery is derived from the incoming signal, there is no impediment to recovering the clock from the output as in Secs. 5.4 and 5.5. Recovery of the clock from the output of the switch has the advantage that the clock is driven by a refurbished signal, free of pedestals, and will therefore improve performance.

5.6.2 Experimental setup

Figure 5.60 displays the 200 km transmission system with 10 Gb/s all optical regeneration. The wavelength of operation is 1305.5 nm. 3 dBm of optical power is launched into the link by SOA-1. After 200 km the line signal is filtered, attenuated and fed into the optical switch. This switch is identical to the TOAD based optical switch depicted in Fig. 5.36. The output of the optical switch is partially guided into the all-optical clock recovery circuit (Fig. 5.36) and into the receiver where the bit error rate is measured. Optical spectra, temporal envelopes and autocorrelation traces can be measured by connecting an optical spectrum analyser, digital sampling oscilloscope or autocorrelator to one of the desired tab-couplers-1, -3, -4 or -5. Booster-1 and SOA-2 to -5 are operated at 400 mA at a temperature of 20°C. SOA-1 is biased with 200 mA, at a temperature of 20°C. The optical switch and clock recovery circuit are operated as described in Sec. 5.4. SOA-6 and SOA-7 are biased with 400 mA and 265 mA, respectively. The input power of the switch signal to the optical switch was adjusted to 0 dBm. During the BER measurements delay-1 and attenuator-2 were continually adjusted for optimum BER performance. The input power to the optical switch varied between -16.5 dBm and -14.9 dBm. Upon switch on of SOA-6 and -7 the optical clock recovery started automatically.

5.6.3 Results and discussion

Figure 5.61 shows that power penalties are reduced when the all-optical regenerator is implemented. The reduction of the power penalty of 2.3 dB amounts to 1.1 dB after 200 km of SSMF transmission. After 100 km the reduction equals 0.6 dB. Back to back measurements reveal a small positive power penalty. In addition to an improved receiver sensitivity the formation of BER floors has ceased. At a BER of $\approx 10^{-12}$ the “200 km with regeneration” curve intersects with the “100 km without regeneration” curve. For low BER performance the

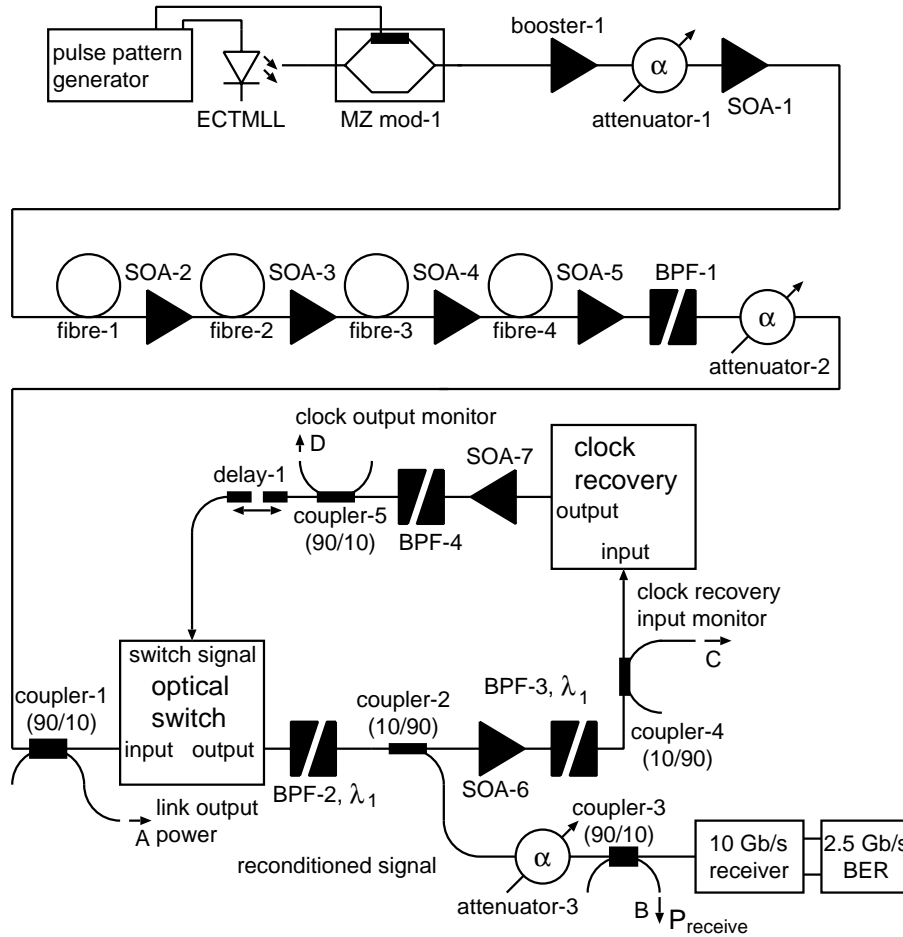


Figure 5.60: Experimental setup of the 200 km transmission system with all-optical regeneration.

transmission distance can be doubled if all-optical regeneration is employed at the receiver side. The eye diagram of the optical signal after 200 km with and without optical regeneration is depicted in Fig. 5.62. Both eye patterns are measured at a BER of 10^{-9} and show an open eye supporting the measured error free transmission. In addition to the eye diagram the optical spectra and autocorrelation traces have been measured after 200 km at a BER of 10^{-9} .

Figure 5.63 (a) shows the spectrum of the 10 Gb/s link input signal. Subplots (b) and (c) display the input to, and the output of the optical switch. Although the spectrum of the line signal has broken up, error free detection was still possible. The 3 nm wide optical filter BPF-2 cuts off part of the spectrum. BPF-2 has been adjusted such that optimal BER performance was measured. When the optical regenerator was inserted BPF-2 remained unchanged. From subplot (c) it follows that the optical power from the switch signal lies 20 dB below the power

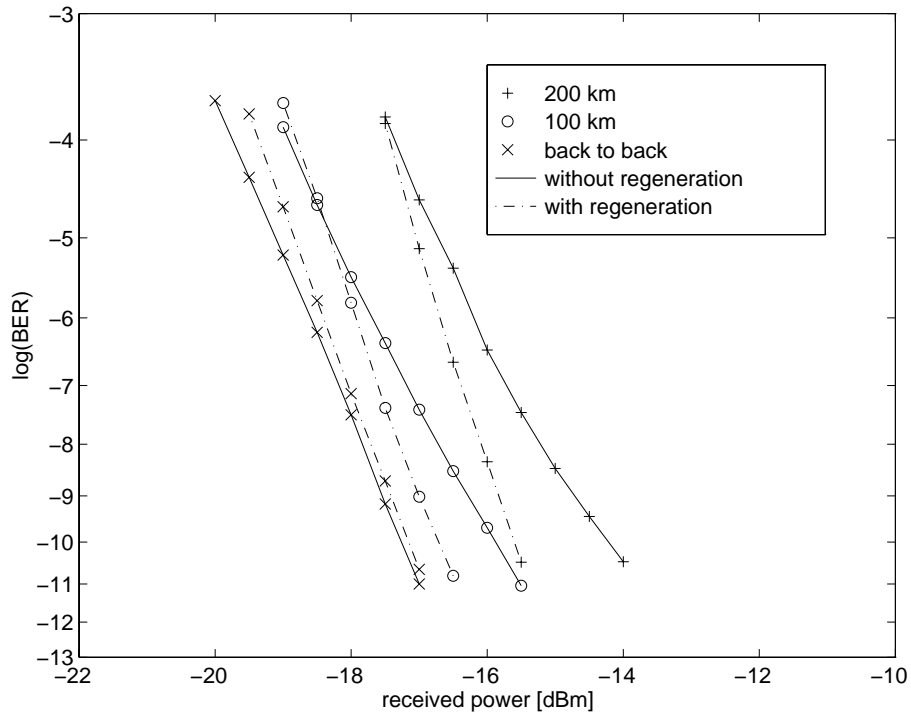


Figure 5.61: Bit error rate performance after 0, 100 and 200 km of a 10 Gb/s RZ formatted $2^{23} - 1$ PRBS data signal.

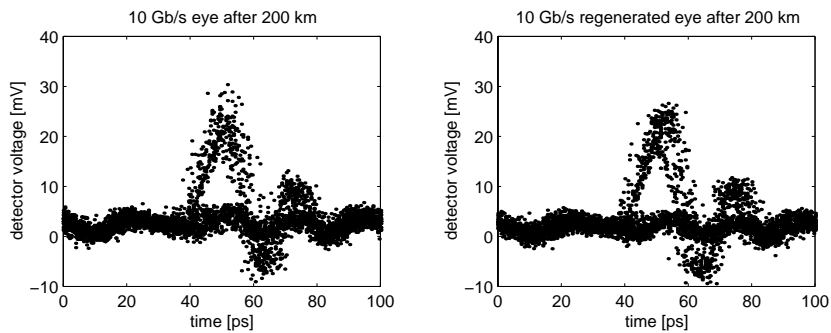


Figure 5.62: Eye diagrams of the received 10 Gb/s signal after 200 km with and without all optical regeneration.

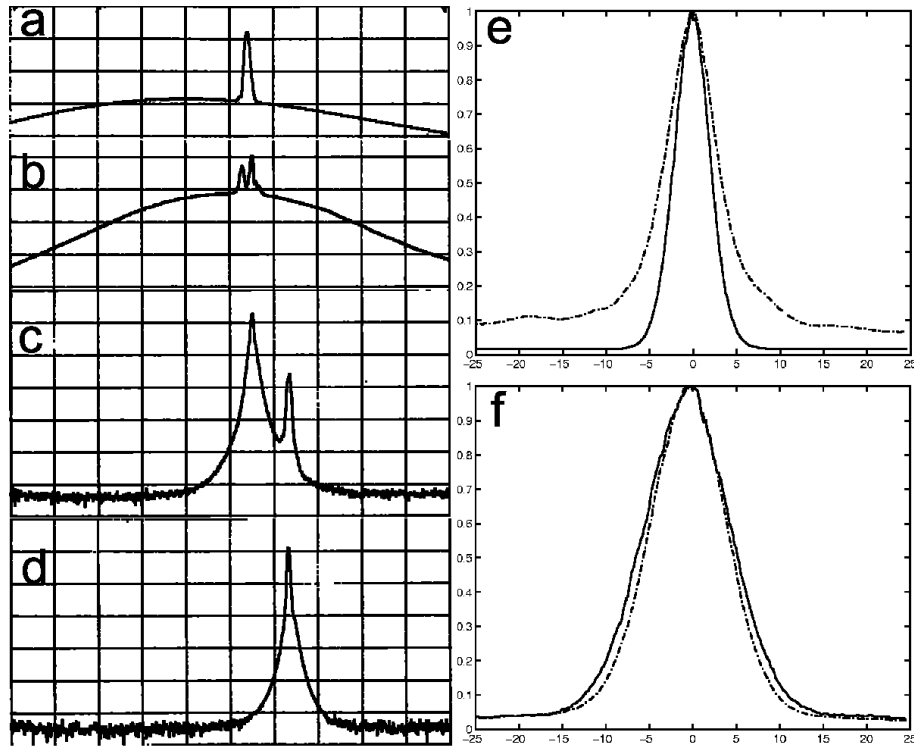


Figure 5.63: (a) spectrum of 10 Gb/s signal launched into the link, (b) spectrum at the input of the optical regenerator after 200 km, (c) spectrum of the recovered signal at the receiver input after 200 km, (d) spectrum of the recovered clock after 200 km, (e) solid: autocorrelation of the signal launched into the link, dashed: autocorrelation of the signal after 200 km, (f) solid: autocorrelation of the recovered clock, dashed: autocorrelation of the regenerated signal. ((a) to (d): centre wavelength 1300 nm, span 100 nm, resolution 0.1 nm, 10 dB/div, (e), (f): 5 ps/div, normalised)

of the reconditioned signal. The spectrum of the recovered clock is depicted in subplot (d) and does not display any aberration from a normal signal. Figure 5.63 (e) shows that the pulses of the 10 Gb/s line signal after 200 km contain a pedestal. This is in correspondence with the spectrum in subplot (b), which shows significant deviation from the spectrum of the initially launched signal (subplot (a)). This pedestal decreases the extinction ratio which results in significant eye closure. The optical switch is able to reduce this pedestal and thus improve the eye opening. Subplot (e) shows the autocorrelation trace after regeneration. It can be seen from subplot (f) that the pedestal is removed but that the pulses have broadened by approximately 30%. This broadening occurred during the switching process where the spectral contents of the line signal was changed. The optical pulses and the recovered clock are of the same width.

5.6.4 Conclusions and recommendations

Successful all-optical regeneration has been performed. It is demonstrated that after 200 km power penalties can significantly be reduced and that formation of noise floors is counteracted. The all-optical regenerator is self-starting. The improvement of system performance is attributed to a reduction of the formation of a pedestal that is responsible for extinction ratio degradation. Extinction ratio degradation makes the system vulnerable to ASE. It is recommended that additional experiments be performed where the recovered signal is launched into a second 200 km link or where the all-optical regenerator is inserted into an optical recirculating fibre loop.

References

- [1] J.P. Sokoloff, P.R. Prucnal, et al. A terahertz optical asymmetric demultiplexer (TOAD). IEEE Photonic Technology Letters, 5:787–790, 1993.
 - [2] J.P. Sokoloff, I. Glesk, et al. Performance of a 50 Gbit/s optical time domain multiplexed system using a terahertz optical asymmetric demultiplexer. IEEE Photonic Technology Letters, 6:98–100, 1994.
 - [3] G. Morthier and P. Vankwikelberge. Handbook of Distributed Feedback Laser Diodes, pages 29–45. Artech House, Norwood, 1997.
 - [4] K. Petermann. Laser diode modulation and noise, pages 5–58. Kluwer Academic Publishers, 1991.
 - [5] H. Ghafouri-Shiraz and B.S.K. Lo. Distributed Feedback Laser Diodes, Principles and Physical Modelling, pages 19–28. John Wiley and Sons, Chichester, 1996.
 - [6] M. Lax. Fluctuations from the nonequilibrium state. Review of Modern Physics, 32:25, 1960.
 - [7] C.H. Henry. Theory of linewidth of semiconductor lasers. IEEE Journal of Quantum Electronics, 18:259–264, 1982.
 - [8] P. Gunning, J.K. Lucek, et al. Gainswitched DFB laser diode pulse source using continuous wave light injection for jitter suppression and an electroabsorption modulator for pedestal suppression. Electronics Letters, 32:1010–1011, 1996.
 - [9] D. Huhse, W. Shell, J. Utz, et al. Generation of low jitter (210 fs) single mode pulses from a laser diode by selfseeding. In Proceedings ECOC'94, Firenze, Italy, pages 437–440, 1994.
 - [10] P. Vasil'ev. Ultrafast Diode Lasers, fundamentals and applications, pages 100–121. Artech House, Norwood, 1995.
 - [11] H.A. Haus. A theory of forced modelocking. IEEE Journal of Quantum Electronics, 11:323–330, 1975.
 - [12] R.G.M. Koumans and R. Van Rooijen. Theory for passive mode-locking in semiconductor laser structures including the effects of selfphase modulation, dispersion, and pulse collision. IEEE Journal of Quantum Electronics, 32:478–492, 1996.
-

-
- [13] H.A. Haus. Theory of modelocking of a laser diode in an external cavity. Journal of Applied Physics, 51:4042–4049, 1980.
- [14] P.P. Vasil'ev. Ultrashort pulse generation in diode lasers. Optical and Quantum Electronics, 24:801–824, 1992.
- [15] A. Mattheus, H. Gruhl, J.J.E. Reid, et al. Final report on link for technical exhibition. “Upgrade” Deliverable D6221 AC045-tzd-ams-DS-P-025-b1, European Commission, Advanced Communications Technologies & Services, Brussels, Belgium, 1997.
- [16] L. Cucala and J.J.E. Reid. Report on operation of repeater modules and implementation of OAM program. “Upgrade” Deliverable D5221 AC045-tef-lcg-DS-P-016-b1, European Commission, Advanced Communications Technologies & Services, Brussels, Belgium, 1997.
- [17] W.A. Pender, P.J. Watkinson, et al. 10 Gbit/s all-optical regenerator. Electronics Letters, 31:1587–1588, 1995.
- [18] W.A. Pender, T. Widdowson, and A.D. Ellis. Error free operation of a 40 Gbit/s all-optical regenerator. Electronics Letters, 32:567–569, 1996.
-

Chapter 6

Discussion

Up to now the simulation and measurement of transmission systems with and without all-OTDM systems has been presented. An important issue is how these results relate to what has been found in this thesis and to what has been previously presented in literature. To this end several topics are treated, starting with implications for long-haul high-speed transmission in Sec. 6.1. All-OTDM, regeneration and all-OCR are discussed in Sec. 6.2. Section 6.3 deals with aspects that have influence on the implementation of the laboratory work either in the field or in a commercial system. Finally, some recent developments and future trends are presented in Sec. 6.4. The complexity and uniqueness (with respect to the wavelength of operation and the use of 1.3 μm polarisation insensitive MQW SOAs) of the research described in this thesis, makes it difficult to compare results with results obtained from literature. Differences in wavelengths, bit rates, components used and experimental conditions hinders fair comparison.

6.1 Long-haul high-speed transmission

6.1.1 Dispersion management

Dispersion management is a measure to prevent chromatic dispersion from broadening the, in the case of RZ transmission, optical pulses. Pulse broadening results via ISI in eye closure and reduced BER performance. There are three different ways of compensating for dispersion. One has already been mentioned in Sec. 1.3, where the fibre nonlinearity induced self-phase modulation is employed to compensate for the dispersion. Other methods involve mid-span spectral inversion (MSSI) and the introduction of dispersion-compensating fibre (DCF) or fibre gratings. MSSI involves flipping over the optical spectrum such that the “red” frequencies become “blue” and vice versa. This is performed utilising FWM based technology which generates an optical phase conjugated (OPC) signal. If this is done in the middle of the transmission link the pulses will broaden in the first half and be compressed to their original width in the second half of the link. The most important drawback is the fact that MSSI must take place near the middle of the link. In [1] 40 Gb/s, 434 km SSMF, MSSI based transmission at 1551 nm is performed successfully. A dispersion-compensating fibre or a fibre grating can be placed anywhere in the link to compensate dispersion. Parameters must

be adjusted to the length of the link and wavelength of operation. Recently, 240 km, 40 Gb/s, unrepeated transmission at 1558 nm has been reported [2] using this kind of dispersion compensation. Self-phase modulation as a means of dispersion compensation is favourite because no external components are required. For wavelengths above the zero-dispersion wavelength of the fibre the Kerr-nonlinearity leads to SPM induced pulse narrowing. Two difficulties arise. Firstly, as a result of fibre losses the pulse power decreases with distance. This reduces SPM and thus the dispersion compensation at the end of the fibre link. A second problem arises when semiconductor optical amplifiers are used. These amplifiers impose pattern effects on the data signals via the effects of gain saturation. Different bits will have different power and consequently a different chirp. Interaction with dispersion causes problems as low powered bits will broaden more than high powered bits. In addition, pulses will tend to become chirped. According to Eq. 1.13 governing soliton shape, spectral components which do not fit this pulse shape manifest themselves as dispersive waves that travel with different velocity and may cause eye-closure when these waves enter neighbouring bits. The results presented in Sec. 4.4 support this. In Chapter 5 the input levels of the 40 Gb/s signals have been reduced to avoid the problems described above. Reduction of input power increases sensitivity to ASE. This leads to the conclusion that performance of the link is limited by saturation of the amplifiers that, via α_H , interacts either with dispersion or by ASE build up. Therefore, introduction of DSF which can act as DCF at 1.31 μm is not a practical alternative for dispersion management. Insertion of DSF increases the total fibre loss which requires additional gain. This results in more ASE. For these kind of dispersion compensating techniques to be implemented either the saturation output power needs to be increased or the amplifier noise figure must be improved. The pulse broadening observed in Sec. 5.5 results from residual second order and from third order dispersion which appears around the zero dispersion point. The wavelength of operation has been adjusted such that minimal pulse broadening occurred. The input power was adjusted to ensure that spectral integrity was maintained at a signal to noise ratio which was as high as possible. Consequently this pragmatic way of configuring the link required input pulses narrower than 4 ps to obtain output pulses narrower than 8 ps, thus exhibiting no ISI. In summary, the system is partly nonlinear. Some amount of dispersion is taken for granted. The benefits of SPM induced dispersion compensation do not outweigh amplifier induced chirp that deteriorates propagation.

6.1.2 In-line amplification

With respect to in-line amplification two distinctions can be made. On the one hand 1.3 μm versus 1.55 μm , and on the other hand lumped or distributed. The polarisation insensitive MQW SOAs used in the experiments described in this thesis belong to the 1.3 μm lumped category. In the 1.3 μm window practical long-haul transmission systems have only been realised with these polarisation insensitive MQW SOAs [3], [4]. The penalty after 437 km, [3], amounted to 5.8 dB which agrees with the 5 dB penalty observed after 420 km [4]. These experiments took place at 10 Gb/s. Earlier 2.5 Gb/s NRZ transmission was performed at 1531 nm resulting in a penalty of 2.3 dB after 516 km of SSMF transmission. In this case polarisation sensitive amplifiers were used [5]. With Raman amplification and a high powered transmitter 453 km was bridged over SSMF at 1561 nm and 2.5 Gb/s NRZ formatted, without in-line amplification [6]. A penalty of 2 dB was observed. In Sec. 4.2, 114 km has been bridged using also a highly powered link input, 12 dBm, and optical pre-amplification. This

experiment was performed around zero dispersion at 10 Gb/s. As booster amplifiers were used which are not easily saturated, no excess chirp was added to the pulses and therefore no interaction with residual second order and third order dispersion around the zero dispersion point existed. Combining this result with the Raman experiments conducted in Sec. 4.3 showed that truly unrepeated RZ transmission at $1.3 \mu\text{m}$ at 10 Gb/s of over ≈ 180 km may be considered feasible. In the case of 40 Gb/s transmission OTDM has a definite advantage compared to WDM (4×10 Gb/s) NRZ transmission at $1.3 \mu\text{m}$ [7]. The main reason is signal deterioration of the individual channels due to cross talk originated by the cross-gain modulation in the SOAs. In the case of OTDM transmission cross-gain modulation between the channels is absent. As a matter of fact the pattern effects are reduced if the bit rate is increased because the amplifier becomes relatively slow compared to the bit rate. With respect to WDM transmission OTDM transmission at $1.3 \mu\text{m}$ is favourite when SOAs are implemented as in-line amplifiers. Raman amplification gives superior performance with respect to SOA based amplification both for OTDM and WDM transmission [8]. In the case of OTDM this is due to the distributed gain that allows soliton shaped RZ pulses to obtain optimum profit from the fibre nonlinearity. 10 Gb/s transmission at 1550 nm with EDFA based loss compensation tips the scale of performance compared to in-line SOA based amplification at 1300 nm. Repeated EDFA based systems transmit across transoceanic distances at speeds of 100 Gb/s (20×5 Gb/s WDM) using an NRZ data format [9] and recently beyond 7200 km with 64 channels of 10 Gb/s RZ formatted data [10].

6.1.3 RZ versus NRZ versus hybrid

Section 4.1 dealt with a theoretical investigation of the performance of RZ and NRZ systems. Under the same conditions (SOA and fibre parameters) it has been demonstrated that RZ propagation is the superior data format. In Sec. 6.1.2 a 4×10 Gb/s WDM NRZ formatted experiment has been compared to the 40 Gb/s soliton shaped RZ formatted experiment of Sec. 5.5. Again it may be concluded that given the longer transmission distance and the larger effort that is put into the demultiplexing operation the latter system shows increased performance. In Ref. [11] a hybrid experiment has been performed where a 10 Gb/s soliton signal is transmitted together with a 2.5 Gb/s NRZ signal at a lower wavelength compared to the soliton signal. The outcomes of the experiment were detrimental for the NRZ signal as error free transmission of the NRZ signal could not be observed although the link had been optimised for the NRZ signal. Soliton transmission remained error free during this experiment. The lower bit rate of the NRZ formatted signal and the equal amount of power that was launched into the link should have resulted in superior performance of the NRZ formatted signal. Hybrid configurations with respect NRZ and RZ (soliton) transmission are therefore not recommended. For the $1.55 \mu\text{m}$ window a comparison between 40 Gb/s NRZ and RZ systems based on cascaded EDFAs has been performed numerically [12]. Results show that an RZ format may be superior to an NRZ format. The transmission distance was found to be three times larger for the RZ format compared to the NRZ format.

6.2 all-OTDM, regeneration and all-OCR

6.2.1 All optical multiplexing

It has already been mentioned in Sec. 5.4.2 that four individual channels at the output of the multiplexer have a random state of polarisation. This has the advantage that interferometric problems of the tails of neighbouring optical pulses caused by the finite pulse widths cancel out. This is not a real situation compared to an ETDM system where the state of polarisation is equal for all four channels as the entire signal is generated by a high-speed modulator instead of interleaved (as is the case with OTDM) after undergoing separate delays where random polarisation rotations occur. In Ref. [13] the optical multiplexer is equipped with polarisation-maintaining fibre (PMF) and a modulator in each branch. The delays of the channels with respect to each other deviate slightly from 25 ps (a 10 Gb/s to 40 Gb/s MUX is considered) which provides a 10 GHz component for easy clock recovery at the transmitter. This is also not a real situation because in a 40 Gb/s signal no spectral 10 GHz component is present. The MUX designed in this thesis is not equipped with PMF and has no individual modulation for each channel. The four individual delays have been adjusted in such a way that the 10 GHz component in the spectrum of the multiplexed 40 Gb/s detected signal is minimal. Contrary to Ref. [13] where more interferometric difficulties can occur but clock recovery has become easier, the MUX configuration in this thesis is less sensitive to interferometric “breathing” of the tails of neighbouring pulses but will pose more difficulties in performing clock recovery.

6.2.2 TOAD and other switches for demultiplexing

Ideal / non-ideal couplers

In Chapter 5 all-OTDM experiments have been performed using the TOAD optical switch [14]. In the case of the 10 Gb/s to 2.5 Gb/s demultiplexing setup an ideal coupler was used with a 90° phase shift between the two output ports. This provided good results with an estimated channel extinction ratio of $R_{channel} = 3$. In the case of the 40 Gb/s experiment, first the same coupler was used resulting in non-error free performance. At this point the coupler was replaced and again non-error free performance occurred with an optimum BER which had increased. Apparently the coupler was of great influence. Following this up, the coupling ratios were investigated but were found to be equal, in correspondence with the manufacturing data. Theoretical and experimental results assumed ideal couplers [15], [16]. This gave rise to the possibility of deviations in the 90° phase difference between the output ports of the coupler. Numerical simulations presented in Chapter 2 have demonstrated that non-ideal couplers can increase the channel extinction ratio from ≈ 3 to ≈ 50 . In addition slightly different coupling coefficients could further improve the channel extinction ratio to values ≥ 200 . Insertion of different couplers resulted in error free operation of which Chapter 5 contains the results. Operation conditions (e.g. τ_{asym} , τ_{delay}) and proper selection of the coupler is of equal or greater importance than the choice of SOA.

10 to 2.5 Gb/s, 40 to 10 Gb/s and 160 to 40 Gb/s ?

The 10 to 2.5 Gb/s demultiplexing required an amplifier current of 100 mA. According to Fig. 2.5 the gain is moderate, saturation energy is low and the literature [17] indicates a

high α_H . At this speed the amplifier recovers fairly well between two successive 2.5 GHz switching pulses. In the case of 40 to 10 Gb/s OTDM the amplifier is allowed to recover less between two successive 10 GHz switch pulses. This means that the amount of gain saturation is also less. The π phase shift between clockwise and counter clockwise travelling signals in the TOAD configuration, which is needed for demultiplexing a channel, is generated by the amount of gain saturation multiplied by α_H . More gain, more switch power and a higher α_H are required to achieve this π phase shift. More gain yields automatically a higher saturation output power and a higher α_H . Between 100 mA and 175 mA bias current the gain is increased by 5.2 dB and the saturation power by 3 dB. In addition, the required switch power is increased by 3 dB. α_H is expected to have increased by a factor of two [17] for small signal gain but for a saturated amplifier α_H remains the same (≈ 3 to ≈ 8). For these values error free demultiplexing from 40 to 10 Gb/s is achieved. For future 160 to 40 Gb/s demultiplexing the gain can no longer be increased with increasing current. In addition, the saturation output power does increase with increasing current. As a result, the switch power needed for the demultiplexing of a 40 Gb/s channel from the 160 Gb/s line signal could become unrealistically high, taking into account that α_H does not significantly increase with increasing current once the amplifier is saturated [17]. Error-free operation is more difficult as the amount of saturation decreases with a larger factor than with which α_H increases. This confirms statements in literature [16], [15] that predict limitations in on SOA gain saturation based switches when switching speeds approach the 100 Gb/s. Shorter carrier lifetimes, τ_c , are essential for ≥ 40 Gb/s all-OTDM. With respect to the dynamic range of the OTDM and the sensitivity of the window to the timing parameters the conclusion can be drawn that with this configuration and implementation 160 Gb/s to 40 Gb/s OTDM is not feasible.

Performance related to other OTDM systems

Differences in BER performance can only be compared if both 10 Gb/s base line curves (without OTDM) and demultiplexed curves (with OTDM) are presented. In [18] a 2 dB penalty is reported with a configuration that resembles the configuration in this thesis. Differences are the wavelength of operation; 1.55 μm instead of 1.3 μm , the width of the switching pulses; 8 ps instead of 5 ps, and the amount of switch signal power, +16 dBm compared to 0 dBm. In addition the switch signal is generated from an electrically mode-locked external cavity semiconductor laser. Compared with the power penalty found in Sec. 5.4.3 of 1.9 dB both systems operate with the same performance. The system of Sec. 5.4 requires less switching power, is polarisation insensitive and operates with full all-optical clock recovery. With respect to the SLALOM configuration, see Sec. 1.2.3, introduced by [16] no BER measurements at high speeds are available for comparison. As the device is saturated twice its performance is expected to be inferior to the performance of the TOAD. The window will be broader because the amplifier is saturated by both the clockwise and counter clockwise travelling switch pulse. Integrated Mach Zehnder interferometer based optical switches have already been employed in a number of systems. Recently, it has been demonstrated that these switches are capable of lossless bi-directional switching with negligible distortion of the control-signal in the output data-signal. Channel extinction ratios of 20 dB have been reported [19]. They are suitable for implementation in switching fabrics of monolithically-integrated cross connects.

6.2.3 Optical clock recovery configurations

The optical clock recovery circuit that was realised in Sec. 5.2 belongs to the category of “figure-eight” lasers because of its shape. Most of these figure-eight lasers have repetition rates equal to the ground frequency of the cavity. For example [20], [21] and [22] describe EDFA based figure-eight lasers which have a repetition rate of 11 MHz, 2.6 MHz and 5.5 MHz, respectively. The full-width half-maximum times of the pulses amount to ≈ 2 ps. Even at these low repetition rates the EDFA remains saturated. For high-speed optical demultiplexing the 2 ps pulses are perfect. However, the repetition rate is too low. Introduction of a saturable amplifier in a Sagnac interferometer to form a figure-eight laser resulted in a higher repetition frequency of 1 GHz while the cavity ground frequency amounted to 4.5 MHz. The pulse width increased to 50 ps [23]. This configuration operated at 1536 nm. The configuration of Sec. 5.2 was based on [23] but extended with an adjustable attenuator and an adjustable delay to manipulate the input powers to and the position of the SOA. In this case the repetition rate of the laser could be synchronised to 10 GHz with a minimum pulse width of ≈ 3 ps. This system operated at 1312 nm. The wavelength of operation does not make the difference but the way the Sagnac based saturable absorber operates does. Because the asymmetry is relatively small the SOA can recover within the 100 ps to obtain a total roundtrip gain ≥ 1 so that it can be switched again. Theoretically one could expect this laser to operate at a repetition rate beyond 10 GHz. This however has not been observed. One of the reasons is that the recovery of the SOA is too slow.

If less bias current is applied to the amplifiers in the ring laser it takes more time for the amplifiers to recover and for the total roundtrip gain to rise above one. In this case the repetition rate drops to 5 GHz where all amplifiers recover to an extent where the roundtrip gain exceeds one. This can also be an advantage as is demonstrated in [24] where all-optical clock division is performed from 2.5 GHz to 1.25 GHz using also a SOA based figure-eight laser.

6.2.4 Optical regeneration

In Sec. 5.6 optical regeneration was performed by restoring the extinction ratio (ER) of an 10 Gb/s RZ signal after 200 km of SSMF with 50 km spaced SOAs. As stated in that section most optical regenerators employ wavelength conversion which will not be touched upon in this section. In Ref. [25] a NOLM (nonlinear optical loop mirror) is used to enhance the extinction ratio. Because the NOLM profits from the instantaneous nonlinearity of the fibre no additional clock signal was required to reduce power penalties from 4.1 dB to 1.6 dB. In the SOA based TOAD configuration the excitation of the nonlinearity can not be performed by the 10 Gb/s data signal. An optical clock is therefore required. In Ref. [26] a TOAD without external switch signal is used to extract a clock signal that is deliberately sent along with the data signal (self-clocking). The TOAD is used to suppress the data while the clock is strong enough to saturate the amplifier which results in clock pulses at the output. The data signal is suppressed by 16.2 dB. This experiment operated at 1313 nm with 2.5 ps pulses from a 100 MHz repetition rate Nd:YLF laser. If an optical signal of 100 MHz was inserted where the zeros are distorted by e.g. dispersive waves from the logical ones, then this configuration is well suited to suppress the distortions on the zeros and to enhance the logical ones. At higher bit rates (≥ 2.5 Gb/s) similar configurations to Fig. 5.60 have not been observed for the 1.3 μm window. To the best knowledge of the author a novel way of all-optical signal

regeneration has been demonstrated for bit times below the carrier life time of the SOA that acts as the nonlinear element in a TOAD based switch.

6.3 Implementation in commercial system designs

6.3.1 Requirements

When communication systems are developed beyond the research stadium, additional demands are made and different issues play a role. In general, economic and practical issues are of major importance. Before the introduction of the EDFA, the distance of transmission was determined by the amount of power launched into the fibre and the receiver sensitivity. Enhancement of the receiver sensitivity by introducing coherent detection techniques did improve the capacity of transmission systems. The complexity of these schemes prevented network operators from installing these systems. Too many components are needed and too many control loops are required in coherent detection schemes. Therefore a few simple but basic (technological) demands made by system houses play a role in the determination of which new technologies will be used in field trials and in commercial systems. These demands vary from application to application e.g. a land link imposes different requirements than a submarine link. A few examples:

1. Power budget should be reserved for link degradation (ageing) in a later stadium (10 dB).
2. Robustness; insensitivity to changes in environment.
3. Use a limited number of optical components. If possible, integrate multiple optical components to a single functional unit.

6.3.2 Stability

The stability of the all-OTDM system described in this thesis can be enhanced by adding control loops. Also the number of components of the all-OTDM systems is extensive. Reduction of the number of components can only be performed by integration (item 3.). In addition, the start-up procedure described in Sec. 5.4 is not desirable in a practical system configuration. Additional control circuits are needed for system fault analysis when for example a fibre breach occurs or a fault exists in the all-OTDM device. Fault determination becomes more difficult if the number of control loops and points increases.

6.3.3 Integration

If all-OTDM systems are to be implemented in a field trial or in a commercial system, integration of the all-optical demultiplexer and all-optical clock recovery circuits is essential. All-optical switches and passively mode-locked ring lasers that can act as all-OCRs have been integrated independently but have not been tested or integrated as a whole. Photonic integrated circuits (PICs) require a smaller number of control loops for stable operation. Polarisation rotations in optical waveguides of the PICs are less severe as influences from the outside (temperature and vibrations) cause less degradation in performance. In [27] a SLA-LOM configuration has been monolithically integrated to perform as a 10 Gb/s and 20 Gb/s

to 5 Gb/s optical time-domain demultiplexer operating at $1.55 \mu\text{m}$. Power penalties of 1.2 dB and 2.7 dB were observed for 10 and 20 Gb/s demultiplexing, respectively. Interpolation suggests a power penalty of ≈ 6 dB for 40 Gb/s to 5 Gb/s demultiplexing. Demultiplexing to a higher bit rate, 10 Gb/s instead of 5 Gb/s, will probably result in an even higher power penalty. Compared to the hybrid setup of Sec. 5.4, the integrated versions indicate a significantly higher power penalty. The contrast ratio of 11 dB between the on and off states and a time window of 30 ps at a 200 ps period estimates a channel extinction ratio of ≈ 2 . Generally the extinction ratio is expected to be lower compared to the TOAD as the SLALOM is saturated by both clockwise and counter clockwise travelling switch signal. A possible explanation is that a multimode interference coupler guarantees a 90° phase shift between the output ports and therefore acts as an ideal coupler. Chapter 2 shows that a deviation from this 90° phase shift improves the extinction ratio. This has been verified in Chapter 5 where only a 2 dB penalty has been found for 40 Gb/s to 10 Gb/s demultiplexing. If future integration of Sagnac based demultiplexers is considered, an active coupler should be used regardless of the TOAD or SLALOM configuration. The coupler parameters of active couplers can be adjusted electronically via the opto-electronic effect (electrical modulation of the refractive index of semiconductor materials).

6.4 Recent and future developments

6.4.1 ETDM or OTDM

There is definitely going to be 40 Gb/s NRZ formatted ETDM transmission systems. In Ref. [28] the first experiments have been performed on a four channel 160 Gb/s WDM system using a 40 Gb/s electrical multiplexer. In the receiver each 40 Gb/s channel is optically and electrically demultiplexed to 10 Gb/s. One year later full ETDM at 40 Gb/s was demonstrated in Ref. [29]. Historically network operators and system houses have implemented ETDM systems up to 10 Gb/s. OTDM systems therefore have only future if they are based on an infinitely fast nonlinearity. Now that 40 Gb/s transmission technology has become under investigation, OTDM systems will focus on 160 to 40 Gb/s or 160 to 10 Gb/s. Although ETDM generally catches up, OTDM technology remains of interest for the investigation of the propagation of data signals in optical fibre and optical amplifiers.

6.4.2 WDM

Today WDM systems are commercially available. There is consensus on at least point to point connections. All-optical routing was recently demonstrated with an integrated optical cross connect [30]. Today, [31] WDM systems employ ≥ 64 channels of 10 Gb/s and are capable of transmitting error free over a distance of 520 km using specially designed fibre and EDFAs. Channel spacings of ≤ 100 GHz are common. Future WDM systems will have more channels with an even smaller spacing. Spectral efficiency can be further improved by using dual-binary coding schemes. With respect to the WDM results at $1.3 \mu\text{m}$ discussed in Sec. 6.1, WDM at $1.3 \mu\text{m}$ using SOAs compared to WDM at $1.5 \mu\text{m}$ with EDFAs is not attractive but can become of importance if Raman amplification is considered or the performance of SOAs is increased significantly. Effort is currently put into increasing the bandwidth (beyond 80 nm) of EDFAs in the $1.55 \mu\text{m}$ window.

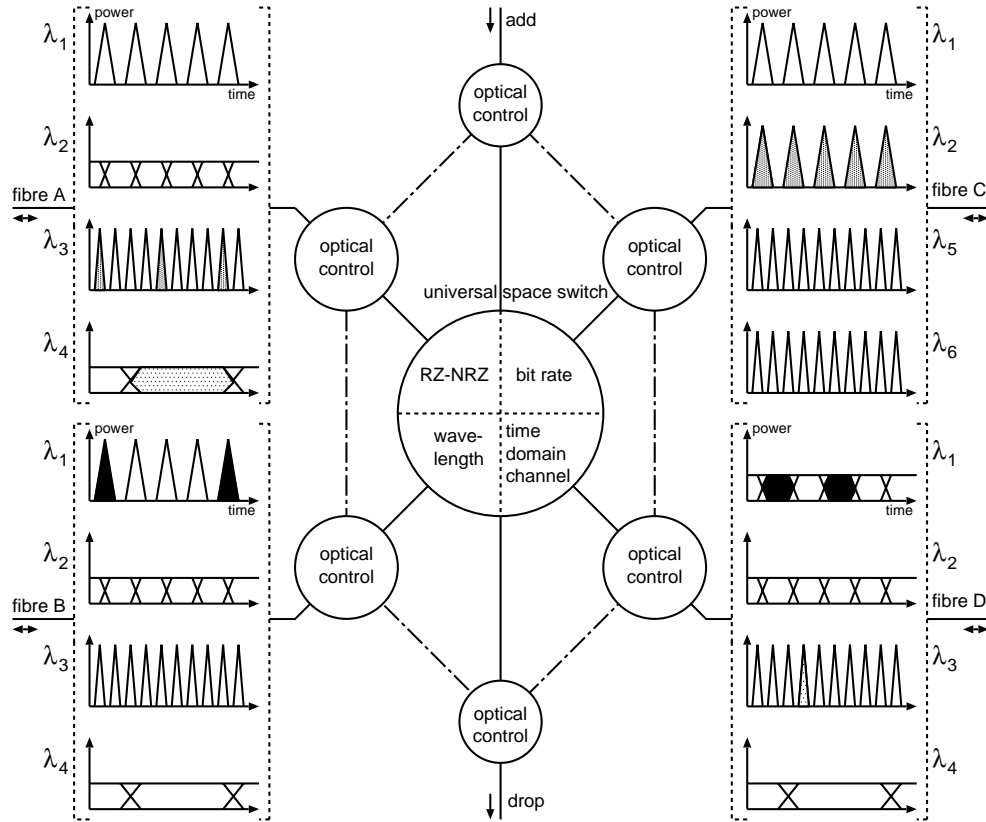


Figure 6.1: Diagram of an all-optical switch capable of performing different all-optical signal processing tasks such as RZ to NRZ conversion, bit rate conversion, wavelength conversion and switching between channels in the time-domain. Routing and switching information is extracted from the signals on a physical level.

6.4.3 Hybrid multiplexing

Hybrid multiplexed transmission employs both soliton transmission as WDM transmission in both the $1.3 \mu\text{m}$ and $1.55 \mu\text{m}$ windows. A transmission scheme was demonstrated employing 13 dense-WDM channels of 80 Gb/s where each 80 Gb/s wavelength is composed of 8 times 10 Gb/s OTDM channels [32]. Such a scheme employs both OTDM and WDM technology. This kind of implementation can fill the entire $1.55 \mu\text{m}$ window. Ref. [33] is a recent example of a 19 channels of 160 Gb/s WDM transmission experiment which filled the entire 70 nm bandwidth of a telluride-based EDFA. As a result, renewed interest exists in the $1.3 \mu\text{m}$ window. Semiconductor optical amplification is a well suited candidate for providing in-line amplification for $1.3 \mu\text{m}$ RZ based systems because of the availability of a large bandwidth.

6.4.4 The future role of (all)-optical signal processing

The role of all-optical signal processing depends on the introduction of an infrastructure for recently developed optical switches and demultiplexers. These optical switches are dedicated to perform a simple task. For an all-optical system platform more functionality is needed such as all-optical memories, all-optical switches, all-optical logic and interfacing. With respect to WDM and hybrid multiplexed systems, wavelength converters are of importance. All-optical circuits for the synchronisation of different optical signals must be built. If these constraints are fulfilled all optical nodes can be constructed which are capable of switching, adding and dropping signals from different wavelength, different fibres, different time-domain channels, different bit rates and modulation formats at the physical layer (see Fig. 6.1). Such an optical circuit can be thought of as being controlled by an optical control circuit where switching and routing is performed at both high and low speeds in the physical layer. The information for this switching and routing is extracted from the data signals by the control circuits and used to configure the universal space switch. This extraction should be performed for different modes and/or protocols of transmission like Asynchronous Transfer Mode (ATM), Synchronous Digital Hierarchy (SDH) and the Internet Protocol (IP).

References

- [1] U. Feiste, R. Ludwig, et al. 40 Gb/s transmission over 434 km standard fibre using polarisation independent mid-span spectral inversion. Electronics Letters, 34:2044–2045, 1998.
 - [2] K. Suzuki and M. Nakazawa. Recent progress in optical soliton communication. Optical Fibre Technology: Materials, Devices and Systems, 1:289–308, 1995.
 - [3] R.C.J. Smets, J.G.L. Jennen, et al. 114 km repeaterless and 437 km repeatered, 10 Gb/s transmission at 1310 nm using an RZ format. In Trends in Optics and Photonics Series, System Technologies, volume 12, pages 416–419. Optical Society of America, 1997.
 - [4] P.I. Kuindersma, G.P.J.M. Cuijpers, J.G.L. Jennen, et al. 10 Gbit/s RZ transmission at 1309 nm over 420 km using a chain of multiple quantum well semiconductor optical amplifier modules at 38 km intervals. In Proceedings of the ECOC'96, volume 2, Oslo, pages 165–168, 1996.
 - [5] S. Yamamoto, H. Taga, et al. 516 km, 2.4 Gbit/s optical fiber transmission experiment using 10 semiconductor laser amplifiers and measurement of jitter accumulation. In IOOC'89 Technical Digest, pages 28–29, 20PDA–9, 1989.
 - [6] E. Brandon and J.-P. Blondel. Raman limited, truly unrepeatered transmission at 2.5 Gb/s over 453 km with +30 km launch signal power. In Proceedings of the ECOC'98, volume 1, Madrid, pages 563–564, 1998.
 - [7] J.G.L. Jennen, R.C.J. Smets, H. de Waardt, et al. 4×10 Gbit/s NRZ transmission in the 1310 nm window over 80 km of standard single mode fibre using semiconductor optical amplifiers. In Proceedings of the ECOC'98, volume 1, Madrid, pages 235–236, 1998.
 - [8] P.B. Hansen et al. 8×10 Gbit/s, $1.3 \mu\text{m}$ WDM unrepeatered transmission system with raman post- and preamplifiers and a fiber span of 141 km. In Proceedings of the ECOC'97, volume 1, Edinburgh, pages 5–8, 1997.
-

-
- [9] N.S. Bergano et al. 100 Gb/s WDM transmission of twenty 5 Gb/s NRZ data channels over transoceanic distances using a gain flattened amplifier chain. In Proceedings of the ECOC'95, post deadline Th.A.3.1, pages 967–970, 1995.
- [10] N.S. Bergano, C.R. Davidson, C.J. Chen, et al. 640 Gb/s transmission of sixty-four 10 Gb/s WDM over 7200 km with 0.33 (bits/s)/Hz spectral efficiency. In Technical Digest of the OFC/IOOC'99, Postdeadline papers, PD2, pages 1–3, 1999.
- [11] J.G.L. Jennen, R.C.J. Smets, and H. de Waardt. WDM transmission of a 10 Gbit/s soliton and a 2.5 Gbit/s NRZ signal over 150 km SSMF using semiconductor laser amplifiers. In Proceedings of the 1997 IEEE/LEOSECOC Symposium Benelux Chapter, Eindhoven, pages 1–4, 1997.
- [12] D. Breuer, K. Ennser, and K. Petermann. Comparison of NRZ and RZ-modulation format for 40 Gbit/s TDM standard-fibre systems. In Proceedings of the ECOC'96, volume 2, Oslo, pages 199–202, 1996.
- [13] P.A. Andrekson. Fiber based OTDM techniques. In Proceedings of the ECOC'89, volume 1, Madrid, pages 557–558, 1998.
- [14] J.P. Sokoloff, P.R. Prucnal, et al. A terahertz optical asymmetric demultiplexer (TOAD). IEEE Photonic Technology Letters, 5:787–790, 1993.
- [15] K.I. Kang, I. Glesk, and P.R. Prucnal. Ultrafast optical demultiplexers using semiconductor optical amplifiers. International Journal of High Speed Electronics and Systems, 7:125–151, 1996.
- [16] M. Eiselt, W. Pieper, and H.G. Weber. SLALOM: Semiconductor laser amplifier in a loop mirror. Journal of Lightwave Technology, 13:2099–2112, 1995.
- [17] L.F. Tiemeijer, P.J.A. Thijs, et al. Self-phase modulation coefficient of multiple-quantum-well optical amplifiers. IEEE Photonic Technology Letters, 8:876–878, 1996.
- [18] A.D. Ellis and D.M. Spirit. Compact 40 Gb/s optical demultiplexer using a GaInAsP optical amplifier. Electronics Letters, 29:2115–2116, 1993.
- [19] E. Gamper J. Leuthold, P.A. Besse et al. Cascadable MZI all-optical switch with separate ports for data- and control-signals. In Proceedings of the ECOC'98, volume 1, Madrid, pages 463–464, 1998.
- [20] T.O. Tsun, M.K. Islam, and P.L. Chu. Tunable dual -wavelength operation of a soliton fiber laser. In Proceedings of the ECOC'97, volume 2, Edinburgh, pages 146–149, 1997.
- [21] V. Pelekhaty, D. Prasad, and R. Zanoni. Stabilization of a figure-8 laser. In Technical Digest of the OFC'95, San Jose, pages 27–28, 1994.
- [22] Irl N. Dulling III. All-fiber ring soliton laser mode locked with a nonlinear mirror. Optics Letters, 16:539–541, 1991.
- [23] L.E. Adams, E.S. Kintzer, and J.G. Fujimoto. All-optical clock recovery using a modelocked figure eight laser with a semiconductor nonlinearity. Electronics Letters, 30:1696–1697, 1994.
- [24] R.J. Manning, A.J. Poustie, and K.J. Blow. All-optical clock division using a semiconductor optical amplifier loop mirror with feedback. Electronics Letters, 32:1504–1506, 1996.
-

-
- [25] B.-E. Olsson and P.A. Andrekson. Extinction ratio improvement using the nonlinear optical loop mirror. IEEE Photonics Technology Letters, 7:120–122, 1995.
- [26] K.-L. Deng, I. Glesk, K.I. Kang, and P.R. Prucnal. Unbalanced TOAD for optical data and clock separation in self-clocked transparent OTDM networks. IEEE Photonics Technology Letters, 9:830–832, 1997.
- [27] E. Jahn, N. Agrawal, W. Pieper, et al. Monolithically integrated nonlinear sagnac interferometer and its application as a 20 Gb/s all-optical demultiplexer. Electronics Letters, 32:782–784, 1996.
- [28] S. Kuwano, N. Takachio, K. Iwahita, et al. 160-Gbit/s (4-ch \times 40-Gbit/s electrically multiplexed data) WDM transmission over 320-km dispersion shifted fiber. In Technical Digest of the OFC'96, Postdeadline paper, B25, pages 1–4, 1996.
- [29] W. Bogner, E. Gottwald, et al. 40 Gbit/s unrepeated optical transmission over 148 km by electrical time division multiplexing and demultiplexing. Electronics Letters, 33:2136–2137, 1997.
- [30] C.G.P. Herben, X.J.M. Leijtjens, F.H. Groen, et al. Ultra-compact polarisation independent phasor demultiplexing. In Proceedings of the ECOC'98, volume 1, Madrid, pages 125–126, 1998.
- [31] A.K. Srivastava, Y. Sun, J.L. Zyskind, et al. Error free transmission of 64 WDM 10 Gb/s channels over 520 km of truewave fiber. In Proceedings of the ECOC'98, volume 1, Madrid, pages 265–266, 1998.
- [32] Y. Miyamoto, K. Yonenaga, et al. 1.04 Tbit/s DWDM transmission experiment based on alternate-polarization 80 Gbit/s OTDM signals. In Proceedings of the ECOC'98, volume 3, Madrid, pages 55–56, 1998.
- [33] S. Kawanishi, H. Takara, et al. 3 Tbit/s (160 Gbit/s \times 19 ch) OTDM/WDM transmission experiment. In Technical Digest of the OFC/IOOC'99, Postdeadline Papers, PD1, pages 1–3, 1999.
-

Chapter 7

Conclusions and recommendations

In this thesis experiments have been described that utilise 1300 nm polarisation-insensitive multiple quantum-well semiconductor optical amplifiers (MQW SOAs). These SOAs have been implemented in all-optical signal processing schemes like all-optical time-domain demultiplexing (all-OTDM), all-optical clock recovery and all-optical regeneration circuits. Numerical simulations have been performed on the operation and performance of these all-optical circuits. Transmission experiments have been conducted at 10 Gb/s, without all-OTDM, and 40 Gb/s, with all-OTDM, that use these SOAs as in-line amplifiers to compensate for optical loss encountered in standard single-mode fibres.

7.1 Conclusions

Transmission without all-OTDM (10Gb/s)

1.3 μm , high-speed, return-to-zero (RZ) transmission compared to non return-to-zero (NRZ) SOA-based transmission displays increased performance (theoretically and experimentally). RZ systems are less sensitive to the formation of bit error rate (BER) floors.

Long semiconductor optical amplifiers (800 μm) result in non error-free operation of RZ formatted transmission over ≥ 200 km links when the gain and saturation output power are maximised. Adjustment of current and temperature lead to a maximum bridged distance of 437 km with 5.8 dB penalty, a new world record. Without in-line amplification a record distance of 114 km has been achieved.

In-line semiconductor optical amplifiers (SOA) must not have excess gain. The gain should match the loss of the fibre sections. This should be achieved by adjusting the length of the gain medium rather than adjusting current or temperature. The length of the amplifier chip should be chosen in such a way that for the drive current, where maximum saturation output power is observed, the gain is not significantly saturated by the self generated ASE. The reduction of the amplifier length from 800 μm to 400 μm resulted in error free demultiplexing in a 40 Gb/s experiment.

Gain saturation of SOAs induces chirp on initially soliton shaped pulses. This chirp does not allow the preservation of optical solitons in standard single-mode fibre (SSMF). 10 Gb/s data signals with input powers above 0 dBm form pedestals underneath the optical pulses and

break up the optical spectrum around the zero dispersion wavelength.

All optical regeneration has been demonstrated to be capable of removing these pedestals. BER performance is improved by 1.1 dB and BER noise floors are eliminated.

All-OTDM

The realisation of an optical cross gain-switched ring laser (OXGSRL) allowed the generation of jitter free optical pulses at 2.5 GHz. The optical wavelength was tuneable over a 50 nm wide interval.

A terahertz optical asymmetrical demultiplexer (TOAD) based optical switch was realised using a polarisation insensitive SOA. In combination with the OXGSRL error free demultiplexing of a 10 Gb/s signal was achieved. The power penalty caused by the demultiplexer amounted to 2.3 dB. The all-OTDM has the potential to compensate for power fluctuations of 13 dB that had been introduced before the demultiplexer. This indicates that the system can operate under severe power penalties occurring in a link before the demultiplexer.

For 40 Gb/s to 10 Gb/s all-OTDM numerical simulations showed that the switch pulse should be as narrow as possible. Long amplifiers required clockwise excitation by the switch pulses to obtain optimum performance. Under special conditions a coupler with a phase difference deviating from 90° between the output ports can improve the channel extinction ratio of the system. These conditions may not always be reached by solely controlling the current and temperature of the amplifier. Selection of a suitable optical coupler for the TOAD appeared to be necessary.

An all-optical clock recovery circuit has been realised using a saturable absorber that is based on a Sagnac interferometer with an asymmetrically placed and excited SOA. The clock recovery recovers 5 ps narrow optical pulses from a 10 Gb/s RZ data signal. Numerical simulations confirm stable operation of this circuit and provide insight into the mode-locking process.

The TOAD is implemented in a feedback configuration with the all-optical clock recovery circuit and has been demonstrated to demultiplex 40 Gb/s signals down to 10 Gb/s error free. The OTDM system introduced a power penalty of 2 dB. The demultiplexer was capable of compensating power fluctuations up to 7 dB at the input.

Transmission with all-OTDM (40 Gb/s)

Insertion of a 216 km link using optical repeater units (ORUs) with short SOAs resulted in error free operation with a total power penalty of 4.0 dB. The penalty was attributed to signal to noise ratio degradation. A dynamic range of 4.2 dB remains at the input of the demultiplexer.

The use of 400 μm long SOAs results in less amplifier saturation. The launched input power was -3 dBm per channel and prevented the formation of pedestals and the breaking up of the optical spectrum.

For future upgrades to 40 Gb/s there are no technical limitations for not using all-OTDM technology based on 1.3 μm MQW SOAs.

The utilisation of fibre pig-tailed components introduces instabilities. Causes are temperature and mechanical stress induced polarisation rotation and interaction between different controls.

Possible implementation of all-OTDM systems in future high-speed systems depends on ad-

ditional issues like the costs and integratebility which the manufacturers of telecommunication systems have to make.

7.2 Recommendations

It is not recommended to increase the demultiplexed bit rate of 10 Gb/s to 40 Gb/s for demultiplexing a 160 Gb/s signal. The gain recovery time of the current SOAs is insufficient for this purpose. A faster amplifier nonlinearity, like four-wave mixing, is preferred.

It is also recommended to use photonic integrated circuits (PICs) if this research is continued as it improves stability and reduces the volume of the experimental setup. PIC implemented technology also allows field trial measurements that have not yet been performed with integrated 1.3 μm polarisation insensitive MQW SOAs.

A more detailed and analytical approach describing the operation of the all-optical clock recovery circuit using the Sagnac interferometer based saturable absorber is recommended. The theory presented in Sec. 5.2.2 could form the basis for a model that e.g. relates values of parameters to stable or unstable operation of the ring laser.

Most simulation software was written in interpreter based numerical evaluation software which was used within the European ACTS project "Upgrade". For conducting future numerical simulations it is recommended that simulation software is compiled so that improved performance of the numerical models allows the computation of the BER instead of the channel extinction ratio for better comparison between theoretically and experimentally obtained data.

Future SOA based transmission experiments at bit rates ≥ 160 Gb/s might use optical fibre gratings not only for compensation of dispersion but also for compensation of average chirp on the data signal which results from SOA saturation.

Appendix A

List of abbreviations

abs.	absorber
ACTS	Advanced Communications Technologies and Services
amp.	amplifier
ASE	amplified spontaneous emission
ATM	asynchronous transfer mode
att.	attenuator
BER	bit error rate
BERT	bit error rate tester
BPF	band pass filter
ccw	counter clockwise
cw	clockwise
cplr	coupler
DCF	dispersion-compensating fibre
DEMUX	demultiplexer
DFB	distributed feed-back
DFP	dispersion-flattened fibre
DSF	dispersion-shifted fibre
ECTMLL	external-cavity tunable mode-locked laser
EDFA	erbium-doped fibre amplifier
ER	extinction ratio
ETDM	electrical time-domain multiplexing electrical time-domain demultiplexer
FOA	fibre optical amplifier
FWHM/fwhm	full-width half-maximum
FWM	four-wave mixing
GVD	group-velocity dispersion
HWP	half-wave Plate
IP	internet protocol
ISI	inter-symbol interference
LD	laser diode
MMF	multimode fibre

MMI	multimode interference
mod.	modulator
MQW	multiple quantum well
MSSI	mid-span spectral inversion
MUX	multiplexer
MZ	Mach Zehnder
NALM	non-linear amplifying loop mirror
NF	noise figure
NOLM	non-linear optical loop mirror
NRZ	non-return to zero
OBPF	optical band-pass filter
OCR	optical clock recovery
OPC	optical phase conjugation
OPR	optically pre-amplified receiver
ORU	optical repeater unit
OS	optical switch
OTDM	optical time-domain multiplexing
	optical time-domain demultiplexer
OXGSRL	optically cross gain-switched ring laser
PD	photodiode
PDFA	praseodymium-doped fibre amplifier
PIC	photonic integrated circuit
PIN	p-doped intrinsic n-doped
PLL	phase locked loop
PMF	polarisation-maintaining fibre
Pol. Ctrl.	polarisation controller
PPG	pulse pattern generator
PRBS	pseudo random bit sequence
QWP	quarter-wave plate
RF	radio frequency
RZ	return to zero
SDH	standard digital hierarchy
SLALOM	semiconductor laser amplifier in a loop mirror
SMF	single mode fibre
SOA	semiconductor optical amplifier
SPM	self-phase modulation
SSMF	standard single-mode fibre
TDM	time-division multiplexing
	time-division demultiplexer
TE	transverse electric
TM	transverse magnetic
TOAD	terahertz optical asymmetrical demultiplexer
WDM	wavelength-division multiplexing

Appendix B

Samenvatting

Gedurende de laatste jaren is volledig optische signaalverwerking een attractieve oplossing gebleken voor capaciteitsvergroting van bestaande optische netwerken. De dispersie van standaard optische glasvezel is minimaal in het $1,3 \mu\text{m}$ golflengte gebied waardoor transmissie op hoge snelheid en over lange afstand hier relatief gemakkelijk is. De introductie van polarisatie ongevoelige quantum put optische halfgeleiderversterkers (MQW SOAs) heeft tot de constructie van volledig optische regeneratoren geleid die conventionele elektrische regeneratoren overbodig maken. Wanneer in de tijd gestapelde datasnelheden te groot worden om elektrisch verwerkt te worden kan verwerking in het optische domein plaats vinden. Deze verwerking is niet-lineair en vergt daarom een niet-lineair component. SOAs komen in aanmerking hiervoor vanwege de niet-lineaire afhankelijkheid tussen de versterking en de lichtsterkte in de versterker. Door een SOA asymmetrisch in een Sagnac interferometer te plaatsen wordt een optische schakelaar verkregen. De schakelaar kan voor een korte duur worden gesloten door een korte puls aan de SOA toe te voeren zodat deze verzadigt. In de literatuur staat deze schakelaar bekend als de “Terahertz Optical Asymmetrical Demultiplexer” of TOAD.

In het geval van 10 Gb/s naar 2,5 Gb/s volledig optische splitsing is een schakelsignaal nodig dat bestaat uit smalle pulsen met een herhalingsfrequentie van 2,5 GHz. Een ringlaser, opgebouwd rond een SOA waarvan de versterking door een extern sinus-vormig optisch signaal gemoduleerd wordt, levert een 2,5 GHz pulstrein waarvan de pulsen 12 – 20 ps smal zijn. In combinatie met de optische schakelaar leverde dit volledig foutloze splitsing van 10 Gb/s naar 2,5 Gb/s op. De ontvangstgevoeligheid ging hierbij met 2,3 dB achteruit. Vermogensfluctuaties van 13 dB aan de ingang van het systeem konden foutloos worden verwerkt.

Voor 40 Gb/s naar 10 Gb/s volledig optische splitsing werd een zelfde optische schakelaar gebruikt. Het doel van dit volledig optische splitscircuit is te onderzoeken hoe polarisatie ongevoelige MQW SOAs gebruikt kunnen worden voor het compenseren van verliezen in een verbinding van meer dan 200 km standaard optische glasvezel. Hiertoe is tevens een volledig optische schakeling voor klokextractie op 10 GHz gerealiseerd. Dit circuit is gebaseerd op een ringlaser met een verzadigbare versterker en absorbers. De absorbers bestaat uit een Sagnac interferometer met daarin een asymmetrisch geplaatste SOA. Een optische verzwakker in de Sagnac interferometer staat toe de SOA asymmetrisch te exciteren en te verzadigen. De uitgangspulsen van deze geometrie zijn versmalde replica's van de ingangspulsen. In het resterende gedeelte van de ringlaser vindt verbreding plaats. Zowel theoretisch

als praktisch leverde dit een stabiele stroom van optische pulsen op. De pulsbreedtes van dit 10 GHz schakelsignaal waren kleiner dan 5 ps. Dit herwonnen schakelsignaal was instaat om in een terugkoppel lus met de TOAD uit een 40 Gb/s signaal een 10 Gb/s signaal foutloos af te splitsen. Hierbij ging 2 dBm aan ontvangstgevoeligheid verloren. Het dynamische bereik aan de ingang bedroeg 7,0 dB. Om het systeem op te starten moest een speciale procedure gevolgd worden. Omdat het systeem vrijlopend is moeten periodiek instellingen bijgesteld worden.

Deze opstelling is gebruikt voor de overbrugging van 216 km standaard optische glasvezel met periodiek geplaatste ORUs. De lengte van de secties werd aangepast aan de versterking van de ORUs om overmaat aan versterking tegen te gaan. Overmatige versterking resulteert in verzadiging, patroon effecten, toename van ruis, hetgeen foutloze transmissie in gevaar brengt. Na 216 km werd een 10 Gb/s van het 40 Gb/s signaal afgesplitst en foutvrij gedetecteerd waarbij de ontvangstgevoeligheid met 4,0 dB afnam. Alle vier de kanalen gedroegen zich bijna identiek.

Dezelfde configuratie werd ook gebruikt als een volledig optische 10 Gb/s regenerator. Overmatige versterking leidde tot bitfoutenkans curven die duidelijk “ruisvloeren” lieten zien. Deze konden verwijderd worden met dezelfde configuratie die gebruikt is in de 40 Gb/s naar 10 Gb/s experimenten.

Theoretische analyses laten een grote afhankelijkheid zien tussen de optische koppeling en de prestaties van de op de Sagnac interferometer gebaseerde optische schakelaar. De kanaalonderdrukkingsverhouding is geïntroduceerd als een kwantitatieve maat voor de prestatie van de optische schakelaar. Deze verhouding is gedefinieerd als de verhouding tussen de hoeveelheid gewenste energie en niet gewenste energie in het afgesplitste signaal aan de uitgang. Verscheidende simulaties voor de splitsing van 40 Gb/s naar 10 Gb/s zijn uitgevoerd met verschillende parameters voor de optische koppeling, de versterker, de TOAD en het schakelsignaal. Drie in complexiteit toenemende SOA modellen zijn numeriek geïmplementeerd in simulatiegereedschappen voor theoretische analyse aan de TOAD.

Toekomstige 40 Gb/s transmissiesystemen in het 1,3 μm golflengte gebied kunnen gerealiseerd worden met 1,3 μm MQW SOAs. Polarisation ongevoelige MQW SOAs kunnen zowel voor lijnversterking als voor niet-lineair onderdeel in signaalverwerkende toepassingen zoals volledig optische splitsing van in de tijd gestapelde signalen, volledig optische klokextractie en volledig optische regeneratie. In toekomstige volledig optische hoge snelheid netwerken kunnen diverse volledig optische signaalverwerkende circuits geïntegreerd worden tot knooppunten die autonoom datastromen (her)configureren en schakelen.

Appendix C

Curriculum vitae

Robert Smets was born on September 25th, 1971 in Eindhoven, the Netherlands. He was raised in the vicinity of Eindhoven and finished his pre-university education in 1989, after which he studied Electrical Engineering at the Eindhoven University of Technology. In August 1994 Robert obtained the M.Sc. degree in Electrical Engineering at the department of Electromagnetics of the school of Electrical Engineering of the Eindhoven University of Technology. During his graduation project he worked in close conjunction with the Netherlands Organization for Applied Scientific Research (TNO Physics and Electronics Laboratory). Subsequently, Robert accepted a position at the department of Telecommunication Technology and Electromagnetics, at the same university, in collaboration with Uniphase Netherlands B.V. to pursue his Ph.D. degree. During this project Robert participated in the European ACTS project "Upgrade" where he was responsible for the realisation of several all-optical processing circuits and where he became an expert in fibre-optic communication technology. He has authored and co-authored eleven scientific contributions and has one patent pending. His field of interest includes nonlinear optics, fibre-optic communication technology, radio technology, electromagnetics, measurement and data acquisition technology. During his Ph.D. project he became an instructor of the Random Signal Theory course, that is mandatory for second-year students.

Robert is a member of the examination board of the department of radio communication of the Dutch administration. He recently accepted a position at the Forward Looking Work group of the Switching and Access Solutions division of Lucent Technologies in Huizen, the Netherlands.

Stellingen behorende bij het proefschrift

All-Optical Time-Domain Demultiplexing and
Signal Regeneration using 1300 nm Semiconductor
Optical Amplifiers

door

R.C.J. Smets

20 september 1999

1. Het niet-ideale gedrag van de optische koppeling in een TOAD configuratie is bepalend voor de asymmetrie waarmee een halfgeleiderversterker in deze configuratie geplaatst dient te worden. Een afweging moet worden gemaakt tussen de kanaalonderdrukking waarmee en de tijdsduur waarin de TOAD (Terahertz Optical Asymmetrical Demultiplexer) een inkomend signaal naar de uitgang doorschakelt.
2. Een Sagnac interferometer met daarin een asymmetrisch geplaatste en aangestuurde verzadigbare halfgeleiderversterker gedraagt zich onder bepaalde voorwaarden als een verzadigbare absorbers.
3. Een datatransportsysteem bestaande uit verzadigbare optische halfgeleiderversterkers en optische glasvezel ondersteunt geen transmissie van solitonen.
4. Een mondiale toepassing van volledig optische signaalverwerking hangt in grote mate af van de beschikbaarheid van geïntegreerde, volledig optische geheugens.
5. De mechanische stabiliteit van peperdure meetapparatuur voor het meten van bitfoutenkansen is soms gelijk aan die van een spotgoedkope draagbare cassettespeler.
6. Het feit dat opwarming van de hersenen door GSM toestellen te verwaarlozen is betekent niet dat het gebruik van GSM toestellen de gezondheid niet zou kunnen schaden.
7. Kijk- en luistergeld is een straf voor mensen die op commerciële zenders afstemmen.
8. Bestrijding van gevaarlijk, agressief en asociaal rijgedrag middels het verhogen van de strafmaat is tot mislukking gedoemd indien de pakkans niet verhoogd wordt en het rijbewijs niet eerder in beslag wordt genomen.
9. De Nederlandse Spoorwegen kan de het gevoel van veiligheid bij haar klanten vergroten door haar product uitsluitend op basis van lidmaatschap aan te bieden.
10. Door de toenemende commerciële houding van de overheid krijgt zij een stevigere greep op technologische vernieuwing. Uit recente schandalen en blunders blijkt niet dat zij deze verantwoordelijkheid aankan.
11. Indien het management van de Nederlandse Spoorwegen (inclusief verkeersleiding) evenveel paardenkrachten zou bezitten als een locomotief dan zou de overmatige vertraging die opgelopen wordt door chronische sein- en wisselstoringen niet meer voorkomen.
12. Education is an admirable thing, but it is well to remember from time to time that nothing that is worth knowing can be taught.

Oscar Wilde